Hans Irschik · Alexander Belyaev
Michael Krommer *Editors*

Dynamics and Control of Advanced Structures and Machines

Springer

Dynamics and Control of Advanced Structures and Machines

Hans Irschik • Alexander Belyaev •
Michael Krommer
Editors

Dynamics and Control of Advanced Structures and Machines

Springer

Editors
Hans Irschik
Institute of Technical Mechanics
Johannes Kepler University Linz
Linz, Austria

Michael Krommer
Institute of Mechanics and Mechatronics
Vienna University of Technology
Vienna, Austria

Alexander Belyaev
Institute of Problems in Mechanical Engineering
Russian Academy of Sciences
St. Petersburg, Russia

ISBN 978-3-319-43079-9 ISBN 978-3-319-43080-5 (eBook)
DOI 10.1007/978-3-319-43080-5

Library of Congress Control Number: 2016955567

Printed on acid-free paper

This Springer imprint is published by Springer Nature
The registered company is Springer International Publishing AG Switzerland

Preface

This book presents a collection of 25 contributions presented during the *2nd International Workshop on Advanced Dynamics and Model Based Control of Structures and Machines*, which was held at TU Wien in September 2015. It contains 9 full-length papers of presentations from Austria, 7 from Russia, 4 from Japan, 3 from Italy and 2 from Taiwan.

The general goal of the workshop was to present and discuss the frontiers in the mechanics of controlled machines and structures. The workshop continued a series of international workshops, the *Japan-Austria Joint Workshop on Mechanics and Model Based Control of Smart Materials and Structures*, the *Russia-Austria Joint Workshop on Advanced Dynamics and Model Based Control of Structures and Machines* and the *1st International Workshop on Advanced Dynamics and Model Based Control of Structures and Machines*. The first two workshops took place in Linz, Austria, in September 2008 and April 2010, and the third one in St. Petersburg, Russia, in July 2012. The key objective of the workshop was to further strengthen the long-standing cooperation between research teams from Austria, Japan and Russia and to initiate new collaborations with other participating renowned scientists from Europe and Taiwan.

We dedicate the book to Franz Ziegler who passed away on January 4th, 2016. Franz Ziegler delivered his last scientific talk on "Free and forced vibrations of fuzzy structures" at the workshop. This contribution, which is included in the present volume, brings his long list of numerous papers published in the most prestigious peer-reviewed journals, books, and conference proceedings to an end.

We, the undersigned Editors, together with all his other friends and colleagues all over the world, will hold Franz Ziegler in grateful memory.

St. Petersburg, Russia — Alexander Belyaev
Linz, Austria — Hans Irschik
Vienna, Austria — Michael Krommer
June 2016

Acknowledgements

Support of the *2nd International Workshop on Advanced Dynamics and Model Based Control of Structures and Machines* from the K2 area of the *Linz Center of Mechatronics GmbH* is gratefully acknowledged. This area is promoted as a K2 project with the project name *Austrian Competence Center of Mechatronics (ACCM)* in the context of *Competence Centers for Excellent Technologies (COMET)* by BMVIT, BMWFJ and by the country Upper Austria.

The editors also wish to thank the *Institute of Mechanics and Mechatronics* at TU Wien for serving as host of the workshop and Mrs. Silvia Schilgerius from *SpringerWienNewYork* for her support during the preparation of this book.

Contents

Free and Forced Vibrations of Fuzzy Structures

Franz Ziegler

Abstract Stochastic free and forced vibrations of layered beams are analyzed that result from a single bounded random stiffness parameter whose probability density function is considered to be zero outside of a given interval, i.e., it is a member of a fuzzy set with bounded uncertainty. The relevant properties of natural vibrations of an ensemble of sandwich beams with three perfectly bonded layers under hard hinged support conditions are worked out in detail when a bounded random shear stiffness of the core material is assigned by employing interval mathematics. The main structure of a compound single-span railway bridge, effectively modeled as a two-layer beam, is subjected to a single moving load as well as to a series of repetitive moving loads traveling with constant speed. It serves as a complex example for the resulting forced random vibrations and resonances under the severe condition of an elastic interface slip of bounded random stiffness. In both cases exact homogenization yields a stochastic sixth-order partial differential equation of motion of the layered beam. Light modal damping is considered. The analysis of the illustrative problems is based on the interval representation with a triangular membership function of the stiffness modulus assigned. A short comment provides information on the limits of such triangular membership functions. Membership functions in the form of envelopes of the random natural frequencies, the dynamic magnification factors, and the phase angles in free vibrations are determined. Both, fuzzy peak deflection and acceleration are derived for the forced single-span compound railway bridge subjected to the moving loads. Approximating superposition of modal maxima is considered by standard routines of reliability analysis.

Franz Ziegler was deceased at the time of publication.

H. Irschik et al. (eds.), *Dynamics and Control of Advanced Structures and Machines*, DOI 10.1007/978-3-319-43080-5_1

1 Introduction

In general, the application of the fuzzy finite element method, see, e.g., [3, 9], is required when the matrix in composite structures exhibits fuzzy randomness of the material parameters. However, when extending the work on two- and symmetric three-layer beam-, plate-, and shell structures based on an exactly homogenized model [1, 4, 5, 8] to include either fuzzy interface slip or fuzzy core stiffness, we can avoid numerical analyses and analytically work out the effects on the random dynamic properties of these fuzzy structures. Exemplarily, random free vibrations of a symmetric three-layer single-span beam with hard hinged supports, exhibiting fuzzy shear stiffness of the core material, are considered first, with details documented in [6, 7]. The practically very important case of a single-span compound bridge consisting in its main structure of two steel girders connected (elastically) to the concrete deck, when exactly homogenized, refers to the model of an asymmetric two-layer elastic beam exhibiting the practically most important defect of elastic interlayer slip with the major uncertainty of its elastic modulus. Life loads of a train are here simply modeled as the passage of concentrated forces, which pass the bridge with constant speed. The presentation of the resulting forced vibrations in the form of non-dimensional response quantities is adopted from a recent comprehensive study on the dynamic effects of high-speed trains on such a simple fuzzy bridge structure [2]. The fundamental parameters are taken from [12]. For a more sophisticated deterministic analysis, see [13]. A full stochastic analysis of such a bridge with temperature effects on stiffness, etc., included is presented in [10].

The analysis of both illustrative examples is based on the interval representation (interval of confidence at a given level of presumption, i.e., α-cut) with a triangular fuzzy membership function of the relevant random stiffness prescribed. Fuzzy membership functions of the response are defined using fuzzy set theory [11, 14], however, avoiding artificial uncertainties. Where possible, envelope functions are defined representing the bounds of the random response. Consequently, such a random stiffness modulus is considered to be an interval number or a member of a fuzzy set which contains the sure design value. Such an interval representation transforms the deterministic parameter to inclusive set values with bounded uncertainty, see Fig. 1a. Another interpretation of such an interval number includes intervals of confidence for α-cuts of fuzzy sets. Such a parametric extension as shown in Fig. 1b may even include a worst-case scenario, i.e., $\min k_2(\alpha = 0) = 0$.

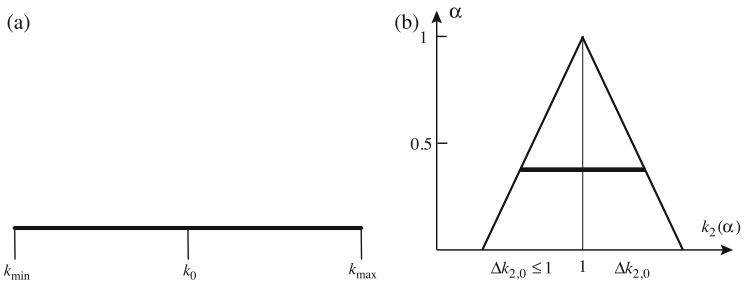

Fig. 1 Single bounded random structural parameter, e.g., stiffness. (**a**) Defined interval contains sure design value k_0. Outside of the interval, probability is zero. (**b**) Fuzzy set: interval of confidence at a given level of presumption α-cut. Non-dimensional stiffness $k_2(\alpha)$ is referred to its design value. Isosceles distribution assigned

2 Effects on Free Vibrations: Example: Fuzzy Sandwich Beam

For linear elastic, symmetrically arranged three-layer beams, Fig. 2, the following assumptions are made: (1) the faces are rigid in shear with their individual flexural stiffness $B_1 = B_3$ considered. (2) The shear stiffness of the elastic core is a bounded random variable while its bending stiffness is neglected. Following [5], an exact homogenization renders the homogeneous partial differential equation (PDE) of sixth order in terms of the common deflection and for the case of free vibrations,

$$w_{,xxxxxx} - \lambda^2 w_{,xxxx} + \frac{\mu}{B_\infty}\ddot{w}_{,xx} - \lambda^2 \frac{\mu}{B_\infty}\ddot{w} = 0, \quad \mu = \sum_{i=1}^{3} \varrho_i h_i, \tag{1}$$

$$B_0 = B_1 + B_3,$$

$$B_\infty = B_0 + (D_1 + D_3)d^2, B_0/B_\infty = 1/\left[1 + 3\,(1 + h_2/h_1)^2\right] \leq 1/4,$$

see again Fig. 2, with the bounded random parameter related to the core shear modulus $\kappa_2^2 G_2(\alpha)$ with its assigned design value $\left(\kappa_2^2 G_2\right)_0$ at $\alpha = 1$ within the level of presumption $0 \leq \alpha \leq 1$,

$$\lambda^2 = \frac{2b}{h_2}\frac{B_\infty}{D_1 B_0}\left(\kappa_2^2 G_2\right)_0 k_2(\alpha), \quad k_2(\alpha) = \left[\kappa_2^2 G_2(\alpha)\right] / \left(\kappa_2^2 G_2\right)_0 . \tag{2}$$

For the single-span beam, length l, under hard hinged support conditions, the ortho-normalized mode shapes result with a stochastic normalization factor,

$$\varphi_n(x) = \sin \beta_{1n} x, \quad \beta_{1n} = n\pi/l, \quad A_n = \left[(\mu l/2B_\infty)\left(\lambda^2 + \beta_{1n}^2 B_\infty/B_0\right)\right]^{-1/2} . \tag{3}$$

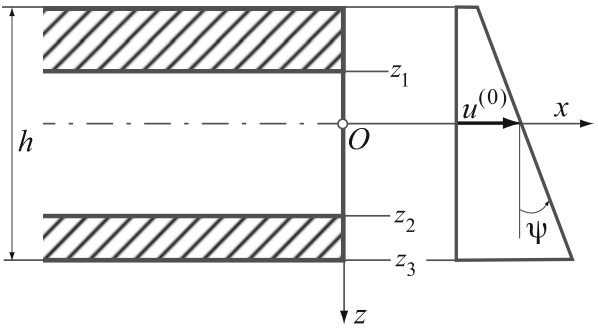

Fig. 2 Dimensions of the sandwich beam. Common cross-sectional rotation after homogenization ψ, as shown, is crucially eliminated. Fuzzy core shear stiffness in layer 2 is considered. Deflection w is referred to the elastic centroid O

The random natural frequencies, referred to the sure values at rigid core shear stiffness, $\omega_{n\infty}^2 = \beta_{1n}^4 B_\infty/\mu$, are

$$[\omega_n(\alpha)/\omega_{n\infty}]^2 = \frac{(B_0/B_\infty) + \gamma_{2,n} k_2(\alpha)}{1 + \gamma_{2,n} k_2(\alpha)}, \quad \gamma_{2,n} = \left(\kappa_2^2 G_2\right)_0 2b/\beta_{1n}^2 D_1 h_2. \tag{4}$$

With light viscous modal damping $\zeta_n = \zeta \ll 1$ understood, the random dynamic magnification factor $\chi_n(\alpha)$ and the stochastic phase angle $\phi_n(\alpha)$ are expressed by textbook formulas; see, e.g., [15],

$$\chi_n = \left\{1 - 2\left(1 - 2\zeta^2\right)(\omega/\omega_n(\alpha))^2 + (\omega/\omega_n(\alpha))^4\right\}^{-1/2},$$

$$\tan\phi_n = 2\xi \frac{\omega}{\omega_{n\infty}} \left[\sqrt{\frac{(B_0/B_\infty) + \gamma_{2,n} k_2(\alpha)}{1 + \gamma_{2,n} k_2(\alpha)}} - \left(\frac{\omega}{\omega_{n\infty}}\right)^2 \sqrt{\frac{1 + \gamma_{2,n} k_2(\alpha)}{(B_0/B_\infty) + \gamma_{2,n} k_2(\alpha)}} \right]^{-1}. \tag{5}$$

Numerical results for bounds and even for envelope functions are thus straightforwardly derived, putting, e.g., the design values $B_0/B_\infty = 0.1 < 1/4$ and $\gamma_{2,n} = 0.25$ in Eqs. (4) and (5). Exemplarily, results are shown in Figs. 3, 4, and 5, for light modal damping $\zeta_n = \zeta = 0.04$. More details are presented in [6, 7].

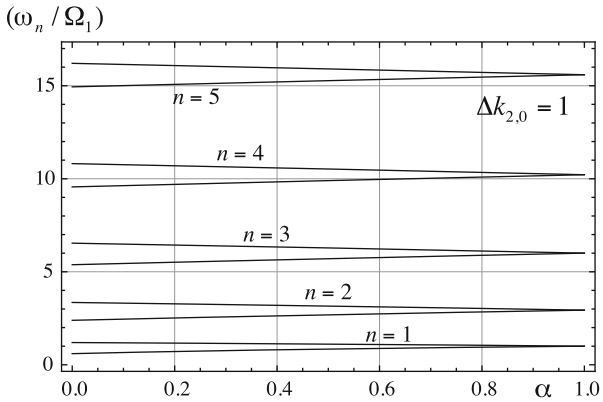

Fig. 3 Bounds of the first five natural frequencies when referred to the sure fundamental frequency: worst-case scenario. Note the increased fuzziness of the higher modes [7]

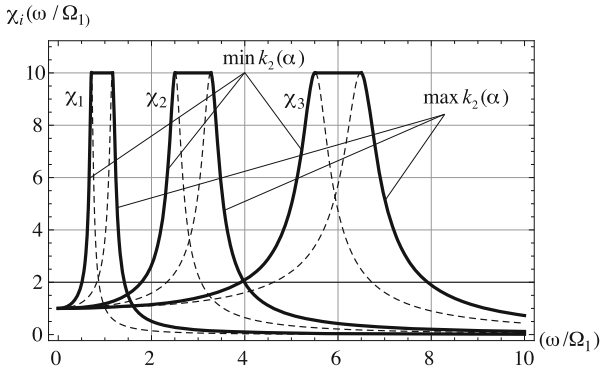

Fig. 4 Envelopes of the first three random DMFs [7]. $\alpha = 0$-cut; worst-case scenario $\alpha = 0$

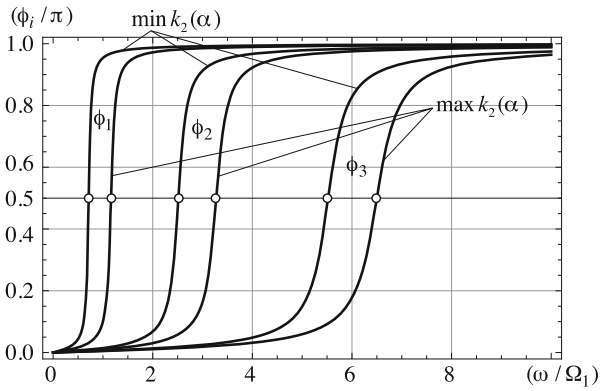

Fig. 5 Envelopes of the first three random phase angles [7]. Conditions likewise to Fig. 4

2.1 *Effects of Non-symmetric Uncertainty*

In the core shear stiffness, Fig. 2, we introduce a non-symmetry factor $\Lambda > 1$, such that $\min k_2(\alpha) = \alpha$ remains unchanged and $\max k_2(\alpha) = 1 + \Lambda(1 - \alpha)$. When considering the bounds of the natural frequencies just in the worst-case scenario, the possibility of $\max \omega_n = \min \omega_{n+1}$ becomes true for $n = 2$ at the minimum of $\Lambda = 12.16$, i.e., overlapping natural frequency intervals occur in an ensemble of fuzzy sandwich beams. Further, for the material parameters $B_0/B_\infty = 1/16$ and $B_0/B_\infty = 0.198 < 1/4$, the fundamental frequency and the next higher one, respectively, exhibit singularities, i.e., the non-symmetric triangular distribution of uncertainty becomes obsolete. However, no singularity is possible for higher modes, $n \geq 3$. For details of analysis, see again [7].

3 Effects on Forced Vibrations: Example: Fuzzy Compound Railway Bridge

The practically very important case of a single-span compound bridge consisting, e.g., of two steel girders connected (elastically) to the concrete deck, when smeared, refers to the model of an asymmetric two-layer elastic beam exhibiting the main defect of elastic interlayer slip with the major uncertainty of its elastic modulus, Fig. 6. This structural uncertainty of the physical interface can be attributed to imperfections, modeling inaccuracies, aging effects, and its design complexity. Consequently, the slip modulus is considered to be a random variable whose

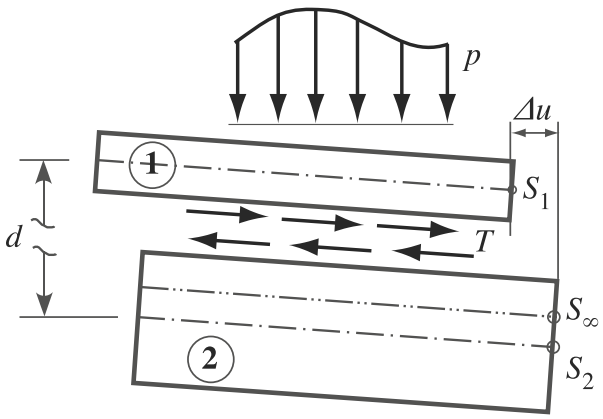

Fig. 6 Model of the main structure of the fuzzy compound bridge [2]: effective elastic two-layer beam with fuzzy elastic interlayer slip. Layer one refers to the RC-concrete deck. Layer two represents the rigidity of two steel girders. Bounded random shear flow $T = k(\alpha)\Delta u$. Stiffness center S

probability density function is not known but is non-zero only in the range of an interval, i.e., it is considered to be an interval number or a member of a fuzzy set, see again Fig. 1. Exact homogenization of the two-layer beam renders the PDE of sixth order, analogously to Eq. (1), see again [1]. Consequently, in the design stage, the simply supported bridge of length l may be simply traveled by a series of repetitive single concentrated forces with equal distance l_d and with constant speed v to model the forcing in the inhomogeneous Eq. (6), where the random parameters are adapted to the fuzzy elastic modulus of the interlayer slip $k(\alpha)$ with the sure design value $k_0 = k(\alpha = 1)$. The parameters of the two elastic layers $j = 1, 2$, are: elastic modulus E_j, effective cross-sectional area A_j, and flexural rigidity $B_j = D_j r_j^2$ with $D_j = E_j A_j$,

$$w_{,xxxxxx} - \lambda^2 w_{,xxxx} + \frac{\mu}{B_0}\ddot{w}_{,xx} - \lambda^2 \frac{\mu}{B_\infty} p + \frac{1}{B_0} p_{,xx}, \quad \lambda^2(\alpha) = k(\alpha)\lambda_0^2/k_0,$$
$$B_0 = B_1 + B_2,\ B_\infty = B_0 + d^2 D_1 D_2/(D_1 + D_2),\ \lambda_0^2 = k_0\left(\frac{1}{D_1} + \frac{1}{D_2} + \frac{d^2}{B_0}\right). \tag{6}$$

Considering just a single concentrated traveling force F_i in Eq. (6), where $w(x,t) \Rightarrow w_i(x,t)$, the lateral load becomes in standard notations [2],

$$p_i = F_i \delta(x - \xi_i)\left[H(t - t_i^0) - H(t - t_i^E)\right], \quad \xi_i = vt - s_i, \quad t_i^0 = \frac{s_i}{v}, \quad t_i^E = \frac{s_i + l}{v}. \tag{7}$$

A properly truncated modal expansion, Eq. (3), with the definitions given in Eq. (6) applies as well,

$$w_i(x,t) = \sum_{i=1}^{N} Y_i^{(n)}(t)\varphi_n(x). \tag{8}$$

By changing the ortho-normalized modal coordinates to $\overline{Y}_y^{(n)}(t;\alpha) = A_n(\alpha)Y_i^{(n)}(t)$ the random load in Eq. (6) is "swallowed" and the modal equations result, crucially simplified, with a deterministic load participation factor $L_i^{(n)}$. Only the natural frequencies are left as the remaining bounded random coefficients in Eq. (9), light modal damping is also added here [2],

$$\ddot{\overline{Y}}_i^{(n)} + 2\zeta_n\omega_n\dot{\overline{Y}}_i^{(n)} + \omega_n^2\overline{Y}_i^{(n)} = \frac{2F_i}{\mu l}L_i^{(n)},$$
$$L_i^{(n)} = [H(t - s_i/v) - H(t - (s_i + l)/v)]\sin n\pi(vt - s_i)/l. \tag{9}$$

Bounds of the modal coordinate $\overline{Y}_i^{(n)}$ and its rate $\dot{\overline{Y}}_i^{(n)}$ are determined by proper time convolution and, subsequently, the corresponding modal acceleration $\ddot{\overline{Y}}_i^{(n)}$ is

determined from a rearranged form of Eq. (9). The bounds of the natural frequencies at α-cuts are inserted. Thus, for a number M of repetitive single concentrated forces, e.g., lateral displacement results by summation

$$w_n(x,t;\alpha) = \overline{Y}_n(t;\alpha)\phi_n(x) \Rightarrow \overline{Y}_n(t;\alpha) = \sum_{i=1}^{M} \overline{Y}_i^{(n)}(t;\alpha). \tag{10}$$

In reliability analysis it suffices to evaluate the maximum response searched for by considering either the minimum or maximum bound of the interface stiffness in an α-cut, e.g., just in the worst-case scenario. It can be found by various methods of approximating superposition of a proper finite number of these random modal coordinates. The following combination rules, common in structural dynamics are evaluated, the absolute sum rule, ABSUM, rendering an upper limit and the square root of the sum of squares, SRSS, the latter was found to be inadequate here, see again [2], and, best suited, the modal series, since it is exact for N modes,

$$w_{\max}(x;\alpha) = \max_t \left| \sum_{n=1}^{N} w_n(x,t;\alpha) \right|. \tag{11}$$

Resonances are observed at critical speeds due to the rhythmic repetition in the load series [12]: for the deterministic bridge $V_j^{(n)} = \omega_n l_d/2\pi j, j = 1,2,3,\ldots$ A resonance of second order is due to a single traveling force, $\overline{V}_n = \omega_n l/\pi n$, it is of minor importance here, see, e.g., [15, p. 626]. For a detailed analysis, see again [2].

3.1 *Some Numerical Results for a Standard Compound Bridge: Concrete Deck, Two Steel Girders*

The single span has the length $l = 40.0\,\mathrm{m}$ and a mass density of $\mu = 15{,}000\,\mathrm{kg\,m^{-1}}$. The design value of the elastic interface slip modulus is $k_0 = 60.0 \times 10^7\,\mathrm{N/m^2}$. We note the fundamental frequency $f_1(\alpha = 1) = 2.81\,\mathrm{Hz}$ and, for the ideal rigid bond, $f_{1,\infty} = 3.04\,\mathrm{Hz}$ [2]. At first, the intervals of uncertainty of the first ten natural frequencies are evaluated for the bounded random interface stiffness $k(\alpha)$, rendering qualitatively analogous results as depicted in Fig. 3,

$$\omega_n^2(\alpha) = \omega_{n\infty}^2 \frac{B_0/B_\infty + \gamma_{2,n}k(\alpha)/k_0}{1 + \gamma_{2,n}k(\alpha)/k_0}, \quad \omega_{n\infty}^2 = \frac{\beta_{1n}^4 B_\infty}{\mu}, \quad \gamma_{2,n} = \frac{k_0}{\beta_{1,n}^2}\frac{1 + D_2/D_1}{D_2}. \tag{12}$$

In a second step, the randomly fuzzy response of the bridge is calculated when a single concentrated force passes with constant speed. Maximum deflection and maximum acceleration, say at mid-span and at the quarter-point, are calculated and

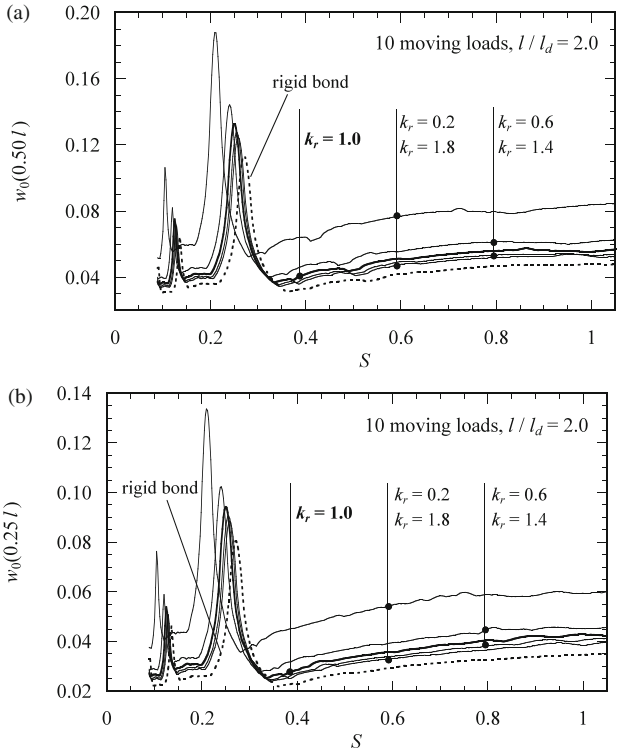

Fig. 7 Uncertain peak lateral deflection induced by ten repetitive moving loads, distance $l_d = 20$ m, speed parameter S, limiting cases for two fuzzy intervals of the random interface stiffness, [2]. (**a**) at mid-span, (**b**) at the quarter-point

stored as functions of the speed parameter $S = \pi v/\Omega_1 l$, where $\Omega_1 = \omega_1(\alpha = 1)$. Maximum deflections induced by ten repetitive moving loads are depicted in Fig. 7, where $w_0(x;\alpha) = w_{\max}(x;\alpha)B_\infty/Fl^3$. For details, see again [2].

In Fig. 7 it is observed that the upper limit of a certain fuzzy interval leads to a larger deviation of the response from that of the deterministic bridge than for the lower limit. That means, the softer the interlayer-slip-modulus the larger the increase of the response magnification becomes. An increase of the interlayer stiffness does not have this pronounced impact on the decrease of the peak deflection.

Finally it is mentioned again that a comprehensive stochastic analysis of a full model of such a railway bridge is performed in [10].

4 Conclusions

For fuzzy symmetric three-layer structures (sandwich beams) and for fuzzy two-layer composites (compound railway bridge) the exact homogenization yields a stochastic partial differential equation of sixth order. Intervals of confidence of the dynamic response are determined either for fuzzy core shear stiffness or for fuzzy elastic interlayer slip. Thus, intervals of confidence of the natural frequencies result. Bounds of the dynamic magnification factor and the phase angles are presented in the form of envelope functions. Effects on resonances in repetitive loadings of the fuzzy railway bridge are studied within reliability measures of the maximum response; say of flexural displacements, presenting bounds as function of the speed parameter. Even the worst-case scenarios can be considered. Truncated modal expansions are transformed such that the modal load participation factors become deterministic leaving only the natural frequencies as the random parameters.

References

1. Adam C, Heuer R, Jeschko A (1997) Flexural vibrations of elastic composite beams with interlayer slip. Acta Mech 125:17–30
2. Adam C, Heuer R, Ziegler F (2012) Reliable dynamic analysis of an uncertain compound bridge under traffic loads. Acta Mech 223:1567–1581
3. Hanss M, Willner K (2000) A fuzzy arithmetical approach to the solution of finite element problems with uncertain parameters. Mech Res Commun 27:257–272
4. Heuer R (2004) Equivalence of the analyses of sandwich beams with or without interlayer slip. Mech Adv Mater Struct 11:425–432
5. Heuer R (2014) On equivalences in the dynamic analysis of layered structures. In: Belyaev AK, Irschik H, Krommer M (eds) Mechanics and model-based control of advanced engineering systems. Springer, Heidelberg, pp 155–162. ISBN:978-3-7091-1570-1
6. Heuer R, Ziegler F (2011) Vibrations of layered structures with fuzzy core stiffness/fuzzy interlayer slip. In: Belyaev AK, Langley RS (eds) Proceedings of the IUTAM-symposium on the vibration analysis of structures with uncertainties. Springer, Dordrecht, pp 29–42
7. Heuer R, Ziegler F (2011) Modal analysis of laminated beams with fuzzy core stiffness/fuzzy interlayer slip. J Mech Mater Struct (JoMMS) 6(1–4):213–230
8. Irschik H, Heuer R, Ziegler F (2000) Statics and dynamics of simply supported polygonal Reissner-Mindlin plates by analogy. Arch Appl Mech 70:231–244
9. Mueller B, Beer M (2004) Fuzzy randomness. Springer, Berlin
10. Salcher P, Pradlwarter H, Adam C (2016) Reliability assessment of railway bridges subjected to high-speed trains considering the effects of seasonal temperature changes. Eng Struct (accepted for publication). doi:10.1016/j.engstruct.2016.08.017
11. Viertl R, Hareter D (2006) Beschreibung und analyse unscharfer information - statistische methoden für unscharfe daten (in German). Springer, Berlin
12. Yang YB, Yau JD, Wu YS (2004) Vehicle-bridge interaction dynamics: with applications to high-speed railways. World Scientific, Singapore
13. Yau JD, Yang YB (2016) Resonance of a train car traveling over multi-unit simple beams. This paper is part of this Springer book, where also this paper of Ziegler will be published
14. Zadeh LA (1965) Fuzzy sets. Inf Control 8:338–353
15. Ziegler F (1998) Mechanics of solids and fluids. Corr. repr. of the 2nd edn. Springer, New York/Wien

Resonance of a Series of Train Cars Traveling Over Multi-Span Continuous Beams

J.D. Yau and Y.B. Yang

Abstract For a train car moving over a multi-span continuous beam of identical span length L at constant speed v, it may encounter repetitive excitations transmitted from the sustaining beam of frequency v/L excited by the previous passing cars. If the exciting frequency v/L coincides with the vehicle frequency f_c, namely $v/L = f_c$, resonance will be developed on the running car. In such a case, when the train car travels over more and more spans of the beam, the response of the car will be accumulated and becomes larger and larger, up to the limit imposed by inherent damping. Using the rigid-vehicle/bridge interaction finite element developed previously by the authors, each train car is modeled as a two-axle vehicle and each span of the continuous beam is simulated as a number of beam elements. Then the resonant response of the train cars running over the multi-span continuous beam is analyzed. The numerical examples indicate that for a high speed train composed of a series of cars traveling over a multi-span continuous beam, the *train-induced* resonance on the bridge takes place at a rather high speed, but the *bridge-induced* resonance on the train cars takes place at a much lower speed.

1 Introduction

To take the advantage of formwork preparation, the railway bridges for carrying high speed trains are often designed as multi-span continuous beams. For a dynamical system subjected to a periodic load, resonance takes place at the system when the exciting frequency coincides with any of the natural frequencies of the system. A similar resonant phenomenon can be observed from the train-bridge system of high speed railways as well. Because of the regular arrangement of bogies in a train, the bridge encounters repetitive excitations caused by a passing train. For

J.D. Yau (✉)
Department of Architecture, Tamkang University, Taipei 25137, Taiwan
e-mail: jdyau@mail.tku.edu.tw

Y.B. Yang
School of Civil Engineering, Chongqing University, 400044 Chongqing, China

Department of Civil Engineering, National Taiwan University, Taipei 10617, Taiwan
e-mail: ybyang@ntu.edu.tw

H. Irschik et al. (eds.), *Dynamics and Control of Advanced Structures and Machines*, DOI 10.1007/978-3-319-43080-5_2

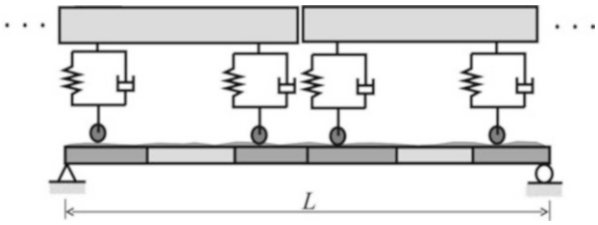

Fig. 1 R-VBI model

this, numerous researchers and scientists have conducted researches on the train-induced resonance of a rail bridge, say, by simulating the train action as a sequence of moving loads with equal intervals [5]. Since a high speed rail bridge must be designed to provide sufficient structural strength for the traveling trains at high speeds, the dynamic response of the train, especially with respect to resonance, has become an issue that dominates the operational safety and riding quality of the train-bridge system. For this reason, vehicle–bridge interaction (VBI) dynamics has received the attention of researchers in the past two decades.

Concerning the VBI of high speed rail bridges, many interesting topics were investigated, such as the train-induced resonance of a bridge, the wind effect on moving trains, the behavior of moving trains under earthquakes, and train-induced ground vibrations. However, there exists relatively little information on the resonant phenomenon of train cars running over continuous beams with multi-spans of identical length. In this paper, the train car is modeled as a two-axle system with *rigid* car body and each span of the continuous beam is discretized as a number of beam elements. Then the *rigid*-vehicle/bridge interaction (R-VBI, see Fig. 1) finite element developed previously by the authors is employed to analyze the dynamic response of the train cars running over a multi-span continuous beam. The numerical results indicated that for a high speed train composed of a series of cars traveling over multi-span continuous beams, the train-induced resonance of the bridge takes place at a rather high speed, but the resonance of the train cars takes place at a much lower speed.

2 VBI Problem

As was schematically shown in Fig. 1, during the passage of the train over a bridge, some elements of the bridge will be directly acted upon by the two-axle train car, while the others are not. In this study, the most commonly used beam element with 12 degrees of freedom (DOFs) will be adopted to simulate the continuous beam, of which the axial displacement is interpolated by linear functions and the transverse displacements by cubic (Hermitian) functions. The number of train cars directly acting on each beam element changes as the train keeps moving, and so do

the contact points between each bridge element and the train cars. As the contact points between the running cars and the bridge move from time to time, the system matrices must be updated and factorized at each time step in the incremental time-history analysis [1]. To overcome the time-varying nature of the problem, Yang et al. proposed a method for condensing the DOF of the two-axle car system with *rigid* car body into those of the element in contact, after the two-axle car system equations are discretized by Newmark's finite difference formulas [4]. The result is an R-VBI element that possesses the same number of DOFs as the parent element, while the properties of symmetry and bandedness are preserved. In the following section, a brief description of the condensation technique for the VBI system considering the pitching effect of the train car will be briefed.

2.1 Rigid-VBI Element

As shown in Fig. 2, the contact forces acting on the two elements i and j are composed of four components: (1) the static weights associated with the car body and wheel assemblies, represented by $M_v g$ and $M_w g$; (2) the damping forces resulting from the relative velocity of the *rigid* car body to the bridge elements, as indicated by the terms containing c_v; (3) the elastic forces resulting from the relative displacement of the car body to the bridge elements, as indicated by the terms involving k_v; and (4) the inertial forces due to the vertical acceleration of the bridge elements, as indicated by the terms $m_w \ddot{u}$.

In analyzing the VBI problem, two sets of equations of motion are written, one for the supporting bridge and the other for each of the moving vehicles. Consider a typical increment from time t to $t + \Delta t$ in time domain. The equations of motion for the car body can be written for the current time step, with $\bar{t} = t + \Delta t$ clearly inserted as the subscript as:

$$\begin{bmatrix} M_v & 0 \\ 0 & I_v \end{bmatrix} \begin{Bmatrix} \ddot{y}_v \\ \ddot{\theta}_v \end{Bmatrix}_{\bar{t}} + \begin{bmatrix} 2c_v & 0 \\ 0 & c_v \frac{d^2}{2} \end{bmatrix} \begin{Bmatrix} \dot{y}_v \\ \dot{\theta}_v \end{Bmatrix}_{\bar{t}} + \begin{bmatrix} 2k_v & 0 \\ 0 & k_v \frac{d^2}{2} \end{bmatrix} \begin{Bmatrix} y_v \\ \theta_v \end{Bmatrix}_{\bar{t}} = \begin{Bmatrix} f_{\text{ver}} \\ f_{\text{rot}} \end{Bmatrix}_{\bar{t}}, \tag{1}$$

where the acting forces are given as

$$\begin{Bmatrix} f_{\text{ver}} \\ f_{\text{rot}} \end{Bmatrix}_{t+\Delta t} = \begin{Bmatrix} c_v(\dot{u}_i + \dot{u}_j) + k_v(u_i + u_j) + k_v(r_i + r_j) \\ 0.5d[c_v(\dot{u}_i - \dot{u}_j) + k_v(u_i - u_j) + k_v(r_i - r_j)] \end{Bmatrix}_{t+\Delta t}. \tag{2}$$

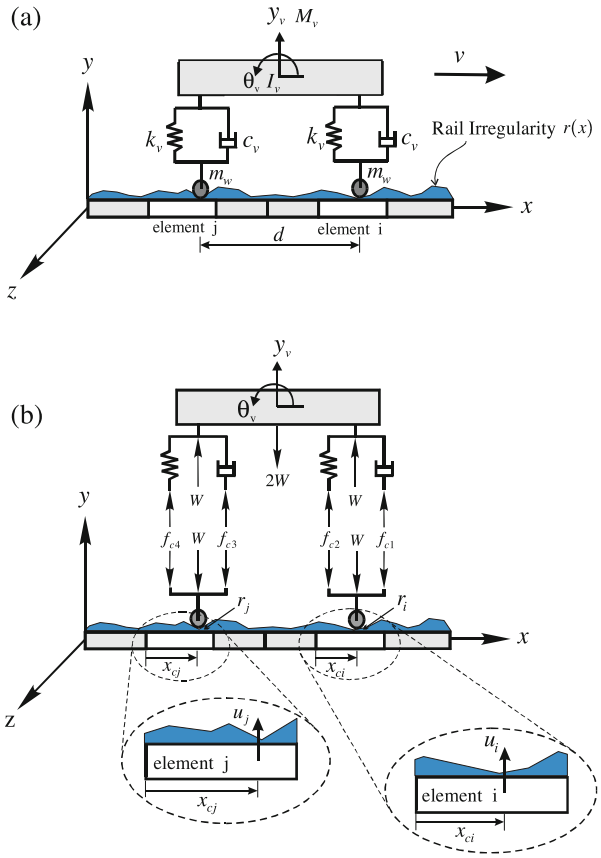

Fig. 2 VBI system considering the pitching effect: (**a**) R-VBI element; (**b**) Free body diagrams

The equations of motion for the bridge elements, i and j, are expressed for the current time step $t + \Delta t$ as

$$\begin{aligned} [m_i]\{\ddot{u}_i\}_{t+\Delta t} + [c_i]\{\dot{u}_i\}_{t+\Delta t} + [k_i]\{u_i\}_{t+\Delta t} &= -p_{i,t+\Delta t}\{N_{ci}\}, \\ [m_j]\{\ddot{u}_j\}_{t+\Delta t} + [c_j]\{\dot{u}_j\}_{t+\Delta t} + [k_j]\{u_j\}_{t+\Delta t} &= -p_{j,t+\Delta t}\{N_{cj}\}, \end{aligned} \tag{3}$$

where the associated contact forces are

$$p_{i,t+\Delta t} = \begin{bmatrix} c_v(\dot{u}_i - \dot{y}_v - 0.5d\dot{\theta}_v) + k_v(u_i + r_i - y_v - 0.5d\theta_v) \\ +0.5M_v g + m_w(g + \ddot{u}_i) \end{bmatrix}_{t+\Delta t}, \tag{4}$$

$$p_{j,t+\Delta t} = \begin{bmatrix} c_v(\dot{u}_j - \dot{y}_v + 0.5d\dot{\theta}_v) + k_v(u_j + r_j - y_v + 0.5d\theta_v) \\ +0.5M_v g + m_w(g + \ddot{u}_j) \end{bmatrix}_{t+\Delta t},$$

the shape function vector $\{N_{ci}\}$ at $x = x_c$ of the i-the beam element is given as

$$\{N_{ci}\} = \left\langle 1 - 3\left(\frac{x_c}{l}\right)^2 + 2\left(\frac{x_c}{l}\right)^3 \; x_c\left(1 - \frac{x_c}{l}\right)^2 \; 3\left(\frac{x_c}{l}\right)^2 - 2\left(\frac{x_c}{l}\right)^3 \; \left(\frac{x_c}{l} - 1\right) \frac{x_c^2}{l} \right\rangle^T, \tag{5}$$

and the shape function vector $\{N_{cj}\}$ is given in a similar way.

Following the condensation procedure developed for a *rigid*-VBI system [4], one can discretize the two-axle car system in advance using Newmark's finite difference formulas and then condensing the corresponding DOFs $\langle y_v \; \theta_v \rangle$ of the two-axle car system into the beam element in contact. Since the R-VBI elements possess the same number of DOFs as the parent element, while the properties of symmetry and bandedness are preserved, this element is particularly suitable for analyzing the dynamic responses of the VBI problems concerning both the bridge and vehicle responses. Readers who are interested in derivation of the R-VBI element should refer to the paper by Yang et al. [4] for further details.

2.2 VBI Analysis Using FEM

Figure 3 shows the response analysis procedure of the train-bridge system using the condensation technique. Because the VBI element and its parent element are fully compatible, the conventional element assembly process can be adopted with no difficulty to form the equations of motion for the entire vehicle–bridge system, that is

$$[M]\{\ddot{U}_b\} + [C_{\mathrm{VBI}}]\{\dot{U}_b\} + [K_{\mathrm{VBI}}]\{U_b\} = \{P_b\} + \{F_{\mathrm{VBI}}\}, \tag{6}$$

where $[M]$, $[C_{\mathrm{VBI}}]$, $[K_{\mathrm{VBI}}]$, respectively, denote the mass, damping, and stiffness matrices of the entire condensed vehicle–bridge system, $\{U_b\}$ the bridge displacements, $\{P_b\}$ the external loads acting on the bridge, and $\{F_{\mathrm{VBI}}\}$ the condensed effective vehicular loads acting on the bridge. The preceding equations are typical second-order differential equations, which can be solved by a number of time-marching schemes. In this study, the Newmark β method with constant average acceleration, i.e., with $\beta = 1/4$ and $\gamma = 1/2$ [5], is employed to render the preceding equations into a set of equivalent stiffness equations, from which the bridge displacements $\{U_b\}$ can be solved for each time step. Once the bridge displacements $\{U_b\}$ are made available, the bridge accelerations and velocities can be computed accordingly. By a backward procedure, the response of the two-axle car system can be computed as well on the element level, which serves as an indicator of the riding comfort.

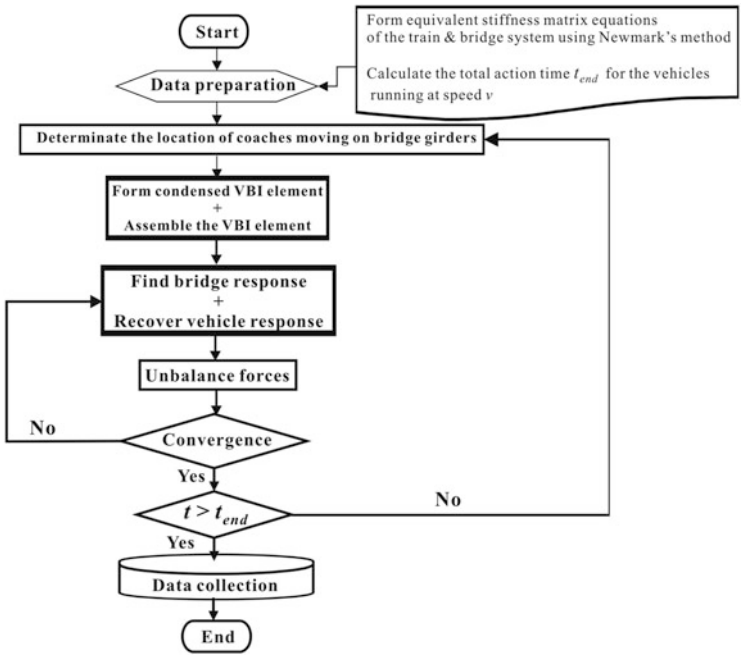

Fig. 3 Flowchart of VBI analysis using the condensation technique

3 Resonant Speeds

Resonance takes place when the exciting frequency of the external forces coincides with any of the natural frequencies of a mechanical system. For a train composed of cars with bogies of equal interval D, when it travels at speed v over a bridge, an exciting frequency v/D will be generated. When the exciting frequency v/D matches one of the bridge frequencies f_b, resonant response will be developed on the bridge, for which the resonant speed is $v_{br} = f_b D$ [3]. Such a phenomenon will be referred to as the *train-induced* resonance on the bridge.

On the other hand, for a train car moving over a multi-span continuous beam with identical span length L at speed v, the train car will encounter repetitive excitation transmitted from the beam with frequency v/L. Once the exciting frequency v/L coincides with one of the vehicle's frequencies f_c, resonance will be developed on the car in running, that is, when $v/L = f_c$. In this case, the corresponding resonant speed is denoted as $v_{vr} = f_c L$ [2]. Such a phenomenon is referred to as the *bridge-induced* resonance on the train cars. For most high speed railways, the bridge-induced resonant speed for the train cars takes place at a lower speed compared with the train-induced resonant speed for the rail bridge.

4 Finite Element Analysis

Figure 4 shows a schematic plot of the planar two-axle car with rigid car body moving over a continuous beam, assumed to be of 5 spans. The properties of the 5-span continuous beam and planar two-axle system are listed in Tables 1 and 2, respectively. By letting f_1 denote the first frequency of the beam, the resonant speed induced by the train car is $v_{\text{res}} = f_1 D$ [1]. In the following examples, each span of the continuous beam shown in Fig. 4 is modeled by 6 beam elements. Based on Newmark's method of direct integration, numerical solutions for the dynamic response of the bridge due to the moving two-axle car system have been computed for a time step of 0.0025 s. To focus on the resonance of the continuous beam of identical spans induced by the train car, the track irregularities will be neglected in performing the VBI analysis with the condensation technique in the following examples. Since the vertical acceleration of the moving vehicle has been regarded as an indicator of the riding comfort or running safety of high speed trains, the acceleration response of the VBI system is of key concern in this study.

4.1 Resonant Response Analysis

In Table 2, the resonant speeds $v_{r,v}$ and $v_{r,p}$ represent the speeds for the resonance to occur on the vehicle due to coincidence of the vertical and pitching frequencies, respectively, of the two-axle car system with the implied frequency v/L of the continuous beam. For the present purposes, let us consider the cases when the two-axle car system moves over the continuous beam at each of the two resonant speeds ($v_{r,v}$ and $v_{r,p}$) as listed in Table 2. Figures 5 and 6 show the vertical and pitching accelerations, respectively, of the midpoint of the two-axle car system computed by the R-VBI element simulation. Evidently, when the vehicle moves at either the

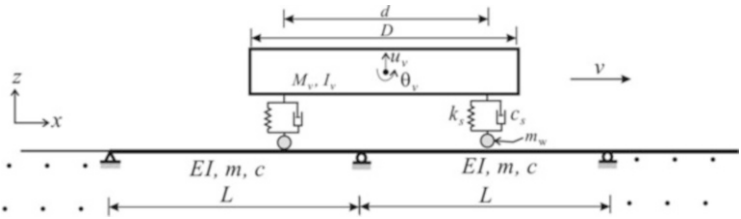

Fig. 4 Two-axle car system moving over a continuous beam with identical spans

Table 1 Properties of the continuous beam

L/m	EJ/Nm^{-2}	m/tm^{-1}	ξ/%	f_1/Hz	f_2/Hz	f_3/Hz	v_{res}/km h^{-1}
35	2.82×10^8	25	1.5	4.3	4.78	5.97	387

Table 2 Properties of the two-axle car system

D/m	D/m	M_y/t	I_v/tm^2	m_w/t	c_s/kN sm^{-1}
25	20	40	2050	4.5	10

k_s/kN m^{-1}	f_v/Hz	f_p/Hz	$v_{r,v}$/km h^{-1}	$v_{r,p}$/km h^{-1}
650	0.91	1.27	115	160

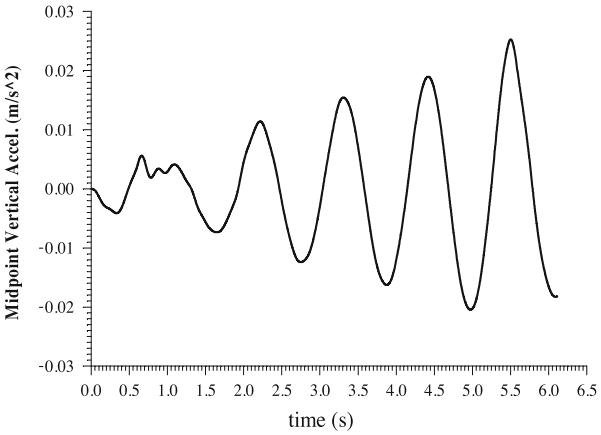

Fig. 5 Resonant response of the vertical acceleration of midpoint of the two-axle car system moving over the continuous beam

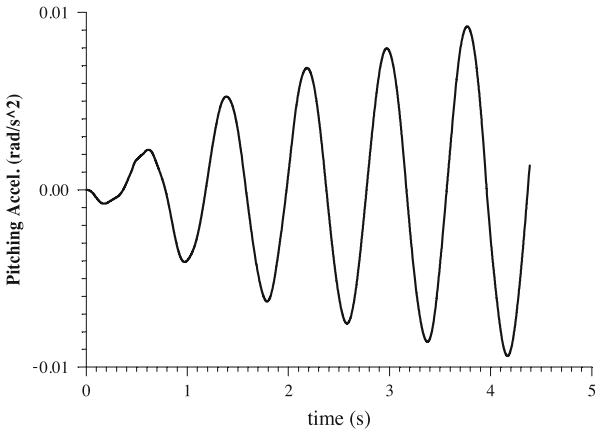

Fig. 6 Resonant response of pitching acceleration of the two-axle car system moving over the continuous beam

vertical or pitching resonant speed, the acceleration response of the vehicle grows monotonically as the vehicle passes through more and more spans.

4.2 Maximum Acceleration of Train Cars Versus Train Speed

In this example, a train composed of 16 coaches is considered for simulating its passage over a continuous beam with identical spans, as shown in Fig. 7. To illustrate the resonant phenomenon, Figs. 8 and 9 show the maximum acceleration for the running train and the beam, respectively, against the train speed. For the present purposes, the maximum vertical acceleration $a_{v,\max}$ for each of the two-axle cars shown in Fig. 7 is defined as:

$$a_{v,\max} = \max\left(\left|\ddot{u}_v \pm \frac{D\ddot{\theta}_v}{2}\right|\right). \tag{7}$$

The maximum acceleration response $a_{v,\max}$ of the two-axle system versus the train speed v was plotted in Fig. 8, which will be referred to as the $a_{v,\max} - v$ plot for the train cars.

From Fig. 8, one observes that there exist three resonant peaks at the speeds of 115, 160, and 387 km/h, corresponding to the bridge-induced vertical and pitching resonant speeds, and the vehicle-induced VBI resonant speed, respectively. The

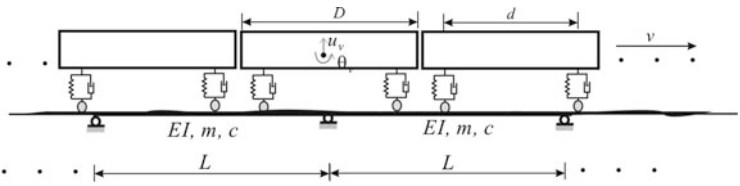

Fig. 7 A series of train cars moving over a multi-span continuous beam

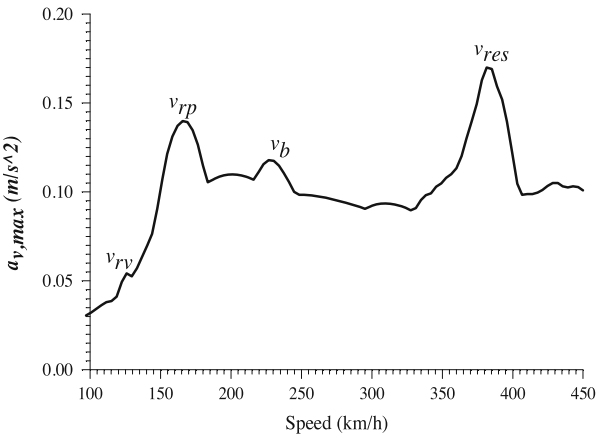

Fig. 8 $a_{v,\max} - v$ plot for the two-axle car system moving over the continuous beam

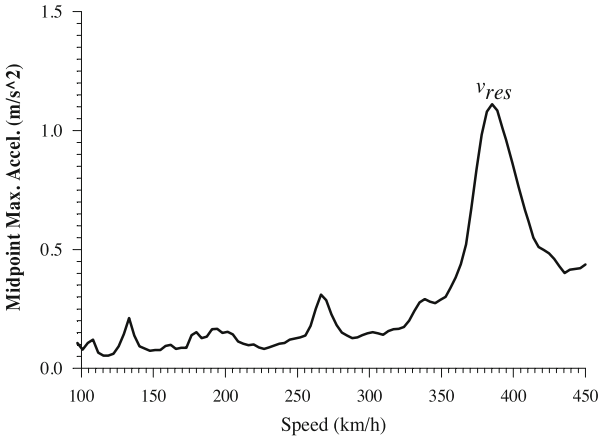

Fig. 9 Maximum midpoint acceleration at the central span of the continuous beam vs. train speed

pitching resonant speed at $v_{r,p} = f_p L$ (= 160 km/h) deserves a special note, since it creates a peak much higher than that of the vertical resonance at a speed that can be encountered in practice. Under such a condition, the vertical component $\pm\ddot{\theta}_v D/2$ induced by the pitching acceleration $\ddot{\theta}_v$ dominates the peak acceleration response of the vehicle, which is a long coach ($D = 25$ m). Furthermore, larger response is induced on the train cars as there are more cars passing the series of spans of the continuous beam, due to the accumulation effect, although it is not shown here. The speed 230 km/h represents another peak for the vehicle, which is caused by the beating phenomenon associated with the pitching rotation. The beating phenomenon is due to the fact that the subresonant excitation of the second frequency of the bridge, i.e., $f_2/2 = 4.78/2 = 2.39$ Hz, couples with the pitching frequency of the vehicles, 1.27 Hz. Their average frequency is $f_{\text{av}} = (2.39 + 1.27)/2 = 1.83$ Hz, which corresponds to the beating speed of $v_b = f_{\text{av}} L = 1.83\,\text{Hz} \times 35\,\text{m} = 64\,\text{m/s} = 230\,\text{km/h}$. Further investigation is needed for this phenomenon.

In contrast, the vehicle-induced resonance at $v_{\text{res}} = f_1 D = 387$ km/h, where f_1 is the frequency of the beam, is caused by the first resonance of the 5-span continuous beam under the action of a series of train cars with car length D. For reference, the maximum vertical acceleration of the midpoint of the central-span of the continuous beam subjected to the same series of train cars constituting the train has been plotted in Fig. 9.

5 Concluding Remarks

Using the VBI finite element developed previously by Yang et al. [4], the key parameters that dominate the vertical and pitching resonance of a two-axle car system running over a multi-span continuous beam are studied. The analysis has

been expanded to include the case of a series of train cars running over a multi-span continuous beam. From the numerical analyses presented herein, the following conclusions are drawn:

1. The resonance of a train car, either in vertical vibration or pitching rotation, is featured by the fact that its response continues to build up when traveling over more and more spans of the continuous beam.
2. The *train-induced resonance* will occur on the bridge when the exciting frequency of the train v/D, where v is train speed and D is car length, coincides with one of the frequencies f_b of the bridge.
3. The *bridge-induced resonance* will occur on the train cars when the exciting frequency of the multi-span bridge v/L, where L is the span length, coincides with any of the car frequencies.
4. For train cars with long axle intervals D, the vertical acceleration induced by the pitching rotation in resonance dominates the peak acceleration of the train cars in running.
5. When in pitching resonance, larger response is induced on the train cars as there are more train cars passing the continuous beam, due to the accumulation effect.

Acknowledgements The research reported herein is sponsored partially by the grant from the Ministry of Science and Technology, Taiwan, through the serial No. 104-2221-E-032-033 and by Chongqing Science and Technology Commission via Grant No. cstc2015jcyjys30003. Such financial aids are gratefully acknowledged.

References

1. Yang YB, Yau JD (1997) Vehicle-bridge interaction element for dynamic analysis. J Struct Eng ASCE 123(11):1512–1518 (Errata: 124(4):479)
2. Yang YB, Yau JD (2015) Vertical and pitching resonance of train cars moving over a series of simple beams. J Sound Vib 337:135–149
3. Yang YB, Yau JD, Hsu LC (1997) Vibration of simple beams due to trains moving at high speeds. Eng Struct 19(11):936–944
4. Yang YB, Chang CH, Yau JD (1999) An element for analysing vehicle-bridge systems considering vehicle's pitching effect. Int J Numer Methods Eng 46:1031–1047
5. Yang YB, Yau JD, Wu YS (2004) Vehicle-bridge interaction dynamics: with applications to high-speed railways. World Scientific, Singapore

Stability and Supercritical Deformation of a Circular Ring with Intrinsic Curvature

Yury Vetyukov

Abstract Stability of a circular ring, pre-stressed by a temperature-like intrinsic deformation, is studied using the equations of the nonlinear theory of rods. The temperature gradient in the radial direction results in a bending moment. The critical state depends on the ratio of the bending stiffness coefficients. In the supercritical range, the ring begins to turn inside out as its cross-sections rotate about the axis. The analytical solutions are successfully compared against results of finite element simulations for a shell model of the ring.

1 Introduction and Statement of the Problem

While Euler buckling of columns is the most famous stability problem in rod mechanics, there are other fascinating and practically relevant examples, which allow for analytic solutions. Classical formulations feature lateral-torsional buckling of deep beams, in-plane buckling of rings and arches under distributed loads, buckling of shafts, etc., see [3, 5, 6, 8, 9]. Relevant for the present study is the less known interesting problem of instable behavior and nonlinear response of a curved shaft, which is twisted in a curved channel [2, 3]. We must also mention here the so-called Michell's instability of twisted elastic rings [4], which are pre-stressed owing to the incompatible intrinsic pre-deformation.

Similarly to the last mentioned example, we consider a circular ring, which is pre-stressed in its undistorted state. A temperature gradient in the radial direction results in a bending moment about the out-of-plane axis, Fig. 1. The temperature pre-strain in the three-dimensional body of the rod may be interpreted on the structural level as an intrinsic curvature, superimposed upon the reference curvature of the circle. Cutting the ring at one of the cross-sections, we allow it open and change its curvature such that the bending moment vanishes, see the right part of Fig. 1. But the original closed ring cannot change its curvature so easily, and the growing temperature difference leads to an increasing bending moment. The

Y. Vetyukov (✉)
Institute of Mechanics and Mechatronics, Vienna University of Technology, Getreidemarkt 9, 1060 Vienna, Austria
e-mail: yury.vetyukov@tuwien.ac.at

H. Irschik et al. (eds.), *Dynamics and Control of Advanced Structures and Machines*, DOI 10.1007/978-3-319-43080-5_3

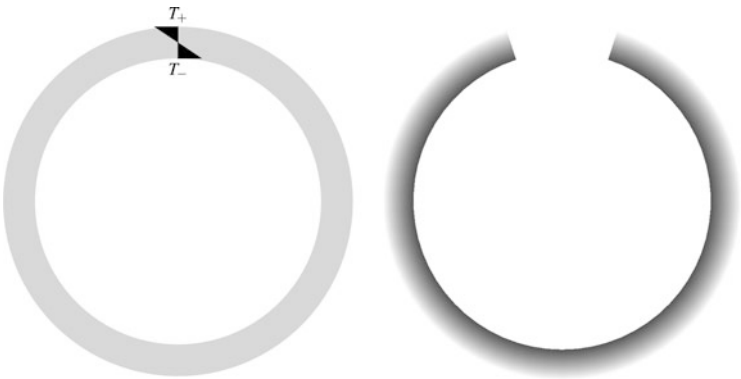

Fig. 1 Circular ring with radial temperature profile (*left*), deformation of an open ring (*right*)

pre-stressed undistorted configuration remains in equilibrium, but it may become instable depending on its stiffness properties and the magnitude of the imposed intrinsic curvature. In the present contribution we determine the critical value of this pre-strain based on the equations of the nonlinear theory of rods, find supercritical solutions after the buckling, and compare the results to the numerical finite element simulations for a shell model of the structure.

2 Nonlinear Theory of Classical Rods

We will employ the equations of the nonlinear theory of rods in the form, suggested by Eliseev [3] and Vetyukov [8], see also [1, 5]. We consider a material line with three translational and three rotational degrees of freedom of particles, and the equations of the theory follow from the principle of virtual work. In the classical theory, conditions of inextensibility and absence of shear impose certain constraints for the possible forms of deformation of the one-dimensional continuum.

Particles of the rod are identified by their material coordinate s. Owing to the inextensibility, we choose s as the arc coordinate along the axis of the rod, see Fig. 2. Position vectors of particles $\underline{r}(s)$ define the geometry of the axis, and the orientation of particles is determined by the rotation of three basis vectors $\underline{e}_k$. Constraints of the classical theory allow choosing the third basis vector in the tangent direction, such that the unit tangent vector is

$$\underline{e}_3 = \underline{r}' = \underline{t}. \tag{1}$$

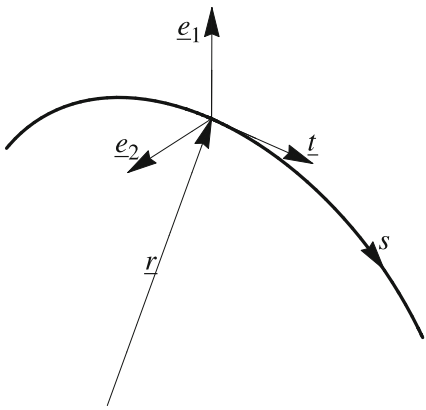

Fig. 2 Rod as a material line with positions of particle $\underline{r}(s)$ and their orientations $\underline{e}_k(s)$ depending on the material coordinate s

The rate of change of the local basis along the axis of the rod is determined by the vector of twist and curvature $\underline{\Omega}$:

$$\underline{e}'_k = \underline{\Omega} \times \underline{e}_k, \quad \underline{\Omega} = \frac{1}{2}\underline{e}_k \times \underline{e}'_k = \Omega_k \underline{e}_k; \tag{2}$$

summation over the repeating index is implied, and Ω_k are the components in the local basis.

The undeformed reference state is defined by the orientations of particles $\mathring{\underline{e}}(s)$, and $\mathring{\underline{\Omega}} = \mathring{\Omega}_k \mathring{\underline{e}}_k$. The deformation from the reference state to the actual one is described by the vector

$$\underline{\kappa} = (\Omega_k - \mathring{\Omega}_k)\underline{e}_k = \kappa_k \underline{e}_k. \tag{3}$$

Components $\kappa_{1,2}$ are responsible for bending, and κ_3 shall be interpreted as torsion of the rod. Computing these strain measures, we deal with components Ω_k and $\mathring{\Omega}_k$, which are, respectively, written in the actual basis and in the reference one. If we write the tensor of rotation of a particle from the reference to the actual state $\underline{\underline{P}}$, then its derivative along the axis is found as if $\underline{\kappa}$ was an angular velocity and s was time:

$$\underline{\underline{P}} = \underline{e}_k \mathring{\underline{e}}_k, \quad \underline{\underline{P}}' = \underline{\kappa} \times \underline{\underline{P}}. \tag{4}$$

The constitutive relation expresses the moment in the rod $\underline{M}(s)$, which acts from the particle $s + 0$ on the particle $s - 0$, $\underline{M} = \underline{\underline{a}} \cdot \underline{\kappa}$. The symmetric tensor of stiffness for bending and torsion $\underline{\underline{a}} = a_{ik} \underline{e}_i \underline{e}_k$ has constant components in the local basis and

rotates together with the particles. In components, the above relation reads

$$\underline{M} = M_k \underline{e}_k, \quad M_i = a_{ik}\kappa_k. \tag{5}$$

Now, we write the equations of balance of forces $\underline{Q}$ and moments in a state of static equilibrium:

$$\underline{Q}' + \underline{q} = 0, \quad \underline{M}' + \underline{t} \times \underline{Q} + \underline{m} = 0. \tag{6}$$

The external distributed forces $\underline{q}$ and moments $\underline{m}$ are counted per unit length of the rod. There is no constitutive relation for the force $\underline{Q}$ in the classical theory, and the constraint (1) shall be used instead. This system of equations is completed by the boundary conditions or periodicity conditions for a closed rod, considered in the following.

3 Linearized Equations of a Pre-stressed Rod and Stability of Static Equilibrium

Small increments in the external forces $\underline{q}^\bullet$ and moments $\underline{m}^\bullet$ result in small displacements $\underline{r}^\bullet = \underline{u}$ and rotations $\underline{e}_k^\bullet = \underline{\theta} \times \underline{e}_k$ away from the static equilibrium. The incremental formulation [3, 8] comprises above equations, linearized in the vicinity of a pre-stressed equilibrium state. The constraint (1) holds during the deformation, which relates displacements and small rotations $\underline{\theta}$:

$$\underline{u}' = \underline{\theta} \times \underline{t}. \tag{7}$$

The constitutive relation

$$\underline{M}^\bullet = \underline{\theta} \times \underline{M} + \underline{\underline{a}} \cdot \underline{\theta}' \tag{8}$$

and the balance equations

$$\underline{Q}^{\bullet\prime} + \underline{q}^\bullet = 0, \quad \underline{M}^{\bullet\prime} + \underline{u}' \times \underline{Q} + \underline{t} \times \underline{Q}^\bullet + \underline{m}^\bullet = 0 \tag{9}$$

feature the force factors $\underline{Q}$, $\underline{M}$ in the rod in the previous equilibrium state and their small increments $\underline{Q}^\bullet$, $\underline{M}^\bullet$.

In Eulerian approach, stability of static equilibrium of a conservative system is judged by the existence of infinitesimally close equilibrium configurations. It means that the configuration is critical if the above linear equations allow for a nontrivial solution $\underline{u}$, $\underline{\theta}$, $\underline{M}^{\bullet}$ and $\underline{Q}^{\bullet}$ with $\underline{q}^{\bullet} = 0$ and $\underline{m}^{\bullet} = 0$; the boundary conditions are to be treated correspondingly. A pitchfork bifurcation of an equilibrium path corresponds to a classical buckling of a conservative system [3, 8, 9].

4 Pre-stressed Ring with Intrinsic Curvature

Consider a circular ring with the radius R in a cylindrical coordinate system with the angular coordinate φ and the local basis $\underline{e}_r$, $\underline{e}_\varphi$, $\underline{k}$, Fig. 3. Now, we choose the material coordinate along the axis of the ring and the local basis:

$$s = \varphi R, \quad \underline{r} = R\underline{e}_r, \quad \underline{e}_1 = \underline{k}, \quad \underline{e}_2 = \underline{e}_r, \quad \underline{e}_3 = \underline{e}_\varphi, \tag{10}$$
$$\underline{k}' = 0, \quad \underline{e}_r' = R^{-1}\underline{e}_\varphi, \quad \underline{e}_\varphi' = -R^{-1}\underline{e}_r.$$

Using (2), we compute the vector of twist and curvature and its components:

$$\underline{\Omega} = R^{-1}\underline{e}_r \times \underline{e}_\varphi = R^{-1}\underline{k}, \quad \Omega_1 = \underline{\Omega} \cdot \underline{e}_1 = R^{-1}, \quad \Omega_{2,3} = 0. \tag{11}$$

We assume that the introduced basis coincides with the principal axes of the stiffness tensor:

$$\underline{\underline{a}} = a_z \underline{e}_1 \underline{e}_1 + a_r \underline{e}_2 \underline{e}_2 + a_\varphi \underline{e}_3 \underline{e}_3, \tag{12}$$

and the stiffness for bending in plane is higher than that out of plane: $a_z > a_r$.

The applied temperature gradient imposes intrinsic curvature αR^{-1}, which "pushes" the ring towards less curved configuration. Although this undeformed state is incompatible for a closed ring, we can virtually cut it and plot the stress-free states with the curvatures

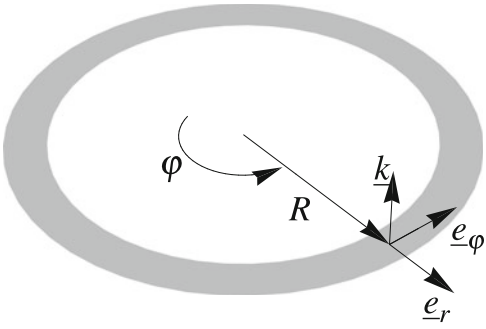

Fig. 3 Undistorted state of the ring and the basis of the cylindrical coordinate system

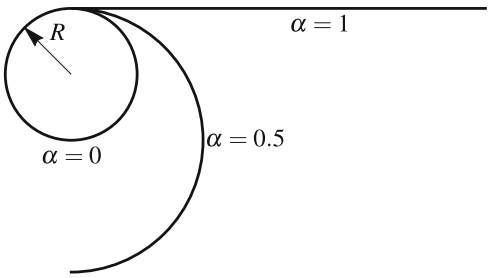

Fig. 4 Undeformed states of the open ring with applied intrinsic curvature

$$\mathring{\Omega}_1 = R^{-1} - \alpha R^{-1} = (1-\alpha)R^{-1}, \quad \mathring{\Omega}_{2,3} = 0 \tag{13}$$

in dependence on the loading parameter α, see Fig. 4. Now we easily find the strains and the bending moment:

$$\kappa_1 = R^{-1} - (1-\alpha)R^{-1} = \alpha R^{-1}, \quad \kappa_{2,3} = 0, \tag{14}$$
$$\underline{\kappa} = \alpha R^{-1}\underline{k}, \quad \underline{M} = a_z \alpha R^{-1}\underline{k} = \text{const},$$

and the equilibrium conditions are fulfilled with $\underline{Q} = 0$.

5 Buckling Analysis

Consider a small axisymmetric perturbation of the undistorted equilibrium state in the form of rotation of particles about the axis of the rod:

$$\underline{u} = 0, \quad \underline{\theta} = \theta \underline{e}_\varphi, \quad \theta = \text{const}. \tag{15}$$

We find the increment of the moment (8):

$$\underline{M}^\bullet = \theta a_z \alpha R^{-1}\underline{e}_r - \underline{\underline{a}}\cdot \theta R^{-1}\underline{e}_r = \theta R^{-1}(\alpha a_z - a_r)\underline{e}_r. \tag{16}$$

The second of the balance equations (9) reads now

$$\theta R^{-1}(\alpha a_z - a_r)\underline{e}_\varphi + \underline{e}_\varphi \times \underline{Q} = 0, \tag{17}$$

which may be fulfilled only when

$$\alpha = \alpha_* = a_r/a_z \tag{18}$$

and the force $\underline{Q}$ is directed along the axis; along with the condition $\underline{Q}' = 0$ it means that $\underline{Q} = 0$. But we are more interested in the obtained value of the critical intrinsic

curvature α_*, which is low for flat rings with small out-of-plane thickness. Indeed, if the cross-section of the rod with the Young modulus E is rectangular with the height in the z direction being h and the width in the radial direction being w, then

$$a_r = Ewh^3/12, \quad a_z = Ehw^3/12, \quad \alpha_* = h^2/w^2, \tag{19}$$

and $\alpha_* \ll 1$ for flat rings with $h \ll w$.

6 Supercritical Deformation

The undistorted shape of the ring becomes instable as $\alpha > \alpha_*$. We seek the new solutions to the nonlinear system of equations in the form

$$\underline{r} = R\underline{e}_r, \quad \underline{e}_1 = \underline{k}\cos\theta + \underline{e}_r \sin\theta, \quad \underline{e}_2 = -\underline{k}\sin\theta + \underline{e}_r\cos\theta, \quad \underline{e}_3 = \underline{e}_\varphi. \tag{20}$$

Similar to the buckling form, the axis of the rod retains its shape, and the cross-sections simply rotate with the angle θ about the tangent direction, see Fig. 5. The stiffness tensor (12) rotates together with the cross-sections, and the vector of twist and curvature remains the same as in (11):

$$\underline{\Omega} = \frac{1}{2}\left(\sin^2\theta + \cos^2\theta + 1\right) R^{-1}\underline{k} = R^{-1}\underline{k}. \tag{21}$$

Its components are changing, however, as the local basis depends on θ:

$$\Omega_1 = \underline{e}_1 \cdot \underline{\Omega} = R^{-1}\cos\theta, \quad \Omega_2 = -R^{-1}\sin\theta, \quad \Omega_3 = 0. \tag{22}$$

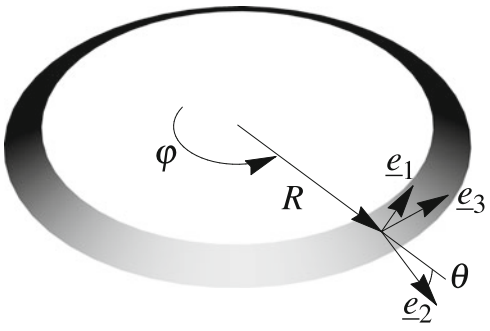

Fig. 5 Supercritical deformation of the ring, cross-sections are rotated with the angle θ about the axis

Subtracting the undeformed components (13), we find strains κ_k and compute the moment

$$\begin{aligned}\underline{M} &= a_z(\Omega_1 - \mathring{\Omega}_1)\underline{e}_1 + a_r\Omega_2\underline{e}_2 \\ &= R^{-1}\sin\theta(a_z(1-\alpha) - (a_r + a_z)\cos\theta)\underline{e}_r \\ &\quad - R^{-1}(a_z(1-\alpha-\cos\theta) + a_r\sin^2\theta)\underline{k}.\end{aligned} \tag{23}$$

Inserting into the second balance equation in (6), we see that $\underline{M}'$ has just a component in the direction $\underline{e}_\varphi = \underline{t}$. It means again that $\underline{Q} = 0$, and

$$R^{-1}\sin\theta(a_z(1-\alpha) - (a_r + a_z)\cos\theta) = 0. \tag{24}$$

This condition of static equilibrium is an algebraic equation for θ. Besides the trivial solution $\sin\theta = 0$, there exists a solution branch, determined by the equality

$$\alpha = 1 - (1 + a_r/a_z)\cos\theta. \tag{25}$$

Solutions for θ exist when $\alpha > \alpha_*$ from (18), which is typical for a pitchfork bifurcation. At $\alpha = 1$ we obtain $\theta = \pm\pi/2$, which means that a flat ring turns into a cylinder when the intrinsic curvature reaches the geometrical one R^{-1} and the undeformed state is straight, see simulation results below.

7 Finite Element Simulation with a Shell Model

We used a finite element simulation [7, 8] for a shell model of a flat ring with $R = 1$, $w = 0.1$, and $h = 0.02$; the intrinsic curvature was applied by changing the circumferential component of the metric of the undeformed shell, which varied linearly in the radial direction depending on the current value of α. Increasing α from 0 to 1 we indeed observed the transformation of a flat shell into a cylindrical surface, as it is predicted by the above analytical study. A small imperfection in the reference geometry "promoted" the system towards stable deformed configurations in the supercritical range. The undistorted and the deformed shapes of the ring for four values of α are presented in the left part of Fig. 6. One of the cross-sections (marked by a line) is fixed, which results in the large rigid-body rotation of the shell along with the axisymmetric deformation as in the study above. The right part of Fig. 6 demonstrates a shell solution for an open ring at $\alpha = 1/3$: the configuration remains plane, and its curvature decreases; at $\alpha = 1$ the ring evolves into a straight strip.

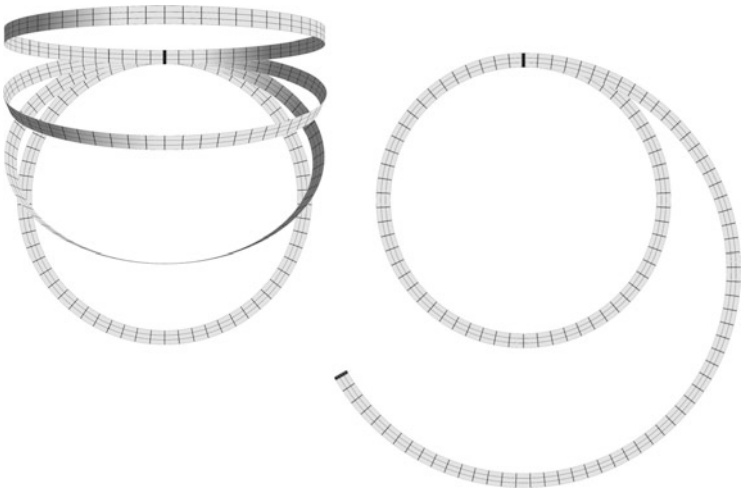

Fig. 6 Shell model analysis: shapes of a closed ring with $\alpha = 0,\ 1/3,\ 2/3,\ 1$ (*left*) and of an open ring with $\alpha = 0,\ 1/3$ (*right*)

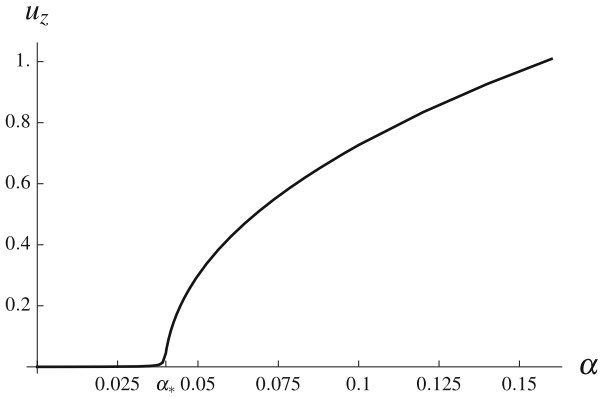

Fig. 7 Maximal out-of-plane displacement in the shell solution depending on the intrinsic curvature parameter

Finally, for the simulation with a closed ring we plotted the maximal out-of-plane displacement u_z depending on α, see Fig. 7. The bifurcation of the flat equilibrium configurations is clearly seen at a value of the loading parameter, which is very close to the theoretically predicted critical value $\alpha_* = 0.04$.

References

1. Antman S (1972) The theory of rods. In: Flügge S, Truesdell C (eds) Handbuch der Physik, vol VIa/2. Springer, Berlin/Heidelberg/New York, pp 641–703
2. Belyaev A, Eliseev V (2002) Dynamic behaviour of wire shaft in an arbitrary passage. In: Indeitsev D (ed) Proceedings of APM 2001 advanced problems in mechanics, St. Petersburg, Russia, pp 119–126
3. Eliseev V (2006) Mechanics of deformable solid bodies (in Russian). St. Petersburg State Polytechnical University Publishing House, St. Petersburg
4. Goriely A (2006) J Elast 84:281–299
5. Simitses GJ, Hodges DH (2006) Fundamentals of structural stability. Elsevier, New York
6. Timoshenko S, Gere J (1961) Theory of elastic stability, 2nd edn. McGraw-Hill, New York
7. Vetyukov Y (2014) Finite element modeling of Kirchhoff-Love shells as smooth material surfaces. Z Angew Math Mech 94(1–2):150–163
8. Vetyukov Y (2014) Nonlinear mechanics of thin-walled structures: asymptotics, direct approach and numerical analysis. Foundations of engineering mechanics. Springer, Vienna
9. Ziegler H (1977) Principles of structural stability, 2nd edn. Birkhäuser Verlag, Basel

Estimation of Mechanical Properties of Micro-Lattice Panel with Irregular Cells

Kuniharu Ushijima and Dai-Heng Chen

Abstract In our study, the uniaxial tensile response of lattice panel with missing cell region was investigated using nonlinear FE analysis. In particular, the effects of missing cell size and shape on the initial stiffness E^* and the plastic collapse strength σ_{pl}^* were discussed. The initial stiffness is mainly affected by the ratio of missing cell height h/h_0 as well as the missing cell width w/w_0, and independent of the unit-cell shape. On the other hand, the plastic collapse strength is mainly dominated by the missing cell width w/w_0 only, which implies that the strength is affected strongly by the tensile strength at the front of the missing cell region.

1 Introduction

Over the decades, cellular structures, such as honeycombs, foams and lattice structures, have been taken much attention, and used for many kinds of structural applications owing to their superior mechanical performance per unit mass. Up to now, many technical papers regarding the mechanical properties of cellular structures have been published [1–8]. In most cases, the cellular structures are composed of uniform cell wall and periodic structural arrangement. On the contrary, Guo and Gibson [1] have investigated the effect of structural non-uniformities in the cellular structures on the compressive response by using FE analysis. Also, Silva and Gibson [2] have studied the effect of randomly removing cell edges in hexagonal honeycombs on the Young's modulus and collapse stresses.

K. Ushijima (✉)
Faculty of Engineering, Tokyo University of Science, Tokyo, Japan
e-mail: kuniharu@rs.tus.ac.jp

D.-H. Chen
Faculty of Civil Engineering and Mechanics, Jiangsu University, Jiangsu, China
e-mail: dhchen@ujs.edu.cn

H. Irschik et al. (eds.), *Dynamics and Control of Advanced Structures and Machines*, DOI 10.1007/978-3-319-43080-5_4

In our study, the uniaxial tensile response of lattice panel with missing cell region is investigated using nonlinear FE analysis. In particular, the effects of missing cell size and shape on the initial stiffness and the plastic collapse strength are discussed.

2 Method of Numerical Analysis

In our numerical calculation, the commercial FE software, MSC.Marc 2012, is used to demonstrate the elastoplastic behaviour of the micro-lattice panel. Figure 1a shows the schematic of numerical model in our FE analysis. The model which consists of 3-D unit cell (length L_x, L_y and L_z in x-, y- and z-directions) as shown in Fig. 1b has a missing cell region at the centre, and is subjected to a uniaxial in-plane tensile load. Each unit cell is composed of eight slender beams (length L, diameter $d = 200\,[\mu\mathrm{m}]$) connected to each other. In our FE analysis, Timoshenko beam element is selected, and each beam is divided into 20 number of elements. Each beam is assumed to be isotropic and homogeneous elastoplastic material. Here, the Young's modulus E_s, Poisson's ratio ν_s and yield stress σ_{pls} are set to 140 [GPa], 0.3 and 144 [MPa], respectively, which are all based on the experimental data of stainless steel SS316L. Also, owing to symmetry of the panel, only one quarter region is modelled in our calculation. The geometrical parameters of our numerical model are shown in Fig. 1c. Here, N_x and N_y represent the number of unit cell in x- and y-direction, respectively. Parameters n_x and n_y show the number of missing cell in x- and y-direction, respectively. Moreover, w_0 and w are the widths of overall

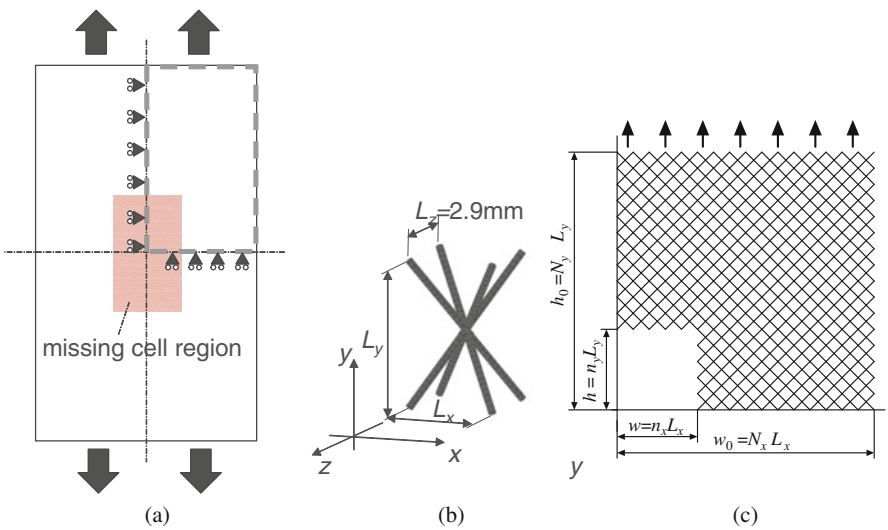

Fig. 1 Schematic of numerical model in FE analysis. (**a**) Overall model; (**b**) Unit cell; (**c**) FE model

lattice panel and missing cell region, and h_0 and h are the heights of overall lattice panel and missing cell region, respectively.

In solving the nonlinear problem, the Mises' yield criterion and the updated Lagrangian method are used in our calculation, and the Newton–Raphson numerical method is applied for finding the root effectively.

In our study, the effect of the existence of missing cell region on the overall response (initial stiffness E^* and plastic collapse strength σ_{pl}^*) of the lattice panel is discussed.

3 Results and Discussion

3.1 Stress–Strain Curves of Lattice Panel With and Without Missing Cell Region

Figure 2 shows the tensile stress–strain curve of the lattice panel by changing the size of missing cell region. When the panel is composed of uniform unit cell and perfect cell arrangement, the initial stiffness termed E_0^* and plastic collapse strength

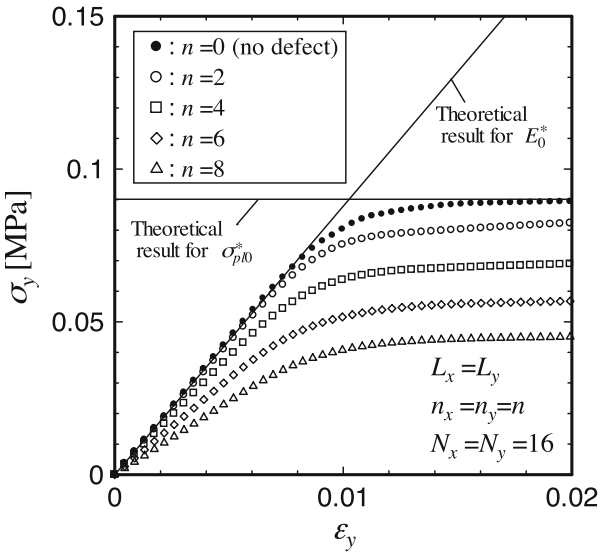

Fig. 2 Comparison of stress–strain curve of lattice by changing the defect size

termed σ^*_{pl0} can be obtained theoretically as follows:

$$E^*_0 = 4\sqrt{3}\pi E_s \cdot \frac{(d/L)^2}{3 + 8\,(L/d)^2} \tag{1}$$

$$\sigma^*_{\mathrm{pl0}} = \frac{\sqrt{6}}{2}\sigma_{pls}\left(\frac{d}{L}\right)^3 \tag{2}$$

It can be found from Fig. 2 that the theoretical results of initial stiffness and plastic collapse strength agree well with FE result for uniform cell model. Also, the stress–strain curve decreases gradually as the defect region expands.

3.2 *Effect of Missing Cell Region on Initial Stiffness E**

Figure 3 shows the variation of initial stiffness E^* as a function of normalized defect width w/w_0. All lattice panels are square-shaped, and have square-shaped defects. In Fig. 3, the stiffness E^* is normalized by E^*_0 for a perfect lattice model. It can be seen that the normalized initial stiffness E^*/E^*_0 decreases nonlinearly as the defect width increases. And this degradation curve cannot be evaluated from the curve of the volume fraction of defect in a lattice plate. In order to investigate the degradation curve of initial stiffness E^*/E^*_0 more in detail, the degradation curves

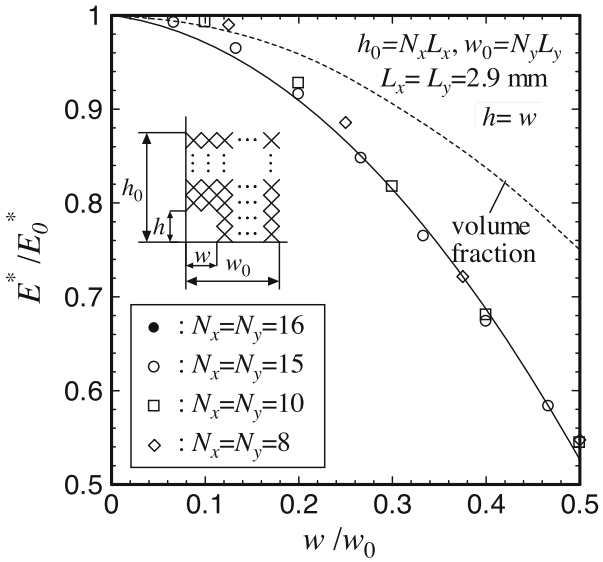

Fig. 3 Variation of initial stiffness E^* for *square-shaped* lattice panels with *square-shaped* missing cell region

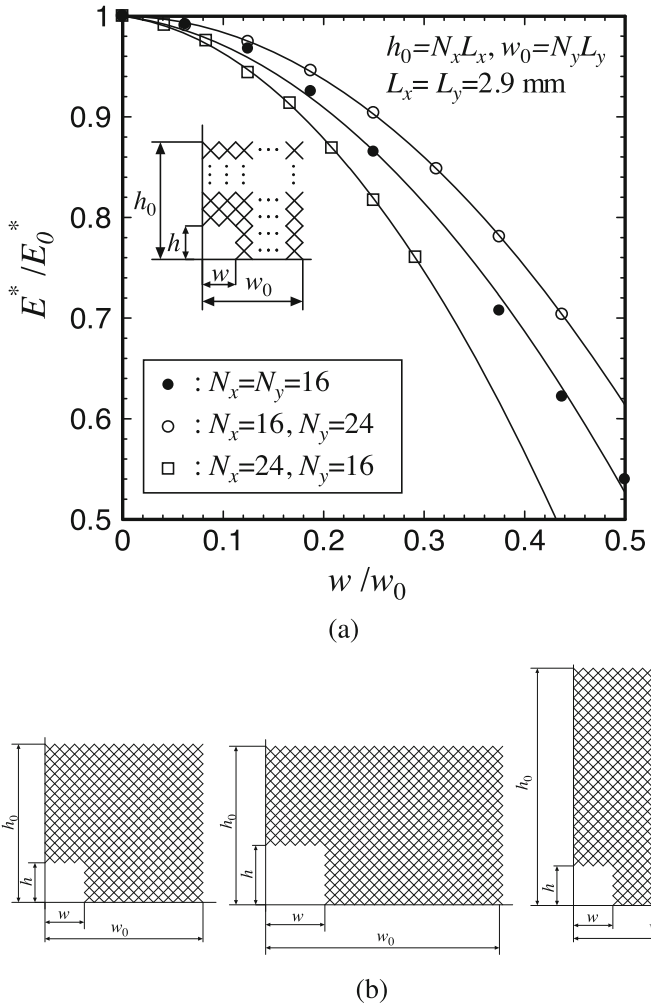

Fig. 4 Comparisons of stiffness versus defect width curve for *square-shaped*, horizontally long and vertically long lattice panels with *square-shaped* missing region. (**a**) Variations of normalized initial stiffness and defect width for lattice plates with *square-shaped* defect region. (**b**) Three types of FE models with *square-shaped* defect region

of lattice models by changing the defect size and overall plate size. Figure 4a shows the comparisons of initial stiffness E^*/E_0^* for three cases of lattice model having the same ratio of defect width w/w_0 but different ratio of defect height h/h_0. These lattice models are shown in Fig. 4b. It can be found from Fig. 4a that the normalized defect height h/h_0 is also the dominant parameter of the initial stiffness E^*/E_0^* as

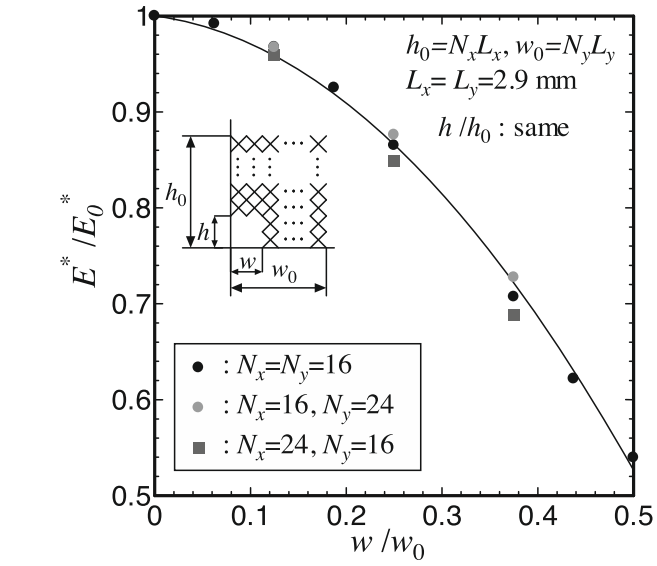

(a)

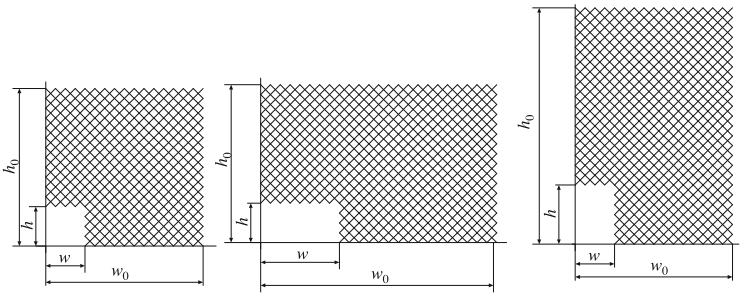

(b)

Fig. 5 Comparisons of stiffness versus defect width curve for three lattice panels with the same ratio of missing cell region h/h_0 and w/w_0. (**a**) Variations of normalized initial stiffness and defect width for lattice plates with similar form of defect region. (**b**) Three types of FE models with similar form of defect region

well as the defect width w/w_0. Figure 5a shows the comparisons of E^*/E_0^* for other three lattice models having the same ratios of defect width w/w_0 and defect height h/h_0. These lattice models are shown in Fig. 5b. When these three types of plate have the same ratios of defect width and defect height, then the obtained degradation curves of E^*/E_0^* are regarded as one curve. Therefore, it can be concluded that the initial stiffness E^*/E_0^* is mainly a function of defect width ratio w/w_0 and defect height ratio h/h_0.

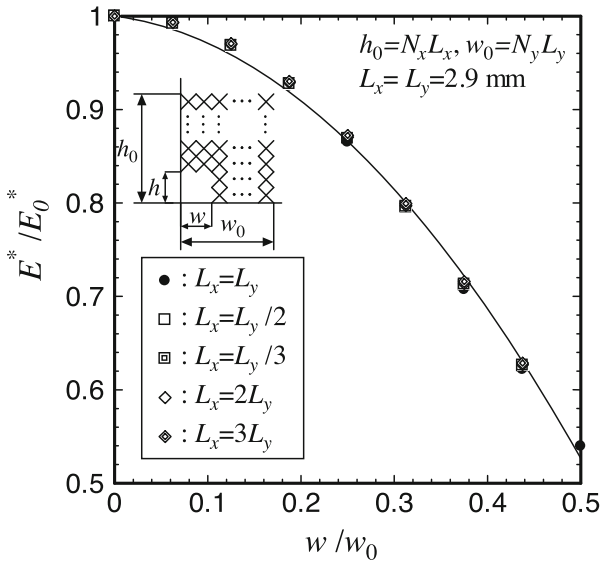

Fig. 6 Comparisons of stiffness versus defect width curve of lattice panel composed of different unit cell

Figure 6 shows the variation of initial stiffness E^*/E_0^* for lattice models having different unit-cell size. It can be understood from Fig. 6 that the degradation curve of initial stiffness is almost independent of the unit-cell shape.

3.3 Effect of Missing Cell Region on Plastic Collapse Strength σ_{pl}^*

Figure 7 shows the variation of plastic collapse strength σ_{pl}^* of square-shaped lattice panels($N_x = N_y$) by changing the missing cell region. Here, the strength σ_{pl}^* is normalized by σ_{pl0}^* for a perfect lattice model. It is found from Fig. 7 that the normalized strength $\sigma_{pl}^*/\sigma_{pl0}^*$ decreases linearly as the defect width w/w_0 increases. Also, Fig. 8 shows the comparisons of $\sigma_{pl}^*/\sigma_{pl0}^*$ of square-shaped, horizontally long and vertically long lattice panels with defect shown in Fig. 5b. It can be observed that the normalized plastic collapses strength $\sigma_{pl}^*/\sigma_{pl0}^*$ depends mainly on the defect width w/w_0, and is independent of the defect height h/h_0. This implies that the plastic collapse of the lattice panel with defect is mainly dominated by the tensile stress at the front of the defect region.

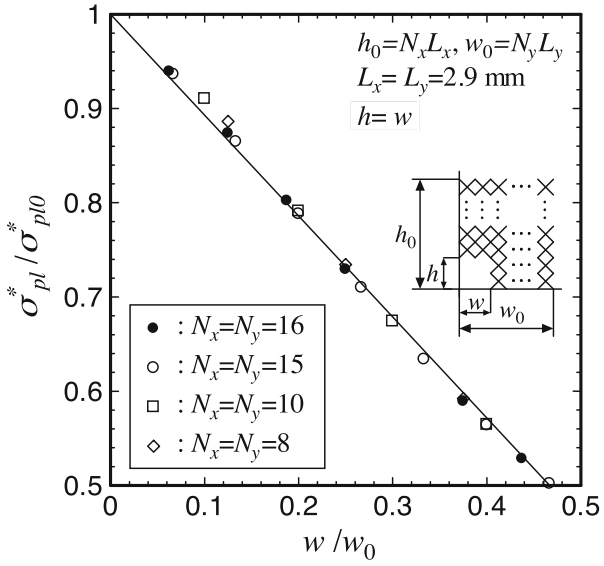

Fig. 7 Variation of plastic collapse strength σ^*_{pl} for *square-shaped* lattice panels with *square-shaped* missing cell region

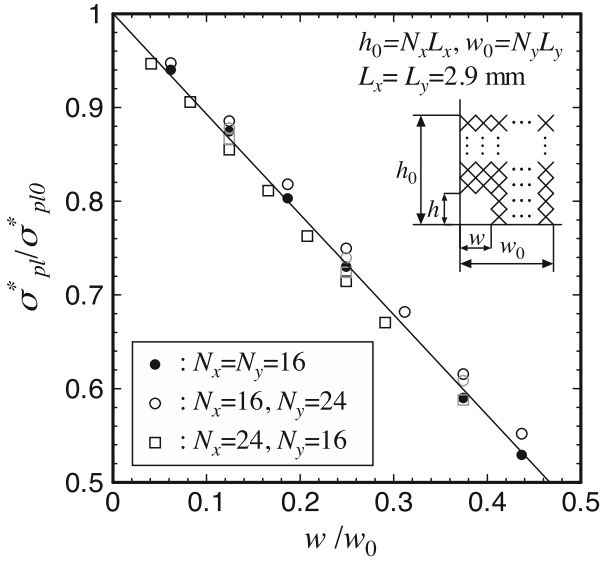

Fig. 8 Comparisons of plastic collapse strength versus defect width curve for *square-shaped*, horizontally long and vertically long lattice panels with *square-shaped* missing region

4 Conclusion

In our study, the uniaxial tensile response of lattice panel with missing cell region was investigated using nonlinear FE analysis. In particular, the effects of missing cell size and shape on the initial stiffness E^* and the plastic collapse strength σ_{pl}^* were discussed.

As for the initial stiffness E^*, the stiffness decreases dramatically as the ratio of missing cell width w/w_0 increases. Also, the stiffness is mainly governed by the ratio of missing cell height h/h_0 as well as the width w/w_0, and independent of the unit-cell shape.

On the other hand, as for the plastic collapse strength, the strength is mainly dominated by the normalized width w/w_0 only, which implies that the strength is affected strongly by the tensile strength at the front of the missing cell region.

References

1. Gibson LJ, Ashby MF (1997) Cellular solids: structure and properties, 2nd edn. Cambridge University Press, Cambridge
2. Silva MJ, Gibson L (1997) The effects of non-periodic microstructure and defects on the compressive strength of two-dimensional cellular solids. Int J Mech Sci 39:549–563
3. Guo XE, Gibson LJ (1999) Behavior of intact and damaged honeycombs: a finite element study. Int J Mech Sci 41:85–105
4. Chen C, Lu TJ, Fleck NA (1999) Effect of imperfections on the yielding of two-dimensional foams. J Mech Phys Solids 47:2235–2272
5. Chen C, Lu TJ, Fleck NA (2001) Effect of inclusions and holes on the stiffness and strength of honeycombs. Int J Mech Sci 43:487–504
6. Zhu HX, Hobdell JR, Windle AH (2001) Effects of cell irregularity on the elastic properties of 2D Voronoi honeycombs. J Mech Phys Solids 49:857–870
7. LI K, Gao XL (2004) Modeling of two-dimensional cellular solids with two types of imperfections. Compos Technol 2020:363–369
8. Buryachenko VA (2005) Effective elastic moduli of triply periodic particulate matrix composites with imperfect unit cells. Int J Solids Struct 42:4811–4832

Overview Reading and Comparing the Seismic Proof Capability of Displacement Dependent Semi-Active Hydraulic Damper and Accumulated Semi-Active Hydraulic Damper

M.-H. Shih and W.-P. Sung

Abstract Structural control technologies are applied to reinforce the building to resist the external forces. Especially, passive control method is widely accepted by earthquake research community; therefore, many researchers are developing semi-active structural control systems. There are two types of semi-active hydraulic dampers—Displacement Dependent Semi-Active Hydraulic Damper (DSHD) and Accumulated Semi-Active Hydraulic Damper (ASHD) have been proposed by Shih et al. In this study, oil circuit and element hysteretic behavior of DSHD and ASHD are discussed. Then, a ten floor shear frame structure installed with DSHD and ASHD with various control conditions is simulated for analyzing the control effect of the maximum story drift, maximum absolute acceleration, and maximum base shear. Test and analysis results reveal that shock absorption ratio of structural displacement of the roof of ten floor structure added with ASHD reaches to 87.9 %. Structural acceleration responses of this structure can be diminished by the synchronization of ASHD. Base shear of this structure installed with these two dampers with various control conditions is reduced 55–60 %. Seismic proof of these two semi-active hydraulic dampers can be demonstrated by this study.

1 Introduction

Global warming affects the ocean temperature to cause the El Nino and anti-El Nino phenomena over and over again. Then, the intensity of typhoons (hurricanes) has been strengthened. Otherwise, the movement of mantle has been accelerated

M.-H. Shih (✉)
National Chi-Nan University, Nantao, Taiwan
e-mail: iloveaachen@gmail.com

W.-P. Sung
National Chin-Yi University of Technology, Taichung, Taiwan
e-mail: wps@ncut.edu.tw

H. Irschik et al. (eds.), *Dynamics and Control of Advanced Structures and Machines*, DOI 10.1007/978-3-319-43080-5_5

to induce some strong earthquakes in the world such as Indian ocean strong earthquake, 2004, Japan earthquake, 2011, Pakistan earthquake, 2013, Nepal earthquake, 2015 to cause much loss of life and properties. Therefore, structural control technologies have been developed to diminish the structural responses, induced by earthquakes and wind forces [1–3].

These structural control technologies have been divided into three parts: active control, passive control, and semi-active control, which semi-active control should add the passive control element on structure. The elements of passive control must be reformed or installed control components to provide local adaptability.

Presently, some of semi-active hydraulic dampers have been developed such as Semi-Active Hydraulic Damper, SHD [4–6], Magnetorheological Damper, MR Damper [7], Electrorheological Damper, ER Damper [8], and Taylor Device [9]. The main purpose of this study is to compare oil circuit, element hysteretic behavior and seismic proof capability of high-rise building added with two special dampers, Displacement Dependent Semi-Active Damper, DSHD and Accumulated Semi-Active Hydraulic Damper, ASHD, proposed by Shih et al. [10–13]. Then, a ten floor shear frame structure is used to simulate and analyze to compare the seismic proof capability between bare structure and structure added with these two types of semi-active hydraulic dampers.

2 Design Concept of Semi-Active Hydraulic Dampers

There are two different types of semi-active hydraulic dampers have been proposed by Shih and Sung: DSHD and ASHD. These two types are composed of Hydraulic Jack, Directional Valve, Check Valve, Relief Valve, and Accumulator to constitute DSHD and ASHD. These two types of semi-active hydraulic dampers are using different combinations of components and oil circuit assembly to produce different reactions of earthquake responses due to its oil circuit and mechanical changes.

The main functions of these components are described as follows: (A) Hydraulic Jack: the main power transmission of these two types of hydraulic dampers with two connection points, one is to join structure with a hinge and another is to articulate with stiffened component; (B) Directional Valve: to transform the flow direction of pressure oil. Electromagnetic type of Directional Valve is used in this study; (C) Check Valve: to keep the operating oil on unidirectional flow without refluxing; (D) Relief Valve: to keep the hydraulic circuit under oil pressure at a certain value; (E) Accumulator: the main function of Accumulator of the ASHD is (1) to keep an initial pressure; (2) to storage oil.

The various combinations of these two types of semi-active hydraulic dampers are described as follows:

2.1 Displacement Dependent Semi-Active Hydraulic Damper

2.1.1 Oil Circuit of DSHD

The oil circuit of DSHD is composed of Hydraulic Jack, Directional Valve, Check Valve, and Relief Valve, the oil path of DSHD is shown in Fig. 1. In order to prevent the DSHD from overloading, the Relief Valve is installed in the oil circuit to avoid bracing yielding due to the large deformation of structure. Therefore, the hysteretic loop of DSHD with and without overflow behavior of DSHD should be discussed to investigate its energy dissipation behavior. Directional Valve of DSHD can present the different state: oil circuit does not pass to the left, both sides of circuit connected, and the circuit access to the right-hand side, so as to achieve the requirement of "free to lengthen," "free to expand and contract," and "free to shorten", as shown in Fig. 2. Figure 2a–c represents the "free to lengthen," "free to expand and contract," and "free to shorten," respectively. The combination of series connection of DSHD and bracing can always do negative work on structure.

2.1.2 Element Hysteretic Behavior of DSHD

Relief Valve is installed in this DSHD, therefore, the energy dissipation behavior of DSHD performs with and without overflow behavior of DSHD. Figure 3 displays the hysteretic loop of DSHD without overflow behavior. This figure shows the energy dissipation influence of amplitude and bracing stiffness. When the structural

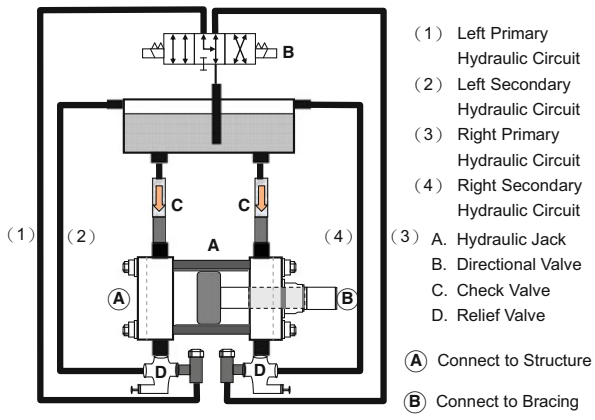

Fig. 1 The organization of DSHD

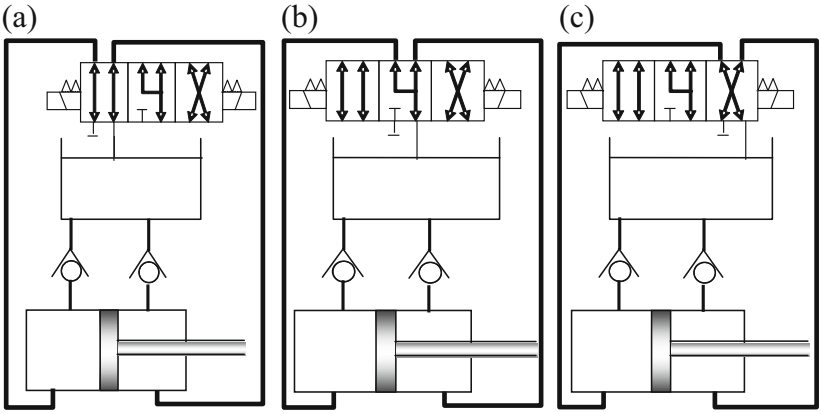

Fig. 2 Different connection states of DSHD device. (**a**) free to lengthen, (**b**) free to expand and contract, (**c**) free to shorten

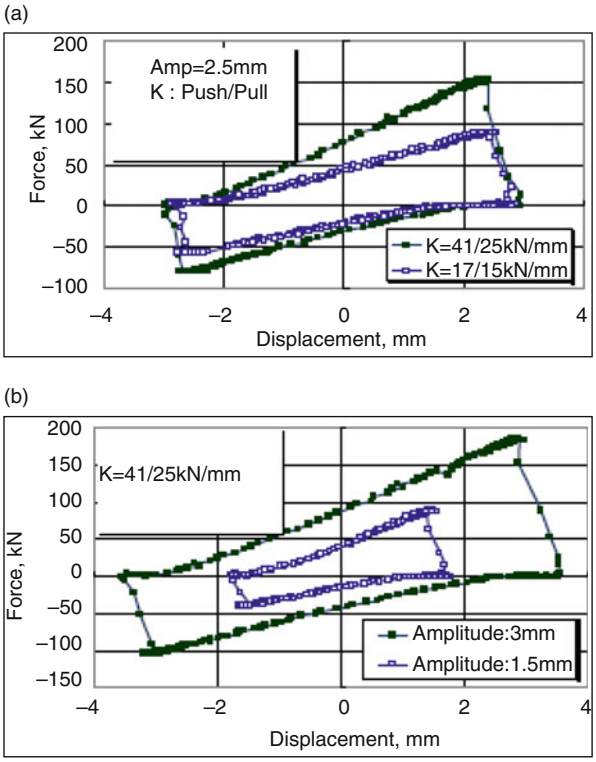

Fig. 3 Energy dissipation influence parameters of DSHD. (**a**) Influence of stiffness of bracing, (**b**) influence of loading amplitude

displacement increases the control force is provided by elastic deformation of bracing, and structural displacement reaches its maximum amplitude, bracing force up to the maximum value. Then, bracing force can be released at this time, then, when structural displacement increases on reverse direction, bracing deformation increases from zero, and provide the reverse resistant force.

2.2 Accumulated Semi-Active Hydraulic Damper

2.2.1 Oil Circuit of ASHD

The combination of ASHD, shown in Fig. 4, is almost the same as DSHD. The difference between ASHD and DSHD is that an Accumulator is connected to the Directional Valve. Aims of installing the Accumulator are (1) to maintain an initial pressure; (2) to storage oil.

2.2.2 Element Hysteretic Behavior of ASHD

Control force of ASHD is provided by the change of oil with pre-pressure magnitude of the Accumulator. The hysteretic energy dissipation behavior of element test result is shown in Fig. 5, the action force is variation between 80 and −60 kN. The action forces at push-side and pull-side maintain the maximum values at all times. The reason for difference between both of the maximum values at two sides is the difference of effective piston area of cylinder. When pressure of each

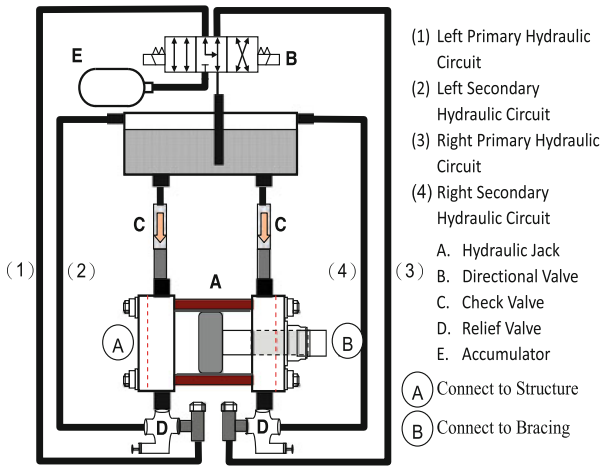

Fig. 4 Organization of ASHD

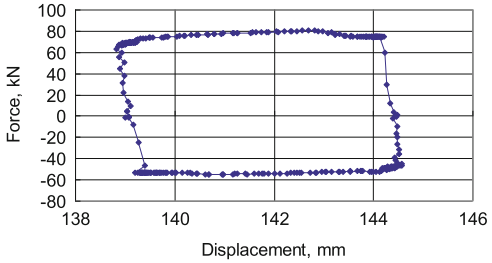

Fig. 5 The energy dissipation behavior of ASHD

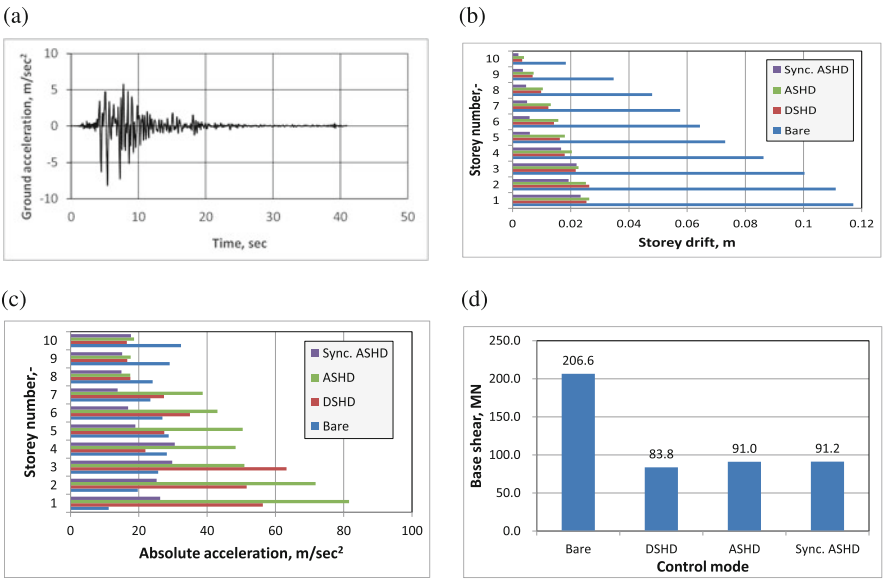

Fig. 6 Ground acceleration and analysis results. (**a**) Record of ground acceleration, Kobe earthquake 1995, (**b**) comparison of the maximum storey drifts responses, (**c**) comparison of the maximum absolute acceleration responses, (**d**) comparison of the maximum base shear responses

cylinder body is equal, the output forces at each side are not the same. But, both of them can preserve the maximum output state at any time for ASHD, installed with accumulator by loaded storage oil into Accumulator to produce pressure for oil inlet, then, the pre-pressure of cylinder can be produced. This is the reason for Fig. 6 to maintain the defined value and avoid the loss of forces because of the cylinder sliding. Therefore, Accumulator can avoid the problem of the cylinder sliding. The energy dissipation behavior of ASHD is dominated by the Accumulator. The control force is directly related to the maximum pressure of the Accumulator.

2.3 Case Study of High-Rise Building Added with DSHD and ASHD

2.3.1 Analysis Model and Control Parameters

In this study, a ten floor shear frame structure is used to simulate and analyze the seismic proof capability of this structure added with DSHD and ASHD. The mass of each floor of this shear frame structure is 1000 tones and the stiffness of each floor is 1763.47 MN/m. Natural frequency of this structure is 1.0 s and assuming the damping ratio of basic model of vibration is 0.5 %. Three control modes are analyzed to compare the seismic proof capability of this building added with different control conditions such as with DSHD, ASHD with and without synchronized control with the structural responses of bare structure. The analysis parameters for each analysis mode are listed in Table 1. The brace stiffness is 7053.88 MN/m and the damper capacity is 50 MN. In this study, the maximum structural story drift, the maximum absolute acceleration, and the maximum base shear of test building under different control conditions are under excitation of Kobe earthquake record, 1995, the maximum acceleration is 0.833 G, shown in Fig. 6a.

2.4 Analysis Results

The analysis results of the maximum story drift, the maximum absolute acceleration, and the maximum base shear of test building under external excitation of Kobe earthquake are shown in Fig. 6, respectively. Figure 6b displays that the decreasing trends of the maximum story drift responses are bottom up. But, it also displays that the maximum story drift reduction percentage of Mode I, II, and III are 78, 78, and 80 %, respectively. There is no obviously difference between Mode I and Mode II, the Accumulator does not perform its seismic proof efficiency. But, Accumulator can raise the saturation of oil of hydraulic damper to avoid the losses of control efficiency resulting from the oil spill from perspective of shock absorption. Otherwise, test results of Mode III also reveal that the structural displacement responses of more than half floors of building have been controlled well, better than those of Mode II. Then, the roof structural displacement responses of bare structure are compared with those of Mode III, the maximum structural

Table 1 The analysis parameters for these three analysis modes

Mode	Damper type	Brace stiffness (MNm^{-1})	Damper capacity (MN)	Synchronization
I	DSHD	7053.88	50	No
II	ASHD	7053.88	50	No
III	ASHD	7053.88	50	Yes

displacement response of top roof for bare structure is smaller than that of Mode III, 0.627 m for bare structure and 0.076 m for Mode III respectively. The shock absorption ratio of the structural displacement of top roof is 87.9 %.

Figure 6c reveals that the absolute acceleration responses of Mode I and Mode II are greater than those of bare structure, the variation trend of these responses is reverse for those of bare structure. Therefore, the structural acceleration responses of Mode I and Mode II have been enlarged for the lower floors of building by added with dampers. After checking the time history of acceleration responses, it is found that the difference of switching time causes the magnification of the structural acceleration responses. The test results of Mode III are mined to show that the transient amplification phenomenon has been eliminated by the synchronization process of ASHD. Not only the maximum structural acceleration responses of all floors are less than those of bare structure, but also the control effects of structural displacement control are better than those of Mode I and II.

The maximum absolute acceleration responses of Mode I and Mode II have no apparent effects because of pulse phenomena. Nevertheless, the shock absorption effects of base shear responses provide obviously mitigation effect for Mode I, II, and III. Each control mode will reduce 55–60 %.

3 Conclusions

The component test of DSHD and ASHD has been executed to discuss the basic energy dissipation behavior. Then, a ten floor shear frame structure is applied to simulate and analyze the seismic proof capability of this building added with DSHD and ASHD without and with synchronized. The test and analysis results are synthesized as follows:

1. A ten floor shear frame structure is used to simulate and analyze the seismic proof capability of this structure added with DSHD and ASHD without and with synchronized control. Simulation results display that there are no obviously difference of the maximum story drift reduction percentage between these three control modes.
2. Simulation results of test structure with ASHD with synchronized control show that the structural displacement responses of more than half of floors have been controlled well, better than test structure with ASHD without synchronized control. Otherwise, a comparison between roof structural displacement responses of bare structure and those of test structure with ASHD with synchronized control, the shock absorption ratio of the roof structural displacement is 87.9 % for test structure under control process of ASHD with synchronized control.
3. Structural acceleration responses of test structure added with DSHD and ASHD without synchronized control have been enlarged for the lower floors of test structure under these two control conditions.
4. The base shear responses of test structure added with DSHD and ASHD without and with synchronized control are reduced 55–60 %.

References

1. Housner GW, Bergman LA, Caughey TK, Chassiakoes AG, Claus RO, Masri SF, Skelton RE, Soong TT, Spencer BF, Yao JTP (1997) Structural control: past present and future. J Eng Mech 123(9):897–971
2. Yao JTP (1972) Concept of structural control. J Struct Div 98(7):1567–1574
3. Meirovitch L (1990) Dynamics and control of structures. Wiley, New York
4. Symans MD, Constantinou MC (1997) Seismic testing of a building structure with a semi-active fluid damper control system. Earthq Eng Struct Dyn 26(7):759–777
5. Kurata N, Kobori T, Takahashi M, Niwa N, Midorikawa H (1999) Actual seismic response controlled building with semi-active damper system. Earthq Eng Struct Dyn 28(11):1427–1447
6. Kurata N, Kobori T, Takaashi M, Ishibashi T, Niwa N, Tagami J, Midorikawa H (2000) Forced vibration test of a building with semi-active damper system. Earthq Eng Struct Dyn 29(5):629–645
7. Dyke SJ, Spencer BF Jr, Sain MK, Carlson JD (1998) An experimental study of MR dampers for seismic protection. Smart Mater Struct 7(5):693–703
8. Xu YX, Qu WL, Ko JM (2000) Seismic response control of frame structures using magnetorheological/electrorheological dampers. Earthq Eng Struct Dyn 29(5):557–575
9. Taylor DP (1996) Fluid dampers for applications of seismic energy dissipation and seismic isolation. Eleventh world conference on Earthquake Engineering, No. 798
10. Shih MH, Lin CI, Sung WP (2006) Numerical analysis for the energy reduction behavior of accumulated semi-active hydraulic damper. J Dyn Syst Geom Theor 4(1):29–45
11. Shih MH, Sung WP (2004) The energy dissipation behavior of displacement dependent semi-active hydraulic damper. J Struct Mech Earthq Eng Jpn Soc Civ Eng 21(2):121s–129s
12. Shih MH, Sung WP, Go CG (2003) A design concept with a displacement dependent semi-active hydraulic damper for energy dissipation. Exp Tech 27(6):53–56
13. Shih MH, Sung WP, Go CG (2002) Development of accumulated semi-active hydraulic damper. Exp Tech 26(5):29–32

On Necessary and Sufficient Conditions for Eigenstrain-Type Control of Stresses in the Dynamics of Force-Loaded Elastic Bodies

Juergen Schoeftner and Hans Irschik

Abstract In the present contribution, the possibility of controlling dynamic stresses in force-loaded bodies by means of actuating eigenstrain fields is addressed. The action of eigenstrains, such as thermal or piezoelectric actuating strains, is subsequently gathered under the notion of actuating stresses. Our study is performed in the framework of the theory of small incremental dynamic deformations superimposed upon a state of possibly large static pre-deformation of a hyperelastic body. Particularly, we present a solution for the general problem of producing certain incremental stress trajectories by means of specifically tailored actuation stresses that are superimposed onto the force-loaded body. This we shortly call the stress tracking problem. The problem of suppressing incremental stresses is contained as a special case. Subsequently, particular emphasis is given to the systematic derivation of necessary and sufficient conditions that must be satisfied in order to solve the stress tracking problem. Necessary conditions are presented that must be satisfied by the intermediate configuration and by the desired incremental stress field that shall be tracked, and sufficient conditions are derived that must be satisfied by the incremental actuating stresses. As an illustrative example, our three-dimensional formulation is eventually applied to the one-dimensional dynamic case of a straight homogeneous rod with a support excitation at one end and a single point-mass at the other end.

J. Schoeftner (✉) • H. Irschik
Johannes Kepler University Linz, Institute of Technical Mechanics, Altenberger Strasse 69, A-4040 Linz, Austria
e-mail: juergen.schoeftner@jku.at; irschik@mechatronik.uni-linz.ac.at

H. Irschik et al. (eds.), *Dynamics and Control of Advanced Structures and Machines*, DOI 10.1007/978-3-319-43080-5_6

1 Fundamental Relations

1.1 Local Balance of Linear Momentum and Boundary Conditions in the Actual Configuration

In the following, we use a natural (unstressed) state of the body as common reference configuration. The local relation of balance of linear momentum reads:

$$\mathrm{Div}\, P + b_0 = \rho_0 \ddot{u} \tag{1}$$

The first Piola–Kirchhoff stress tensor is denoted as P, and Div stands for the divergence operator with respect to the place in the reference configuration. The imposed body force per unit volume in the reference configuration is b_0, and ρ_0 is the mass density in the reference configuration. The total displacement vector from the reference configuration is written as u, and a superimposed dot denotes the material time derivative. On some portions ∂B_1 of the boundary $\partial B = \partial B_1 \cup \partial B_2$, kinematic boundary conditions are prescribed:

$$\partial B_1 : \quad u = u^* \tag{2}$$

The imposed surface displacements at ∂B_1 are denoted as u^*. At ∂B_2, dynamic boundary conditions (boundary conditions of traction) are given:

$$\partial B_2 : \quad P\, n_0 = t_0^* \tag{3}$$

Here, n_0 stands for the unit outer normal vector at the surface in the reference configuration, and t_0^* is the imposed Lagrange surface traction.

1.2 Introduction of a Static Intermediate Configuration

Incremental dynamic displacements and stresses are considered relative to an intermediate configuration, which in general may be a (possibly) large static pre-deformation from the reference configuration. The use of a common reference configuration allows applying the following additive decomposition:

$$b_0 = b_{0i} + b_{0+}, \quad t_0^* = t_{0i}^* + t_{0+}^*, \quad u = u_i + u_+, \quad P = P_i + P_+ \tag{4}$$

The subscript (i) refers to the static intermediate configuration, and the subscript $(+)$ indicates the dynamic increments from the intermediate configuration. Substituting into Eqs. (1)–(4) and subtracting the relations for the intermediate state gives:

$$\mathrm{Div}\, P_+ + b_{0+} = \rho_0 \ddot{u}_+ \tag{5}$$

$$\partial B_1: \quad u_+ = u_+^* \tag{6}$$

$$\partial B_2: \quad P_+ n_0 = t_{0+}^* \tag{7}$$

Since the intermediate state is assumed to be static, i.e., it is at rest, trivial initial conditions for the incremental motion are obtained:

$$t = 0: \quad u_+ = 0, \quad \dot{u}_+ = 0 \tag{8}$$

1.3 Linearization About the Incremental State

From now on, we consider infinitesimally small incremental dynamic deformations superimposed upon the intermediate state. The latter may represent a large static pre-deformation from the common reference configuration. Considering a hyperelastic body, the linearized constitutive relations read

$$P_+ = A_i \left[\mathrm{Grad}\, u_+\right] + P_{a+} \tag{9}$$

The fourth order tensor of elastic constants in the intermediate configuration is abbreviated by A_i, and Grad denotes the gradient operator with respect to the place in the reference configuration. For the square bracket notation, which indicates the linear mapping of a second order tensor onto a second order tensor via a fourth order tensor, see Gurtin [1]. The incremental actuation stress tensor, a second order tensor, is denoted as P_{a+}. It represents a linear mapping of the actuating incremental eigenstrains. In case of thermal eigenstrains, it relates the stress to the temperature via the second order stress–temperature tensor, see Carlson [2] for the linear theory of thermoelasticity, i.e., when intermediate and natural reference configuration do coincide. When using eigenstrains for the purpose of controlling deformations, one also talks about a smart actuation in the literature. Note that in case of an intermediate state with a large deformation from the reference configuration, A_i as well as P_{a+} depend on the intermediate state and thus do vary across the body, even if it is homogeneous in the natural reference configuration.

1.4 Stress-Based Reformulation

Since we deal with stress tracking, a stress-based reformulation of the above incremental relations is desirable. In the framework of the linear theory of elasticity, i.e., when the intermediate configuration coincides with the natural reference configuration, this strategy dates back to Ignaczak [3] and [4]. This reformulation

requires that A_i is invertible:

$$\text{Grad}\, u_+ = K_i \left[P_+ - P_{a+}\right] \quad \text{with} \quad K_i = {A_i}^{-1} \tag{10}$$

The existence of the compliance tensor K_i in any point of the body represents a first necessary condition in order that our subsequent solutions for the stress tracking problem make sense. Substituting Eq. (10) into Eqs. (5)–(8), we obtain the following stress-based reformulation of the incremental initial boundary value problem under consideration:

$$\text{Grad}\left({\rho_0}^{-1}\left(\text{Div}\, P_+ + b_{0+}\right)\right) = K_i\left[\ddot{P}_+ - \ddot{P}_{a+}\right] \tag{11}$$

$$\partial B_1\text{:} \quad \text{Div}\, P_+ + b_{0+} = \rho_0\, \ddot{u}^*_+ \tag{12}$$

$$\partial B_2: \quad P_+\, n_0 = t^*_{0+} \tag{13}$$

$$t = 0: \quad P_+ - P_{a+} = 0, \quad \dot{P}_+ - \dot{P}_{a+} = 0 \tag{14}$$

2 The Dynamic Stress Tracking Problem

2.1 Formulation of the Stress Tracking Problem

We now formulate the stress tracking problem as follows: derive a space- and time-wise distribution of an incremental actuation stress field P_{a+}, such that the above initial boundary value problem, Eqs. (5)–(9), results in a desired incremental stress field Z everywhere in the body under consideration and for all times:

$$P_+ \equiv Z \tag{15}$$

Note that the desired incremental stress field Z may be both, space- and time-dependent. For a convenient solution strategy, we introduce an error stress field:

$$P_e = P_+ - Z \tag{16}$$

Our goal in the following will be enforcing that the error stress field does vanish everywhere and for all times, $P_e = 0$.

2.2 Direct Solution of the Stress Tracking Problem

In a first step, we derive a direct solution strategy for the stress tracking problem by replacing the incremental stress P_+ by the entities Z and P_e, see Eq. (16), in the stress-based formulation in Eqs. (11)–(14). Putting the expressions that contain P_e

onto the left-hand side of the corresponding relations yields:

$$\begin{aligned}
&\mathrm{Grad}\left({\rho_0}^{-1}\mathrm{Div}\,P_e\right) - K_i\left[\ddot{P}_e\right] \\
&\quad = -\,\mathrm{Grad}\left({\rho_0}^{-1}\left(\mathrm{Div}\,Z + b_{0+}\right)\right) + K_i\left[\ddot{Z} - \ddot{P}_{a+}\right] && (17)\\
&\partial B_1\colon \quad \mathrm{Div}\,P_e = -\mathrm{Div}\,Z - b_{0+} + \rho_0\,\ddot{u}^*_+ && (18)\\
&\partial B_2\,: \quad P_e\,n_0 = -Z\,n_0 + t^*_{0+} && (19)\\
&t = 0\,: \quad P_e = P_{a+} - Z, \quad \dot{P}_e = \dot{P}_{a+} - \dot{Z} && (20)
\end{aligned}$$

The desired goal, $P_e \equiv 0$, then may be reached, when the right-hand sides of Eqs. (17)–(20) do vanish. First, note that Eqs. (18) and (19) result into two necessary conditions that must be satisfied by the desired incremental stress field Z:

$$\begin{aligned}
&\partial B_1\colon \quad \mathrm{Div}\,Z = -b_{0+} + \rho_0\,\ddot{u}^*_+ && (21)\\
&\partial B_2\,: \quad Z\,n_0 = t^*_{0+} && (22)
\end{aligned}$$

In other words, at the boundary of the body B, the desired incremental stress field Z cannot be chosen independently from the imposed incremental body forces and boundary data. Moreover, two sufficient conditions for the incremental actuation stress follow from Eqs. (17) and (20):

$$\begin{aligned}
&\ddot{P}_{a+} = -A_i\left[\mathrm{Grad}\left({\rho_0}^{-1}\left(\mathrm{Div}\,Z + b_{0+}\right)\right]\right] + \ddot{Z} && (23)\\
&t = 0\,: \quad P_{a+} = Z, \quad \dot{P}_{a+} = \dot{Z} && (24)
\end{aligned}$$

In the present context of (infinitesimally) small incremental deformations superimposed upon the large pre-deformation of the intermediate state, it is required that the latter is stable in some sense, such that a further necessary condition must be formulated.

2.3 *Stability Issues*

In order to derive a condition for the necessary stability of the intermediate configuration, we now utilize a strategy originally suggested by Ignaczak [3] for studying the completeness of a stress-based formulation in the framework of the linear case. By analogy, we introduce the following scalar error integral over the volume in the reference configuration, but referring to the incremental error stress:

$$I_e\,(t) = \int_{B_0}\left(\rho_0^{-1}\,\mathrm{Div}\,P_e \cdot \mathrm{Div}\,P_e + K_i\left[\dot{P}_e\right]\cdot\dot{P}_e\right)\,dV_0 \qquad (25)$$

Now assume that initially no errors are present:

$$P_e\,(t=0)=0, \quad \dot{P}_e\,(t=0)=0 \;\Rightarrow\; I_e\,(t=0)=0 \tag{26}$$

Considering the major symmetry property of the fourth order tensor of compliance

$$K_i\,[B]\cdot D = K_i\,[D]\cdot B \tag{27}$$

see, e.g., Knops and Wilkes [5], the time derivative of Eq. (25) follows to:

$$\frac{1}{2}\frac{d}{dt}I_e = \int_{B_0}\left(\rho_0^{-1}\,\mathrm{Div}\,P_e\cdot\mathrm{Div}\,\dot{P}_e + \ddot{P}_e\cdot K_i\left[\dot{P}_e\right]\right)\,dV_0 \tag{28}$$

Using some results from tensor algebra and analysis, it can be shown after some reformulations, using Eqs. (21)–(24) and (26), that the necessary and sufficient conditions for $P_e \equiv 0$ yield that

$$\begin{aligned}&\frac{d}{dt}I_e = 0 \Rightarrow I_e\,(t) = \text{const.} = I_e\,(t=0)\\ &\Rightarrow I_e\,(t) = \int_{B_0}\left(\rho_0^{-1}\,\mathrm{Div}\,P_e\cdot\mathrm{Div}\,P_e + K_i\left[\dot{P}_e\right]\cdot\dot{P}_e\right)\,dV_0 \equiv 0\end{aligned} \tag{29}$$

Now, the first part of the integral in Eq. (29) is positive semi-definite:

$$\int_{B_0}\left(\rho_0^{-1}\,\mathrm{Div}\,P_e\cdot\mathrm{Div}\,P_e\right)\,dV_0\;\begin{cases}=0 & \text{for}\quad P_e=0\\ >0 & \text{for}\quad P_e\neq 0\end{cases} \tag{30}$$

However, the second part of the integral is generally indefinite

$$\int_{B_0}\left(K_i\left[\dot{P}_e\right]\cdot\dot{P}_e\right)\,dV_0\;\begin{cases}=0 & \text{for}\quad \dot{P}_e=0\\ <0 & \\ >0 & \text{for}\quad \dot{P}_e\neq 0\end{cases} \tag{31}$$

Thus, vanishing of the error integral implies that the error stress vanishes only if:

$$P_e\equiv 0 \quad \text{if} \quad \int_{B_0} K_i\left[\dot{P}_e\right]\cdot\dot{P}_e\,dV_0 > 0 \quad \text{for} \quad \dot{P}_e\neq 0 \tag{32}$$

This necessary condition is analogous to the Hadamard stability condition, see Knops and Wilkes [5]

$$\int_{B_0} K_i\left[\dot{P}_e\right] \cdot \dot{P}_e \, dV_0 > 0 \quad \text{for} \quad \dot{P}_e \neq 0 \tag{33}$$

This necessary condition is also known as infinitesimal superstability of the intermediate configuration under consideration. When the intermediate configuration and the natural reference configuration do coincide, i.e., in the linear theory of infinitesimally small deformations superimposed upon an undeformed configuration, stability is pre-assumed. In the present case of a possibly large deformation of the intermediate configuration from the reference configuration, however, Eq. (33) represents a practically important requirement.

2.4 Recalling the Three-Dimensional Solution

The above results for solving the stress tracking problem are shortly summarized. If the following two necessary conditions hold at the boundary of the body:

$$\partial B_1: \quad \mathrm{Div}\, Z = -b_{0+} + \rho_0 \, \ddot{u}^*_+, \tag{34}$$

$$\partial B_2: \quad Z\, n_0 = t^*_{0+}, \tag{35}$$

and moreover if the compliance tensor does exist in every point in the intermediate configuration, and if the Hadamard stability condition stated in Eq. (33) does hold, then, in order that the goal of stress tracking is reached,

$$P_+ \equiv Z, \tag{36}$$

it is sufficient to use an eigenstrain actuation satisfying the following two relations:

$$\ddot{P}_{a+} = -A_i\left[\mathrm{Grad}\left({\rho_0}^{-1}\left(\mathrm{Div}\, Z + b_{0+}\right)\right)\right] + \ddot{Z}, \tag{37}$$

$$t = 0: \quad P_{a+} = Z, \quad \dot{P}_{a+} = \dot{Z} \tag{38}$$

For preliminary formulations concerning the linear case of infinitesimally small deformations superimposed upon the natural reference configuration, see Irschik, Gusenbauer and Pichler [6] and Irschik [7]. The solution strategy gathered in Eqs. (34)–(38) will be subsequently exemplified.

3 Illustrative Example: Straight Rod

3.1 One-Dimensional Boundary Value Problem

In the one-dimensional case, the relation of balance of incremental linear momentum, Eq. (5), becomes

$$\frac{\partial}{\partial X} P_+(X,\ t) + b_{0+}(X,\ t) = \rho_0(X)\ \frac{\partial^2}{\partial t^2}\, u_+(X,\ t) \tag{39}$$

The axial coordinate in the reference configuration is denoted as $0 \leq X \leq L$. The incremental boundary conditions of place and traction, Eqs. (6) and (7), and the trivial initial conditions for the incremental motion from the static intermediate configuration, see Eq. (8), read

$$X = 0: \quad u_+(X = 0,\ t) = u_+^*(t) \tag{40}$$

$$X = L: \quad P_+(X = L,\ t) = t_{0+}^*(t) \tag{41}$$

$$t = 0: \quad u_+(X,\ t = 0) = 0, \quad \dot{u}_+(X,\ t = 0) = 0 \tag{42}$$

The one-dimensional form of the linearized constitutive relation in Eq. (10) is

$$\frac{\partial}{\partial X}\, u_+(X,\ t) = K_i(X)\,(P_+(X,\ t) - P_{a+}(X,\ t)) \tag{43}$$

The Hadamard stability condition for the intermediate configuration, Eq. (33), locally reduces to

$$K_i = 1/A_i > 0 \tag{44}$$

3.2 Conditions for Stress Tracking in the One-Dimensional Case

We assume a support excitation $u_+^*(t)$ at $X = 0$ and boundary conditions of traction at $X = L$:

$$X = 0: \quad \frac{\partial}{\partial X}\, Z(0,\ t) = -b_{0+}(0,\ t) + \rho_0(0)\ \frac{\partial^2}{\partial t^2} u_+^*(t) \tag{45}$$

$$X = L: \quad Z(L,\ t) = t_{0+}^*(t) \tag{46}$$

Sufficient conditions for stress tracking, $P_+(X,\ t) \equiv Z(X,\ t)$, then become, see Eqs. (37) and (38):

$$\frac{\partial^2}{\partial t^2} P_{a+}(X,\ t) = -A_i(X) \left[\frac{\partial}{\partial X} \left({\rho_0}^{-1}(X) \left(\frac{\partial}{\partial X} Z(X,\ t) + b_{0+}(X,\ t) \right) \right) \right] + \frac{\partial^2}{\partial t^2} Z(X,\ t) \tag{47}$$

$$t = 0: \quad P_{a+}(X,\ 0) = Z(X,\ 0), \quad \dot{P}_{a+}(X,\ 0) = \dot{Z}(X,\ 0) \tag{48}$$

3.3 Linear Elastic Rod with End-Mass and Support Excitation

For simplicity sake, from now on we restrict to the case of an intermediate configuration, which coincides with the natural reference configuration, such that we deal with the linear theory of elastic bodies in the presence of eigenstrains. We take body forces to be absent, $b_{0+}(X,\ t) = 0$, and assume that the mass density ρ_0, the cross-section a_0 and the elastic constant A_0 (the effective Young's modulus) of the rod are constant. As complicating aspects, the rod, however, is assumed to be firmly connected to a single point-mass M at the free end $X = L$. The boundary condition of traction at this end of the rod thus becomes, see Eqs. (39) and (41):

$$X = L: \quad P_+(L,\ t) = t^*_{0+}(t) = -\frac{M}{a_0} \frac{\partial^2}{\partial t^2} u_+(L,\ t) = -\frac{M}{\rho_0\, a_0} \frac{\partial}{\partial X} P_+(L,\ t) \tag{49}$$

Now, let the desired stress be separable in space and time $Z(X, t) = z(X)\ \rho_0 \frac{\partial^2}{\partial t^2} u^*_+(t)$, then the necessary conditions stated in Eqs. (45) and (46) yield that

$$X = 0: \quad \frac{\partial}{\partial X} z(0) = 1 \tag{50}$$

$$X = L: \quad z(L) + \frac{M}{\rho_0\, a_0} \frac{\partial}{\partial X} z(L) = 0 \tag{51}$$

A suitable function $z(X)$ is chosen, which satisfies the necessary conditions, Eqs. (50) and (51), and the sufficient conditions, Eqs. (47) and (48), are eventually solved for a given $u^*_+(t)$, resulting in an actuation stress field that satisfies $P_+(X,\ t) \equiv Z(X,\ t)$. This strategy is subsequently demonstrated in an example. The following peak-type functional dependence for the support excitation is taken into consideration in this example, see also Fig. 1, where C and α are constants:

$$u^*_+(t) = C(\alpha\, t)^3 \exp(-\alpha\, t)\, L \tag{52}$$

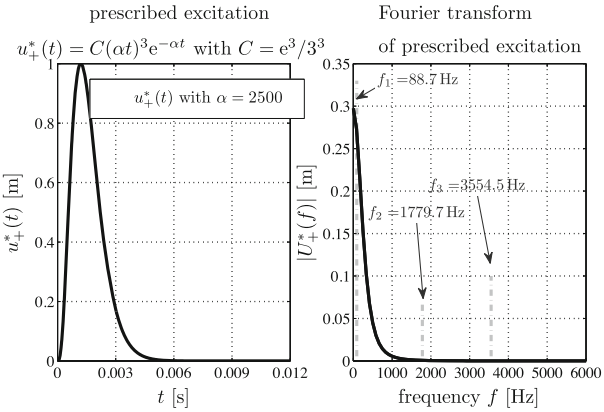

Fig. 1 Support excitation at $X = 0$ and Fourier transform

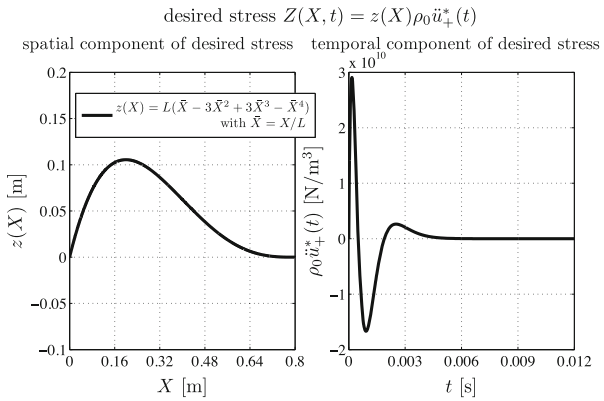

Fig. 2 Spatial and temporal distribution of the desired stress $Z(X,\ t)$

In Fig. 1, the first three natural frequencies of the rod are marked as f_1, f_2 and f_3. The following values (in SI-units) have been chosen in the numerical computations: $C = (e/3)^3$, $\alpha = 2500$, modulus of elasticity $A_0 = 6.29 \times 10^9$, cross-section $a_0 = 4 \times 10^{-5}$, mass density $\rho_0 = 7750$, single mass $M = 10$, length of rod $L = 0.8$. From Eqs. (48) and (52), we find that:

$$P_{a+}(X,\ 0) = 0, \quad \frac{\partial}{\partial t} P_{a+}(X,\ 0) = 0 \tag{53}$$

For the desired stress $Z(X,\ t)$, we use, see also Fig. 2:

$$z(X) = L\left(\bar{X} - 3\bar{X}^2 + 3\bar{X}^3 - \bar{X}^4\right) \quad \text{with} \quad \bar{X} = X/L \tag{54}$$

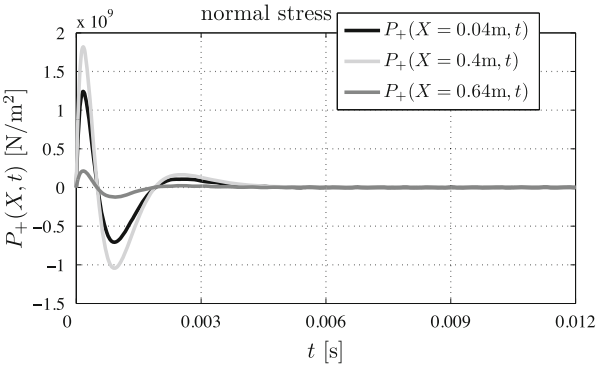

Fig. 3 Time-wise distribution of stress in three locations; controlled case

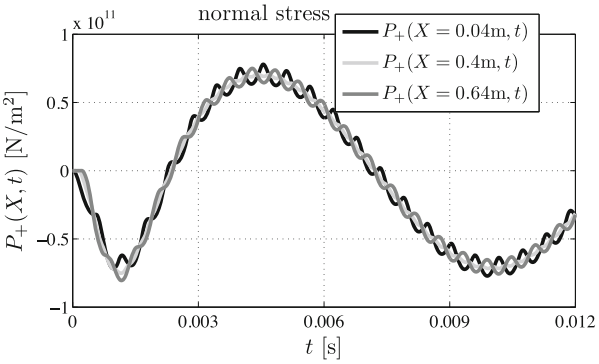

Fig. 4 Time-wise distribution of stress in three locations; uncontrolled case ($P_{a+}(X,\ t) = 0$)

Note that the selected spatial distribution $z(X)$ in Eq. (54) satisfies the necessary conditions stated in Eqs. (50) and (51). The required actuation stress $P_{a+}(X,\ t)$ is eventually found by integration of Eq. (47), using the trivial initial conditions stated in Eq. (53). It is found that the desired stress $Z(X, t)$ is indeed obtained by our method. Results are depicted in the following figures for the controlled (Fig. 3) and the uncontrolled case (Fig. 4). Note that the stress maxima in the uncontrolled case are substantially higher than in the controlled case. A more detailed discussion and further examples will be given in a forthcoming contribution, Schoeftner and Irschik [8].

Acknowledgements J. Schoeftner and H. Irschik acknowledge support from the Austrian Science Fund FWF (P 26762-N30).

References

1. Gurtin MW (1972) The linear theory of elasticity. Handbuch der Physik, vol VIa/2. Springer, Berlin, pp 1–296
2. Carlson DE (1972) Linear thermoelasticity. Handbuch der Physik, vol VIa/2. Springer, Berlin, pp 297–346
3. Ignaczak J (1963) A completeness problem for the stress equation of motion in the linear theory of elasticity. Arch Mech Stosow 15:225–234
4. Ignaczak J (1963) On the stress equations of motion in the linear thermoelasticity. Arch Mech Stosow 15:691–695
5. Knops RJ, Wilkes EW (1973) Theory of elastic stability. Handbuch der Physik, vol VIa/3. Springer, Berlin, pp 125–302
6. Irschik H, Gusenbauer M, Pichler U (2004) Dynamic stress compensation by smart actuation. In: Smith RC (ed) Proceedings of SPIE on smart structures and materials 2004: modeling, signal processing, and control, paper no. 386, San Diego, CA
7. Irschik H (2007) Generation of transient desired displacement or stress fields in force loaded solids and structures by smart actuation. In: Book of abstracts of XXXV summer School advanced problems in mechanics (APM 2007), Saint-Petersburg
8. Schoeftner J, Irschik H (2016) Stress tracking in thin bars by eigenstrain actuation. http://www.sciencedirect.com/science/article/pii/S0022460X16303558

Variational Principles for Different Representations of Lagrangian and Hamiltonian Systems

Markus Schöberl and Kurt Schlacher

Abstract In this contribution we show, mainly based on an example, how Hamiltonian counterparts for partial differential equations that allow for a variational principle can be derived in a systematic manner. The main tool will be the appropriate use of the Lagrange multiplier technique, which allows us to obtain several well-known Hamiltonian formulations by using a common principle. The Mindlin plate will be used to visualize the presented approach

1 Introduction

Calculus of variations is one important tool to derive the partial differential equations (PDEs) of physical systems, see, e.g., [1, 2, 5–7]. The outcome of the variational principle are PDEs in the so-called Lagrangian setting, as the Euler–Lagrange operator plays an important role. However, based on the Lagrangian formulation it is of interest to derive Hamiltonian counterparts. This has been discussed in various settings, e.g., based on Stokes–Dirac structures as well as on the underlying structure of a jet-bundle in [3, 8, 12, 13] and the references therein.

In this contribution, we will show that some of the Hamiltonian pictures from above have a common origin, see also [9]. The main idea is to adopt the concept of Lagrange multipliers to get rid of derivative variables in the Lagrangian by imposing constraints—this can be uniquely performed for ordinary differential equations and leads to the well-known Hamiltonian counterpart. For systems described by PDEs, more than one independent variable exists, and thus several choices for constraints can be made, which then lead to different Hamiltonian representations.

M. Schöberl (✉) • K. Schlacher
Institute of Automatic Control and Control Systems Technology, Johannes Kepler University Linz, Linz, Austria
e-mail: markus.schoeberl@jku.at; kurt.schlacher@jku.at

H. Irschik et al. (eds.), *Dynamics and Control of Advanced Structures and Machines*, DOI 10.1007/978-3-319-43080-5_7

2 Variational Calculus and the Hamiltonian Counterparts

In this section we shortly review variational calculus for first-order field theories. In particular we show how one derives the Euler–Lagrange equations and furthermore we discuss the derivation of several Hamiltonian counterparts by using the Lagrange multiplier technique. All these theoretical foundations will be extensively discussed in more detail in Sect. 3 by using an illustrative example.

Let us consider a variational problem that can be described using the dependent coordinates x^α, $\alpha = 1, \ldots, r$ and the independent variables X^i, $i = 1, \ldots, p$. Furthermore, we consider the derivative variables x^α_i. Given a map σ as $x^\alpha = \sigma^\alpha(X^1, \ldots, X^p)$ then, roughly speaking, x^α_i is a container for the partial derivatives of a map σ, i.e., $\partial_{X^i}\sigma^\alpha(X^1, \ldots, X^p)$, see, e.g., [2] for an extensive and a (geometrically) precise introduction of these concepts.

Remark 1 In a geometric framework one can introduce a bundle $\mathscr{X} \to \mathscr{D}$ with coordinates (X^i, x^α) for $\mathscr{X}$ and (X^i) for $\mathscr{D}$. The map σ is called a section of the bundle and the first jet-manifold $\mathscr{J}^1(\mathscr{X})$ possesses the induced coordinates $(X^i, x^\alpha, x^\alpha_i)$ including the derivative coordinates x^α_i.

Based on this setting a Lagrangian density of first-order is a differential p-form $\mathscr{L}\Omega$ with the volume element $\Omega = \mathrm{d}X^1 \wedge \ldots \wedge \mathrm{d}X^p$ and where the Lagrangian $\mathscr{L}(X^i, x^\alpha, x^\alpha_i)$ explicitly depends on first-order derivative variables. Stating a variational problem implies to find the so-called critical maps σ such that the functional[1]

$$\epsilon \to \int_{\mathscr{D}} (\mathscr{L} \circ \phi_\epsilon(\sigma))\, \Omega$$

becomes stationary, where ϕ_ϵ is a map (based on a flow that only acts on the dependent coordinates x^α) that distorts the map σ. Furthermore, the relation that $v^\alpha = \partial_\epsilon(\phi^\alpha_\epsilon)|_{\epsilon=0}$, i.e., v is the variational field or the generator of the map (flow) ϕ_ϵ, will be used together with integration by parts. Then, from $\partial_\epsilon \int_{\mathscr{D}} (\mathscr{L} \circ \phi_\epsilon(\sigma))\, \Omega\big|_{\epsilon=0} = 0$ using Einstein's convention on sums, we derive the important result

$$\int_{\mathscr{D}} \left(v^\alpha(\partial_{x^\alpha}\mathscr{L} - d_{X^i}(\partial^i_{x^\alpha}\mathscr{L})) \circ \sigma\right) \Omega + \int_{\partial\mathscr{D}} \left(v^\alpha \partial^i_{x^\alpha}\mathscr{L} \circ \sigma\right) \Omega_i = 0 \tag{1}$$

[1] In the integrand $\mathscr{L} \circ \phi_\epsilon(\sigma)$ it is implicitly assumed that one plugs in the derivative of $\phi_\epsilon(\sigma)$ as the derivative variables x^α_i are present in $\mathscr{L}$. Using a more precise notation this could be written as $\mathscr{L} \circ j^1(\phi_\epsilon(\sigma))$, but to enhance the readability we will not indicate the jet-prolongations (i.e. j^1) when it follows from the context.

with[2] $\Omega_i = \partial_{X^i} \rfloor \Omega$. In (1) the Euler–Lagrange operator

$$\delta_{x^\alpha} = \partial_{x^\alpha} - d_{X^i} \partial^i_{x^\alpha} , \quad \partial_{x^\alpha} = \frac{\partial}{\partial x^\alpha} , \quad \partial^i_{x^\alpha} = \frac{\partial}{\partial x^\alpha_i} \tag{2}$$

appears where d_{X^i} is the total derivative, and consequentially $\delta_{x^\alpha} \mathscr{L} = 0$ leads to the desired PDEs of the field problem, whereas the second term in (1) delivers the boundary conditions.

To derive possible Hamiltonian counterparts the following strategy can be adopted. We first split the independent coordinates into time and spatial coordinates. It is convenient to label $X^1 = t$ and X^A with $A = 2, \ldots, p$ denote the spatial variables. To enhance the readability we set $x^\alpha_1 = x^\alpha_t$ and x^α_A only corresponds to spatial derivative variables. Introducing the constraint $x^\alpha_t = u^\alpha$, the Lagrangian density is of the following form:

$$\mathscr{L}(t, X^A, x^\alpha, u^\alpha, x^\alpha_A) \Omega \tag{3}$$

and we can consider the variational problem

$$\partial_\epsilon \int_{\mathscr{D}} (\mathscr{L} \circ \phi_\epsilon(\sigma)) \, \Omega + (\lambda_\alpha \circ \sigma) \left(x^\alpha_t \circ \phi^x_\epsilon(\sigma) - u^\alpha \circ \phi^u_\epsilon(\sigma) \right) \Omega \Big|_{\epsilon=0} = 0$$

with the Lagrange multipliers λ_α. This setting leads to a symplectic formulation of the PDEs, as one derives evolution equations for the Lagrange multipliers λ_α.

Remark 2 It should be noted that here $\phi_\epsilon = (\phi^x_\epsilon, \phi^u_\epsilon)$ corresponds to the variation of the x^α and the u^α variables. As these variables are coupled by the relation $x^\alpha_t = u^\alpha$ the Lagrange multipliers have been introduced.

In a similar manner also the Lagrangian density

$$\mathscr{L}(t, X^A, x^\alpha, u^\alpha_i) \Omega \tag{4}$$

with the constraint $x^\alpha_i = u^\alpha_i$ can be considered, where $i = t, A$, and the corresponding variational problem will lead to the so-called De-Donder Weyl formulation, where it should be noted that in contrast to x^α_i the variables u^α_i are no derivative variables.

Remark 3 It should be noted that the symplectic picture and the De-Donder Weyl representation are well-known in the literature, see, e.g., [2, 7, 10]. However, their common derivation by using the Lagrange multiplier technique has been pointed out just recently in [9].

[2] $\rfloor$ denotes the natural contraction, i.e., $\partial_{X^i} \rfloor \Omega = (-1)^{i-1} dX^1 \wedge \ldots \wedge \hat{dX}^i \wedge \ldots \wedge dX^p$ where $\hat{dX}^i$ is omitted.

Alternatively, it might be possible to introduce the so-called energy coordinates e^ρ such that the Lagrangian takes the form

$$\mathscr{L}(X^i, e^\rho) \tag{5}$$

where we will show in Sect. 3 that this latter approach is connected to the Stokes–Dirac formulation, see, e.g., [13].

It is worth noting that the basic idea of the presented approaches is to hide derivative variables x_i^α in the Lagrangian by introducing additional variables and to take these relations into account by applying the Lagrange multiplier technique. In (3) only the time derivative variables are hidden and hence one obtains evolutionary equations in a Hamiltonian setting, where the Lagrange multipliers can be interpreted as the canonical momenta. Contrary, in (4) all the derivative variables are hidden and the Lagrange multipliers turn out to be the multi-momenta. A significantly different approach is based on energy coordinates as in (5), where the constraints that have to be taken into account result from integrability conditions due to the introduction of the coordinates e.

3 An Extended Example

Let us consider a rectangular plate with lengths l_x, l_y, where h will denote the thickness, which will be modeled based on the hypothesis stated by Mindlin. Therefore, we choose as independent coordinates the vertical deflection w of the mid-plane as well as the rotations of a transverse normal to the X and Y direction termed ψ and ϕ, respectively. The kinetic energy density $\mathscr{K}\Omega$ and the potential energy density $\mathscr{V}\Omega$ can be introduced with $\mathscr{K} = \frac{1}{2}(\alpha_1(\psi_t^2 + \phi_t^2) + \alpha_2 w_t^2)$ and

$$\begin{aligned}\mathscr{V} = &\frac{1}{2}\alpha_3\left[(w_X - \psi)^2 + (w_Y - \phi)^2\right] + \frac{1}{2}\alpha_4\frac{1-\nu}{2}(\psi_Y + \phi_X)^2 \\ &+\frac{1}{2}(\alpha_4(\psi_X^2 + \nu\phi_Y\psi_X) + \alpha_4(\phi_Y^2 + \nu\phi_Y\psi_X)).\end{aligned}$$

Here, $\alpha_1 = \rho\frac{h^3}{12}$, $\alpha_2 = \rho h$ and $\alpha_3 = kGh$ as well as $\alpha_4 = D$. Furthermore, ν is the Poisson ratio, $k = \frac{\pi^2}{12}$, and G, D are the plate stiffness and the plate module, see [4] and the references therein.

Remark 4 In our setting we have $(x^1, x^2, x^3) = (w, \psi, \phi)$ and $(X^1, X^2, X^3) = (t, X, Y)$, thus $r = p = 3$. Furthermore, a subscript t, X or Y corresponds to derivative variables. It should be noted that a subscript x or y does not indicate a derivative variable, e.g., in l_x or l_y.

3.1 The Lagrangian Picture

To derive the PDEs in a Lagrangian (variational) setting we have to evaluate $\delta_{x^\alpha}\mathscr{L}$ with (2) and $\mathscr{L} = \mathscr{K} - \mathscr{V}$ where the volume element meets $\Omega = \mathrm{d}t \wedge \mathrm{d}X \wedge \mathrm{d}Y$. The variational derivatives follow as $\delta_\alpha = \partial_\alpha - d_t\partial^t_\alpha - d_X\partial^X_\alpha - d_Y\partial^Y_\alpha$ where, by slight abuse of notation, $\alpha = \{w, \psi, \phi\}$ and the PDEs read as

$$\begin{aligned} \alpha_2 w_{tt} &= d_X Q_x + d_Y Q_y \\ \alpha_1 \psi_{tt} &= Q_x + d_X M_x + d_Y M_{xy} \\ \alpha_1 \phi_{tt} &= Q_y + d_Y M_y + d_X M_{xy} \end{aligned} \tag{6}$$

with

$$\begin{aligned} M_x &= D(\psi_X + \nu\phi_Y)\,,\ M_y = D(\phi_Y + \nu\psi_X)\,,\ M_{xy} = D\frac{1-\nu}{2}(\psi_Y + \phi_X) \\ Q_x &= kGh(w_X - \psi)\,,\ \ Q_y = kGh(w_Y - \phi). \end{aligned} \tag{7}$$

The boundary conditions follow from the boundary integral in (1) together with (7) as

$$\int_{\partial\mathscr{D}} \left(w_L Q_x + \psi_L M_x + \phi_L M_{xy}\right) \mathrm{d}t \wedge \mathrm{d}Y - \int_{\partial\mathscr{D}} \left(w_L Q_y + \psi_L M_{xy} + \phi_L M_y\right) \mathrm{d}t \wedge \mathrm{d}X = 0 \tag{8}$$

where the variational vector field v takes the form $v = w_L\partial_w + \psi_L\partial_\psi + \phi_L\partial_\phi$ and on the time-boundary no variation takes place. Thus, we can conclude that if, e.g., at $X = 0$ we have that w_L is arbitrary, then Q_x has to vanish or has to be compensated by an external boundary term, see also [11].

3.2 The Hamiltonian Counterparts

Based on the partial differential equations (6) we discuss two of the presented port-Hamiltonian formulations. In particular we focus on the symplectic approach and the formulation using energy coordinates.

3.2.1 Symplectic Approach

The symplectic approach is based on imposing the constraints $w_t = u^1$, $\psi_t = u^2$ and $\phi_t = u^3$ and thus

$$\mathscr{K} = \frac{1}{2}(\alpha_1((u^2)^2 + (u^3)^2) + \alpha_2(u^1)^2)$$

is met. As the variation of x^i and u^i is not independent as $x_t^\alpha = u^\alpha$ (x_t^α corresponds to w_t , ψ_t and ϕ_t, respectively, for $\alpha = 1, \ldots, 3$) the variational problem has to be augmented by Lagrange multipliers in the form

$$\begin{aligned}\partial_\epsilon \int_{\mathscr{D}} \big\{ & \mathscr{L}(\psi, \phi, u^1, u^2, u^3, w_X, \psi_X, \phi_X, w_Y, \psi_Y, \phi_Y) \circ \phi_\epsilon(\sigma) \\ & + \lambda_1(w_t - u^1) \circ \phi_\epsilon(\sigma) + \lambda_2(\psi_t - u^2) \circ \phi_\epsilon(\sigma) \\ & + \lambda_3(\phi_t - u^3) \circ \phi_\epsilon(\sigma) \big\}\, \Omega \big|_{\epsilon=0} = 0. \end{aligned} \tag{9}$$

Performing the variation (and applying integration by parts) the PDEs in the domain

$$\begin{aligned} d_t(\lambda_1) &= -d_X(\partial_w^X \mathscr{L}) - d_Y(\partial_w^Y \mathscr{L}) \\ d_t(\lambda_2) &= \partial_\psi \mathscr{L} - d_X(\partial_\psi^X \mathscr{L}) - d_Y(\partial_\psi^Y \mathscr{L}) \\ d_t(\lambda_3) &= \partial_\phi \mathscr{L} - d_X(\partial_\phi^X \mathscr{L}) - d_Y(\partial_\phi^Y \mathscr{L}) \end{aligned}$$

follow, as well as

$$\partial_{u^1} \mathscr{L} = \lambda_1\,, \quad \partial_{u^2} \mathscr{L} = \lambda_2\,, \quad \partial_{u^3} \mathscr{L} = \lambda_3.$$

Renaming the Lagrange multipliers as

$$\lambda_1 = p_w = \alpha_2 w_t\,, \quad \lambda_2 = p_\psi = \alpha_1 \psi_t\,, \quad \lambda_3 = p_\phi = \alpha_1 \phi_t \tag{10}$$

and introducing the Hamiltonian as

$$\mathscr{H} = \big(w_t p_w + \psi_t p_\psi + \phi_t p_\phi - \mathscr{L}\big) \circ l$$

where l is the inverse of the map (10) we derive a system of evolutionary PDEs

$$\begin{bmatrix} d_t w \\ d_t \psi \\ d_t \phi \\ d_t p_w \\ d_t p_\psi \\ d_t p_\phi \end{bmatrix} = \begin{bmatrix} 0 & 0 & 0 & 1 & 0 & 0 \\ 0 & 0 & 0 & 0 & 1 & 0 \\ 0 & 0 & 0 & 0 & 0 & 1 \\ -1 & 0 & 0 & 0 & 0 & 0 \\ 0 & -1 & 0 & 0 & 0 & 0 \\ 0 & 0 & -1 & 0 & 0 & 0 \end{bmatrix} \begin{bmatrix} \delta_w \mathscr{H} \\ \delta_\psi \mathscr{H} \\ \delta_\phi \mathscr{H} \\ \delta_{p_w} \mathscr{H} \\ \delta_{p_\psi} \mathscr{H} \\ \delta_{p_\phi} \mathscr{H} \end{bmatrix}. \tag{11}$$

The variational derivatives in this setting take the form $\delta_\alpha = \partial_\alpha - d_X \partial_\alpha^X - d_Y \partial_\alpha^Y$ where $\alpha = \{w, \psi, \phi\}$ together with $\delta_{p_w} = \partial_{p_w}$, $\delta_{p_\psi} = \partial_{p_\psi}$, $\delta_{p_\phi} = \partial_{p_\phi}$.

The representation (11) has been derived in [11] without the use of Lagrange multipliers by using the Legendre transformation. In this latter reference also the energy balance and the possible boundary ports are discussed in connection with

the boundary conditions (8). This is omitted here, as the focus is on the derivation of the PDEs in a variational setting using the Lagrange multiplier technique.

3.2.2 Energy Variables

Let us introduce the following variables:

$$\Gamma_x = -\psi_X\,,\ \Gamma_y = -\phi_Y\,,\ \Gamma_{xy} = -(\psi_Y + \phi_X)\,,\ \Gamma_{xz} = w_X - \psi\,,\ \Gamma_{yz} = w_Y - \phi$$

together with $w_t = v\,,\ \psi_t = \chi$ and $\phi_t = \omega$. Then

$$\mathscr{K} = \frac{1}{2}(\alpha_1(\chi^2 + \omega^2) + \alpha_2 v^2)$$

as well as

$$\mathscr{V} = \frac{1}{2}\alpha_3\left[\Gamma_{xz}^2 + \Gamma_{yz}^2\right] + \frac{1}{2}\alpha_4\frac{1-\nu}{2}\Gamma_{xy}^2 + \frac{1}{2}(\alpha_4(\Gamma_x^2 + \nu\Gamma_x\Gamma_y) + \alpha_4(\Gamma_y^2 + \nu\Gamma_x\Gamma_y))$$

is met. We have introduced eight new variables, the so-called energy variables, which have been derived by derivations of the three dependent variables $w\,,\psi$ and ϕ and thus, obviously, the constraints

$$\dot{\Gamma}_x = -\chi_X\,,\quad \dot{\Gamma}_y = -\omega_Y\,,\quad \dot{\Gamma}_{xy} = -\chi_Y - \omega_X\,,\quad \dot{\Gamma}_{xz} = v_X - \chi\,,\quad \dot{\Gamma}_{yz} = v_Y - \omega \tag{12}$$

follow, where by slight abuse of notation we use the 'dot' to indicate a total time derivative. Now we apply again the variational principle as in (9) but we observe that now the Lagrangian is of the form $\mathscr{L}(\chi, \omega, v, \Gamma_x, \Gamma_y, \Gamma_{xy}, \Gamma_{xz}, \Gamma_{yz})$—hence no derivative variables appear at all—but we have to augment the problem with the constraints in the following form:

$$\lambda_1(\dot{\Gamma}_x+\chi_X)+\lambda_2(\dot{\Gamma}_y+\omega_Y)+\lambda_3(\dot{\Gamma}_{xy}+\chi_Y+\omega_X)+\lambda_4(\dot{\Gamma}_{xz}-v_X+\chi)+\lambda_5(\dot{\Gamma}_{yz}-v_Y+\omega).$$

Performing again the variation gives the following domain conditions:

$$\begin{aligned}\alpha_2 v + d_X(\lambda_4) + d_Y(\lambda_5) &= 0\\ \alpha_1\chi - d_X(\lambda_1) - d_Y(\lambda_3) + \lambda_4 &= 0\\ \alpha_1\omega - d_Y(\lambda_2) - d_X(\lambda_3) + \lambda_5 &= 0\end{aligned}$$

as well as $d_t(\lambda_1) = -\alpha_4(\Gamma_x + \nu\Gamma_y)\,,\ d_t(\lambda_2) = -\alpha_4(\Gamma_y + \nu\Gamma_x)$ and

$$d_t(\lambda_3) = -\alpha_4\frac{1-\nu}{2}\Gamma_{xy}\,,\ d_t(\lambda_4) = -\alpha_3\Gamma_{xz}\,,\ d_t(\lambda_5) = -\alpha_3\Gamma_{yz}.$$

Taking the total time derivatives of the first three relations and combining this with spatial derivatives of the latter five equations we derive

$$
\begin{aligned}
d_t p_w &= \alpha_3 (d_X \Gamma_{xz} + d_Y \Gamma_{yz}) \\
d_t p_\psi &= -d_X(\alpha_4(\Gamma_x + \nu \Gamma_y) - d_Y \left(\alpha_4 \frac{1-\nu}{2} \Gamma_{xy} \right) + \alpha_3 \Gamma_{xz} \\
d_t p_\phi &= -d_Y(\alpha_4(\Gamma_y + \nu \Gamma_x) - d_X \left(\alpha_4 \frac{1-\nu}{2} \Gamma_{xy} \right) + \alpha_3 \Gamma_{yz}
\end{aligned}
$$

with $p_w = \alpha_2 v = \alpha_2 w_t$, $p_\psi = \alpha_1 \chi = \alpha_1 \psi_t$, $p_\phi = \alpha_1 \omega = \alpha_1 \phi_t$. Furthermore, the constraints read as

$$
d_t \Gamma_x = -d_X \left(\frac{1}{\alpha_1} p_\psi \right) , \quad d_t \Gamma_y = -d_Y \left(\frac{1}{\alpha_1} p_\phi \right) , \quad d_t \Gamma_{xy} = -d_Y \left(\frac{1}{\alpha_1} p_\psi \right) - d_X \left(\frac{1}{\alpha_1} p_\phi \right)
$$

$$
d_t \Gamma_{xz} = d_X \left(\frac{1}{\alpha_2} p_w \right) - \frac{1}{\alpha_1} p_\psi , \quad d_t \Gamma_{yz} = d_Y \left(\frac{1}{\alpha_2} p_w \right) - \frac{1}{\alpha_1} p_\phi
$$

and consequently we have a relation of the form

$$
d_t \eta = \mathfrak{J} \epsilon \tag{13}
$$

with a formally skew-adjoint differential operator $\mathfrak{J}$ together with the so-called effort variables $\epsilon = \partial_\eta \mathscr{H}$ with $\mathscr{H} = \mathscr{H} + \mathscr{V}$ and $\eta = [p_w, p_\psi, p_\phi, \Gamma_x, \Gamma_y, \Gamma_{xy}, \Gamma_{xz}, \Gamma_{yz}]$.

It should be noted that the systems (11) and (13) both are Hamiltonian representations of the same physical system. Indeed the first three PDEs of (13) correspond to the lower three PDEs of (11). Also the Hamiltonian is the same function in the two scenarios, but based on different coordinates. The representation as in (13) corresponds to the Stokes–Dirac formulation as in [4]—it is worth noting that in contrast to (11) in (13) the mechanical degrees of freedom (w, ψ, ϕ) are not present anymore, this comes from the choice of the energy variables and leads to a higher dimensional system (eight PDES compared to six). Furthermore, the choice of energy coordinates leads to the integrability conditions (12) that have to be included into the setting—this does not occur in the symplectic approach where the mechanical degrees of freedom (w, ψ, ϕ) are still present—similar as in the Lagrangian scenario, where (w, ψ, ϕ) are the field variables.

Acknowledgements This work has been partially supported by the Linz Center of Mechatronics (LCM) in the framework of the Austrian COMET-K2 programme.

References

1. Abraham R, Marsden JE (1978) Foundations of mechanics. Addison Wesley, Redwood city
2. Giachetta G, Mangiarotti L, Sardanashvily G (1997) New Lagrangian and Hamiltonian methods in field theory. World Scientific, Singapore
3. Macchelli A, van der Schaft AJ, Melchiorri C (2004) Port hamiltonian formulation of infinite dimensional systems I. modeling. In: Proceedings 43rd IEEE conference on decision and control (CDC), pp 3762–3767
4. Macchelli A, Melchiorri C, Bassi L (2005) Port based modelling and control of the Mindlin plate. In: Proceedings 44th IEEE conference on decision and control (CDC), pp 5989–5994
5. Marsden JE, Hughes TJR (1994) Mathematical foundations of elasticity. Dover Publications, New York
6. Marsden JE, Pekarsky S, Shkoller S, West M (2001) Variational methods, multisymplectic geometry and continuum mechanics. J Geom Phys 38:253–284
7. Olver PJ (1986) Applications of lie groups to differential equations. Springer, New York
8. Schlacher K (2008) Mathematical modeling for nonlinear control: a Hamiltonian approach. Math Comput Simul 97:829–849
9. Schlacher K, Schöberl M (2015) How to choose the state for distributed-parameter systems, a geometric point of view. In Proceedings 8th Vienna international conference on mathematical modelling, pp 500–501
10. Schöberl M, Schlacher K (2011) First order hamiltonian field theory and mechanics. Math Comput Model Dyn Syst 17:105–121
11. Schöberl M, Siuka A (2013) Analysis and comparison of port-hamiltonian formulations for field theories - demonstrated by means of the Mindlin plate. In: Proceedings 12th European control conference (ECC), pp 548–553
12. Schöberl M, Siuka, A (2014) Jet bundle formulation of infinite-dimensional port-hamiltonian systems using differential operators. Automatica 50:607–613
13. van der Schaft AJ, Maschke BM (2002) Hamiltonian formulation of distributed-parameter systems with boundary energy flow. J Geom Phys 42:166–194

Hardware-in-the-Loop Testing of High-Speed Pantographs Using Real-Time Catenary Emulation

Alexander Schirrer, Guilherme Aschauer, and Stefan Jakubek

Abstract This contribution outlines key developments and first results towards an innovative hardware-in-the-loop test rig for high-speed pantographs that can accurately emulate high-speed train rides. This allows for efficient pantograph testing in laboratory and thus reduces the need for expensive track tests. Efficient real-time-capable models of the relevant and complex catenary dynamics are needed, but due to the distributed-parameter dynamics and weak damping, special care in the model formulation has to be taken. A novel moving coordinate formulation combined with controlled absorbing boundary layers yields an accurate and efficient catenary model. A model-based predictive test rig impedance control scheme is then used to emulate the catenary behavior on the test rig. Additionally, physical conservation laws (energy and momentum) can be considered by the controller as control goals. First experimental results demonstrate the test rig ability to emulate catenary behavior and eliminate errors in energy and momentum between the coupled systems.

1 Introduction

High demands are put on modern high-speed railway current collectors (pantographs). They need to maintain a stable contact with the current-carrying contact wire of the overhead catenary system to ensure reliable energy supply and prevent arcing that is caused by loss of contact and leads to heavy wear.

Examining the dynamic response of an actual pantograph on a test rig is called hardware-in-the-loop (HiL) testing. One use case is to apply realistic load scenarios that also emerge on real track rides by accurately emulating the catenary behavior on the test rig. The so-called impedance control concepts are needed to shape the test rig's dynamic behavior rather than only track pre-defined trajectories.

For this purpose realistic real-time-capable catenary models are required. In this work this is achieved by describing the behavior of the catenary by two coupled

A. Schirrer • G. Aschauer • S. Jakubek (✉)
Institute of Mechanics and Mechatronics, Workgroup of Control and Process Automation, Technische Universität Wien, Getreidemarkt 9, 1060 Vienna, Austria
e-mail: stefan.jakubek@tuwien.ac.at

H. Irschik et al. (eds.), *Dynamics and Control of Advanced Structures and Machines*, DOI 10.1007/978-3-319-43080-5_8

partial differential equations (PDEs). Classical modeling approaches thereby require a large computational domain or high damping to avoid distorted solutions by spurious reflections from the boundaries. Specific model formulations and boundary treatment methods can, however, significantly increase model efficiency and finally produce real-time-capable models of high accuracy.

Another application issue is that existing HiL test rigs often suffer from intrinsic phase lag when using impedance control realized by classical control strategies. This could lead to the accumulation of energy errors that may emerge between the catenary model and the pantograph caused, for example, by ubiquitous imperfections in control.

The main contributions of this work solve the described issues by presenting an efficient real-time-capable Eulerian modeling approach to solve the distributed-parameter catenary dynamics combined with special absorbing boundary layers. Additionally, a novel impedance control strategy incorporating energy and momentum conservation, solved by a model predictive control (MPC) approach to consider constraints and predict the complex catenary dynamics, is outlined. For a high-dynamic test rig setup, first promising experimental results of the test rig control concept are shown.[1]

2 Catenary Model

A typical catenary consists of a carrier wire that is attached to inertia-fixed masts and of a contact wire that is attached to the carrier wire via droppers. The simplified structure of the catenary that was the basis for the modeling is shown in Fig. 1. The bending behavior of each wire can be described by the Euler–Bernoulli bending beam under axial pretension, see [1]. The corresponding PDE with constant coefficients reads

$$\rho A\ddot{w} + \beta\dot{w} = -EIw'''' + Tw'' + f, \tag{1}$$

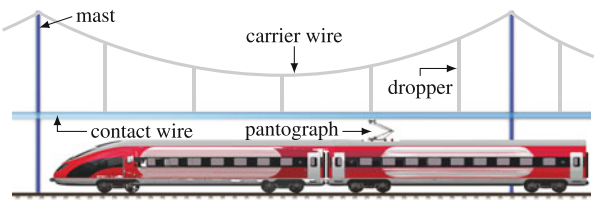

Fig. 1 Typical railway catenary system setup

[1]The HiL test rig (Fig. 3) has been jointly developed by TU Wien and Siemens pantographs team (Siemens AG Austria, MO MLT BG PN).

where ρA is the specific mass, $w(x,t)$ the vertical displacement field, β a velocity-proportional damping coefficient, E Young's modulus of elasticity, I the geometrical moment of inertia, T the axial pretension force, and $f(x,t)$ denotes the vertical force density acting on the wire. The spatial coordinate x is (horizontally) aligned along the undeformed wire, and t denotes time. Partial derivatives with respect to x and t are denoted by a prime and a dot, respectively. The droppers that cause the coupling between the two wires as well as the pantograph/contact wire contact are modeled as linear (possibly one-sided) springs. The resulting vertical coupling forces are incorporated via the force density term $f(x,t)$. Dropper slackening and loss of pantograph contact can be modeled via one-sided springs and result in a variable-structure system description.

Equation (1) is valid for a non-moving wire in a fixed coordinate reference system. Here, we use a Eulerian-based modeling approach where instead of a moving pantograph with a fixed catenary, a pantograph-fixed coordinate system is chosen with a moving catenary, see [6]. Hence, the coordinate transform $z = x + vt$ is introduced such that the displacements of the wires are described in a moving coordinate system (moving with velocity v). This leads to mixed derivative terms and periodic time-varying coupling coefficients in the linear/piecewise-linear PDE.

In the following, an approximate solution of the PDE problem is obtained by the method of Finite Differences. Thereby the PDEs' field variables are approximated at discrete points in space and time,

$$w(z_k, t_n) = w(k\Delta z, n\Delta t) = w_k^n, \qquad f(z_k, t_n) = f_k^n, \tag{2}$$

where Δz and Δt are the uniform step sizes in space and time, and the partial derivatives are approximated by suitable difference quotients. A set of linear algebraic equations is obtained that can be solved in a time-marching manner.

Initial and boundary conditions are needed for a well-posed PDE problem. These are also discretized and substituted into the set of equations. In the most simple form the outmost boundary points' displacements are set to zero for all times, realizing clamped boundary conditions. This choice, however, leads to the total reflection of all outgoing waves at the boundary back into the domain interior. For weakly damped systems (as for catenaries), these spurious reflections from artificial boundaries destroy physical trustworthiness of the results. One viable countermeasure is to apply absorbing boundary conditions (ABCs) instead, but their analytic derivation for complex PDEs is often not possible. An optimization-based approach to obtain them for a wide range of PDEs was shown in [8]. Another option is to extend the computational domain with an additional damping layer, called perfectly matched layer (PML). However, its derivation is mathematically challenging, even for simple PDEs, if possible at all. In this contribution, a novel approach towards controlled boundary layers (developed in [7]) is utilized that emulates the behavior of a PML.

3 Perfectly Matched Layer-Based Boundary Dynamics via Control

The idea of a PML is to extend the computational domain with a small region with damping properties chosen such as to attenuate all incoming waves significantly by adding an exponential decay to the harmonic wave solution: $w_k^n = \exp(-\sigma(k\Delta x))\exp(\mathrm{i}\omega_x \Delta x)^k \exp(\mathrm{i}\omega_t \Delta t)^n$, with the damping profile $\sigma(x)$. See [3] for more information on harmonic wave solutions of PDEs and basic absorbing boundary conditions for the wave equation. Care has to be taken to avoid additional reflections at the interface between the PML and the computational domain (impedance matching). In this work, a controlled boundary layer is utilized (taken from [7]) as depicted in Fig. 2, and the state-space system of the discretized PDE from a PML point of view thus becomes

$$\boldsymbol{x}_{\mathrm{PML}}(k+1) = \mathbf{A}_{\mathrm{PML}}\boldsymbol{x}_{\mathrm{PML}}(k) + \mathbf{B}_{\mathrm{PML}}\boldsymbol{u}_{\mathrm{PML}}(k), \quad \boldsymbol{u}_{\mathrm{PML}}(k) = \mathbf{K}\boldsymbol{x}_{\mathrm{PML}}(k), \tag{3}$$

where a force on nodes inside the PML is applied by the feedback gain matrix $\mathbf{K}$ such that the desired exponential decay is obtained.

The optimal reference tracking control gain $\mathbf{K}$ is derived by minimizing a quadratic cost function for each time step:

$$\underset{\boldsymbol{u}_{\mathrm{PML}}}{\text{minimize}} \sum_{i=1}^{n_\mathrm{p}} \left(\boldsymbol{y}_{\mathrm{ref},i} - \boldsymbol{y}_i\right)^{\mathrm{T}} \mathbf{Q} \left(\boldsymbol{y}_{\mathrm{ref},i} - \boldsymbol{y}_i\right) + \sum_{j=0}^{n_\mathrm{c}-1} \boldsymbol{u}_{\mathrm{PML},j}^{\mathrm{T}} \mathbf{R} \boldsymbol{u}_{\mathrm{PML},j}, \tag{4}$$

where $\mathbf{Q}$ and $\mathbf{R}$ are the weighting matrices that can be tuned by the user, $\boldsymbol{y}_{\mathrm{ref}}$ is the reference solution that is constructed by a modal decomposition and exploiting the PDE's dispersion relation, and $\boldsymbol{y}$ is the displacement field inside the PML. n_p is the prediction horizon over which the deviation from the reference solution is evaluated and n_c is the control horizon over which the forthcoming control moves are penalized. Linear control theory can be applied to derive a constant feedback gain matrix $\mathbf{K}$, see [7] for a detailed derivation.

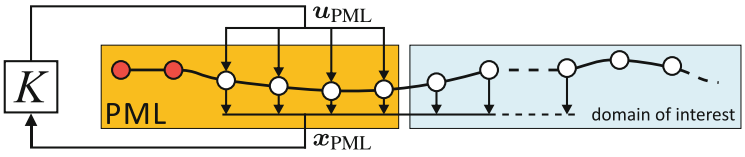

Fig. 2 Control scheme for the proposed controlled PML

4 Emulation of Catenary Behavior on a HiL Test Rig

Having formulated a catenary model in moving coordinates (Sect. 2) and its augmentation by absorbing boundary layers (Sect. 3), the central HiL testing task is to realistically emulate this virtual catenary dynamics at the physical interface between a test rig and the pantograph (unit under test). A high-dynamic HiL test rig has been developed as depicted in Fig. 3 (joint development of the authors with Siemens MO MLT BG PN). It consists of a six-degree-of-freedom industrial robot and an attached linear drive that together enable high-dynamic maneuvers in a large operating range. Contact forces and the linear drive position are measured. The emulation of accurate catenary behavior is accomplished by the setup illustrated in Fig. 4: instead of applying classical tracking control, here the control goal is to shape the test rig response to behave dynamically like the catenary model—a concept called impedance control [4]. As seen in Fig. 4, the controller's main task is to steer the test rig (via u_{rig}) so that the test rig's contact point displacement x_{rig} stays close to the catenary model's contact point displacement x_{cat}. The measured contact force F_{ext} is thereby applied to the catenary model. Additionally, an artificial catenary correction force F_{cor} is introduced as an additional control input available to the impedance controller. This force will be helpful to control the consistency of conserved quantities exchanged between the real pantograph and the virtual catenary model. The control law is realized as an MPC, in which the control inputs

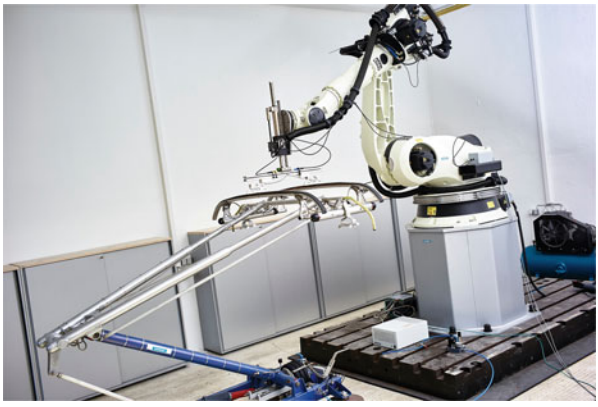

Fig. 3 Pantograph HiL test rig (Siemens MO MLT BG PN)

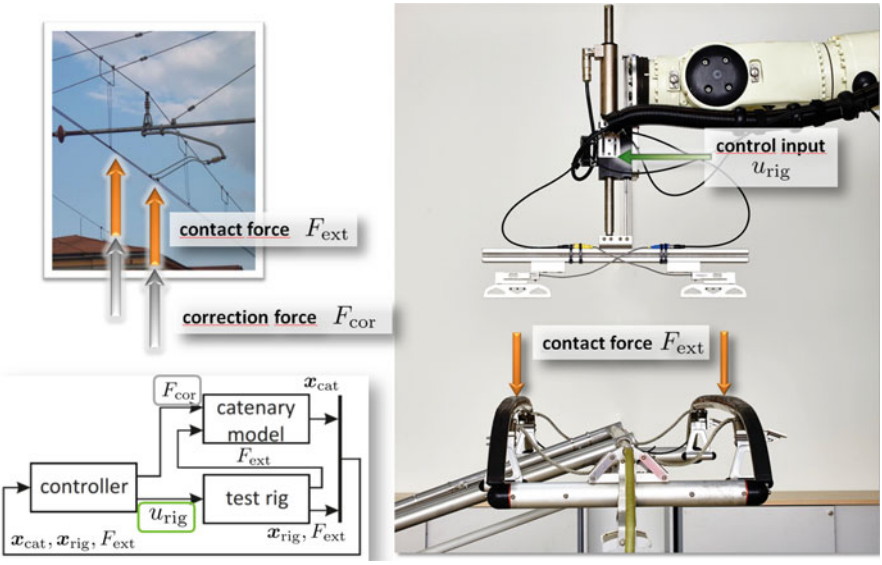

Fig. 4 Control concept

are determined by solving a constrained convex quadratic problem of the form

$$\begin{aligned} &\underset{\boldsymbol{u}_{\text{rig}}(k),\boldsymbol{F}_{\text{cor}}(k)}{\text{minimize}} && J\left(\boldsymbol{u}_{\text{rig}}(k),\, \boldsymbol{F}_{\text{cor}}(k),\, \boldsymbol{x}(k), k\right) \\ &\text{subject to} && \boldsymbol{g}\left(\boldsymbol{u}_{\text{rig}}(k),\, \boldsymbol{F}_{\text{cor}}(k),\, \boldsymbol{x}(k), k\right) \leq \boldsymbol{0}. \end{aligned} \tag{5}$$

at each time step. There, a sequence of future test rig control inputs and artificial catenary correction forces,

$$\boldsymbol{u}_{\text{rig}}(k) = \left[u_{\text{rig}}(k),\, u_{\text{rig}}(k+1),\, \ldots,\, u_{\text{rig}}(k+n_{\text{c}}-1)\right]^{\text{T}}, \tag{6}$$

$$\boldsymbol{F}_{\text{cor}}(k) = \left[F_{\text{cor}}(k),\, F_{\text{cor}}(k+1),\, \ldots,\, F_{\text{cor}}(k+n_{\text{c}}-1)\right]^{\text{T}}, \tag{7}$$

comprise the decision variables, the objective function J formulates the deviation from the control goals (see below), and the constraints $\boldsymbol{g}$ formulate input-, state-, and output-constraints that the controller needs to fulfill. The first values $(u_{\text{rig}}(k), F_{\text{cor}}(k))$ of the optimal input sequences are applied to the test rig, respectively, the catenary model, so a receding-horizon impedance control law is realized. It is noteworthy that this control law exploits model-based predictions of the dynamics to eliminate lag in tracking, typically resulting in superior control performance compared to classical tracking control designs, and it can explicitly account for constraints such as actuator limits.

The terms in the objective function and the constraints are carefully formulated to achieve both, optimal tracking of the contact point displacement and velocity, as well as ensuring correctness of conserved quantities transferred between the pantograph and the virtual catenary model. The tracking goals are formulated by the objective terms

$$J_{\text{track}} = q \sum_{j=1}^{n_{\text{p}}} \left(x_{\text{cat}}(k+j) - x_{\text{rig}}(k+j)\right)^2 + r \sum_{j=0}^{n_{\text{c}}-1} \left(u_{\text{rig}}(k+j)\right)^2, \tag{8}$$

where x denotes the contact point displacements and $q, r > 0$ are weighting factors.

It is known from earlier test rig control works that the adherence to physical conservation laws on HiL test rigs is crucial to produce physically trustworthy results. In [5] an automotive engine test rig has been observed to produce different fuel consumption in HiL testing and on a real test track. Imperfect impedance emulation leads to accumulating energy errors. This discrepancy could be eliminated by ensuring that the exchange of energy and momentum between the impedance model and the unit under test was consistent.

Here, these two relevant conserved quantities are addressed by the control concept and according control goals and constraints: the *momentum* exchanged between the pantograph and the virtual catenary differs by

$$\Delta p(t) = \int_0^t \left(F_{\text{ext}}(\tau) + F_{\text{cor}}(\tau)\right) \mathrm{d}\tau - \int_0^t F_{\text{ext}}(\tau) \mathrm{d}\tau = \int_0^t F_{\text{cor}}(\tau) \mathrm{d}\tau. \tag{9}$$

This quantity is considered in the discrete-time MPC objective as

$$J_{\text{momentum}} = \sum_{j=0}^{n_{\text{c}}-1} \left(F_{\text{cor}}(k+j)\right)^2, \qquad J = J_{\text{track}} + \alpha J_{\text{momentum}}, \qquad \alpha \geq 0. \tag{10}$$

The momentum balance can thus be ensured by classic linear control concepts and would, without a correction force, automatically be fulfilled.

The error in *energy* (specifically its mechanical part, *work*) exchanged between the catenary and the pantograph is

$$\Delta W(t) = \int_0^t F_{\text{ext}} \dot{x}_{\text{rig}} \mathrm{d}\tau - \int_0^t \left(F_{\text{ext}} + F_{\text{cor}}\right) \dot{x}_{\text{cat}} \mathrm{d}\tau. \tag{11}$$

This nonlinear expression cannot be directly incorporated into a linear MPC scheme. However, suitable constraints on F_{cor} can be formulated to keep the energy error sufficiently small.

5 Numerical Results

The absorbing properties of the proposed boundary control layer that mimics PML dynamics compared with other methods to realize absorbing boundaries are shown in Fig. 5 for the case of a one-dimensional wave (string) where analytic boundary conditions can be derived. In Fig. 6 (left), first results of emulating a high-speed train ride on the test rig are presented. The overall dynamics of the catenary are already well captured by the tested controller and, as can be seen in Fig. 6 (right), initial nonzero errors in energy and momentum are successfully eliminated.

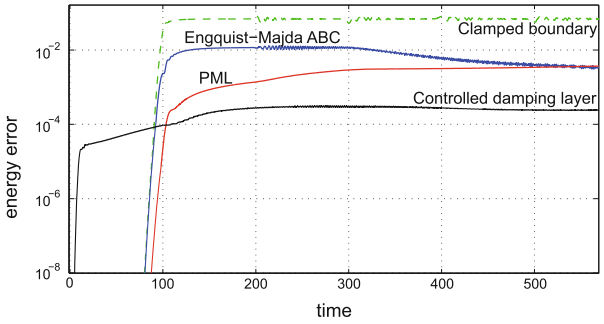

Fig. 5 Simulation error for different realizations of absorbing boundaries, taken from [7]. Engquist–Majda ABC for the wave equation is taken from [3], the PML is obtained through complex coordinate stretching, see [2], and the controlled damping layer is presented in [7]

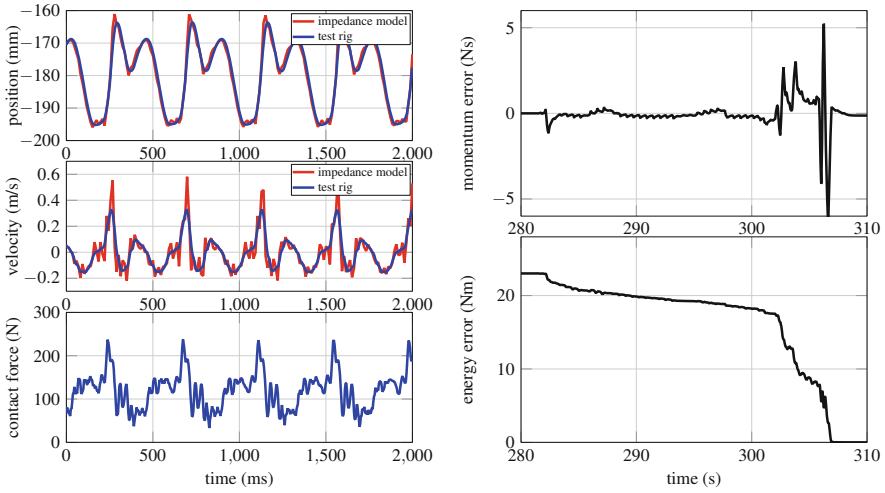

Fig. 6 Preliminary results from the pantograph HiL test rig. Test case (*left*): tracking of the catenary model. Test case (*right*): energy and momentum conservation

6 Discussion and Conclusions

In this contribution some key technologies and preliminary results of a HiL pantograph test rig were presented. It is shown how a realistic, real-time-capable catenary model can be obtained. First, moving (train-fixed) coordinates are introduced when modeling the wires as Euler–Bernoulli beams. Then the computational domain is extended with a newly developed form of controlled boundary layers. The obtained periodic, linear, time-varying model represents a theoretically unbounded catenary domain at a high detail level.

This catenary model is then used in an advanced real-time MPC-based impedance control scheme to emulate high-speed train rides in the laboratory. Conservation laws at the pantograph/catenary interface are made consistent by the controller. For that, an artificial virtual force that directly affects the catenary model is utilized.

A range of first, promising results (numerical results of the controlled absorbing boundary layer and experimental results from an actual test rig with a real pantograph) are shown. The publication of the comprehensive methodology and detailed experimental validation are in preparation.

Acknowledgements This work was financially supported by the Austrian Research Promotion Agency (project 841331). The authors are grateful for the support of Siemens MO MLT BG PN.

References

1. Arnold M, Simeon B (2000) Pantograph and catenary dynamics: A benchmark problem and its numerical solution. Appl Numer Math 34(4):345–362
2. Grote M, Sim I (2010) Efficient PML for the wave equation. arXiv:1001.0319
3. Higdon R (1987) Numerical absorbing boundary conditions for the wave equation. Math Comput 49(179):65–90
4. Hogan N (1985) Impedance control: an approach to manipulation: Part II: implementation. J Dyn Syst Meas Control 107(1):8–16
5. Jakubek S, Luchini E, Oberhummer A, Pfister F (2016) A model-based interfacing concept for accurate power hardware-in-the-loop systems. In: Mathematical and computer modelling of dynamical systems. Math Comput Model Dyn Syst 22(1):1–20. doi:10.1080/13873954.2015.1069748. http://dx.doi.org/10.1080/13873954.2015.1069748
6. Ritzberger D, Talic E, Schirrer A (2015) Efficient simulation of railway pantograph/ catenary interaction using pantograph-fixed coordinates. In: Vienna international conference on mathematical modelling, vol 8, pp 61–66
7. Ritzberger D, Schirrer A, Jakubek S, Absorbing boundary layer control for linear one-dimensional wave propagation problems. J Vib Control (Under review)
8. Schirrer A, Talic E, Aschauer G, Kozek M, Jakubek S (2016) Optimization based determination of highly absorbing boundary conditions for linear finite difference schemes. J Sound Vib 365:45–69

Swelling-Induced Bending of Hydrogel Bistrips

Takuya Morimoto, Fumihiro Ashida, and Yu Hayashi

Abstract We study swelling-induced bending of hydrogel bistrips comprising an elastomer strip and a gel strip by using finite element method. The constitutive laws of the elastomer and gel strips are assumed to be the neo-Hookean and Flory–Rehner models, respectively. We explore the swelling-induced bending of bistrips due to chemical potential and specifically focus on how the stiffness and thickness ratios between the elastomer and gel strips affect their swelling-equilibrium shapes. We show that there exist the specific values to maximize their bending curvatures.

1 Introduction

Stimuli-responsible gels have a three-dimensional structure of crosslinked polymer network that can realize a large reversible deformation in response to a specific external stimulus such as temperature, solvent concentration, pH, light, and electromagnetic field [1, 2]. In particular, temperature-responsive hydrogels have potential application in smart structures such as sensors and actuators, drug delivery systems, and micro-fluidic devices since the volume phase transition of the gel can cause large swelling at around room temperature. Bending actuation in response to temperature requires generating inhomogeneous misfit stresses in a specific spatial direction. The easiest way to create a swelling-induced bending structure is to utilize a layered structure. Bending is achieved when one of the polymer layers swells more than the other in response to temperature.

We have theoretically considered for the swelling-induced bending of bilayer comprising a first elastomer layer and a second temperature-responsive gel layer [3]. In the analytical model, the deformation was assumed to be isochoric, and the stretches were given by Rivlin's semi-inverse solution. Also, the total deformation gradient was decomposed into transversely homogeneous swelling part and non-swelling pure bending part. Then, we imposed the self-equilibrium condition that the bending moment in the bistrip is in the equilibrium without any external forces

T. Morimoto (✉) • F. Ashida • Y. Hayashi
Interdisciplinary Graduate School of Science and Engineering, Shimane University,
1060 Nishikawatsu, Matsue, Shimane 690-8504, Japan
e-mail: morimoto@riko.shimane-u.ac.jp

H. Irschik et al. (eds.), *Dynamics and Control of Advanced Structures and Machines*, DOI 10.1007/978-3-319-43080-5_9

and moments, and numerically determined the equilibrium shapes with the various geometrical and material parameters. For more practical applications, we need to simulate the inhomogeneous swelling fields by using finite element method and modeling a bilayer or a bistrip in response to changes in environment conditions.

Here we first establish the finite element model for swelling-induced bending of hydrogel bistrips in a plane strain condition. The constitutive laws of the elastomer and gel strips are described by the neo-Hookean and Flory–Rehner models, respectively. We then explore the swelling-induced bending responses of hydrogel bistrips due to chemical potential and specifically focus on the effects of the ratios between the elastomer and gel strips on their swelling-equilibrium shapes.

2 Continuum Theory of Polymeric Gels

We briefly summarize the continuum theory of polymeric gels under an isothermal condition, developed in [4–6]. Let us consider a polymeric gel in the reference state of volume V_0 enclosed by a surface S_0, subjected to a distributed body force B_i and surface traction T_i. The gel is immersed in a solvent with the chemical potential $\hat{\mu}$ per solvent molecule; the solvent molecules migrate within the gel body and across the surface S_0. A part of the surface may also be mechanically constrained and/or chemically isolated from the solvent. The equilibrium state of the gel can be characterized by two fields: $x_i(\boldsymbol{X})$ and $C(\boldsymbol{X})$. The first field represents the deformation mapping from an arbitrary material point in the reference state, $\boldsymbol{X}$, to that in the actual state, $\boldsymbol{x}$, with deformation gradient $F_{ij} = \mathrm{d}x_i(\boldsymbol{X})/\mathrm{d}X_j$. The second field represents the concentration of solvent molecules at an arbitrary material point with respect to the reference coordinates $\boldsymbol{X}$. In the thermodynamic equilibrium state, the variation of the free energy of gel is equal to the sum of the work done by the external mechanical forces (B_i and T_i) and the external solvent ($\hat{\mu}$), namely

$$\int_{\Omega_0} \delta W \,\mathrm{d}V_0 = \int_{\Omega_0} B_i \delta x_i \,\mathrm{d}V_0 + \oint_{\Gamma_0} T_i \delta x_i \,\mathrm{d}S_0 + \hat{\mu} \int_{\Omega_0} \delta C \,\mathrm{d}V_0, \tag{1}$$

where δx_i and δC are arbitrary variations of x_i and C from the equilibrium state, respectively. The nominal stress S_{ij} and chemical potential μ may be defined as work conjugates of the deformation gradient and solvent concentration, respectively:

$$S_{ij} = \frac{\partial W}{\partial F_{ij}}, \quad \mu = \frac{\partial W}{\partial C}. \tag{2}$$

The free energy density function of the gel per unit volume in the dry state is described by the Flory–Rehner model [7],

$$W(\boldsymbol{F}, C) = \frac{G^{(\mathrm{g})}}{2}(I - 3 - 2\ln J) + \frac{k_{\mathrm{B}}T}{v_{\mathrm{s}}}\left[v_{\mathrm{s}} C \log\left(\frac{v_{\mathrm{s}} C}{1 + v_{\mathrm{s}} C}\right) + \chi\left(\frac{v_{\mathrm{s}} C}{1 + v_{\mathrm{s}} C}\right)\right], \tag{3}$$

where the shear modulus of elasticity $G^{(g)}$ is related to the crosslink density $n^{(g)}$, Boltzmann constant k_B, and temperature T: $G^{(g)} = n^{(g)} k_B T$. $I = \lambda_1^2 + \lambda_2^2 + \lambda_3^2$ is the first deviatoric strain invariant in terms of the stretches λ_i, χ is a dimensionless parameter that represents the disaffinity between the polymer and solvent, and v_s is the volume per solvent molecule. Assuming the molecular incompressibility, the volume swelling ratio of the gel is $J = V/V_0 = 1 + v_s C$. A Legendre transformation of the free energy density function $\hat{W}(\boldsymbol{F}, \mu) = W(\boldsymbol{F}, C) - \mu C$ leads to

$$\hat{W}(\boldsymbol{F}, \mu) = \frac{G^{(g)}}{2}(I - 3 - 2\ln J) + \frac{k_B T}{v_s}\left[(J-1)\ln\frac{J-1}{J} + \chi\frac{J-1}{J}\right] - \frac{\mu}{v_s}(J-1). \tag{4}$$

This function involves the volume change due to swelling, so that it is regarded as a compressible hyperelastic material to implement it using the user subroutine UMAT in Abaqus/Standard [5]. Furthermore, Eq. (4) can give rise to $\int_{\Omega_0} \delta W \, dV_0 = \int_{\Omega_0} B_i \delta x_i \, dV_0 + \oint_{\Gamma_0} T_i \delta x_i \, dS_0$ instead of Eq. (1), which is reduced to the same form of the equilibrium condition for a hyperelastic material.

It is noted that the chemical potential is singular ($\mu = -\infty$) because of $J = 1$ and $I = 1$ in Eq. (4) at the dry state. To avoid the singularity, as shown in Fig. 1, we decompose the total deformation gradient $\boldsymbol{F} = \boldsymbol{F}^{(1)}\boldsymbol{F}^{(0)}$ into the deformation from the dry state to the equilibrium state where the chemical potential μ must be constant at the swelling equilibrium; the internal chemical potentials μ are equal to the external one $\hat{\mu}$, i.e., ($\mu = \hat{\mu}$). In the present study, we introduce a free swelling state of a uniform stretching with $\boldsymbol{F}^{(0)} = \lambda_0 \boldsymbol{I}$ in numerical calculations [5, 6]. Once the initial stretch λ_0 in the initial state is given, one can determine the corresponding chemical potential $\mu^{(0)}$ by the following condition of the free-swelling equilibrium:

$$\frac{n^{(g)} v_s}{\lambda_0^3}(\lambda_0^2 - 1) + \ln\left(1 - \frac{1}{\lambda_0^3}\right) + \frac{1}{\lambda_0^3} + \frac{\chi}{\lambda_0^6} = \frac{\mu}{k_B T}. \tag{5}$$

The temperature variable in Abaqus/Standard is utilized to mimic the external chemical potential $\hat{\mu}$.

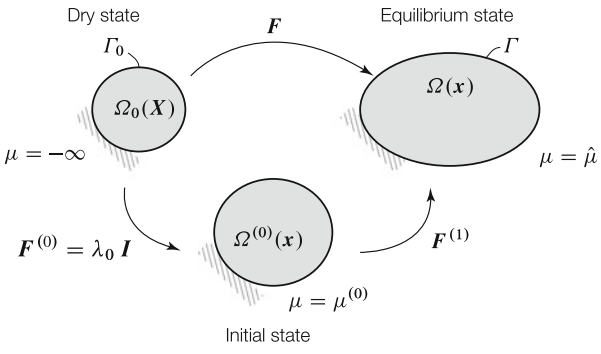

Fig. 1 Schematic of the swelling kinematics of gel

3 Finite Element Modeling of Hydrogel Bistrips

We constructed a finite element model of swelling-induced bending of hydrogel bistrips due to chemical potential by using Abaqus/Standard (Dassault Systèmes). Figure 2 shows a half model of bistrip according to its symmetry about the side AFE. Specifically, we consider the bistrip with length $L/2 = 400\,\mathrm{mm}$, thickness of elastomer strip (ABCF) $H^{(\mathrm{e})} = 5\,\mathrm{mm}$, and thickness of gel strip (FCDE) $H^{(\mathrm{g})} = 5\,\mathrm{mm}$. The superscript $s = (\mathrm{e}, \mathrm{g})$ denotes the elastomer and gel strips, respectively. We introduced the cylindrical coordinate system in the deformed configuration as shown in Fig. 2. After bending of the bistrip due to swelling, the kinematics were characterized by the radius of curvature at the bottom surface of elastomer strip and the thicknesses of the elastomer and gel strip denoted by $h^{(\mathrm{e})}$ and $h^{(\mathrm{g})}$, respectively. The full-integration quadrilateral plane strain elements for incompressible elastomer (CPE4H) and for gel (CPE4) were used. A mesh refinement study required 50 elements in elastomer strip and 50 elements in gel strip through the thickness direction and 400 elements in the axial direction. The nodes along the side AFE were constrained in $\mathbf{e}_2$-direction and the middle node F was pinned in $\mathbf{e}_1$-direction. At the nodes along the side BCD were constrained so as to maintain a straight line but may increase in thickness so that the resulting deformation is pure bending. The free energy density functions of the elastomer and gel strips per unit volume in the reference (dry) state are described by the neo-Hookean model, $W^{(\mathrm{e})} = (G^{(\mathrm{e})}/2)(I-3)$, and the Flory–Rehner model, $W^{(\mathrm{g})} \equiv \hat{W}$, given by Eq. (4), respectively. $G^{(s)} = n^{(s)} k_{\mathrm{B}} T$ is the shear modulus of elasticity for each strip.

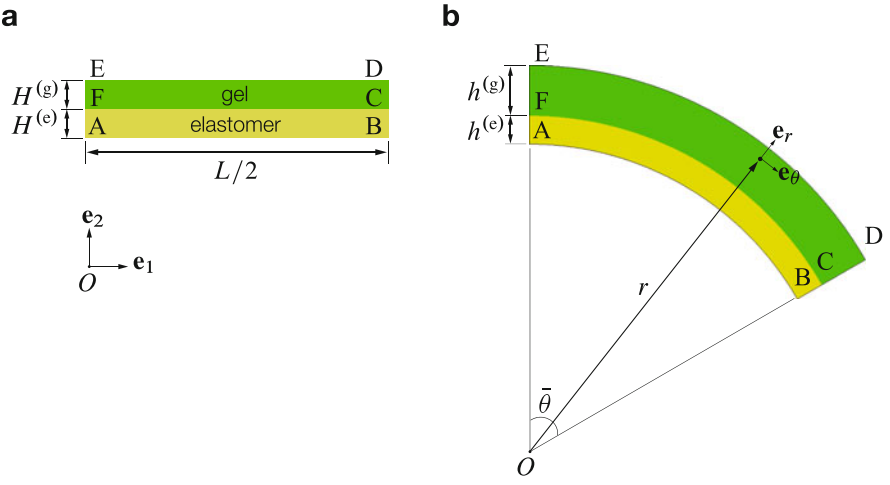

Fig. 2 Finite element model of the bistrip comprising of gel and elastomer. (**a**) Initial state of the half-symmetric model of bistrip according to its symmetry about the side AFE. (**b**) The swelling-equilibrium state of the model at $\mu = \hat{\mu}$

4 Results and Discussion

In order to understand how the material and geometrical parameters can control the shapes of hydrogel bistrip at the state of swelling equilibrium, we explore the effects of the stiffness ratio $G^{(g)}/G^{(e)}$ and thickness ratio $H^{(g)}/H^{(e)}$ between the elastomer and the gel on the bending responses of the bistrip.

Figure 3 shows the effect of the stiffness ratio between elastomer and gel strips, $G^{(g)}/G^{(e)} \in [10^{-4}, 10^{2}]$, on the shapes of swelling-induced bending. The stiffness

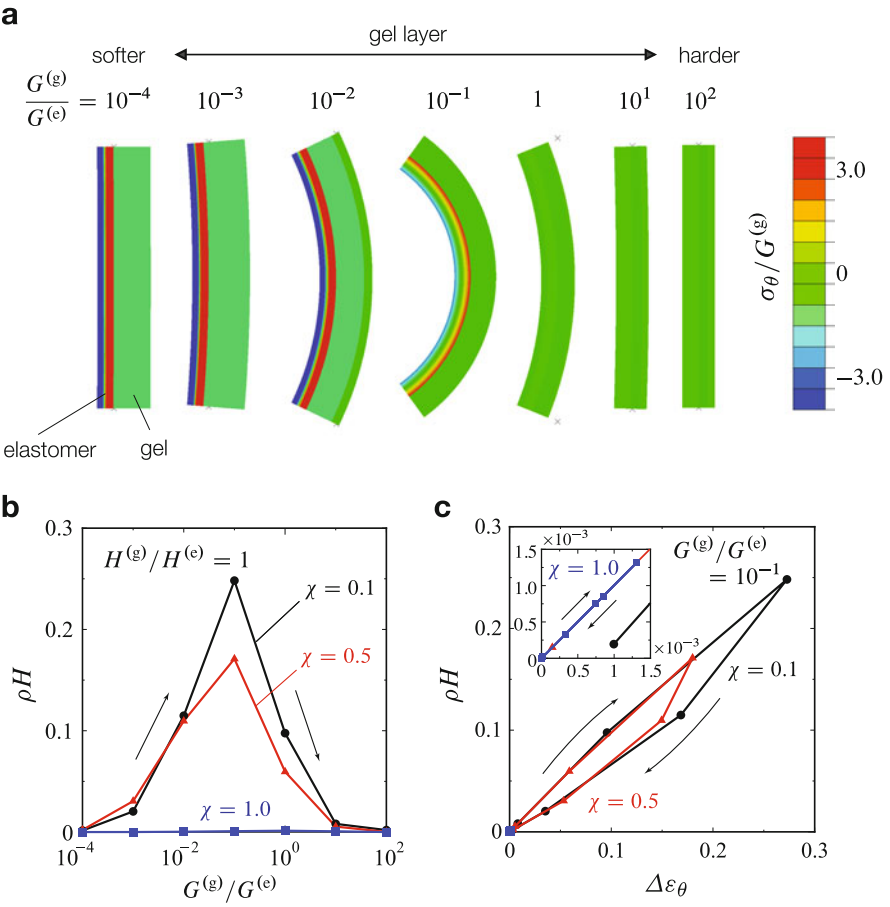

Fig. 3 Effect of the stiffness ratio on the responses of swelling-induced bending. Computationally used conditions: $H^{(g)}/H^{(e)} = 1$ and $L/H = 8$. (**a**) Swelling-equilibrium shapes with $\chi = 0.1$. $G^{(g)}/G^{(e)}$ defines the stiffness ratio of gel strip to that of elastomer strip. Contour level represents circumferential stress normalized by the shear modulus of gel strip $G^{(g)}$. (**b**) Dependence of normalized bending curvature ρH on the stiffness ratio $G^{(g)}/G^{(e)}$. (**c**) Normalized bending curvature ρH as a function of the differential strain $\Delta\varepsilon_\theta$

ratio is varied by changing the crosslink density $n^{(g)}v_s$ through the relation $G^{(g)} = n^{(g)}k_BT$, while the shear modulus of elastomer strip is fixed. We take the values of $T = 300\,\mathrm{K}$, $v_s = 3.0 \times 10^{-29}\,\mathrm{m}^3$, and $k_B = 1.38 \times 10^{-23}\,\mathrm{J/K}$. The χ-parameter may be served as measuring the magnitude of swelling. We consider the three values of $\chi = \{0.1, 0.5, 1.0\}$. Figure 3a represents the swelling-equilibrium shapes with various stiffness ratios for $H^{(g)}/H^{(e)} = 1$, $\chi = 0.1$, and $L/H = 8$. The contour level exhibits the circumferential stress normalized by the shear modulus of gel $G^{(g)}$. The stress level is high at the interface between the gel and elastomer strips. Figure 3b shows the dependence of bending curvature ρ, normalized by multiplying the total thickness H in the reference state, on the stiffness ratio. The curvature is defined as the inverse of bending radius of curvature measuring at the bottom surface of the elastomer strip. We observe that there exists the optimum value of stiffness ratio to maximize the bending curvature: $(G^{(g)}/G^{(e)})_{opt} \approx 10^{-1}$ for $\chi = \{0.1, 0.5\}$ and $(G^{(g)}/G^{(e)})_{opt} \approx 10^{0}$ for $\chi = 1.0$. When the stiffness ratio is lower than the optimum value, the curvature increases as the stiffness ratio increases from 10^{-4} to $(G^{(g)}/G^{(e)})_{opt}$. On the other hand, for the case that the stiffness ratio is higher than the optimum value, $G^{(g)}/G^{(e)} > (G^{(g)}/G^{(e)})_{opt}$, the curvature decreases as the stiffness ratio increases from $(G^{(g)}/G^{(e)})_{opt}$ to 10^2. We can understand the optimum value of stiffness ratio through the differential strain $\Delta\varepsilon_\theta$, defined as the maximum misfit strain between upper and lower surfaces of the bistrip. Figure 3c plots the normalized bending curvature ρH as a function of the differential strain $\Delta\varepsilon_\theta$. We can directly see that the maximum curvature occurs at the maximum value of the differential strain at which the stiffness ratio takes the optimal ones $(G^{(g)}/G^{(e)})_{opt} \approx 10^{-1}$ for $\chi = \{0.1, 0.5\}$ or $(G^{(g)}/G^{(e)})_{opt} \approx 10^{0}$ for $\chi = 1.0$ when cross-referring to both Fig. 3b and c. We also find that the relation between the differential strain and the normalized curvature exhibits a loop, depending on the stiffness ratio.

Next we explored the effect of thickness ratio between elastomer and gel strips, $H^{(g)}/H^{(e)} \in [\frac{1}{19}, \frac{19}{1}]$, on the responses of swelling-induced bending, as shown in Fig. 4. The thickness ratio is varied so that the total thickness of bistrip is kept constant. Figure 4a represents the swelling-equilibrium shapes with various thickness ratios $H^{(g)}/H^{(e)}$ for fixed values of $G^{(g)}/G^{(e)} = 1$, $\chi = 0.1$, and $L/H = 8$. The contour level exhibits the circumferential stress normalized by the shear modulus of gel strip, $G^{(g)}$. We observe that there exists the optimum value of stiffness ratio to maximize the bending curvature, $(H^{(g)}/H^{(e)})_{opt} \approx 3/2$. This tendency is the same for all the values of χ-parameter. When the stiffness ratio is lower than the optimum value $(H^{(g)}/H^{(e)} < 3/2)$, the curvature increases as the thickness ratio increases from $1/19$ to $3/2$. On the other hand, when the stiffness ratio is higher than the optimum value $(H^{(g)}/H^{(e)} > 3/2)$, the curvature decreases as the stiffness ratio increases from $3/2$ to $19/1$. As the same of preceding discussion, we can understand that the optimum value of thickness ratio is also determined by the differential strain $\Delta\varepsilon_\theta$. Figure 4c plots the bending curvature ρ as a function of the differential strain $\Delta\varepsilon_\theta$. We can see that the maximum curvature occurs corresponding to the maximum value of the differential strain at the thickness ratio $H^{(g)}/H^{(e)} \approx 3/2$. We also find that the relation between the differential strain and the normalized curvature exhibits a linear, depending on the thickness ratio.

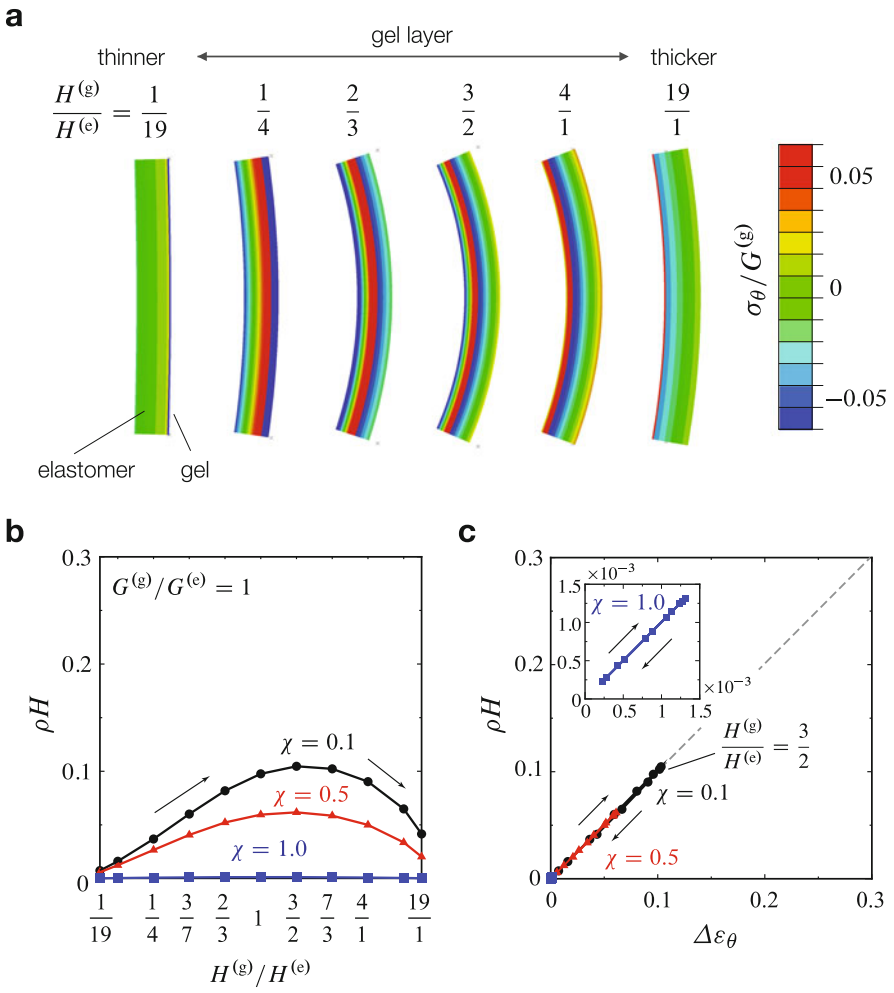

Fig. 4 Effect of the thickness ratio on the responses of swelling-induced bending. Computationally used conditions: $G^{(g)}/G^{(e)} = 1$ and $L/H = 8$. (**a**) Swelling-equilibrium shapes with $\chi = 0.1$. $H^{(g)}/H^{(e)}$ defines the thickness ratio of gel strip to elastomer strip, and the total thickness is kept constant. Contour level represents circumferential stress normalized by the shear modulus of gel strip $G^{(g)}$. (**b**) Dependence of normalized bending curvature ρH on the thickness ratio $H^{(g)}/H^{(e)}$. (**c**) Normalized bending curvature ρH as a function of the differential strain $\Delta\varepsilon_\theta$

5 Conclusions

We explored the swelling-induced bending of bistrips due to chemical potential and specifically focused on the effects of the stiffness and thickness ratios between the elastomer and gel strips on their swelling-equilibrium shapes. As a result, we found the followings:

- The curvature of hydrogel bistrip depends on three parameters: χ, $G^{(g)}/G^{(e)}$, and $H^{(g)}/H^{(e)}$.
- There exists the optimum combination of the stiffness and thickness ratios to maximize the curvature.
- The curvature becomes large when χ is decreased since the gel strip much more swell and the differential strain level is high.

Acknowledgements This work was supported by JSPS KAKENHI Grant Number 15K17941.

References

1. Gracias DH (2013) Stimuli responsive self-folding using thin polymer films. Curr Opin Chem Eng 2:112–119
2. Ionov L (2014) Hydrogel-based actuators: possibilities and limitations. Mater Today 17:494–503
3. Morimoto T, Ashida F (2015) Temperature-responsive bending of a bilayer gel. Int J Solids Struct 56–57:20–28
4. Hong W, Zhao X, Zhou J, Suo Z (2008) A theory of coupled diffusion and large deformation in polymeric gels. J Mech Phys Solids 56:1779–1793
5. Kang MK, Huang R (2010) A variational approach and finite element implementation for swelling of polymeric hydrogels under geometric constraints. J Appl Mech 77:061004
6. Hong W, Liu Z, Suo Z (2009) Inhomogeneous swelling of a gel in equilibrium with a solvent and mechanical load. Int J Solids Struct 46:3282–3289
7. Flory PJ, Rehner J (1943) Statistical mechanics of cross-linked polymer networks II. J Chem Phys 11:521

Determination of Parameters of the External Electric Circuits Providing Maximum Damping of Vibrations of Electroelastic Bodies

V.P. Matveenko, N.V. Sevodina, N.A. Yurlova, D.A. Oshmarin, M.A. Yurlov, and A.S. Ivanov

Abstract The paper considers the piece-wise homogeneous bodies composed of elastic deformable elements, some of which show piezoelectric properties and can be coupled with series-connected external circuits via the electroded surfaces of piezoelements. The objective of this study is to develop effective algorithms of mathematical modeling, which will allow us to find the values of the circuit element parameters providing maximum damping of the system vibrations at the prescribed resonant frequencies. The optimal values of the parameters for the circuit elements are determined based on the natural vibration problem and equivalent circuits for elastic system incorporating piezoelectric element and external electric circuit. The efficiency of the proposed approach is demonstrated by solving particular problems.

1 Introduction

Embedment of piezoelectric elements into different structures and their connection to the external electric circuits open up new possibilities in controlling the dynamic behavior of engineering structures.

In work [1], the authors have demonstrated for the first time that the external electric circuits composed of series-connected inductance (L) and resistance (R) elements can be effectively used for damping one vibration mode.

Different variants of piezoelement connection with shunt electric circuits allowing vibration damping are discussed in works [2–6].

Because of the abundance of shunt piezoelectric techniques for controlling the dynamic characteristics of smart-structures with embedded piezoelectric elements, a search for optimal variants should rely mainly on the mathematical modeling. At present, the literature in this area numbers thousands of works, but there are still problems that call for further investigation. In the majority of studies the numerical simulation of vibration damping with the use of piezoelectric elements and external

V.P. Matveenko (✉) • N.V. Sevodina • N.A. Yurlova • D.A. Oshmarin • M.A. Yurlov • A.S. Ivanov
Institute of Continuous Media Mechanics of the Ural Branch of RAS, Perm, Russia
e-mail: mvp@icmm.ru

H. Irschik et al. (eds.), *Dynamics and Control of Advanced Structures and Machines*, DOI 10.1007/978-3-319-43080-5_10

electric circuits is performed based on the finite element method. In particular, the review articles [7, 8] published from 1986 to 2002 collected and systemized 2074 papers dealing with the application of the finite element method to the analysis and simulation of smart-materials and structures. All these works focus on the development of new algorithms and discussion of the results obtained with the aid of commercial software packages.

In numerical simulation, the damping properties of smart-systems are generally estimated by the value of resonance mode amplitude or by the rate of transient processes. In the first case it is necessary to solve the problem of sustained forced vibrations and in the second case the dynamic problem with initial conditions. A search for optimal parameters of piezoelectric elements and external electric circuits in the context of these problems is associated with certain difficulties. Thus, the evaluation of the resonance mode amplitudes in the framework of the sustained forced vibration problem requires that this particular problem be solved repeatedly at different frequencies of external actions. Nevertheless, the application of sustained forced vibration problem and the dynamic problem with initial conditions allowed us to obtain optimal solutions for the examined loading regimes.

In this paper, optimization of the dynamic characteristics of smart-systems with piezoelectric elements and external electric circuits is accomplished based on the natural vibration problem and equivalent circuit technique.

2 Optimization of the External Electric Circuit Parameters Based on the Solution of Natural Vibration Problem

Let us consider a piece-wise homogeneous body of volume $V = V_1 + V_2$, where the volume V_1 consists of homogeneous elastic and viscoelastic elements and the volume V_2 consists of piezoelectric elements. The piezoelectric elements can be connected through the electroded surface to the *RLC*-circuits of arbitrary structure involving the resistance, capacitance, and inductance elements.

For the problem of natural vibrations under homogeneous boundary conditions the desired solutions are written in the following form:

$$u_i(x,t) = \bar{u}_i(\mathbf{x})\, e^{i\omega t}, \quad \varphi(x,t) = \bar{\varphi}(\mathbf{x})\, e^{i\omega t} \tag{1}$$

where $\omega = \omega_R + i\omega_I$ is the complex natural frequency; ω_R corresponds to the natural frequency; ω_I characterizes the rate of vibration damping, $\bar{u}_i(\mathbf{x})$, $\bar{\phi}(\mathbf{x})$ is the eigenvibration.

A mathematical statement of the problem is given in works [9, 10]. Numerical implementation of the problem is based on the finite element method.

Consider a cantilevered plate, the surface of which is coupled with a piezoelectric element and external, series-connected electric *RL*-circuit shunted to the electroded surface of the element. The size of the plate is $210 \times 26 \times 0.6$ mm, and the size of piezoelement is $50 \times 20 \times 0.36$ mm. The piezoelement is attached at a distance of 12 mm away from the clamped end of the plate and symmetrically with respect to the plate axis.

The plate was made of elastic material with the following mechanical characteristics: elastic modulus $E = 2 \times 10^{11}$ N/m^2, Poisson's ratio $\nu = 0.3$, specific density ρ =7800 kg/m^3. The piezoelement polarized through the thickness was made of piezoceramics PZT-4-z [9].

The eigenfrequencies of the plate with the attached piezoelement and shunt electric circuit were calculated at different values of resistance R and inductance L of the external circuit using the developed software package for computing the eigenfrequencies. In this case, the eigenfrequencies of vibrations are complex even in electroelastic bodies due to the presence of the dissipative mechanism in the external electric circuit. Table 1 summarizes the first nine eigenfrequencies at different values of R and L. It also presents eigenfrequencies of the plate, which has no external circuit, only the attached piezoelement with short-circuited electroded surfaces.

A comparison of these results shows that the external electric circuit leads to the appearance of additional eigenfrequency.

Table 1 Vibration eigenfrequencies of structure (plate with piezoelement) with and without external electric circuit

No.		$\omega = \omega_R + i\omega_I$	No.	ω
	$R = 10^2\ \Omega$,	$R = 10^4\ \Omega$,		
	$L = 10^3$ H,	$L = 11.66 \times 10^2$ H,		
1	$13.55 - i4.50 \times 10^{-5}$	$12.38 - i3399.00 \times 10^{-5}$	1	13.56
2	$47.35 - i78.70 \times 10^{-5}$	$15.20 - i3423.00 \times 10^{-5}$		
3	$72.47 - i261.50 \times 10^{-5}$	$72.34 - i2.71 \times 10^{-5}$	2	72.15
4	$198.35 - i18.80 \times 10^{-5}$	$198.32 - i1.36 \times 10^{-5}$	3	197.90
5	$204.46 - i0.07 \times 10^{-5}$	$204.45 - i0.23 \times 10^{-5}$	4	204.45
6	$404.22 - i3.71 \times 10^{-5}$	$404.16 - i4.6 \times 10^{-5}$	5	399.79
7	$489.40 - i0.01 \times 10^{-5}$	$489.40 - i0.17 \times 10^{-5}$	6	489.40
8	$584.10 - i0.00 \times 10^{-5}$	$584.10 - i7.00 \times 10^{-5}$	7	584.10
9	$675.01 - i3.76 \times 10^{-5}$	$674.96 - i0.38 \times 10^{-5}$	8	665.45

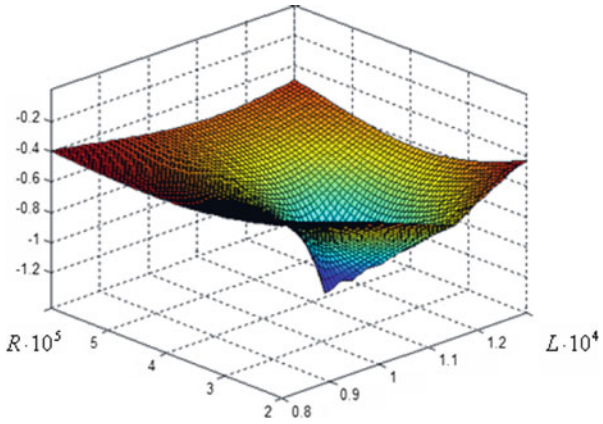

Fig. 1 Behavior of imaginary part of the first eigenfrequency of the structure, depending on the parameters of the external electric circuit

Figure 1 illustrates the variation in the imaginary part of the first eigenfrequency of structure vibrations in the range of the values of parameters L and R, at which the rate of vibration damping reaches its maximum value.

Actually, this result demonstrates the possibility of constructing an optimization algorithm for computing the values of L and R, ensuring maximal damping of nearly all vibration modes except for the modes, at which the electrode surface potential is zero.

3 Verification of the External Circuit Parameters Using the Equivalent Circuit Approach

In the electromechanical processes under consideration the piezoelement shows capacitive properties and forms together with external circuit a series-connected *RLC*—oscillatory circuit (Fig. 2), which leads to the appearance of additional vibrational eigenfrequency. In the case when this frequency coincides with one of the eigenfrequencies of the electroelastic body, damping of the corresponding vibration mode reaches its maximum level [11].

In papers [2, 4, 5, 12, 13], the simplest model of a piezoelement consisting of a single capacitor of zero capacitance C_0 was used as its electric analogue. In this case the relations for the real and imaginary parts of vibrational eigenfrequency can be derived based on the relations describing the behavior of current and voltage in the

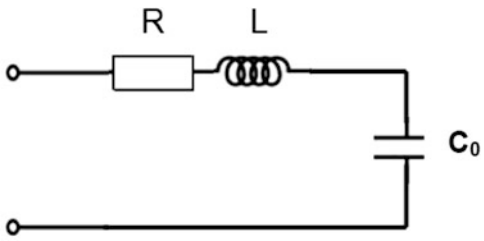

Fig. 2 Series resonant circuit formed by external electric circuit and piezoelement with constant capacitance

series-connected oscillatory circuit [14]

$$\omega_{Re} = \frac{1}{2\pi}\sqrt{\frac{1}{LC_0} - \frac{R^2}{4L^2}} \qquad \omega_{Ie} = -\frac{1}{2\pi}\frac{R}{2L} \tag{2}$$

The capacitance C_0 is specified by the value of the charge produced on the surface of piezoelectric element as a result of its deformation by the electric potential V, applied to one of the electroded surfaces $-C_0 = Q_s/V$, where Q_s is the total electric charge on the electroded surface.

The electroelastic static problem was solved using the ANSYS package. In the example problem under consideration C_0=11.79 nF. This value of peizoelement capacitance is taken as a static one.

Relation (2) allows us to evaluate the values of R and L, sustaining the specified vibration frequency. In particular, the value $\bar{\omega} = 46.36 - \mathrm{i}7.96 \times 10^{-4}$, falling in the middle of the interval between the first and the second eigenfrequencies of the plate with the attached piezoelement and short-circuiting (*s/c*), occurs at $R = 10^2\,\Omega$, $L = 10^3$ H, whereas the value $\bar{\omega} = 13.58 - \mathrm{i}6.82 \times 10^{-2}$, which are practically consistent with the first vibration frequency, occurs at $R = 10^3\,\Omega$, $L = 11660$ H. The eigenfrequencies of the plate with the attached piezoelement and external circuit obtained from the solution of natural vibration problem (1) for the above-mentioned parameters of the circuit elements are given in Table 2. These results demonstrate that the additional frequency occurring in the presence of the external electric circuit differs insignificantly from the estimates made by formula (2) only at the frequencies far from resonance.

The above examples, as well as the analogous calculations made for other eigenfrequencies, lead us to conclude that the piezoelectric element behaves as a capacitor of constant capacitance C_0 only at the frequencies that are far from the resonant frequencies of the initial system (plate with piezoelectric element). Therefore, the parameters R and L obtained by formula (2) cannot provide the maximum damping level.

A more adequate description of piezoelement behavior can be gained by using the equivalent electric circuit models composed of electric elements with fixed

Table 2 Vibration eigenfrequencies of plate with piezoelement obtained by direct calculations and on the basis of equivalent electric circuit

Eigenfrequencies of the plate with piezoelement at *s/c*	Eigenfrequencies of the plate with electric circuit R=456348 Ω L=11054 H $\bar{\omega}_1 = 13.79 - i85.10 \times 10^{-2}$ $\bar{\omega}_2 = 13.79 - i243.50 \times 10^{-2}$	piezoelement and external R=168491 Ω L=325.4 H $\bar{\omega}_1 = 72.276 - i19.95 \times 10^{-2}$ $\bar{\omega}_2 = 72.276 - i4100.55 \times 10^{-2}$
13.58	$13.79 - i85.00 \times 10^{-2}$	$13.57 - i4.83 \times 10^{-2}$
13.58	$13.79 - i243.4 \times 10^{-2}$	$13.57 - i4.83 \times 10^{-2}$
72.15	$72.34 - i0.04 \times 10^{-2}$	$72.28 - i19.94 \times 10^{-2}$
72.15	$72.34 - i0.04 \times 10^{-2}$	$72.25 - i4085.68 \times 10^{-2}$
197.90	$198.32 - i0.00$	$198.40 - i0.00$
204.45	$204.45 - i0.00$	$204.45 - i0.00$
399.80	$404.16 - i0.00$	$404.34 - i0.00$
489.41	$489.30 - i0.00$	$489.40 - i0.00$
584.11	$584.10 - i0.00$	$584.10 - i0.00$
665.46	$674.96 - i0.04 \times 10^{-2}$	$675.11 - i1.88 \times 10^{-2}$

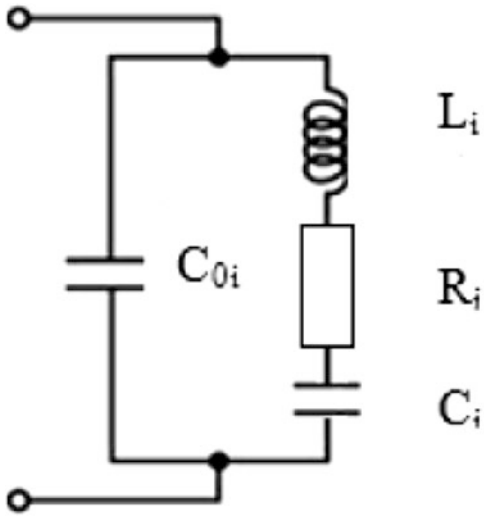

Fig. 3 The equivalent electrical model with fixed parameters of electrical components for describing the behavior of a piezoelement

parameters. Figure 3 shows one of these models, which is seen to be a parallel connection of the capacitance C_i, inductance L_i, resistance R_i, and capacitance of the piezoelectric element C_{0i}. The equivalent resistor R_i in the series-connected oscillatory circuit $R_iL_iC_i$ corresponds to the loss of energy in the structure due to viscoelastic properties of the structure material. Since in the problem under consideration the piezoelectric element is made from piezoceramics that possesses elastic properties, the resistance R_i can be neglected. In this model [15–18], the

capacitance of the piezoelement is not a constant. It means that the piezoelement behaves as an ordinary capacitor of capacitance C_{0i} only at the off-resonance frequencies. The parameters of the equivalent circuit C_i, L_i (dynamic capacitance and inductance) reveal themselves only at vibration frequencies that approach the self-resonant frequency of the piezoelement.

The equivalent electric model of the plate with short-circuited piezoelectric element and one resonant frequency allows us to describe the simulated object only in the neighborhood of the eigenfrequency ω_i.

The computation of the external circuit parameters was done using the algorithm designed for describing vibrations in the examined electric circuit.

Table 2 presents the obtained set of eigenfrequencies for the plate with a short-circuited piezoelement and the eigenfrequencies for the plate with piezoelement and external *RL*-circuit, which were calculated on the basis of the equivalent electric model and was responsible for the occurrence of the additional eigenfrequency in the neighborhood of the first and second resonances of the plate and piezoelement at s/c. Table 2 also presents the values of R and L and eigenfrequencies $\bar{\omega}$ of the electric analogue.

The obtained results demonstrate that the equivalent electric model composed of elements with lumped parameters can be effectively used to identify the appropriate parameters for the elements of the external electric circuit, at which the additional eigenfrequency coincides with the frequency of the damped mode providing thereby the maximum suppression of system vibrations.

4 Conclusion

In this paper we propose a mathematical formulation of the problem on natural vibrations of piece-wise homogeneous elastic bodies composed of elastic deformable elements, some of which show piezoelectric properties and are coupled via the electroded surfaces of piezoelements with the series-connected external electric circuits comprising the resistance, inductance, and capacitance elements.

By numerical example we have demonstrated that the problem of natural vibrations of electroelastic body with external electric circuit can be used to identify the parameters of its elements, which will provide the maximum rate of vibration damping at the prescribed resonant frequency.

We have considered two variants of equivalent electric circuits for a piece-wise homogeneous elastic body with piezoelectric elements: on the basis of the capacitor with constant capacitance and on the basis of the circuit composed of electric elements with fixed parameters.

It has been shown that the replacement of the piece-wise homogeneous body containing piezoelectric element by the capacitor of constant capacitance yields insignificant error only at the off-resonance frequencies. The second circuit provides rather high accuracy over the whole frequency range.

The reliability and efficiency of the application of equivalent circuits for evaluation of desired parameters for the elements of external electric circuits have been justified through a comparison of the obtained results with the calculations made in the framework of the problem on natural vibrations of deformable elastic bodies with piezoelectric elements and external electric circuits.

Acknowledgements The work was supported by RFBR under grants No. 14-01-96003-r-ural-a and No. 15-01-03976-a.

References

1. Hagood NW, Von Flotow A (1991) Damping of structural vibrations with piezoelectric materials and passive electrical networks. J Sound Vib 146(2):243–268
2. Agneni A, Mastroddi F, Polli GM (2003) Shunted piezoelectric patches in elastic and aeroelastic vibrations. Comput Struct 81:91–105
3. Sodano HA (2003) Macro-fiber composites for sensing, actuation and power generation. Ph.D. Thesis, Blacksburg, Virginia, 151 pp.
4. Thomas O, Ducarne J, Deu J-F (2012) Performance of piezoelectric shunts for vibration reduction. Smart Mater Struct 21(1):015008
5. Caruso G (2001) A critical analysis of electric shunt circuits employed in piezoelectric passive vibration damping. Smart Mater Struct 10:1059–1068
6. Kawiecki G, Jesse S (2002) Rosette piezotransducers for damage detection. Smart Mater Struct 11:196–201
7. Mackerle J (1998) Smart materials and structures - a finite-element approach: a bibliography (1986–1997). Model Simul Mater Sci Eng 6:293–334
8. Mackerle J (2003) Smart materials and structures - a finite element approach–an addendum: a bibliography (1997–2002). Modell Simul Mater Sci Eng 11:707–744
9. Matveenko VP, Kligman EP, Yurlov MA, Yurlova NA (2012) Numerical modeling and optimization of dynamic characteristics of smart structures incorporating piezo materials. Phys Mesomech 15(3):190–199
10. Matveenko VP, Kligman EP, Yurlova NA, Yurlov MA (2011) Optimization of the dynamic characteristics of electroviscoelastic systems by means of electric circuits. In: Irschik H, Krommer M, Belyaev AK (eds) Advanced dynamics and model based control of structures and machines. Springer, Wien, pp 151–158
11. Nashif A, Jones D, Henderson J (1988) Vibration damping (Translated by L.G. Rorneychuk, edited by E. I. Grigoljuk). Mir, Moscow, p 448
12. Viana FAC, Steffen V Jr (2006) Multimodal vibration damping through piezoelectric patches and optimal resonant shunt circuits. J. Braz. Soc. Mech. Sci. Eng. XXVIII(3):293–310
13. Fleming AJ, Behrens S, Moheimani SOR (2003) Reducing the inductance requirements of piezoelectric shunt damping systems. Smart Mater Struct 12:57–64
14. Khokhlov AV (2005) Theoretical foundations of radioelectronics. Saratov University Publishers, Saratov, p 296
15. Dyke V (1925) The electric network equivalent of a piezoelectric resonator. Phys Rev 25:895A
16. Park CH (2001) On the circuit model of piezoceramics. J Intell Mater Syst Struct 12:515–522
17. Sherrit S, Wiederick HD, Mukherjee BK Sayer M (1997) An accurate equivalent circuit for the unloaded piezoelectric vibrator in the thickness mode. J Phys D Appl Phys 30(16):2354–2363
18. Kim J, Grisso BL, Kim JK, Ha DS, Inman DJ (2008) Electrical modeling of piezoelectric ceramics for analysis and evaluation of sensory systems. In: SAS 2008 - IEEE sensors applications symposium Atlanta, GA, February 12–14, pp 122–127

Forming of Woven-Reinforced Thermoplastic-Matrix Composites: Characterization, Modelling, and Validation

Martín Machado and Zoltan Major

Abstract The objective of this article is to give an overview of the methods available in literature to model the forming of woven-reinforced thermoplastic-matrix composites. Modelling approaches, namely kinematic and mechanics-based, to simulate the forming process are discussed. The experimental tests for the determination of the necessary parameters are listed and discussed. A great part of the efforts has been devoted to the shear characterization since it is the most important deformation mode. The bending behaviour is usually neglected but it is starting to be considered since it is important to simulate the shape of wrinkles.

1 Introduction

Automotive industry started to analyse metal replacement strategies for their vehicles in order to reduce carbon dioxide emissions. Up to 14 % fuel economy improvement could be achieved through a 20 % weight reduction [1]. In the case of automobiles, more than 75 % of fuel consumption automobiles is directly related to their weight [2]. Polymer-matrix composites play an important role in this context since they offer similar strength, stiffness, and toughness to steel but their density is significantly lower.

Large-scale production of automotive composites components is only plausible if high production rates can be achieved. Woven-reinforced thermoplastic-matrix composites can be processed via forming/stamping, implicating considerable shorter cycle times than traditional thermoset-matrix composites [3]. The original sheet, provided as pre-preg by the material manufacturer, is heated employing an infrared heater, then is pressed between two moulds to achieve the desired geometry, and finally a laser cuts the outer contour.

Numerical simulations are nowadays an essential tool in development stages of almost all industrial process. As draping of dry woven reinforcement and forming of woven composites made their way to automotive and aerospace industries, the corresponding simulation strategies started to be developed. In this sense, the field

M. Machado (✉) • Z. Major
Institute of Polymer Product Engineering, Johannes Kepler University Linz, Linz, Austria
e-mail: martin.machado@jku.at; zoltan.major@jku.at

H. Irschik et al. (eds.), *Dynamics and Control of Advanced Structures and Machines*, DOI 10.1007/978-3-319-43080-5_11

of woven and woven composite modelling has seen intense activity during the last two decades. Although a wide diversity of approaches has been explored, most of them can be divided in kinematic and mechanics-based models.

This paper provides a brief overview of the experimental characterization techniques and the different modelling approaches employed to model the forming process. First, the mechanical characterization of the three predominant deformation modes of these materials, namely in-plane shear [4], in-plane tensile [5], and out-of-plane bending [6], is discussed. Special focus is given to the in-plane shear characterization as it is the most relevant deformation mode and it has been consequently studied in more detail. The two more popular tests to characterize the shear behaviour (picture frame test and bias extension test) are analysed. In the subsequent section different modelling approaches are discussed. Kinematic and mechanics-based approaches are mentioned. Then some forming experiments are remarked with emphasis on the shear angle measurements aimed to validate forming simulations.

2 Mechanical Characterization

2.1 In-Plane Shear

Most of the literature has been focussed on the study of the shear behaviour. This is logical because woven composites undergo large fibre relative rotations while forming [7] and this rotation is mainly determined by the shear properties of the material. As orientation determines the final properties of the component, especially its stiffness [8], a good description of the shear behaviour yields a better prediction of the fibre orientation and consequently a more accurate prediction of its mechanical performance during service.

Two main tests have been used during the last decades to characterize the shear behaviour of dry woven and woven-reinforced composites, namely picture test frame and bias extension test [9]. Picture frame test consists of applying a uniform shear strain using a deformable frame as shown in Fig. 1a and b. The shear angle ($\gamma = 90\,^\circ - 2\theta$) is related to the applied displacement as in Eq. (1). The shear force F_{sh} is easily calculated considering the geometry of the tests [Eq. (2)]. As the shear force depends on the sample size, Harrison et al. [6] proposed a normalized shear force F^*_{sh} with respect to the rig length (L in Fig. 1a), i.e., $F^*_{\text{sh}} = F_{\text{sh}}/L$. In this way, two samples of different size exhibit the same ratio between axial force and side length when sheared to the same shear angle.

$$\gamma = \frac{\pi}{2} - \arccos\left(\frac{\sqrt{2}L + d}{2L}\right) \tag{1}$$

$$F_{\text{sh}} = \frac{F}{2\cos\theta} \tag{2}$$

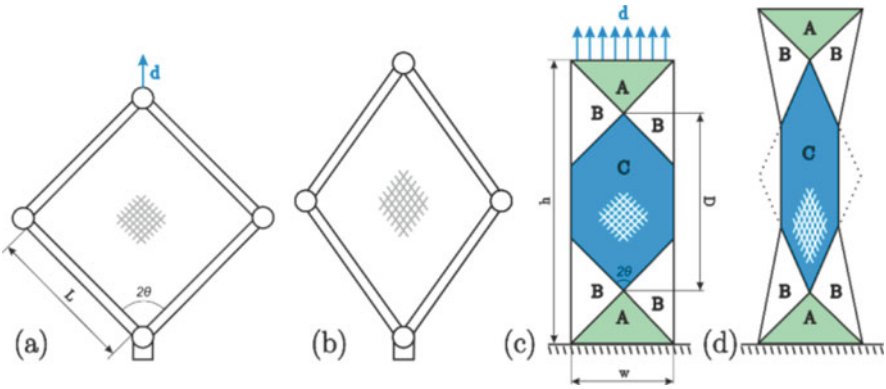

Fig. 1 Picture frame test (**a**, **b**) and bias extension test (**c**, **d**). Figures (**a**) and (**c**) show the initial configuration. Figures (**b**) and (**d**) show the deformed configuration

Bias extension test consists basically of a tensile test of a $\pm 45\,^{\circ}$-oriented plate with aspect ratio larger than 2 (see Fig. 1c and d). Assuming no relative slippage between yarns, the central region C is subjected to pure shear, the shear angle in region B is the half of that in region C, and the region A is not deformed. On the basis of geometrical considerations the shear angle can be related to the axial displacement as shown in Eq. (3). However, this equation loses accuracy as the shear angle increases and approximates the locking angle [6]. In order to avoid this, the shear angle is usually measured using optic systems [10].

$$\gamma = \frac{\pi}{2} - 2\arccos\left(\frac{D+d}{\sqrt{2}D}\right) \tag{3}$$

Normalization of the shear force is not as straightforward as in the case of the picture frame test, mainly due to the fact the deformation is not homogeneous in the sample. Recently, Härtel and Harrison [11, 12] presented a detailed review of the normalization methods. Considering the power dissipated in regions B and C, the normalized shear force of a bias extension test can be calculated as in Eq. (4). As $F^*_{\mathrm{sh}}(\gamma)$ depends on $F^*_{\mathrm{sh}}(\gamma/2)$ an iterative process is needed [13].

$$F^*_{\mathrm{sh}}(\gamma) = \frac{1}{(2h-3w)\cos\gamma}\left(\left(\frac{h}{w}-1\right)F\left(\cos\frac{\gamma}{2}-\sin\frac{\gamma}{2}\right) - wF^*_{\mathrm{sh}}\left(\frac{\gamma}{2}\right)\cos\frac{\gamma}{2}\right) \tag{4}$$

The former analysis is the most widely used to normalized bias extension results although it was conceived, in principle, only for rate-independent materials.

One of the few alternatives available for rate-dependent materials was proposed by Harrison et al. [6]. Based also on power dissipation considerations they introduced the following expression:

$$F_{\text{sh}}^{*}(\gamma) = \frac{\left(\frac{h}{w} - 1\right)}{2\frac{h}{w} - 3 + 2X} \frac{F}{\frac{\sqrt{2}w}{2}} \tag{5}$$

where X is a function exclusively of the shear angle [6] if the material is considered as a constrained Newtonian fluid. This assumption obviously introduces some error but it can avoid an artificial drop of the shear force obtained when using the expression for rate-independent materials [11].

Published works show a certain preference of researchers for the bias extension test over the picture frame when investigating the shear behaviour of woven and woven-reinforced composites. Regarding the shear force determination in the bias extension test, most works prefer the rate-independent relationship of Eq. (4). This equation has shown satisfactory results even when applied to rate dependent thermoplastic composites [14, 15].

2.2 In-Plane Tensile

Tensile stiffness is considerably higher than in-plane and out-of-plane shear stiffness. Buet-Gautier and Boisse [16] analysed biaxial tensile behaviour of glass fibre longitudinal-to-transversal strain ratios. Similar set-up was used by Xue et al. in [7]. The undulations of the yarns in a woven material lead to strong nonlinearities especially at low loads. It has been shown experimentally that the tensile behaviour shows almost no dependence on the shear angle [16]. Biaxial as well as uniaxial textile testing of fabrics is done mainly by state-of-the-art and non-standardized characterization methods, which are still under development [17]. This mode is, however, often not studied in detail as the strains in fibre direction are relatively small during forming.

2.3 Out-of-Plane Bending

Bending behaviour plays an important role in the development of wrinkle during forming [18]. Traditionally two standard tests were available to determine the bending stiffness of fabrics: cantilever bending test [19] and Kawabata bending test [20]. The principle of the cantilever test is shown in Fig. 2. The length L of the specimen hanging under the action of the gravity is registered when the angle α reaches a specific value. However, these tests have been developed for clothing textiles and are not well adapted to textile reinforcement and much less to woven composites which are much thicker and stiffer. Recently, Liang et al. [21] developed a new cantilever test performed in a temperature chamber. The position of every

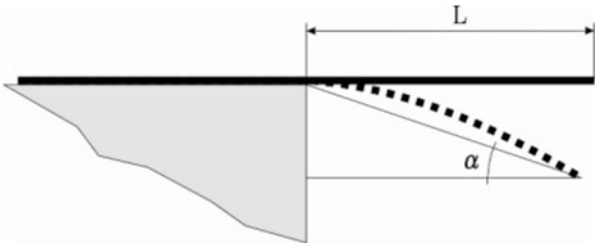

Fig. 2 Cantilever bending test. Deformed sheet is shown as a *dotted line*

point of the sample is measured with an optical measuring system. The moment at each point is calculated considering the gravitational force acting at the local section and is correlated with the local curvature. In order to extend the range of curvatures obtained in the test, they carried out tests with a lump mass at the free end of the sample. It is found that the deflection increases strongly with temperature until a limit value is reached. At this temperature the resin is entirely molten and the bending stiffness practically equal to that of the fabric.

3 Constitutive Modelling

3.1 Kinematic Models

The simplest approach to simulate draping/forming consists of using kinematic models [22]. These models are basically mapping algorithms where the material is considered as a pin-jointed net with inextensible yarns. This means that the yarns can rotate freely at each intersection point but they do not change in length. Kinematic models provide a fast solution in several cases but since forces are not involved they cannot evaluate the effect of different holder systems and fail when predicting fibre orientation in unsymmetrical moulds [23].

3.2 Mechanics-Based Models

Mechanics-based approaches, despite being more time-consuming, can take into account all relevant aspects of the material constitutive behaviour. Mesoscopic or semi-discrete approaches [24] analyse the woven mechanical behaviour at the scale of a woven unit cell and this behaviour is implemented in finite elements composed by unit cells. On the contrary, continuous approaches [14, 15] discretize the material as a homogeneous medium using shell or membranes elements. Continuous models are usually preferred because they can be easily applied to standard finite elements.

Rate constitutive equations have been adopted in continuous models which describe dry woven [25] and woven-reinforced composites [14]. In such models

the relationship between an objective derivative of the Cauchy stress $\boldsymbol{\sigma}^{\nabla}$ and the strain rate $\mathbf{D}$ is given by a constitutive tensor ${}^{4}\mathbb{C}$ as follows:

$$\boldsymbol{\sigma}^{\nabla} = {}^{4}\mathbb{C} : \mathbf{D} \tag{6}$$

Most FE-codes consider an objective derivative of the stress based on the material rotation. Badel et al. [25] demonstrated that this can produce spurious stresses in some cases and introduced an objective derivative based on the warp and weft yarns rotation. This model was later extended in [14] to include strain rate dependence. In order to highlight the importance of following the yarns rotation and the use of a non-orthogonal formulation, Fig. 3 compares simulation results using the non-orthogonal model of [14] (Fig. 3b) and its orthogonal variant (Fig. 3c) with experimental results (Fig. 3a). It can be seen that neither the shear angle distribution nor the shear angle value in the pure shear region is well reproduced if an orthogonal formulation is used.

Woven composites present a complex nonlinear rate and temperature dependence. This, however, is usually attributed in the models only to the shear behaviour since tensile behaviour is dictated by fibres which are not viscous and bending stiffness is usually neglected or estimated by trial-and-error procedures. Guzman-Maldonado et al. [15] and Machado et al. [14] are within the few who detailed studied the shear stiffness for the specific case of the woven-reinforced thermoplastic-matrix composites.

Recent works indicate that the bending stiffness influences the shape of the wrinkles in a forming simulation but the results available on bending properties of thermoplastic pre-pregs are scarce. Consequently, the viscous character of the out-of-plane stiffness is usually neglected and focus is placed on the shear modelling.

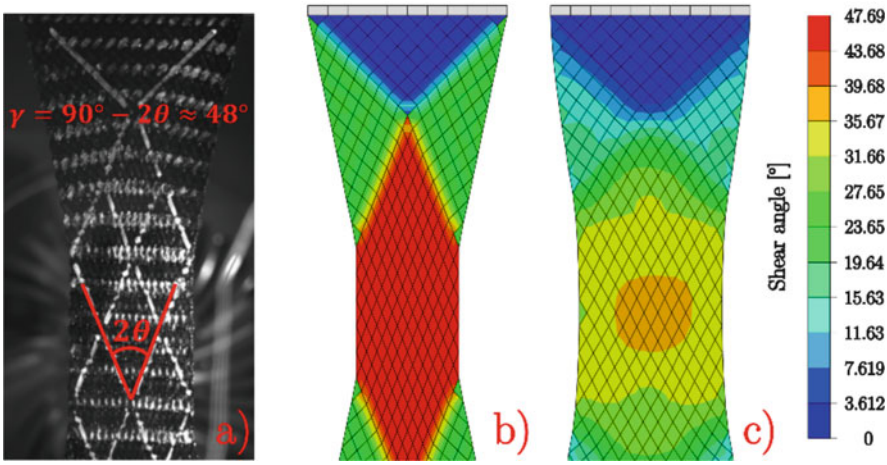

Fig. 3 Comparison between bias extension test and simulation results at same axial displacement. (**a**) Experiment, (**b**) simulation (non-orthogonal model), (**c**) simulation (orthogonal)

4 Validation

Validation experiments are usually performed on hemispherical shapes or extended hemispherical geometries which lead to large shear angles (up to $\approx 50°$). Identifying the fibre orientation after a forming/draping can be a challenging task. The change in the angle between the warp and the weft was measured using a parallel reference pattern in [23]. In [14, 26] points as grid markers are used as in traditional grid strain analysis performed in metal forming industry. In all cases, the main challenges are the misalignment of the applied pattern with respect to the actual fibre direction and the destruction of the pattern during the forming due to friction with the tools.

5 Outlook

A brief review of the state-of-the-art methods regarding characterization and modelling of woven-reinforced composites was presented. Viscous behaviour (rate and temperature dependence) and nonlinearities are usually attributed to the shear behaviour in current modelling trends. Efforts towards a more detailed bending behaviour are possibly the future challenge to be addressed in this field.

Acknowledgements Financial support by the Austrian Federal Government for research and development in the framework of the Austrian Competence Headquarter Program operated by ENGEL AUSTRIA GmbH is gratefully acknowledged.

References

1. Plotkin SE (2009) Examining fuel economy and carbon standards for light vehicles. Energy Policy 37:3843–3853. doi:10.1016/j.enpol.2009.07.013
2. Golzar M, Poorzeinolabedin M (2009) Prototype fabrication of a composite automobile body based on integrated structure. Int J Adv Manuf Technol 49:1037–1045. doi:10.1007/s00170-009-2452-6
3. Machado M, Fischlschweiger M, Major Z (2015) Strength of single-lap-joint assemblies of continuous unidirectional carbon fibre-reinforced thermoplastic matrix tapes under tensile loading. J Compos Mater 49:1977–1987. doi:10.1177/0021998314541308
4. Harrison P, Clifford MJ, Long AC (2004) Shear characterisation of viscous woven textile composites: a comparison between picture frame and bias extension experiments. Compos Sci Technol 64:1453–1465. doi:10.1016/j.compscitech.2003.10.015
5. Willems A, Lomov SV, Verpoest I, Vandepitte D (2008) Optical strain fields in shear and tensile testing of textile reinforcements. Compos Sci Technol 68:807–819. doi:10.1016/j.compscitech.2007.08.018
6. Lahey TJ, Heppler GR (2004) Mechanical modeling of fabrics in bending. J Appl Mech 71:32–40. doi:10.1115/1.1629757
7. Xue P, Peng X, Cao J (2003) A non-orthogonal constitutive model for characterizing woven composites. Compos Part A Appl Sci Manuf 34:183–193. doi:10.1016/S1359-835X(02)00052-0

8. Sam Huang H (2015) Influence of phase shift on the responses of woven laminated composites. Compos Struct 130:143–154. doi:10.1016/j.compstruct.2015.04.008
9. Cao J, Akkerman R, Boisse P et al (2008) Characterization of mechanical behavior of woven fabrics: experimental methods and benchmark results. Compos Part A Appl Sci Manuf 39:1037–1053. doi:10.1016/j.compositesa.2008.02.016
10. Pierce RS, Falzon BG, Thompson MC, Boman R (2014) Implementation of a non-orthogonal constitutive model for the finite element simulation of textile composite draping. Appl Mech Mater 553:76–81. doi:10.4028/www.scientific.net/AMM.553.76
11. Härtel F, Harrison P (2014) Evaluation of normalisation methods for uniaxial bias extension tests on engineering fabrics. Compos Part A Appl Sci Manuf 67:61–69. doi:10.1016/j.compositesa.2014.08.011
12. Harrison P, Härtel F (2016) Erratum to Evaluation of normalisation methods for uniaxial bias extension tests on engineering fabrics. Compos Part A Appl Sci Manuf 80:104–106. doi:10.1016/j.compositesa.2015.10.013
13. Hivet G, Duong AV (2010) A contribution to the analysis of the intrinsic shear behavior of fabrics. J Compos Mater 45:695–716. doi:10.1177/0021998310382315
14. Machado M, Fischlschweiger M, Major Z (2016) A rate-dependent non-orthogonal constitutive model for describing shear behaviour of woven reinforced thermoplastic composites. Compos Part A Appl Sci Manuf 80:194–203. doi:10.1016/j.compositesa.2015.10.028
15. Guzman-Maldonado E, Hamila N, Boisse P, Bikard J (2015) Thermomechanical analysis, modelling and simulation of the forming of pre-impregnated thermoplastics composites. Compos Part A Appl Sci Manuf 78:211–222. doi:10.1016/j.compositesa.2015.08.017
16. Buet-Gautier K, Boisse P (2001) Experimental analysis and modeling of biaxial mechanical behavior of woven composite reinforcements. Exp Mech 41:260–269. doi:10.1007/BF02323143
17. Gereke T, Döbrich O, Hübner M, Cherif C (2013) Experimental and computational composite textile reinforcement forming: a review. Compos Part A Appl Sci Manuf 46:1–10. doi:10.1016/j.compositesa.2012.10.004
18. Boisse P, Hamila N, Vidal-Sallé E, Dumont F (2011) Simulation of wrinkling during textile composite reinforcement forming. Influence of tensile, in-plane shear and bending stiffnesses. Compos Sci Technol 71:683–692. doi:10.1016/j.compscitech.2011.01.011
19. de Bilbao E, Soulat D, Hivet G, Gasser A (2010) Experimental Study of Bending Behaviour of Reinforcements. Exp Mech 50:333–351. doi:10.1007/s11340-009-9234-9
20. Kawabata S (1980) The standardization and analysis of hand evaluation second edition (HESC). The Textile Machinery Society of Japan, Osaka
21. Liang B, Hamila N, Peillon M, Boisse P (2014) Analysis of thermoplastic prepreg bending stiffness during manufacturing and of its influence on wrinkling simulations. Compos Part A Appl Sci Manuf 67:111–122. doi:10.1016/j.compositesa.2014.08.020
22. Sharma SB, Potluri P, Porat I (1999) Moulding analysis of 3D woven composite preforms: mapping algorithms. In: Proceedings of 12th international conference on composite materials
23. Vanclooster K, Lomov SV, Verpoest I (2009) Experimental validation of forming simulations of fabric reinforced polymers using an unsymmetrical mould configuration. Compos Part A Appl Sci Manuf 40:530–539. doi:10.1016/j.compositesa.2009.02.005
24. Hamila N, Boisse P (2008) Simulations of textile composite reinforcement draping using a new semi-discrete three node finite element. Compos Part B Eng 39:999–1010. doi:10.1016/j.compositesb.2007.11.008
25. Badel P, Gauthier S, Vidal-Salle E, Boisse P (2009) Rate constitutive equations for computational analyses of textile composite reinforcement mechanical behaviour during forming. Compos Part A Appl Sci Manuf 40:997–1007. doi:10.1016/j.compositesa.2008.04.015
26. Ritt R, Machado M, Fischlschweiger M et al (2015) An inverse finite element approach to calculate full-field forming strains. Key Eng Mater 651–653:363–368

Model Predictive Temperature Control of a Distribution System for Chemicals

S. Koch, M. Ponikvar, M. Steinberger, and M. Horn

Abstract In semiconductor manufacturing tight temperature control of chemicals is crucial for meeting clean application requirements. The use of multiple chemistries as well as various configuration options makes precise temperature control a challenging task. In this paper a generic solution for the temperature control in a single wafer manufacturing machinery for wet-chemical processing based on a model predictive control technique is presented. The developed control strategy is implemented and evaluated on a real world unit with realistic wafer cleaning recipes.

1 Introduction

Shrinking sizes, higher integration densities and more complex structures in semiconductor devices steadily increase the demands placed on single wafer processing equipment. The fast technological progress calls particularly for advanced wafer wet-chemical etching tools. Wet-chemical processing of wafers is a crucial step that has to be repeated several times during semiconductor manufacturing. The process result depends on a wide number of machine parameters and process variables such as the rotational speed of the wafer, the flow rate and pressure of the chemical fluid and its temperature [5, 8].

The control of such process variables mainly relies on linear feedback controllers like PID control [1]. However, rising demands toward the accuracy and precision as well as the support of flexible processing recipes makes the accurate chemistry control a challenging task. On the other hand, the increasing available computational power allows the implementation of advanced control strategies. In this article the

S. Koch (✉) • M. Steinberger • M. Horn
Institute of Automation and Control, Graz University of Technology, Inffeldgasse 21/B/I, 8010 Graz, Austria
e-mail: stefan.koch@tugraz.at

M. Ponikvar
Lam Research AG, SEZ-Straße 1, 9500 Villach, Austria
e-mail: matija.ponikvar@lamresearch.com

H. Irschik et al. (eds.), *Dynamics and Control of Advanced Structures and Machines*, DOI 10.1007/978-3-319-43080-5_12

design of a model predictive control (MPC) scheme for temperature stabilization in a chemical distribution system of a semiconductor fabrication tool is discussed.

The remainder of this paper is organized as follows: Sect. 2 provides an overview of the considered chemical distribution system. A mathematical model is presented, followed by the controller design in Sect. 3. The implementation and performance of the developed controller is discussed based on experimental data in Sect. 4.

2 Plant Description and Mathematical System Model

A process flow diagram of the chemical distribution system is shown in Fig. 1. The wafer processing takes place in individual process chambers. The number of active chambers varies during operation. If no chamber is active, the fluid circulates from the tank through the heater and back to the tank. In case of the so-called low temperature processes an additional cooler, which is connected to the "optional" branch, compensates for heat transfer introduced from the surrounding. As soon as processing starts, the fluid is routed into a particular chamber and afterwards either reused, i.e., fed back to the tank ("reclaim mode") or drained ("single pass mode"). In the latter case the tank level has to be frequently refilled with fresh media as soon as the filling level drops below a specified threshold. This procedure is called "tank top-up". Depending on the specific cleaning application the tool may be equipped with different components, e.g., heater, cooler and tanks.

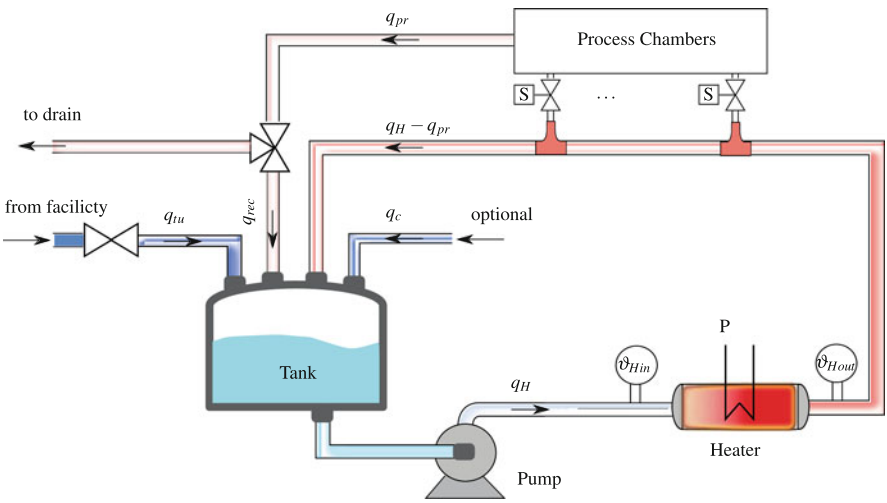

Fig. 1 Process flow diagram of the chemical distribution system of the considered single wafer cleaning tool. The diagram illustrates the routing of the chemical fluid and provides an overview of the main components

Assuming spatially uniform temperatures a simplified mathematical model of the heater can be obtained by using the so-called method of lumped capacitance leading to a first order time delay system of the form

$$\frac{\mathrm{d}\Delta\vartheta}{\mathrm{d}t} = -\frac{1}{\tau_H}\Delta\vartheta + \frac{K_H}{\tau_H}P(t-D), \quad \vartheta_{H\mathrm{out}} = \Delta\vartheta + \vartheta_{H\mathrm{in}} \tag{1}$$

where the parameter K_H is the thermal gain, τ_H the thermal time constant. Both parameters depend on the mass flow rate, the specific heat capacity and the density of the chemical fluid as well as the heater volume. According to Fig. 1 $y_H := \vartheta_{H\mathrm{out}}$ represents the heater outlet temperature which is the variable to be controlled. The heater inlet temperature is represented by $d := \vartheta_{H\mathrm{in}}$ and can be considered as disturbance acting directly on the output temperature. Both are available from measurements. The actuating signal $u := P$ is the electrical power supplied to the heater. An in-depth analysis of such a heater is carried out in [3]. Under sampling the linear system (1) can be written in the discrete time state-space form:

$$\begin{aligned} \boldsymbol{x}_{H,k+1} &= \left[\begin{array}{c|c} e^{-\frac{T_s}{\tau_H}} & \mathbf{0}_{1\times n_z} \\ \hline \boldsymbol{I}_{n_z\times n_z} & \mathbf{0}_{n_z\times 1} \end{array}\right]\boldsymbol{x}_{H,k} + \left[\begin{array}{c} \mathbf{0}_{n_z\times 1} \\ \hline 1 \end{array}\right]u_k \\ y_{H,k} &= \left[\mathbf{0}_{n_z\times 1} \; -(e^{-\frac{T_s}{\tau_H}}-1)K_H\right]\boldsymbol{x}_{H,k} + d_k. \end{aligned} \tag{2}$$

The time delay is taken into account as multiples of the sampling time (T_s) where k denotes the sampling instant, i.e., $t = kT_s$. The system order increases to $N = 1+n_z$ with $n_z = \lceil \frac{D}{T_s} \rceil$. The mathematical model of the heater is compared to measured data in Fig. 2.

In a similar way a dynamic model of the tank can be derived. Applying first law of thermodynamics for heat transfer problems gives

$$\frac{\mathrm{d}}{\mathrm{d}t}(V_T\vartheta_{H\mathrm{in}})\rho C_p = \rho C_p\left(\sum_{i=1}^{r} q_{\mathrm{in}_i}\vartheta_{T\mathrm{in}_i} - \vartheta_{H\mathrm{in}}q_H\right)$$

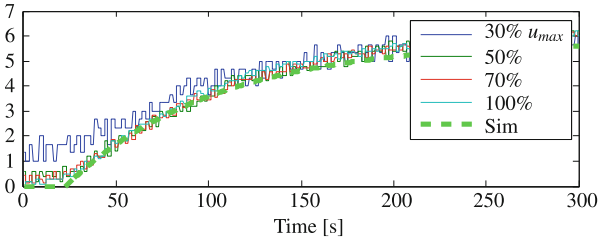

Fig. 2 Normalized step response of system model (2) compared to experimental data. The model parameters, obtained from the measured step response, are $\tau_H \approx 80\,\mathrm{s}$, $K_H \approx 0.06$ and $D \approx 25\,\mathrm{s}$

which eventually leads to the second order model

$$\frac{\mathrm{d}V_T}{\mathrm{d}t} = \sum_{i=1}^{r} q_{\mathrm{in}_i} - q_H, \quad \frac{\mathrm{d}\vartheta_{H\mathrm{in}}}{\mathrm{d}t} = -\frac{1}{V_T}\sum_{i=1}^{r} q_{\mathrm{in}_i}\vartheta_{H\mathrm{in}} - \frac{1}{V_T}\sum_{i=1}^{r} q_{\mathrm{in}_i}\vartheta_{T\mathrm{in}_i} \tag{3}$$

In the above equations ρ denotes the density and C_p the specific heat capacity of the chemical solvent which are assumed to be constant. The quantity q_i denotes the volumetric flow rate of the various flows entering the tank. As indicated in the process diagram in Fig. 1, the number of flows depends on the specific tool configuration as well as the processing recipe. The flow rate q_H is the pump supply rate, i.e., the overall flow supplied to the system. The filling capacity of the tank is denoted by V_T. A discrete time version of the model (3) can be obtained by applying *Euler* forward discretization:

$$V_{T,k+1} = V_{T,k} + T_s\left(\sum_{i=1}^{r} q_{\mathrm{in}_i,k} - q_{H,k}\right) \tag{4}$$

$$\vartheta_{H\mathrm{in},k+1} = \underbrace{\left(1 - T_s\frac{1}{V_{T,k}}\sum_{i=1}^{r} q_{\mathrm{in}_i,k}\right)}_{\phi_{d,k}}\vartheta_{H\mathrm{in},k} - \underbrace{T_s\frac{1}{V_{T,k}}}_{\gamma_{d,k}}\underbrace{\sum_{i=1}^{r} q_{\mathrm{in}_i,k}\vartheta_{T\mathrm{in}_i,k}}_{w_k}. \tag{5}$$

The input w_k is separated into flows entering the tank with temperature $\vartheta_{H\mathrm{out}}$, which is the overall flow supplied by the pump less the flow routed to the process chambers, i.e., $(q_H - q_{\mathrm{Pr}})$, and flows with arbitrary temperature like top-up-, reclaimed- and cooler-media flow which are summarized by the quantity ψ_k, i.e.,

$$w_k = (q_H - q_{\mathrm{Pr}})\vartheta_{H\mathrm{out},k} + \psi_k.$$

Combining the discrete time heater model (2) and the tank (5) leads to the following discrete linear time-varying system in state-space representation:

$$\boldsymbol{x}_{k+1} = \underbrace{\left[\begin{array}{c:c} \boldsymbol{\Phi}_H & \mathbf{0}_{N+1\times 1} \\ (q_H - q_{\mathrm{Pr}})\gamma_{d,k}\boldsymbol{c}_H^T & \phi_{d,k} + \gamma_{d,k}(q_H - q_{\mathrm{Pr}}) \end{array}\right]}_{\boldsymbol{\Phi}_k}\boldsymbol{x}_k + \underbrace{\left[\begin{array}{c} \boldsymbol{\Gamma}_H \\ 0 \end{array}\right]}_{\boldsymbol{\Gamma}} u_k + \underbrace{\left[\begin{array}{c} \mathbf{0}_{N+1\times 1} \\ \gamma_{d,k} \end{array}\right]}_{\boldsymbol{\Gamma}_{d,k}}\psi_k$$

$$y_k = \underbrace{\left[\boldsymbol{c}_H^T\ 1\right]}_{\boldsymbol{c}^T}\left[\begin{array}{c} \boldsymbol{x}_{H,k} \\ d_k \end{array}\right]$$

with the augmented state vector $\boldsymbol{x}_k = [\boldsymbol{x}_{H,k} \quad d_k]^T$.

3 Controller Design

A model predictive controller is designed based on the mathematical system description developed in Sect. 2.

In order to achieve offset free reference temperature tracking the following integral cost function, discussed in, e.g., [4], is considered

$$\mathscr{J}(\Delta\bar{\boldsymbol{u}}_k) = \|\bar{\boldsymbol{y}}_{k+1} - \bar{\boldsymbol{r}}_{k+1}\|_{\boldsymbol{Q}}^2 + \|\Delta\bar{\boldsymbol{u}}_k\|_{\boldsymbol{R}}^2 + \|\bar{\boldsymbol{z}}_{k+1}\|_{\boldsymbol{S}}^2 \tag{6}$$

where $\boldsymbol{Q}$, $\boldsymbol{R}$, $\boldsymbol{S}$ are appropriately chosen weighting matrices. The predicted output is defined by $\bar{\boldsymbol{y}}_{k+1} = \begin{bmatrix} y_{k+1} & y_{k+2} & \dots & y_{k+np} \end{bmatrix}^T$, respectively, the reference trajectory $\bar{\boldsymbol{r}}_{k+1} = \begin{bmatrix} r_{k+1} & r_{k+2} & \dots & r_{k+np} \end{bmatrix}^T$ and the input $\Delta\bar{\boldsymbol{u}}_k = \begin{bmatrix} \Delta u_k & \Delta u_{k+1} & \dots & \Delta u_{k+nc-1} \end{bmatrix}^T$ with $\Delta u_k = u_k - u_{k-1}$. The indices n_p and n_c represent the prediction and control horizon. The integral state vector is defined by

$$\bar{\boldsymbol{z}}_{k+1} = \begin{bmatrix} z_{k+1} & z_{k+2} & \dots & z_{k+np} \end{bmatrix}^T, \quad \text{where} \quad z_k = z_{k-1} + r_{k-1} - y_{k-1}.$$

It is obtained by

$$\bar{\boldsymbol{z}}_{k+1} = \boldsymbol{M}(z_k + r_k - y_k) + \boldsymbol{N}(\bar{\boldsymbol{r}}_{k+1} - \bar{\boldsymbol{y}}_{k+1}), \quad \text{with} \quad \boldsymbol{N} = \begin{bmatrix} 0 & 0 & \dots & 0 \\ 1 & 0 & \dots & 0 \\ \vdots & \vdots & \ddots & \vdots \\ 1 & 1 & \dots & 1 \end{bmatrix}, \quad \boldsymbol{M} = \begin{bmatrix} 1 \\ 1 \\ \vdots \\ 1 \end{bmatrix}.$$

According to the Receding Horizon MPC formulation (see, e.g., [2]) the predicted system output is

$$\bar{\boldsymbol{y}}_{k+1} = \boldsymbol{F}_k\boldsymbol{x}_k + \boldsymbol{G}_k u_{k-1} + \boldsymbol{H}_k\Delta\bar{\boldsymbol{u}}_k + \boldsymbol{H}_{dk}\bar{\boldsymbol{\psi}}_k$$

where

$$\boldsymbol{H}_{dk} = \begin{bmatrix} \boldsymbol{c}^T\boldsymbol{\Gamma}_{dk} & 0 & \dots & 0 \\ \vdots & & \dots & \vdots \\ \boldsymbol{c}^T\boldsymbol{\Phi}_k^{np-1}\boldsymbol{\Gamma}_{dk} & \boldsymbol{c}^T\boldsymbol{\Phi}_k^{np-2}\boldsymbol{\Gamma}_{dk} & \dots & \boldsymbol{c}^T\boldsymbol{\Gamma}_{dk} \end{bmatrix}.$$

In order to formulate the optimization problem in a compact way the vectors $\bar{\boldsymbol{g}}_k^* := \boldsymbol{F}_k\boldsymbol{x}_k + \boldsymbol{G}_k u_{k-1} + \boldsymbol{H}_{dk}\bar{\boldsymbol{\psi}}_k$ and $\bar{\boldsymbol{e}}_k := \bar{\boldsymbol{g}}_k^* - \bar{\boldsymbol{r}}_{k+1}$ are introduced.

In the design it is also necessary to consider two hard constraints. The control input is limited within 0–100 % and the temperature is not allowed to exceed an upper limit. The limit depends heavily on the used chemical solvent and the process

recipe. Incorporating these two constraints in the control problem leads to the optimization problem:

Minimize

$$\mathscr{J}(\Delta\bar{\boldsymbol{u}}_k) = 2\Delta\bar{\boldsymbol{u}}_k\boldsymbol{H}_k^T\tilde{\boldsymbol{Q}}\bar{\boldsymbol{e}}_k + \Delta\bar{\boldsymbol{u}}_k^T(\boldsymbol{H}_k^T\tilde{\boldsymbol{Q}}\boldsymbol{H}_k + \boldsymbol{R})\Delta\bar{\boldsymbol{u}}_k - 2\Delta\bar{\boldsymbol{u}}_k\boldsymbol{H}_k^T\boldsymbol{N}^T\boldsymbol{S}\boldsymbol{M}(z_k + r_k - y_k)$$

subject to

$$\boldsymbol{W}\Delta\bar{\boldsymbol{u}}_k \leq \bar{\boldsymbol{w}} \tag{7}$$

where $\tilde{\boldsymbol{Q}} := \boldsymbol{N}^T\boldsymbol{S}\boldsymbol{N} + \boldsymbol{Q}$ and

$$\boldsymbol{W} = \begin{bmatrix} -\boldsymbol{L} \\ \boldsymbol{L} \\ -\boldsymbol{H}_k \\ \boldsymbol{H}_k \end{bmatrix}, \qquad \bar{\boldsymbol{w}} = \begin{bmatrix} -\bar{\boldsymbol{u}}^{\min} + \boldsymbol{M}u_{k-1} \\ \bar{\boldsymbol{u}}^{\max} - \boldsymbol{M}u_{k-1} \\ -\bar{\boldsymbol{y}}^{\min} + \boldsymbol{g}_k^* \\ \bar{\boldsymbol{y}}^{\max} - \boldsymbol{g}_k^* \end{bmatrix}, \quad \boldsymbol{L} = \begin{bmatrix} 1 & 0 & \dots & 0 \\ 1 & 1 & \dots & 0 \\ \vdots & \vdots & \ddots & \vdots \\ 1 & 1 & \dots & 1 \end{bmatrix}.$$

The solution to this problem yields an optimal control sequence. The first value of the obtained vector is applied to the plant.

It should be noted that the solution of (7) requires a prediction of the disturbance vector $\bar{\boldsymbol{\psi}}_k$. Due to the comprehensive knowledge of the future evolution of the process and the available mathematical models a model based prediction of the disturbance is proposed in the present case. Its computation basically breaks down into two phases:

1. The predictive information on processing flows, tank filling flows and tank volume is provided on the basis of the predefined processing recipe:

   A typical processing characteristic is, e.g., shown in the lowest plot in Fig. 3. The black line represents the cumulative flow into the process chambers. The stepwise increasing or decreasing of the flow indicates an on/off switching of individual process chambers. As an example the green line shows the predicted values 10 s ahead. The gray pulses illustrate the frequently appearing tank top-up flow, the yellow one is the predicted value.
2. The calculation of the reclaimed chemistry temperature and the estimation of the cooler outlet temperature:

   The reclaim temperature is estimated, respectively, predicted depending on the processing temperatures, processing flows, wafer rotational speed and ambient temperature [7]. The estimated value is assumed to remain constant during processing. The cooler outlet temperature is predicted based on a dynamic model, see, e.g., [6].

4 Implementation and Experimental Results

The developed controller is implemented with a sampling time of $T_s = 1\,\text{s}$. The optimization problem is solved online using *Hildreth's* quadratic programming procedure [9]. The prediction horizon is set to $n_p = 60\,\text{s}$, the control horizon to $n_c = 5\,\text{s}$.

The MPC performance is compared to the currently used PID controller. Therefore two test runs with deionized water have been performed on the real tool. In the first configuration a low temperature single pass recipe was tested. As mentioned, in this mode it is necessary to frequently refill the tank. The scenario is depicted in Fig. 3 in the two bottom plots. The second last shows the tank volume over time. The last plot shows the tank refilling flow and the cumulative flow into the process chambers with its predicted values as discussed in the previous section. The plot on the top shows the temperature to be controlled, the second the tank temperature followed by the heater power. Due to confidentiality agreements all values are normalized, i.e., set-point temperature equals $r_k = 1$. The second test is a high temperature process to reclaim recipe. The tank level remains approximately constant on its initial filling level. The disturbance is mainly caused by heat

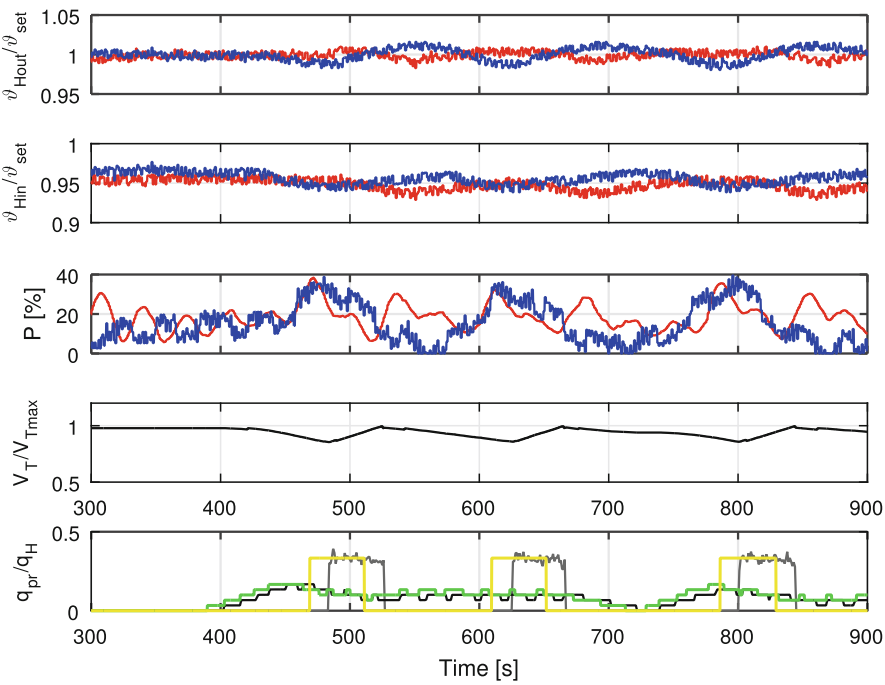

Fig. 3 Comparison of *red line* MPC and *blue line* PID controller performance during a low temperature single pass recipe

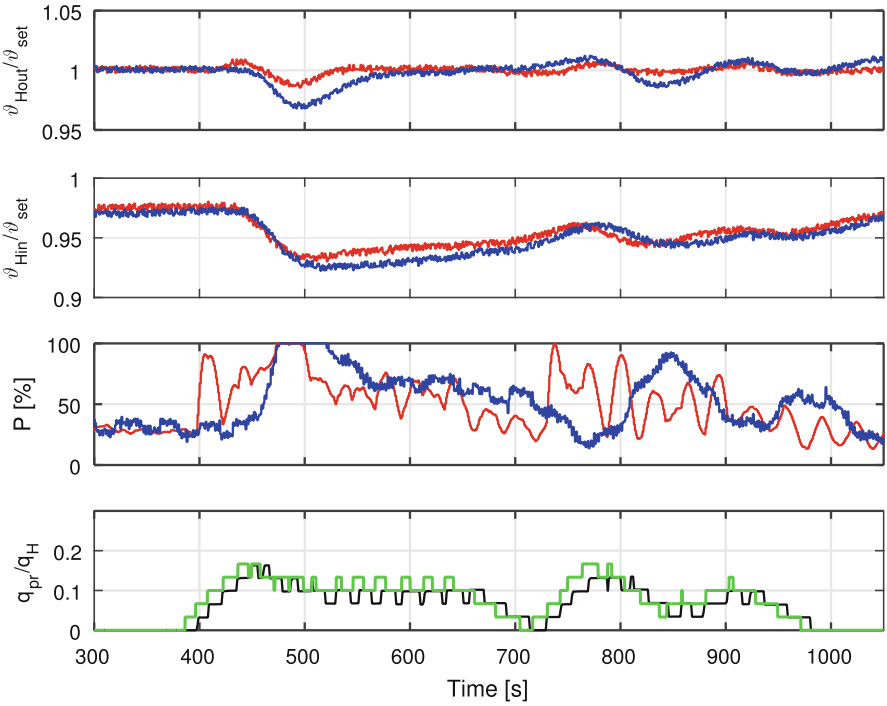

Fig. 4 Comparison of *red line* MPC and *blue line* PID controller performance during high temperature process to reclaim recipe

dissipation in the process chambers leading to larger temperature differences in the reclaim flow compared to the first test. The results are presented in Fig. 4.

In both cases it can be seen that the MPC outperforms the PID controller. The MPC can provide temperature stabilization within $\pm 1.5\,\%$ of the set-point temperature. Especially in the high temperature test it can be observed, when comparing the two control signals at time instant $t \approx 400\,\mathrm{s}$ or $t \approx 700\,\mathrm{s}$, that the MPC controller starts to counteract the disturbance way earlier than the PID controller leading to significant smaller temperature losses.

5 Conclusion and Outlook

In this paper a model predictive control approach was applied to a single wafer cleaning tool for temperature stabilization of chemical fluids. The performance of the developed controller has been evaluated via test runs on the real unit with realistic processing recipes. It has been shown that the developed controller offers significantly improved temperature stabilization compared to a classical linear

feedback control and thus ensures high repeatability of process recipes. The model based approach allows for configuring the controller for various available tool options.

Future work will focus on the performance evaluation of the developed controller in various tool configurations, i.e., combinations of different heaters, coolers and tank types. Furthermore the incorporation of active cooler control in the design leading to a multi-input/single-output system will be approached.

References

1. Emami-Naeini A, Ebert J, Kosut R, de Roover D, Ghosal S (2004) Model-based control for semiconductor and advanced materials processing: an overview. In: American control conference, 2004. Proceedings of the 2004, vol. 5, June 2004, pp 3902–3909
2. Maciejowski J (2002) Predictive control - with constraints. Pearson Education, Amsterdam
3. Mimura K, Shiotsuki T (2007). Temperature control of deionized (DI) water heater by combination of PID control and modern control theory. In: ICM2007 4th IEEE international conference on mechatronics, May 2007, pp 1–5
4. Peek CS (2008) High performance control theory, design and applications. Dissertation, University of Florida
5. Reinhardt KA, Reidy RF (2011) Handbook for cleaning for semiconductor manufacturing - fundamentals and applications. Wiley, New York.
6. Sarkar PK (2014) Advanced process dynamics and control. PHI Learning Pvt. Ltd., New Delhi
7. Shevchuk IV (2009) Convective heat and mass transfer in rotating disk systems, aufl. edition. Springer Science & Business Media, Berlin, Heidelberg
8. Staudegger F, Hofbaur MW, Kruwinus H-J (2009) Analyses and modeling of a wet-chemical-etch process on rotating silicon wafers with an impinging etchant jet. J Electrochem Soc 156(5):H340–H345 .
9. Wang L (2009) Model predictive control system design and implementation using MATLAB, 2009 edition. Springer Science & Business Media, Berlin, Heidelberg

Hidden Oscillations in Electromechanical Systems

Maria Kiseleva, Natalya Kondratyeva, Nikolay Kuznetsov, and Gennady Leonov

Abstract In this paper an electromechanical system with two different types of motor is considered. It is shown that during the spin-up, the system with DC motor may experience unwanted vibration—the *Sommerfeld effect*. This is a well-known effect when the motor of electromechanical system gets stuck near the resonance zone instead of reaching its nominal power. The absence of this effect is demonstrated in the system with synchronous motor. Nowadays, there are many works devoted to the study of this effect in various systems. Here we discuss the Sommerfeld effect from the point of view of localization of the so-called *hidden oscillations.*

1 Introduction

In order to obtain a well-operating electromechanical system, it is important to perform the stability and oscillation analysis of its corresponding mathematical model. An oscillation in a dynamical system is either self-excited or hidden attractor [7, 8, 10, 11]. An attractor is called a *hidden attractor* if its basin of attraction does not intersect with small neighborhoods of equilibria, otherwise, it is called a *self-excited attractor*. The basin of attraction of self-excited attractor is associated with

M. Kiseleva (✉)
St. Petersburg State University, St. Petersburg, Russia
e-mail: m.kiseleva@spbu.ru

N. Kondratyeva
St. Petersburg State University, St. Petersburg, Russia

St. Petersburg Polytechnic University, St. Petersburg, Russia

N. Kuznetsov
St. Petersburg State University, St. Petersburg, Russia

University of Jyväskylä, Jyväskylä, Finland
e-mail: nkuznetsov239@gmail.com

G. Leonov
St. Petersburg State University, St. Petersburg, Russia

Institute of Problems of Mechanical Engineering, RAS, St. Petersburg, Russia

H. Irschik et al. (eds.), *Dynamics and Control of Advanced Structures and Machines*, DOI 10.1007/978-3-319-43080-5_13

an unstable equilibrium. In other words, the self-excited attractors can be localized numerically by the following *standard computational procedure:* a trajectory, which starts from a point of an unstable manifold in a neighborhood of an unstable equilibrium, after a transient process is attracted to the state of oscillation and traces it. In contrast, hidden attractor's basin of attraction is not associated with unstable equilibria. Recent examples of hidden attractors can be found in *The European Physical Journal Special Topics: Multistability: Uncovering Hidden Attractors*, 2015 (see [2, 4–6, 12–16, 18–20]).

Hidden oscillations appear naturally in systems without equilibria, describing various mechanical and electromechanical models with rotation. In 1902 Arnold Sommerfeld described one of the first examples of such models [17]. He studied vibrations caused by a motor actuating on unbalanced rotor and discovered the resonance capture phenomenon (Sommerfeld effect). Discussing the nature of this capture phenomenon, Sommerfeld wrote: "*This experiment corresponds roughly to the case in which a factory owner has a machine set on a poor foundation running at 30 horsepower. He achieves an effective level of just 1/3, however, because only 10 horsepower are doing useful work, while 20 horsepower are transferred to the foundational masonry*" [3].

Further we will consider mechanical model actuated by DC motor, where the Sommerfeld effect corresponds to the existence of hidden oscillation. We will also demonstrate when Sommerfeld effect is absent for the same model actuated by synchronous motor.

2 Unbalanced Rotor on a Rigid Platform

Following the work [1], we consider the first electromechanical system, which is unbalanced rotor placed on a rigid platform. The platform can move only horizontally and is connected to a wall by means of damping and elastic elements (see Fig. 1). The system of equations of motion is the following:

$$\begin{aligned} J\ddot{\varphi} &= \mathscr{G}(\dot{\varphi}) + m_0 l\ddot{x}\sin\varphi, \\ (M+m_0)\ddot{x} + \beta\dot{x} + cx &= m_0 l\left(\dot{\varphi}^2\cos\varphi + \ddot{\varphi}\sin\varphi\right). \end{aligned} \tag{1}$$

Here φ is the rotation angle of the rotor, x is the displacement of the platform, J is the moment of inertia of the rotor, m_0 is the eccentric mass of the rotor, M is the mass of the platform, c is stiffness, β is friction coefficient, l is the eccentricity of mass m_0, and $\mathscr{G}(\dot{\varphi})$ is the motor torque.

Let us consider two different types of motor for this system and see whether the Sommerfeld effect can be found.

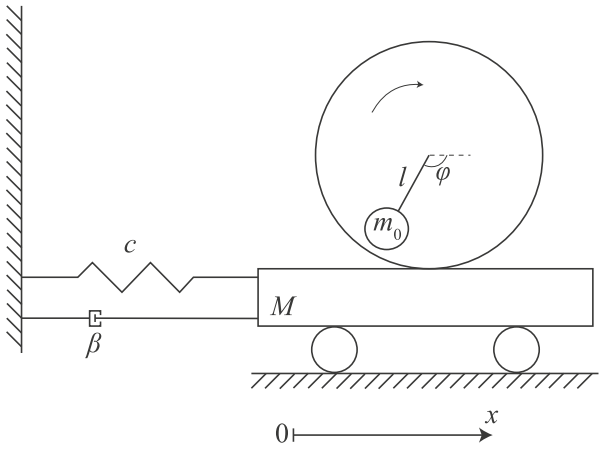

Fig. 1 Scheme of unbalanced rotor on a rigid platform

2.1 Sommerfeld Effect in the System

First, we consider a limited power DC motor

$$\mathscr{G}(\dot{\varphi}) = \Delta - k\dot{\varphi}, \tag{2}$$

where Δ and k are constant parameters of the motor.

For computer simulation we take the following parameters: $J = 0.014$, $M = 10.5$, $m_0 = 1.5$, $l = 0.04$, $k = 0.005$, $c = 5300$, $\beta = 5$, and $\Delta = 0.49$. For initial data $\dot{x}(0) = x(0) = \varphi(0) = \dot{\varphi}(0) = 0$ the Sommerfeld effect occurs. For other initial data $\dot{x}(0) = x(0) = \varphi(0) = 0, \dot{\varphi}(0) = 40$ we observe normal operation—the achievement of desired rotational velocity of our mechanical system.[1] The transient processes for both the initial data and the corresponding attractors are shown in Fig. 2. Comparison of this situation with experiment of Sommerfeld gives the following result: when the Sommerfeld effect occurs, the effective level of only about 1/4 is achieved (comparing to the normal operation). Note that in this example we have the coexistence of attractors, which are hidden in the sense of mathematical definition. But from a physical point of view, the zero initial data correspond to typical start of the system, so the Sommerfeld effect can be easily localized, while the normal operation is hidden.

[1]For this system with $\beta = 0.005$, $k = 5$, $\Delta = 0.5$, or $\Delta = 0.51$ both the effects were discussed in [1]. Here we give more precise parameter values.

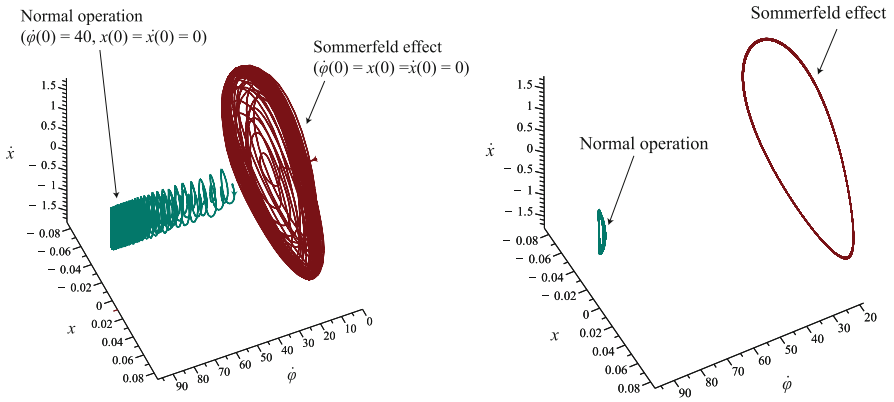

Fig. 2 Sommerfeld effect and normal operation in unbalanced rotor on a rigid platform

2.2 *Absence of the Sommerfeld Effect*

Consider now the following mathematical model of synchronous motor:

$$J\ddot{\theta} = -\alpha\dot{\theta} - \sin\theta, \tag{3}$$

where θ is the phase difference between the rotating magnetic field and the rotor ($\theta = \varphi - \omega t$, where φ is the rotation angle of the rotor as before), α is the coefficient of damper windings, and ω is the current frequency in the stator windings.

Then the equations of "unbalanced rotor on a rigid platform" system take the form:

$$\begin{gathered} J\ddot{\theta} = -\alpha\dot{\theta} - \sin\theta + m_0 l\ddot{x}\sin(\omega t + \theta), \\ (M + m_0)\ddot{x} + \beta\dot{x} + cx = m_0 l\left((\omega + \dot{\theta})^2\cos(\omega t + \theta) + \ddot{\theta}\sin(\omega t + \theta)\right). \end{gathered} \tag{4}$$

In [9] it was mathematically rigorously proved that there is no Sommerfeld effect in system (4) if it is actuated asynchronously (asynchronous actuation means that $x(0) = \dot{x}(0) = \dot{\theta}(0) = 0$). It is shown that the following equation is valid for sufficiently small l and large t:

$$(M + m_0)\ddot{x} + \beta\dot{x} + cx = m_0 l\omega^2\cos\omega t + O(l^2). \tag{5}$$

After the transient process the synchronous machine reaches normal operation mode with the rotation frequency of rotor equal to $\omega + O(l)$. The platform oscillations can be approximated by the harmonic oscillation with the frequency $\omega + O(l)$ and the amplitude

$$\frac{m_0 l\omega^2}{\sqrt{(c - (M + m_0)\omega^2)^2 + \beta^2\omega^2}} + O(l^2). \tag{6}$$

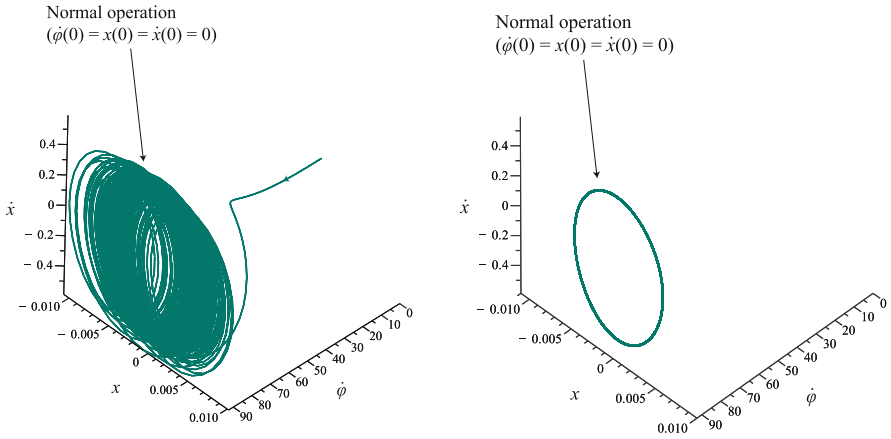

Fig. 3 Normal operation in unbalanced rotor on a rigid platform

Thus, if the eigenfrequency of the platform is less than ω, then in the case of asynchronous actuation system (4) always passes resonance and enters normal operation mode after transient process.

Computer simulation of (4) with parameters $J = 0.014$, $M = 10.5$, $m_0 = 1.5$, $l = 0.04$, $\alpha = 0.5$, $c = 5300$, $\beta = 5$, $\omega = 90$, and initial data $\dot{x}(0) = x(0) = \varphi(0) = \theta(0) = \dot{\varphi}(0) = \dot{\theta}(0) + \omega = 0$ gives a normal operation, which is shown in Fig. 3. The normal operation is a hidden attractor in the sense of mathematical definition, but from a physical point of view, it is easily localized. Remark that the computation with other initial data does not reveal any other coexisting attractors, thus our experiments expand the work [9], where the limitation on initial data is assumed.

3 Conclusion

In this paper two types of vibrational units with unbalanced rotors are considered. It is demonstrated that under certain conditions system (1) and (2) experiences the Sommerfeld effect, namely the resonance capture phenomenon. Here the Sommerfeld effect can be regarded as the coexistence of hidden oscillations since the system has no equilibrium states. Also an example of similar model without Sommerfeld effect is shown.

Acknowledgements Authors were supported by Saint-Petersburg State University (6.38.505.2014).

References

1. Blekhman II, Indeitsev DA, Fradkov AL (2007) Slow motions in systems with inertially excited vibrations. IFAC Proc Vol (IFAC-PapersOnline) 3(1):126–131
2. Brezetskyi S, Dudkowski D, Kapitaniak T (2015) Rare and hidden attractors in van der Pol-Duffing oscillators. Eur Phys J: Spec Top 224(8):1459–1467
3. Eckert M (2013) Arnold Sommerfeld: science, life and turbulent times 1868–1951. Springer, Berlin
4. Feng Y, Wei Z (2015) Delayed feedback control and bifurcation analysis of the generalized Sprott B system with hidden attractors. Eur Phys J: Spec Top 224(8):1619–1636
5. Feng Y, Pu J, Wei Z (2015) Switched generalized function projective synchronization of two hyperchaotic systems with hidden attractors. Eur Phys J: Spec Top 224(8):1593–1604
6. Jafari S, Sprott JC, Nazarimehr F (2015) Recent new examples of hidden attractors. Eur Phys J: Spec Top 224(8):1469–1476
7. Kuznetsov NV (2016) Hidden attractors in fundamental problems and engineering models. A short survey. Lecture notes in electrical engineering, vol. 371, pp 13–25 [plenary lecture at AETA 2015: Recent Advances in Electrical Engineering and Related Sciences]
8. Kuznetsov NV, Leonov GA, Vagaitsev VI (2010) Analytical-numerical method for attractor localization of generalized Chua's system. IFAC Proc Vol (IFAC-PapersOnline) 4(1):29–33
9. Leonov GA (2008) The passage through resonance of synchronous electric motors mounted on an elastic base. J Appl Math Mech 72(6):631–637
10. Leonov GA, Kuznetsov NV (2013) Hidden attractors in dynamical systems. From hidden oscillations in Hilbert-Kolmogorov, Aizerman, and Kalman problems to hidden chaotic attractors in Chua circuits. Int J Bifurcation and Chaos 23(1). Art. no. 1330002
11. Leonov GA, Kuznetsov NV, Mokaev TN (2015) Homoclinic orbits, and self-excited and hidden attractors in a Lorenz-like system describing convective fluid motion. Eur Phys J Spec Top 224(8):1421–1458
12. Li C, Hu W, Sprott JC, Wang X (2015) Multistability in symmetric chaotic systems. Eur Phys J: Spec Top 224(8):1493–1506
13. Pham VT, Vaidyanathan S, Volos CK, Jafari S (2015) Hidden attractors in a chaotic system with an exponential nonlinear term. Eur Phys J: Spec Top 224(8):1507–1517
14. Saha P, Saha DC, Ray A, Chowdhury AR (2015). Memristive non-linear system and hidden attractor. Eur Phys J: Spec Top 224(8):1563–1574
15. Shahzad M, Pham V-T, Ahmad MA, Jafari S, Hadaeghi F (2015) Synchronization and circuit design of a chaotic system with coexisting hidden attractors. Eur Phys J: Spec Top 224(8):1637–1652
16. Sharma PR, Shrimali MD, Prasad A, Kuznetsov NV, Leonov GA (2015) Control of multistability in hidden attractors. Eur Phys J Spec Top 224(8):1485–1491
17. Sommerfeld A (1902) Beitrage zum dynamischen ausbau der festigkeitslehre. Zeitschrift des Vereins deutscher Ingenieure 46:391–394
18. Sprott JC (2015) Strange attractors with various equilibrium types. Eur Phys J: Spec Top 224(8):1409–1419
19. Vaidyanathan S, Pham V-T, Volos CK (2015). A 5-D hyperchaotic Rikitake dynamo system with hidden attractors. Eur Phys J: Spec Top 224(8):1575–1592
20. Zhusubaliyev ZT, Mosekilde E, Churilov AN, Medvedev A (2015) Multistability and hidden attractors in an impulsive Goodwin oscillator with time delay. Eur Phys J: Spec Top 224(8):1519–1539

Effect of Material Layers in a Compound Circular Receiver Model Design for Concentrating Solar Power

Ryuusuke Kawamura, Yoshinori Nagase, and Shigeki Tomomatsu

Abstract The present study intends to evaluate heat conductance and mechanical strength at elevated temperature of a prototype of flat type receiver composed of carbon steel fin and copper tubes. Considering a compound circular plate composed of different kinds of material layers as an analytical model of the receiver, a mathematical analysis of plane axisymmetric transient heat conduction and thermal stresses for the plate is developed. Performing numerical calculation for a compound circular plate consisted of carbon steel layer and copper one, the effect of thickness of copper layer on spatial variations and time-evolutions of temperature change and thermal stresses is discussed briefly.

1 Introduction

Effective use of solar energy becomes important issues all over the world, since solar energy has been very promising as one of renewables which enable to reduce greenhouse gas emissions. Concentrating solar power (CSP) [1] is a system in which steam generated by solar heat drives a turbine to generate electricity. CSP is divided into two parts: one is the solar collector part and the other is power generation part. Direct normal irradiation in sunlight is only concentrated by the solar collector. The concentrated sunlight is converted into heat on the surface of receiver. For stable operation of CSP, the structure and materials in the solar collector part have to possess heat resistance and mechanical strength. Miyazaki Prefectural Government in Japan built a beam-down solar thermal collector at University of Miyazaki in 2012, the government is supporting and promoting the study and development of new energy. The collector [2] is the plant composed of reflectors and a receiver. Sunlight concentrated by reflectors which is referred to as

R. Kawamura (✉) • Y. Nagase • S. Tomomatsu
Institute of Education and Research for Engineering, University of Miyazaki, Miyazaki 889-2192, Japan
e-mail: rkawamura@cc.miyazaki-u.ac.jp

H. Irschik et al. (eds.), *Dynamics and Control of Advanced Structures and Machines*, DOI 10.1007/978-3-319-43080-5_14

heliostat is converted into heat on the surface of a receiver. Solar energy research project team in University of Miyazaki is working the study of receivers which enable them to convert concentrated sunlight into heat with high efficiency.

Before the beam-down solar thermal collector was established at University of Miyazaki, we considered a prototype of flat type receiver which is consisted of carbon steel fin and copper tubes. We focused on the effect of copper tubes on thermal conductance and mechanical strength at elevated temperatures in the receiver. To evaluate the prototype of the receiver, heating experiment was carried out by using a solar simulator [3]. A xenon short arc lamp of rating lamp input 500 W is used as a light source of the solar simulator. A xenon lamp is considered as a point light source with continuous spectra, which radiates light that is the closest of all artificial light sources to sunlight. An elliptical mirror is used to concentrate the light radiated by the lamp. When the light source in the lamp is set at the first focal point of the mirror, the radiated light which is reflected by the mirror is concentrated at the second focal point of the mirror. When the receiver is set at the second focal point of the mirror, the concentrated light absorbed by the receiver is converted into heat. The heat causes temperature rise in the receiver. Heat conducts along a copper tube in the receiver, and temperature rise of carbon steel fin on the copper tube can be observed. To elucidate heat conduction of the receiver from a theoretical viewpoint, we considered a compound flat plate composed of two different material layers as an analytical model, and one-dimensional heat conduction analysis was conducted as a first approximation [4]. When the numerical result of time-evolution of temperature on the top surface calculated by the theoretical analysis is compared with the experimental result, there is an inconsistency in time up to steady temperature state between the theoretical result and experimental one. Heat flows in the thickness direction in the one-dimensional heat conduction of the compound flat plate in which the top surface is subjected to uniform heat supply. Heat conduction from heated area to non-heated area cannot be considered in the one-dimensional heat conduction model of the plate.

The present study intends to evaluate heat conductance and mechanical strength at elevated temperature of a flat type receiver from a theoretical viewpoint. Considering a compound circular plate composed of two different kinds of material layers as an analytical model of the receiver, a mathematical analysis of plane axisymmetric transient heat conduction and thermal stresses for the plate is developed. It is assumed that the plate is subjected to heat flux on the top surface axisymmetrically and that the plate transfers heat with surrounding media. Analytical solutions of transient temperature change and thermal stresses are derived under a plane axisymmetric condition. Performing numerical calculations for the compound circular plate composed of carbon steel layer and copper one, the effect of thickness of carbon steel and copper layers on spatial variations and time-evolution of temperature change and thermal stresses in the plate is discussed briefly.

2 Analysis

2.1 Heat Conduction Problem

Consider a compound circular plate of radius a and of thickness B that is composed of two different kinds of material layers as an analytical model shown in Fig. 1. The origin O of radial coordinate r and transverse coordinate z is set on the top surface of the plate. The layers are numbered, and thickness of i-th layer is b_i; local coordinate in the thickness direction whose origin is set on the top surface of the layer is z_i; temperature of the layer is θ_i. Initial temperature in the plate is assumed to be constant temperature θ_0. Consider heat flux $q(r, t)$ which has plane axisymmetric distribution is supplied on the top surface of the plate at time t. There are heat transfer between on the top, the bottom, and the side surfaces and surrounding media with temperatures θ_a, θ_b, θ_s. Coefficients of heat transfer on the top, the bottom, and the side surfaces are γ_a, γ_b, γ_s, respectively.

First, temperature change T_i of each layer is defined as

$$T_i(r, z_i, t) = \theta_i(r, z_i, t) - \theta_0 \ , \quad i = 1, 2. \tag{1}$$

The fundamental equation of transient heat conduction, the initial condition, the boundary conditions, and the continuity conditions in temperature change and heat flux are expressed in dimensionless forms as below:

$$\frac{\partial \bar{T}_i}{\partial \tau} = \bar{\kappa}_i \left\{ \frac{1}{\bar{r}} \frac{\partial}{\partial \bar{r}} \left(\bar{r} \frac{\partial \bar{T}_i}{\partial \bar{r}} \right) + \frac{\partial^2 \bar{T}_i}{\partial \bar{z}_i^2} \right\} \ , \quad i = 1, 2, \tag{2}$$

$$\bar{T}_i = 0 \quad \text{at} \quad \tau = 0 \ , \quad i = 1, 2, \tag{3}$$

$$-\frac{\partial \bar{T}_1}{\partial \bar{z}_1} + \bar{h}_a(\bar{T}_1 - \bar{T}_a) = \frac{1}{\bar{\lambda}_1} f(\bar{r}) g(\tau) \quad \text{at} \quad \bar{z}_1 = 0, \tag{4}$$

$$\frac{\partial \bar{T}_2}{\partial \bar{z}_2} + \bar{h}_b(\bar{T}_2 - \bar{T}_b) = 0 \quad \text{at} \quad \bar{z}_2 = \bar{b}_2, \tag{5}$$

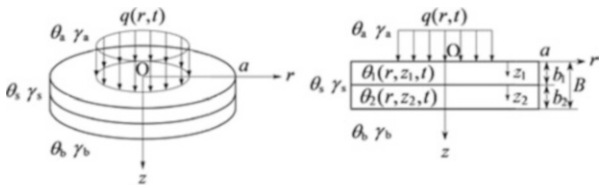

Fig. 1 Analytical model of compound circular plate

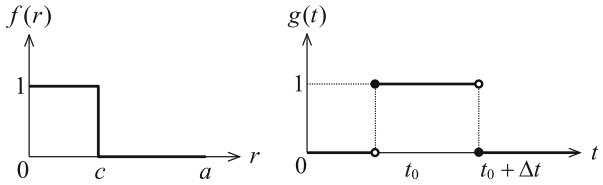

Fig. 2 Step heating

$$\frac{\partial \bar{T}_i}{\partial \bar{r}} + \bar{h}_{si}(\bar{T}_i - \bar{T}_s) = 0 \quad \text{at} \quad \bar{r} = \bar{a}\,, \quad i = 1, 2, \tag{6}$$

$$\bar{T}_1 = \bar{T}_2 \quad \text{at} \quad \bar{z}_1 = \bar{b}_1\,,\ \bar{z}_2 = 0, \tag{7}$$

$$\bar{\lambda}_1 \frac{\partial \bar{T}_1}{\partial \bar{z}_1} = \bar{\lambda}_2 \frac{\partial \bar{T}_2}{\partial \bar{z}_2} \quad \text{at} \quad \bar{z}_1 = \bar{b}_1\,,\ \bar{z}_2 = 0. \tag{8}$$

Assuming the step heating shown in Fig. 2, functions of heat flux $f(\bar{r})$ and $g(\tau)$ are expressed in dimensionless forms as

$$f(\bar{r}) = H(\bar{c} - \bar{r}), \tag{9}$$

$$g(\tau) = H(\tau - \tau_0) - H(\tau - \tau_0 - \Delta\tau), \tag{10}$$

in which $H(\ )$ is Heaviside step function; $\bar{c}$ is a dimensionless form of radius of heated area on the top surface of the plate c; τ, τ_0, $\Delta\tau$ are dimensionless forms of time t, heating start time t_0, and the duration of heating Δt.

Dimensionless quantities introduced in Eqs. (2)–(10) are defined by

$$\left.\begin{aligned} &(\bar{z}_i, \bar{b}_i, \bar{r}, \bar{a}, \bar{c}) = \frac{(z_i, b_i, r, a, c)}{B},\ \bar{\kappa}_i = \frac{\kappa_i}{\kappa_0},\ \bar{\lambda}_i = \frac{\lambda_i}{\lambda_0} \\ &\bar{q} = \frac{q}{q_0},\ T_0 = \frac{q_0 B}{\lambda_0},\ (\bar{T}_i, \bar{T}_a, \bar{T}_b, \bar{T}_s) = \frac{(T_i, T_a, T_b, T_s)}{T_0} \\ &(\tau, \tau_0, \Delta\tau) = \frac{\kappa_0}{B^2}(t, t_0, \Delta t),\ (\bar{h}_a, \bar{h}_b, \bar{h}_{si}) = B \times (h_a, h_b, h_{si}) \end{aligned}\right\}, \tag{11}$$

in which κ_i and λ_i are the thermal diffusivity and the heat conductivity of i-th layer; κ_0 and λ_0 are the typical values of the thermal diffusivity and the heat conductivity, respectively; q_0 is the intensity of heat flux; T_0 is the typical temperature change; h_a, h_b, and h_{si} are relative heat transfer coefficients defined as

$$h_a = \frac{\gamma_a}{\lambda_1}\,,\ h_b = \frac{\gamma_b}{\lambda_1}\,,\ h_{si} = \frac{\gamma_s}{\lambda_i}\,, \quad i = 1, 2. \tag{12}$$

Analytical solution of temperature change in the plate is obtained by the superposition of both solution to the heat conduction problem such that the plate is subjected

to heat flux at top surface whose intensity varies with time and solution to the heat conduction problem such that the plate has heat transfer between the boundary surfaces and surrounding media.

$$\bar{T}_i = \sum_{k=1}^{\infty} T_{ik} J_0(q_{ik}\bar{r}) \ , \quad i = 1, 2, \tag{13}$$

$$\begin{aligned} T_{ik} = \frac{2q_{ik}^2}{\bar{a}^2(q_{ik}^2 + h_{si}^2)J_0^2(q_{ik}\bar{a})} \Bigg\{ & -\sum_{j=1}^{m} \frac{2\mu_j I_{\mathrm{T}}(\tau)}{\Delta'(\mu_j)} [\bar{A}_{\mathrm{u}\,ikj} \cosh(\alpha_{ikj}\bar{z}_i) + \bar{B}_{\mathrm{u}\,ikj} \sinh(\alpha_{ikj}\bar{z}_i)] \\ & - \sum_{j=m+1}^{\infty} \frac{2\mu_j I_{\mathrm{T}}(\tau)}{\Delta'(\mu_j)} [\bar{A}_{\mathrm{u}\,ikj} \cos(\beta_{ikj}\bar{z}_i) + \bar{B}_{\mathrm{u}\,ikj} \sin(\beta_{ikj}\bar{z}_i)] \\ & + \sum_{j=1}^{m} \frac{2e^{-\mu_j^2\tau}}{\mu_j \Delta'(\mu_j)} [\bar{A}_{ikj} \cosh(\alpha_{ikj}\bar{z}_i) + \bar{B}_{ikj} \sinh(\alpha_{ikj}\bar{z}_i)] \\ & + \sum_{j=m+1}^{\infty} \frac{2e^{-\mu_j^2\tau}}{\mu_j \Delta'(\mu_j)} [\bar{A}_{ikj} \cos(\beta_{ikj}\bar{z}_i) + \bar{B}_{ikj} \sin(\beta_{ikj}\bar{z}_i)] \\ & + \frac{1}{D} [\bar{A}'_{ik} \cosh(q_{ik}\bar{z}_i) + \bar{B}'_{ik} \sinh(q_{ik}\bar{z}_i) + D \frac{\bar{a}\bar{h}_{si}\bar{T}_{\mathrm{s}}}{q_{ikj}^2} J_0(q_{ik}\bar{a})] \Bigg\} \ . \end{aligned} \tag{14}$$

In Eqs. (13) and (14), $J_0(\ )$ is the Bessel function of the first kind of order zero; $I_T(\tau)$ is defined as

$$I_{\mathrm{T}}(\tau) = \int_0^{\tau} e^{-\mu_j^2(\tau-\tau')} [H(\tau' - \tau_0) - H(\tau' - \tau_0 - \Delta\tau)] \, \mathrm{d}\tau'. \tag{15}$$

The details of symbols in Eq. (14) are omitted due to lack of space.

2.2 Thermal Stress Problem

We now consider stress and bending deformation in the compound circular plate subjected to thermal loads. If the origin of the coordinate in the thickness direction is appropriately selected in the cross-section of the plate, thermal bending of the plate can be treated easily. Thus, the coordinate in the thickness direction z' whose position of the origin is located at $z = \eta$ from the top surface $z = 0$ is defined as

$$\bar{z}' = \bar{z} - \bar{\eta}, \tag{16}$$

When the Poisson ratios of two layers assume to be same value ν, the position η of the origin of the coordinate z' is defined as

$$\bar{\eta} = \bar{B}_1 / \bar{A}_1, \tag{17}$$

in which $\bar{\eta}$ is dimensionless form of the position of neutral plane of the plate η. It is assumed that Kirchhoff–Love hypothesis holds for the bending deformation of the plate subjected to plane axisymmetric heating. When body forces are absent, the equilibrium equations of the plate under plane axisymmetric condition are expressed in dimensionless forms in terms of resultant forces N_r, N_θ and resultant moments M_r, M_θ as

$$\frac{\mathrm{d}\bar{N}_r}{\mathrm{d}\bar{r}} + \frac{\bar{N}_r - \bar{N}_\theta}{\bar{r}} = 0, \tag{18}$$

$$\frac{\mathrm{d}^2\bar{M}_r}{\mathrm{d}\bar{r}^2} + \frac{2}{\bar{r}}\frac{\mathrm{d}\bar{M}_r}{\mathrm{d}\bar{r}} - \frac{1}{\bar{r}}\frac{\mathrm{d}\bar{M}_\theta}{\mathrm{d}\bar{r}} = 0. \tag{19}$$

Dimensionless forms of resultant forces $\bar{N}_r$, $\bar{N}_\theta$ and resultant moments $\bar{M}_r$, $\bar{M}_\theta$ are expressed as

$$\left.\begin{aligned}
\bar{N}_r &= \bar{A}_1\left(\frac{\mathrm{d}\bar{u}_{r0}}{\mathrm{d}\bar{r}} + \nu\frac{\bar{u}_{r0}}{\bar{r}}\right) - \bar{N}_\mathrm{T} \\
\bar{N}_\theta &= \bar{A}_1\left(\nu\frac{\mathrm{d}\bar{u}_{r0}}{\mathrm{d}\bar{r}} + \frac{\bar{u}_{r0}}{\bar{r}}\right) - \bar{N}_\mathrm{T} \\
\bar{M}_r &= -\left(\bar{D}_1 - \frac{\bar{B}_1^2}{\bar{A}_1}\right)\left(\frac{\mathrm{d}^2\bar{w}}{\mathrm{d}\bar{r}^2} + \nu\frac{1}{\bar{r}}\frac{\mathrm{d}\bar{w}}{\mathrm{d}\bar{r}}\right) - \bar{M}_\mathrm{T} \\
\bar{M}_\theta &= -\left(\bar{D}_1 - \frac{\bar{B}_1^2}{\bar{A}_1}\right)\left(\nu\frac{\mathrm{d}^2\bar{w}}{\mathrm{d}\bar{r}^2} + \frac{1}{\bar{r}}\frac{\mathrm{d}\bar{w}}{\mathrm{d}\bar{r}}\right) - \bar{M}_\mathrm{T}
\end{aligned}\right\}, \tag{20}$$

in which $\bar{u}_{r0}$ and $\bar{w}$ are dimensionless forms of radial displacement on the neutral plane u_{r0} and deflection w; $\bar{A}_1$, $\bar{B}_1$, and $\bar{D}_1$ are dimensionless forms of rigidities of the plate A_1, B_1, and D_1; $\bar{N}_T$ and $\bar{M}_T$ are dimensionless forms of thermal resultant force N_T and thermal resultant moment M_T. Their details are omitted due to lack of space.

Substituting Eq. (20) into the equations of equilibrium (18) and (19), and solving them under the restraint condition in deflection at the center of the plate and the mechanical boundary conditions

$$\left.\begin{aligned}
&\bar{w} = 0 \quad \text{at} \quad \bar{r} = 0 \\
&\bar{N}_r = 0, \bar{M}_r = 0 \quad \text{at} \quad \bar{r} = \bar{a}
\end{aligned}\right\}, \tag{21}$$

radial displacement on the neutral plane and deflection are expressed in dimensionless forms as

$$\bar{u}_{r0} = \frac{1}{\bar{A}_1} \sum_{k=1}^{\infty} \sum_{j=1}^{2} \frac{F_{jk}}{q_{ik}} \left\{ \frac{1}{1-\nu} J_1(q_{ik}\bar{r}) + \frac{1}{1+\nu} \frac{\bar{r}}{\bar{a}} J_1(q_{ik}\bar{a}) \right\}, \tag{22}$$

$$\bar{w} = \frac{\bar{A}_1}{\bar{A}_1\bar{D}_1 - \bar{B}_1^2} \sum_{k=1}^{\infty} \sum_{j=1}^{2} \frac{G_{jk}}{q_{ik}^2} \left[\frac{1}{1-\nu} \{J_0(q_{ik}\bar{r}) - 1\} - \frac{1}{1+\nu} \frac{J_0(q_{ik}\bar{a})}{\bar{a}} \frac{\bar{r}^2}{2} \right]. \tag{23}$$

Then, dimensionless forms of thermal stress components $\bar{\sigma}_{rri}$, $\bar{\sigma}_{\theta\theta i}$ of i-th layer are expressed as

$$\bar{\sigma}_{rri} = \frac{\bar{E}_i}{1-\nu^2} \sum_{k=1}^{\infty} \sum_{j=1}^{2} \left(\frac{F_{jk}}{\bar{A}_1} + \frac{\bar{A}_1 G_{jk} \bar{z}'}{\bar{A}_1\bar{D}_1 - \bar{B}_1^2} \right) \left\{ \frac{J_0(q_{ik}\bar{r})}{1-\nu} - \frac{1}{q_{ik}} \left(\frac{J_1(q_{ik}\bar{r})}{\bar{r}} - \frac{J_1(q_{ik}\bar{a})}{\bar{a}} \right) \right\} - \frac{\bar{\alpha}_i \bar{E}_i}{1-\nu} \bar{T}_i, \tag{24}$$

$$\bar{\sigma}_{\theta\theta i} = \frac{\bar{E}_i}{1-\nu^2} \sum_{k=1}^{\infty} \sum_{j=1}^{2} \left(\frac{F_{jk}}{\bar{A}_1} + \frac{\bar{A}_1 G_{jk} \bar{z}'}{\bar{A}_1\bar{D}_1 - \bar{B}_1^2} \right) \left\{ \frac{\nu J_0(q_{ik}\bar{r})}{1-\nu} + \frac{1}{q_{ik}} \left(\frac{J_1(q_{ik}\bar{r})}{\bar{r}} - \frac{J_1(q_{ik}\bar{a})}{\bar{a}} \right) \right\} - \frac{\bar{\alpha}_i \bar{E}_i}{1-\nu} \bar{T}_i, \tag{25}$$

in which $\bar{\sigma}_{rri}$ and $\bar{\sigma}_{\theta\theta i}$ are dimensionless forms of radial and circumferential components of thermal stress σ_{rri}, $\sigma_{\theta\theta i}$ of i-th layer; $\bar{E}_i$ and $\bar{\alpha}_i$ are dimensionless forms of the Young's modulus E_i and the coefficient of linear thermal expansion α_i of i-th layer. Details of coefficients F_{jk} and G_{jk} are omitted.

Dimensionless quantities introduced in Eqs. (16)–(25) are defined as

$$\left.\begin{aligned} &(\bar{z}, \bar{z}', \bar{\eta}) = \frac{(z, z', \eta)}{B},\ (\bar{u}_{r0}, \bar{w}) = \frac{(u_{r0}, w)}{\alpha_0 T_0 B},\ \bar{E}_i = \frac{E_i}{E_0},\ \bar{\alpha}_i = \frac{\alpha_i}{\alpha_0} \\ &(\bar{N}_r, \bar{N}_\theta, \bar{N}_{\mathrm{T}}) = \frac{(N_r, N_\theta, N_{\mathrm{T}})}{\alpha_0 E_0 T_0 B},\ (\bar{M}_r, \bar{M}_\theta, \bar{M}_{\mathrm{T}}) = \frac{(M_r, M_\theta, M_{\mathrm{T}})}{\alpha_0 E_0 T_0 B^2} \\ &(\bar{\sigma}_{rri}, \bar{\sigma}_{\theta\theta i}) = \frac{(\sigma_{rri}, \sigma_{\theta\theta i})}{\alpha_0 E_0 T_0},\ \bar{A}_1 = \frac{A_1}{E_0 B},\ \bar{B}_1 = \frac{B_1}{E_0 B^2},\ \bar{D}_1 = \frac{D_1}{E_0 B^3} \end{aligned}\right\}, \tag{26}$$

in which E_0 and α_0 are typical values of the Young modulus and the coefficient of linear thermal expansion.

3 Numerical Results and Discussion

Assuming heating experiment of the compound circular plate composed of carbon steel and copper layers using a solar simulator, numerical calculations are performed by making use of analytical solutions formulated in Sect. 2. The effect of thickness of copper layer on the spatial variations and time-evolutions of the temperature change and the thermal stress is examined.

Parameters in numerical calculation are given by

$$\left.\begin{array}{l} a = 50\,\mathrm{mm},\ c = 15\,\mathrm{mm},\ \Delta t = 600\,\mathrm{s},\ q_0 = 92.4\,\mathrm{kW/m^2} \\ b_1 = 0.3\,\mathrm{mm},\ \theta_0 = 25\,^\circ\mathrm{C},\ \theta_\mathrm{a} = \theta_\mathrm{b} = \theta_\mathrm{s} = 30\,^\circ\mathrm{C} \\ \gamma_\mathrm{a} = \gamma_\mathrm{b} = \gamma_\mathrm{s} = 50\,\mathrm{W/m^2K} \end{array}\right\}, \tag{27}$$

in which b_1 is thickness of carbon steel layer; c is radius of region which is subjected to heat supply; Δt is the duration of heating; and q_0 is the intensity of heat flux, respectively. The thickness of copper layer b_2 was changed parametrically as $b_2 = (0.0\,,\ 0.3\,,\ 1.2\,,\ 2.1\,,\ 3.0)$ mm. The material properties of carbon steel and copper are shown in Table 1.

Figure 3 shows the effect of thickness of copper layer on radial variations of temperature on the top surface $z = 0$ mm at time $t = 600$ s. As the thickness of copper layer increases, temperature rise over the area of the plate which is subjected to heat supply decreases, meanwhile temperature rise around the area increases. Temperature has a maximum at the center of the plate $r = 0$ mm, and has a minimum at the circumference $r = 50$ mm. As the thickness of copper layer increases, the maximum temperature decreases, and the difference between maximum temperature and minimum one becomes small. The heat conductivity of copper layer is larger than that of carbon steel, which raises the temperature around the area which is not subjected to heat supply.

Figure 4 shows the effect of thickness of copper layer on time-evolution of temperature at the center on the top surface $r = 0$ mm, $z = 0$ mm. As the thickness of copper layer increases, time up to steady temperature state becomes longer and maximum temperature decreases.

Table 1 Material properties

Material properties	Carbon steel	Copper
Mass density (kg m^{-3})	7850	8890
Specific heat (J kg^{-1} K^{-1})	498	385
Thermal conductivity (W m^{-1} K^{-1})	48.5	373.9
Thermal diffusivity (m^2 s^{-1})	12.4×10^{-6}	109.2×10^{-6}
Coefficient of linear thermal expansion (K^{-1})	12.2×10^{-6}	18.4×10^{-6}
Young's modulus (GPa)	188.2	108.8
Poisson ratio/1	0.3	0.3

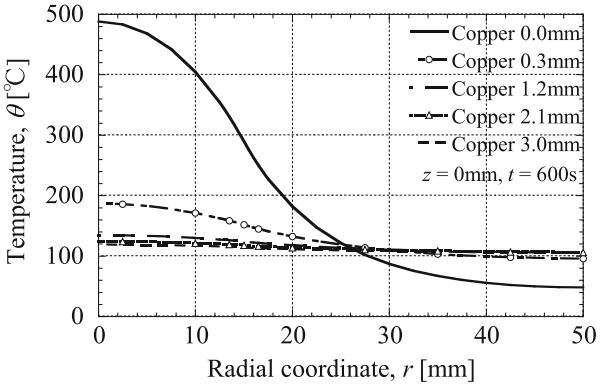

Fig. 3 Effect of thickness of copper layer on radial variation of temperature on the top surface $z = 0$ mm at time $t = 600$ s

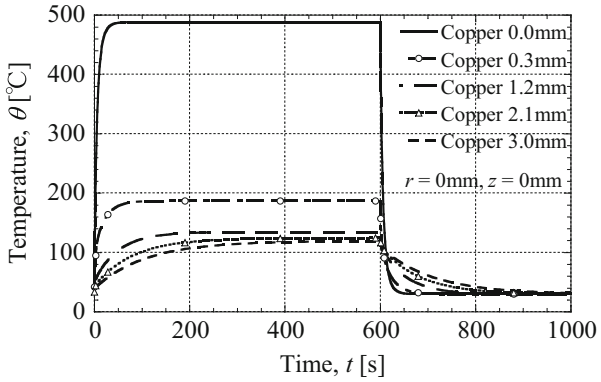

Fig. 4 Effect of thickness of copper layer on time-evolution of temperature at the center on the top surface $r = 0$ mm, $z = 0$ mm

Figure 5 shows the effect of thickness of copper layer on the radius of the area in which temperature is above 110 °C. As the thickness of copper layer increases, the radius of the area increases. However, the radius of the area decreases, when the thickness exceeds a certain value. That means that there is an optimal thickness of the copper layer so as to maximize the radius of the area in which temperature is above a certain value. These results indicate that we may determine the thickness of the copper layer in the compound plate so as to maximize the temperature and the radius of the area.

Figure 6 shows the effect of the thickness of copper layer on the radial variation of the circumferential component of thermal stress $\sigma_{\theta\theta}$ on the top surface $z = 0$ mm at time $t = 600$ s. When the thickness of copper is zero millimeters, compressive

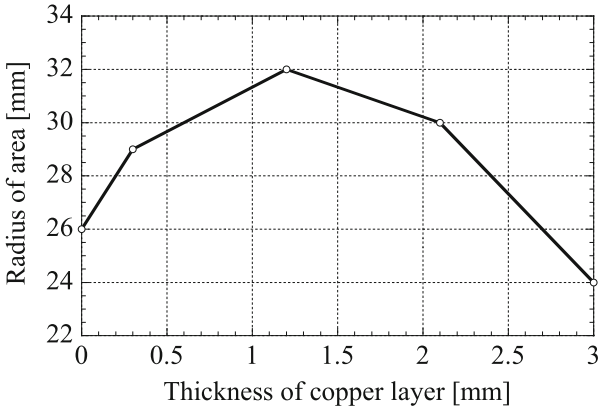

Fig. 5 Effect of thickness of copper layer on the radius of the area in which temperature is above 110 °C

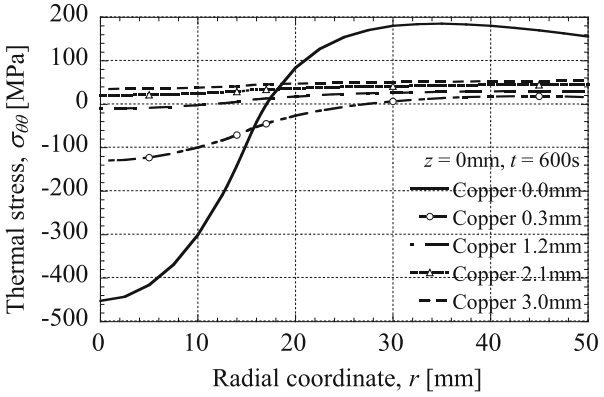

Fig. 6 Effect of thickness of copper layer on the radial variation of thermal stress $\sigma_{\theta\theta}$ on the top surface $z = 0$ mm at time $t = 600$ s

stress occurs in the heated area and tensile stress occurs in the unheated area. As the thickness of copper layer increases, the radial variation of the stress becomes flat and the maximum compressive stress at the center on the top surface.

Figure 7 shows the effect of thickness copper layer on the maximum compressive thermal stress $\sigma_{\theta\theta}$ on the top surface of the plate $z = 0$ mm. Maximum compressive stress occurs at the center on the top surface $r = 0$ mm at time $t = 600$ s when temperature has maximum value. As the thickness of copper layer increases, the maximum compressive thermal stress $\sigma_{\theta\theta}$ decreases monotonously.

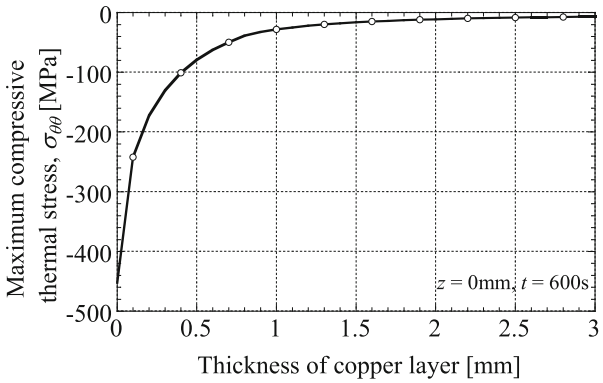

Fig. 7 Effect of thickness of copper layer on the maximum compressive thermal stress $\sigma_{\theta\theta}$ on the top surface $z = 0$ mm at time $t = 600$ s

4 Conclusion

In the present study, a mathematical analysis of plane axisymmetric transient thermal stress of a circular plate composed of two different material layers is developed. Analytical solutions of temperature change, radial displacement at a neutral plane, deflection, and thermal stresses are derived under mechanical boundary condition of free surface at the whole side edge. Performing numerical calculation for a compound circular plate consisted of carbon steel layer and copper one, the effect of thickness of copper layer is discussed.

Numerical results on the effect of thickness of copper layer on spatial variations and time-evolutions of temperature change and thermal stresses are summarized as follows:

1. As the thickness of copper layer increases, time up to steady temperature state becomes longer and maximum temperature at the center of the plate decreases.
2. As the thickness of copper layer increases, temperature rise over the area of the plate which is subjected to heat supply decreases, meanwhile temperature rise around the area increases.
3. There is an optimal thickness of the copper layer so as to maximize the radius of the area in which temperature is above a certain value.
4. As the thickness of copper layer increases, the radial variation of the stress becomes flat and the maximum compressive stress at the center on the top surface of the plate.
5. As the thickness of copper layer increases, maximum temperature change and maximum compressive stress at the center on the top surface of the plate decreases, and the radial variations become flat.

The information obtained from this study can give an instruction for design of receiver which converts concentrated sunlight into heat with high efficiency and possesses mechanical strength at elevated temperature.

Acknowledgments This work was supported by JSPS KAKENHI Grant Number JP15K05680. The authors would like to express their gratitude to Professor Hans Irschik, Professor Alexander Belyaev, and Professor Michael Krommer. They do full honor memory of the late Dr. Franz Ziegler, Professor Emeritus at the Vienna University of Technology.

References

1. New Energy and Industrial Technology Development Organization (ed.) (2010) NEDO renewable energy technology white paper, p 253 (in Japanese)
2. Nakamura K, Nakamura M, Matsuba T, Ishima M, Onomura T (2010) The development of a new heliostat and beam-down solar thermal collector in Japan J Jpn Inst Energ 89:349–354 (in Japanese)
3. Harakawa T, Nagase Y, Tomomatsu S, Kawamura R (2013) Development of solar thermal receiver using solar simulator (study by model of solar thermal receiver), Memoirs of Faculty of Engineering University of Miyazaki, No. 42, pp 183–188 (in Japanese)
4. Kawamura R, Tokumaru F, Nagase Y, Tomomatsu S (2013) Transient heat conduction and thermal stress analyses of a compound plate subjected to concentrated sunlight. Trans Jpn Soc Mech Eng Ser A 79(805):1396–1400 (in Japanese)

On Multiple Support Excitation Analysis of Bridges

R. Heuer and D. Watzl

Abstract Multiple support excitations of elastic multi-span beams are studied. Based on the common set of equations of motion an efficient formulation is developed in order to reduce the degrees of freedom. The resulting equations are formally identical to those that are valid for structures under uniform support excitations. Applying classical modal analysis results in a set of uncoupled differential equations with time-dependent participation factor. A numerical example is given for a two-span railway bridge.

1 Introduction

Long extended structures such as bridges or structures supported on several foundations behave very complex when subjected to ground motions, e.g., earthquakes. Analysis of seismic response cannot be based on the single assumption that free-field ground motions are spatially uniform. Therefore common discretization procedures, originally derived for structures under uniform support excitations, must be extended accordingly resulting in a larger system of equations of motion, see, e.g., [1] and [2].

The structural response of bridges subjected to deterministic multiple support excitation has been investigated by various researchers [3–5]. The dynamic behavior of railway bridges under seismic excitation is studied in [6]. Random vibrations of bridges have been analyzed generally by spectral analysis approach in the last two decades. In [7] the response of continuous two- and three-span beams to varying ground motions is evaluated and the validity of the commonly used assumption of equal support motion is examined. An extensive comparison of random vibration methods for multiple support seismic excitation analysis of long-span bridges can be found in [8].

R. Heuer (✉)
TU Wien, Karlsplatz 13/E2063, A-1040 Vienna, Austria
e-mail: rudolf.heuer@tuwien.ac.at

D. Watzl
Zwinzstraße 7/379, A-1160 Vienna, Austria
e-mail: watzl_daniel@yahoo.de

H. Irschik et al. (eds.), *Dynamics and Control of Advanced Structures and Machines*, DOI 10.1007/978-3-319-43080-5_15

In this contribution a new formulation for linear elastic multi-span beams under multiple support excitation is proposed in order to reduce the degrees of freedom in a mechanically consistent manner. The resulting differential equations are formally identical to those of structures under uniform support excitations. To demonstrate the application of the introduced method, an example is given where the discretized system of a continuous two-span railway bridge is evaluated by means of modal analysis where it becomes necessary to introduce time-dependent participation factors.

2 Basic Equations of Motion

The equation of motion of a discretized linear elastic beam subjected to uniform support excitation,

$$w_{\mathbf{g}1}(t) = w_{\mathbf{g}2}(t) = \ \ldots \ = w_{\mathbf{g}M}(t) = w_{\mathbf{g}}(t), \tag{1}$$

reads, compare [1],

$$\mathbf{m\ddot{u}} + \mathbf{c\dot{u}} + \mathbf{ku} = -\mathbf{m e^s} \ddot{w}_{\mathbf{g}}, \tag{2}$$

where **m**, **c**, and **k** stand for the mass, damping, and stiffness matrix, respectively (Fig. 1).

$\mathbf{u}(t)$ denotes the vector of the nodal transverse deflections $w_i(t)\,,\ i = 1, \ldots, N$. If the discretization is extended to include also nodal rotations, $\mathbf{u}(t)$ contains additional rotatory degrees of freedom, and the corresponding system matrices have to be extended accordingly. The uniform ground acceleration is expressed by $\ddot{w}_{\mathbf{g}}$. The

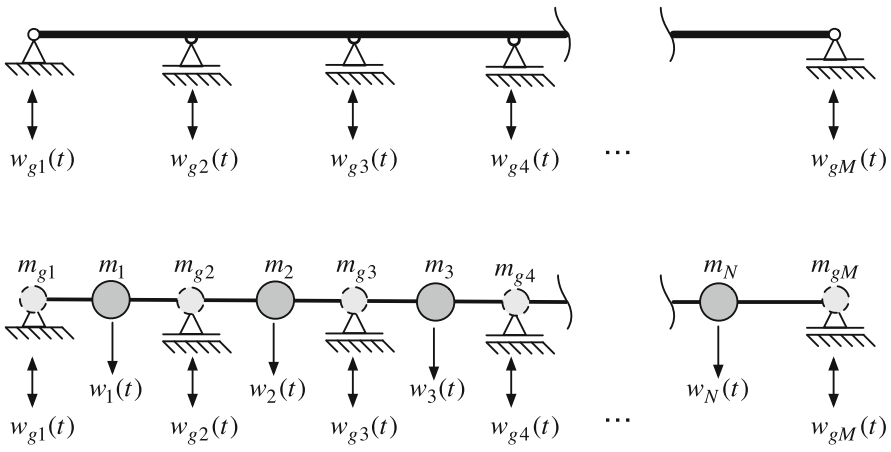

Fig. 1 Multi-span beam and its discretization as lumped-mass model

influence vector $\mathbf{e^s}$ represents the displacements (and rotations) of the masses resulting from the static application of a ground displacement. In case of a lumped-mass model, where only nodal deflections (and no rotations) are considered, it is a vector with each element equal to unity, $\mathbf{e^s} = \mathbf{1}$.

Contrary, the coupled equations of motion of multi-span beams under multiple support excitation can be written formally as, compare [2],

$$\begin{bmatrix} \mathbf{m} & \mathbf{m_g} \\ \mathbf{m_g}^T & \mathbf{m_{gg}} \end{bmatrix} \begin{bmatrix} \ddot{\mathbf{u}}^{\mathbf{t}} \\ \ddot{\mathbf{u}}_{\mathbf{g}} \end{bmatrix} + \begin{bmatrix} \mathbf{c} & \mathbf{c_g} \\ \mathbf{c_g}^T & \mathbf{c_{gg}} \end{bmatrix} \begin{bmatrix} \dot{\mathbf{u}}^{\mathbf{t}} \\ \dot{\mathbf{u}}_{\mathbf{g}} \end{bmatrix} + \begin{bmatrix} \mathbf{k} & \mathbf{k_g} \\ \mathbf{k_g}^T & \mathbf{k_{gg}} \end{bmatrix} \begin{bmatrix} \mathbf{u}^{\mathbf{t}} \\ \mathbf{u}_{\mathbf{g}} \end{bmatrix} = \begin{bmatrix} \mathbf{0} \\ \mathbf{p_g} \end{bmatrix}, \tag{3}$$

or abbreviated,

$$\mathbf{M}\ddot{\mathbf{U}}(t) + \mathbf{C}\dot{\mathbf{U}}(t) + \mathbf{K}\mathbf{U}(t) = \mathbf{P}(t). \tag{4}$$

The displacement vector now contains two parts: $\mathbf{u^t}$ includes the degrees of freedom of the beam, and $\mathbf{u_g}$ contains the components of support excitation. $\mathbf{m_g}$, $\mathbf{m_{gg}}$, $\mathbf{c_g}$, $\mathbf{c_{gg}}$ and $\mathbf{k_g}$, $\mathbf{k_{gg}}$ are submatrices associated with the support motion, and $\mathbf{p_g}(t)$ is the vector of support forces. Note that in case of a lumped-mass model, $\mathbf{m_g}$ is a null matrix,

$$\mathbf{m_g} = \mathbf{0}. \tag{5}$$

In the following a new, efficient representation of Eq. (3) is derived, which is related to the form of Eq. (2). Thus it becomes possible to use numerical procedures that are common in the field of structures under uniform support excitation.

3 Modeling Procedure

In a first step the individually prescribed support displacements, $w_{gj}(t)$, $j = 1, \ldots, M$, are interpreted as additional degrees of freedom, i.e., $u_k(t)$, $k = N + 1, \ldots, N + M$, see Fig. 2. Next, the (singular) stiffness matrix of the complete discretized beam has to be evaluated, e.g., using the direct stiffness method by

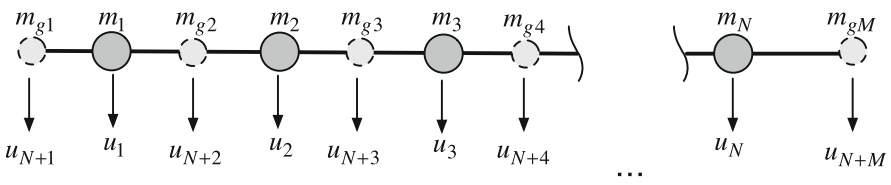

Fig. 2 Free body diagram of the lumped-mass model

applying static unit deformations, which leads to

$$\mathbf{K} = \begin{bmatrix} k_{11} & k_{12} \ldots & k_{1N} & k_{1(N+1)} & \ldots & k_{1(N+M)} \\ k_{21} & k_{22} \ldots & k_{2N} & \vdots & & \vdots \\ \vdots & \ddots & & & & \\ k_{N1} & \ldots & k_{NN} & k_{N(N+1)} & \ldots & k_{N(N+M)} \\ k_{(N+1)1} & \ldots & k_{(N+1)N} & k_{(N+1)(N+1)} & \ldots & k_{(N+1)(N+M)} \\ \vdots & & \vdots & \vdots & \ddots & \vdots \\ k_{(N+M)1} & \ldots & k_{(N+M)N} & k_{(N+M)(N+1)} & \ldots & k_{(N+M)(N+M)} \end{bmatrix}. \tag{6}$$

Mass and damping matrices of Eq. (4) are of analogous form.

In the analysis of such dynamic system it is common to decompose the response into pseudo-static and dynamic components,

$$\mathbf{U}(t) = \begin{bmatrix} \mathbf{u^t}(t) \\ \mathbf{u_g}(t) \end{bmatrix} = \begin{bmatrix} \mathbf{u^s}(t) \\ \mathbf{u_g}(t) \end{bmatrix} + \begin{bmatrix} \mathbf{u}(t) \\ \mathbf{0} \end{bmatrix}. \tag{7}$$

The pseudo-static component satisfies the equation

$$\begin{bmatrix} \mathbf{k} & \mathbf{k_g} \\ \mathbf{k_g}^T & \mathbf{k_{gg}} \end{bmatrix} \begin{bmatrix} \mathbf{u^s}(t) \\ \mathbf{u_g}(t) \end{bmatrix} = \begin{bmatrix} \mathbf{0} \\ \mathbf{p_g^s}(t) \end{bmatrix}, \tag{8}$$

from which one can solve for $\mathbf{u^s}(t)$:

$$\mathbf{u^s}(t) = -\mathbf{k}^{-1}\mathbf{k_g}\,\mathbf{u_g}. \tag{9}$$

Substituting Eqs. (7) and (9) into Eq. (3) and by assuming a lumped-mass model, Eq. (5), results in

$$\mathbf{m}\,\ddot{\mathbf{u}} + \mathbf{c}\,\dot{\mathbf{u}} + \mathbf{k}\,\mathbf{u} = -\mathbf{m}(-\mathbf{k}^{-1}\mathbf{k_g})\ddot{\mathbf{u}}_\mathbf{g} + \left[\mathbf{c}\,(\mathbf{k}^{-1}\mathbf{k_g}) - \mathbf{c_g}\right]\dot{\mathbf{u}}_\mathbf{g} \equiv \mathbf{p_{eff}}. \tag{10}$$

Considering that either the damping terms in the effective forcing function $\mathbf{p_{eff}}$ can be neglected when the motions are not uniform, or

$$\mathbf{c} = a_1\mathbf{k}\,,\ \mathbf{c_g} = a_1\mathbf{k_g}, \tag{11}$$

or the damping forces are assumed to be proportional to the relative velocity vector instead to the absolute velocity, i.e.,

$$\begin{bmatrix} \mathbf{c} & \mathbf{c_g} \\ \mathbf{c_g}^T & \mathbf{c_{gg}} \end{bmatrix} \begin{bmatrix} \dot{\mathbf{u}}^\mathbf{t} \\ \dot{\mathbf{u}}_\mathbf{g} \end{bmatrix} \rightarrow \begin{bmatrix} \mathbf{c} & \mathbf{c_g} \\ \mathbf{c_g}^T & \mathbf{c_{gg}} \end{bmatrix} \begin{bmatrix} \dot{\mathbf{u}} \\ \mathbf{0} \end{bmatrix}. \tag{12}$$

Then Eq. (10) simplifies to

$$\mathbf{m}\ddot{\mathbf{u}} + \mathbf{c}\dot{\mathbf{u}} + \mathbf{k}\mathbf{u} = -\mathbf{m}(-\mathbf{k}^{-1}\mathbf{k}_\mathbf{g})\ddot{\mathbf{u}}_\mathbf{g}. \tag{13}$$

Defining a non-dimensional ground acceleration vector,

$$\mathbf{F_g}^{\mathbf{T}}(t) = \left[\, \ddot{u}_{g1}/\ddot{u}_{g\mathrm{ref}} \;\; \ddot{u}_{g2}/\ddot{u}_{g\mathrm{ref}} \cdots 1 \;\; \ddot{u}_{gM}/\ddot{u}_{g\mathrm{ref}} \,\right], \tag{14}$$

where $\ddot{u}_{g\mathrm{ref}} \neq 0$ represents a reference acceleration component leads to

$$\mathbf{m}\ddot{\mathbf{u}} + \mathbf{c}\dot{\mathbf{u}} + \mathbf{k}\mathbf{u} = -\mathbf{m}(-\mathbf{k}^{-1}\mathbf{k}_\mathbf{g})\ddot{\mathbf{u}}_\mathbf{g} = -\mathbf{m}\mathbf{E}(t)\,\ddot{u}_{g\mathrm{ref}}, \tag{15}$$

with the time-dependent influence vector

$$\mathbf{E}(t) = (-\mathbf{k}^{-1}\mathbf{k}_\mathbf{g})\mathbf{F}_\mathbf{g}(t). \tag{16}$$

When comparing Eq. (15) to Eq. (2) of the beam under uniform support excitation it turns out that both are of the same dimension and structure.

In order to prove the validity of the formulation according to Eq. (15) the limit case of uniform support excitation is examined as follows: the stiffness matrix must satisfy the rigid body condition as

$$\begin{bmatrix} \mathbf{k} & \mathbf{k}_\mathbf{g} \\ \mathbf{k}_\mathbf{g}^T & \mathbf{k}_{\mathbf{gg}} \end{bmatrix} \begin{bmatrix} \mathbf{e}^\mathbf{s} \\ \mathbf{e}_\mathbf{g} \end{bmatrix} = \begin{bmatrix} \mathbf{0} \\ \mathbf{0} \end{bmatrix} \quad \Rightarrow \quad \mathbf{k}_\mathbf{g}\mathbf{e}_\mathbf{g} = -\mathbf{k}\mathbf{e}^\mathbf{s}, \tag{17}$$

where $\mathbf{e}^\mathbf{s}$ and $\mathbf{e}_\mathbf{g}$ are the rigid body displacement vectors associated with the active direction of support motion. In the case of uniform excitation,

$$\ddot{\mathbf{u}}_\mathbf{g} = \mathbf{e}_\mathbf{g}\ddot{w}_g = -\mathbf{k}_\mathbf{g}^{-1}\mathbf{k}\mathbf{e}^\mathbf{s}\ddot{w}_g \tag{18}$$

and finally

$$\mathbf{m}\ddot{\mathbf{u}} + \mathbf{c}\dot{\mathbf{u}} + \mathbf{k}\mathbf{u} = -\mathbf{m}\mathbf{e}^\mathbf{s}\ddot{w}_g. \tag{19}$$

Equation (19) is identical to Eq. (2) and thus represents the classical equation of a multi-degree of freedom system subjected to uniform ground motion.

4 Modal Expansion Technique

Classical approaches for solving the linear system of differential equations, Eq. (13), are either numerical time-integration procedures or modal analysis, see, e.g., [2].

In the following Eq. (13) is transformed into a set of uncoupled equations of motions by modal superposition, that is, assuming

$$\mathbf{u}(t) = \sum_{i=1}^{N} \boldsymbol{\phi}_i y_i(t) = \boldsymbol{\Phi}\mathbf{y}(t), \tag{20}$$

where $\boldsymbol{\Phi}$ represents the modal matrix containing N eigenvectors $\boldsymbol{\phi}_i$, and $\mathbf{y}(t)$ stands for the vector of generalized coordinates y_i. Inserting Eq. (20) into Eq. (13), pre-multiplying by $\boldsymbol{\Phi}^T$, and considering the orthogonality conditions as well as the assumptions of proportional modes for the damped structure, transforms Eq. (13) into

$$\ddot{y}_i + 2\zeta_i\omega_i\dot{y}_i + \omega_i^2 y_i = -\Gamma_i(t)\ddot{u}_{g\text{ref}}, \quad , i = 1, 2, \ldots, N, \tag{21}$$

with the time-dependent participation factor

$$\Gamma_i(t) = \frac{\boldsymbol{\phi}_i^T \mathbf{m}\mathbf{E}(t)}{\boldsymbol{\phi}_i^T \mathbf{m}\boldsymbol{\phi}_i} = \frac{\boldsymbol{\phi}_i^T \mathbf{m}(-\mathbf{k}^{-1}\mathbf{k}_\mathbf{g})}{\boldsymbol{\phi}_i^T \mathbf{m}\boldsymbol{\phi}_i}\mathbf{F}_\mathbf{g}(t). \tag{22}$$

5 Example Problem

For studying the influence of multiple support excitation on the response of a railway bridge, a two-span beam structure with simply support conditions, made of steel and with span length $l_1 = l_2 = 56\,\text{m}$, is excited by the El Centro earthquake. The geometry of the cross-section is given qualitatively in Fig. 3. A detailed compilation of all additional input parameters can be found in [6]. All three supports are excited by the accelerogram recorded from El Centro earthquake [9], see Fig. 4. The first

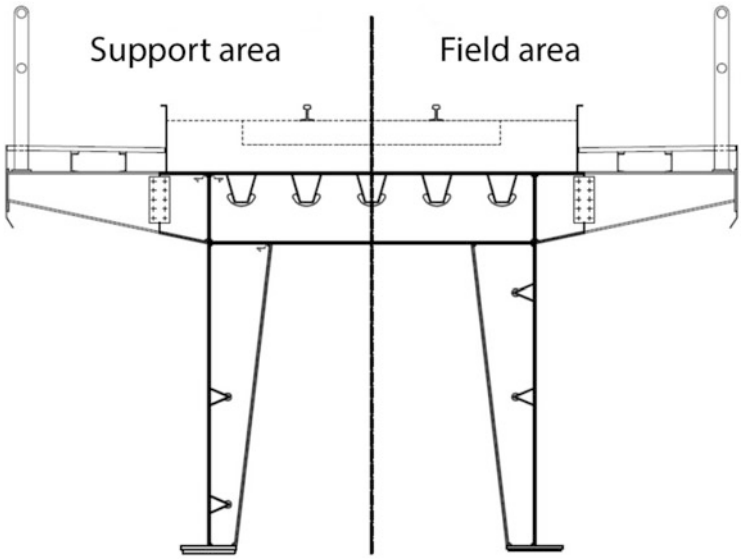

Fig. 3 Cross-section of a two-span railway bridge

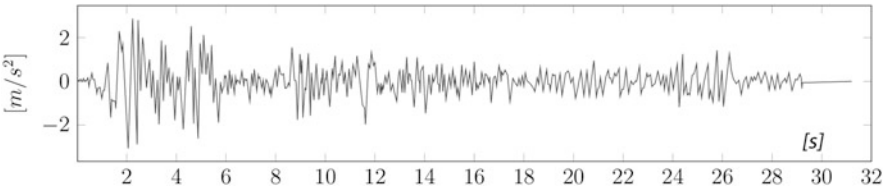

Fig. 4 Accelerogram recorded from El Centro earthquake, May 8, 1940 (NS component)

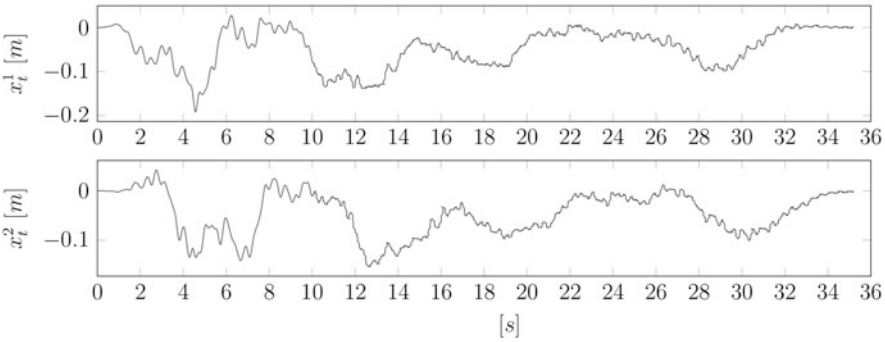

Fig. 5 Midspan deflections x_t^1 and x_t^2 due to multiple support excitation

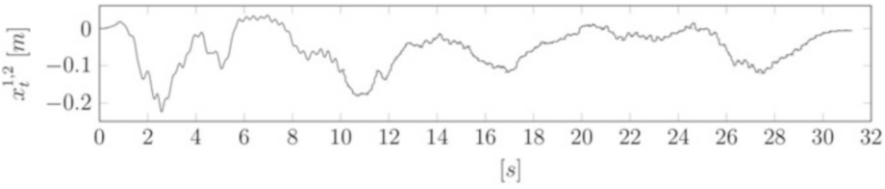

Fig. 6 Midspan deflection $x_t^{1,2} \equiv x_t^1 = x_t^2$ due to uniform support excitation

support is excited with the original signal, for support 2 and 3 a time shift of 1 and 2 s are considered. In a second calculation, for comparison, all three supports are excited uniformly. Figures 5 and 6 show the dynamic midspan deflections due to multiple and uniform support excitation, respectively, denoted as x_t^1, x_t^2, and $x_t^{1,2} \equiv x_t^1 = x_t^2$.

References

1. Clough RW, Penzien J (1993) Dynamics of structures. McGraw-Hill, New York
2. Chopra AK (2012) Dynamics of structures. Prentice Hall, Boston
3. Garevski M, Dumanoglu AA, Sevem RT (1988) Dynamic characteristics and seismic behaviour of Jindo bridge, South Korea. Struct Eng Rev 1:141–149

4. Dusseau RA, Wen RK (1989) Seismic response of deck type arch bridges. Earthq Eng Struct Dyn 18:701–715
5. Abdel-Ghaffar AM, Rubin LI (1989) Vertical seismic behaviour of suspension bridges. Earthq Eng Struct Dyn 11:1–19
6. Watzl D (2015) Railway bridges under seismic multiple support excitation. Master's Theses (in German language), TU Wien
7. Zerva A (1991) Effect of spatial variability and propagation of seismic ground motions on the response of multiply supported structures. Probab Eng Mech 6:212–221
8. Soyluk K (2004) Comparison of random vibration methods for multi-support seismic excitation analysis of long-span bridges. Eng Struct 26:1573–1583
9. El Centro Earthquake Page. http://www.vibrationdata.com/elcentro.html, February 2015

Control of Friction by Surface Microgeometry Variation

Irina Goryacheva

Abstract Some models of a sliding contact of the surfaces with periodic microgeometry over a viscoelastic body are presented. The various gap conditions, such as complete contact, boundary friction, and the contact of dry surfaces with adhesive interaction, are considered. Based on the analytical or semi-analytical solutions of the periodic contact problems, the effects of the microgeometry parameters on the contact pressure distribution and the mechanical component of the friction force are analyzed for various gap and load/velocity conditions.

The main causes of energy dissipation in sliding contact of deformable bodies are hysteresis losses and adhesive interaction of the contacting surfaces (Bowden and Tabor, The friction and lubrication of solids. Part 2. Clarendon, Oxford, 1964; Kragelsky et al., Friction and wear: calculation methods. Pergamon Press, Oxford, 1982). Their influence on friction force depends on the mechanical properties of the contacting bodies and their surface layers, conditions in the gap between surfaces, operation conditions, such as applied load, sliding velocity, temperature, and environment conditions. Besides, surface microgeometry has the significant effect on friction force, particular under conditions of dry contact and boundary lubrication.

In this paper some models of a sliding contact of the surfaces with periodic microgeometry over a viscoelastic base are presented. Based on the models, the dependences of the friction force on the microgeometry parameters are analyzed for various contact conditions.

1 Complete Sliding Contact of the Surfaces with Regular Waviness

Under the condition of complete contact the main course of energy dissipation is the imperfect elasticity of the contacting bodies or their surface layers [1, 2]. To study this effect the model of complete sliding contact of wavy surface was developed in

I. Goryacheva (✉)
Ishlinsky Institute for Problems in Mechanics, Russian Academy of Sciences, Prospect Vernadskogo, 101 Bld 1, Moscow 117526, Russia
e-mail: goryache@ipmnet.ru

H. Irschik et al. (eds.), *Dynamics and Control of Advanced Structures and Machines*, DOI 10.1007/978-3-319-43080-5_16

[3]. The analytical solution of the contact problem for the punch with surface shape described by the periodic function, $f(x) = f(x+l)$, sliding over the viscoelastic half-plane with a constant velocity V along the axis Ox is based on the expansion of the functions of the pressure distribution and surface displacement into Fourier series, and on the establishment of the relations between the coefficients of the series. The relations between the strain $\varepsilon_{x^0}, \varepsilon_{y^0}, \varepsilon_{z^0}$ and the stress $\sigma_{x^0}, \sigma_{y^0}, \tau_{x^0y^0}$ components in an isotropic viscoelastic body are taken in the following form [4]:

$$\begin{aligned}
\varepsilon_{x^0} + T_\varepsilon \frac{\partial \varepsilon_{x^0}}{\partial t} &= \frac{1-\nu^2}{E}\left(\sigma_{x^0} + T_\sigma \frac{\partial \sigma_{x^0}}{\partial t}\right) - \frac{\nu(1+\nu)}{E}\left(\sigma_{y^0} + T_\sigma \frac{\partial \sigma_{y^0}}{\partial t}\right) \\
\varepsilon_{y^0} + T_\varepsilon \frac{\partial \varepsilon_{y^0}}{\partial t} &= \frac{1-\nu^2}{E}\left(\sigma_{y^0} + T_\sigma \frac{\partial \sigma_{y^0}}{\partial t}\right) - \frac{\nu(1+\nu)}{E}\left(\sigma_{x^0} + T_\sigma \frac{\partial \sigma_{x^0}}{\partial t}\right) \quad (1) \\
\gamma_{x^0y^0} + T_\varepsilon \frac{\partial \gamma_{x^0y^0}}{\partial t} &= \frac{1+\nu}{E}\left(\tau_{x^0y^0} + T_\sigma \frac{\partial \tau_{x^0y^0}}{\partial t}\right)
\end{aligned}$$

Here T_ε and T_σ are constants characterizing the viscous properties of the half-plane ($T_\varepsilon > T_\sigma$), E and ν are the longitudinal Young's modulus of elasticity and Poisson's ratio, respectively; $H = T_\varepsilon E/T_\sigma$ is the instantaneous modulus of elasticity. Equation (1) constitutes the two-dimensional extension of the Kelvin model.

The following dimensionless parameters and functions are used for the analysis:

$$\begin{aligned}
\tilde{x} &= \frac{x}{l}, \qquad \tilde{p}(\tilde{x}) = \frac{2\left(1-\nu^2\right)}{\pi E} p(\tilde{x}l), \\
\tilde{u}(\tilde{x}) &= \frac{u(\tilde{x}l)}{l}, \qquad \tilde{P} = \frac{2\left(1-\nu^2\right)}{\pi E l} P = \int_0^1 \tilde{p}(\tilde{x})d\tilde{x}, \quad (2) \\
\alpha &= \frac{T_\varepsilon}{T_\sigma}, \qquad \beta = \frac{h}{l}, \qquad \zeta = \frac{l}{2VT_\varepsilon}
\end{aligned}$$

It is shown that if the punch shape is described by the function

$$\tilde{u}(\tilde{x}) = \sum_{k=1}^{\infty} (a_k \cos 2\pi k\tilde{x} + b_k \sin 2\pi k\tilde{x}) \quad (3)$$

the contact pressure has the form

$$\tilde{p}(\tilde{x}) = \int_0^1 \tilde{p}(t)dt + \sum_{k=1}^{\infty} (A_k \cos 2\pi k\tilde{x} + B_k \sin 2\pi k\tilde{x}). \quad (4)$$

The following relationships between the coefficients a_k, b_k and A_k, B_k are reduced in [3]:

$$A_k = -2k \cdot \frac{\left(1 + \frac{1}{\alpha}\left(\frac{\pi k}{\zeta}\right)^2\right) a_k - \frac{\pi k}{\zeta}\left(1 - \frac{1}{\alpha}\right) b_k}{1 + \left(\frac{\pi k}{\alpha\zeta}\right)^2} \qquad k = 1, 2, 3, \ldots \tag{5}$$

$$B_k = -2k \cdot \frac{\left(1 + \frac{1}{\alpha}\left(\frac{\pi k}{\zeta}\right)^2\right) b_k + \frac{\pi k}{\zeta}\left(1 - \frac{1}{\alpha}\right) a_k}{1 + \left(\frac{\pi k}{\alpha\zeta}\right)^2}$$

The dimensionless tangential force $\tilde{T}$ arising due to hysteretic losses in the viscoelastic body in sliding contact (mechanical component of the friction force) is calculated from the following relationship reduced from Eqs. (2)–(5):

$$\begin{aligned} \tilde{T} &= \frac{2\left(1 - \nu^2\right)}{\pi E l} T \\ &= \int_0^1 \tilde{p}(x)\tilde{u}'(x)\,dx = \pi \sum_{k=1}^{\infty} k\left(A_k b_k - a_k B_k\right) \\ &= \frac{2\pi^2}{\zeta}\left(1 - \frac{1}{\alpha}\right) \sum_{k=1}^{\infty} \frac{k^3\left(a_k^2 + b_k^2\right)}{1 + \left(\frac{\pi k}{\alpha\zeta}\right)^2} \end{aligned} \tag{6}$$

Eq. (6) is used to study the dependence of the mechanical component of friction force on the parameters α and ζ for given microgeometry of the sliding indenter. It is worth noting that for the elastic half-plane $\alpha = 1$, and as it follows from Eq. (6), $\tilde{T} = 0$, so the mechanical component of friction force is zero at this case. Figure 1 illustrates the dependences of the mechanical component $\tilde{T}$ of the friction force on parameter ζ (2), which is inversely proportional to the sliding velocity V.

The curves in Fig. 1 correspond to the same mechanical properties of the half-plane, the same waviness amplitude and nominal pressure, but different shapes of asperities and their densities. The waviness of the punch is described by the following functions:

$$\begin{aligned} &\text{curve 1:} \quad f(x) = \beta \cos^2 \pi x \\ &\text{curve 2:} \quad f(x) = \beta \cos^4 \pi x \\ &\text{curve 3:} \quad f(x) = \beta \cos^2 2\pi x \end{aligned}$$

The results of calculations make it possible to conclude that the mechanical component of friction is no monotonic function of parameter ζ with maximum at

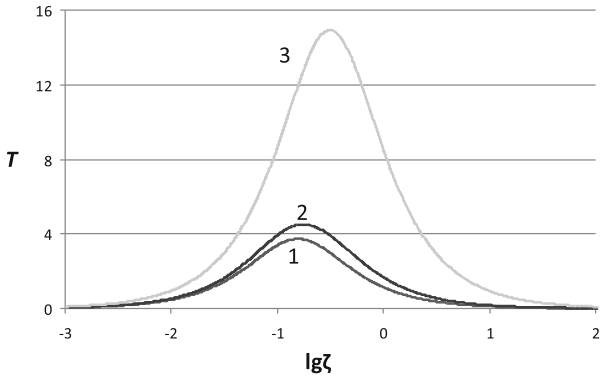

Fig. 1 Dependences of the friction force $\tilde{T}$ on parameter ζ for $\alpha = 20$, $\beta = 0.5$, and various values of microgeometry parameters

some value ζ^* which depends on viscous parameters of the base and on the wave length. The results also indicate that the change in the shape of each asperity leads to the variations in the friction force/velocity dependence. Increasing of the density of the asperities leads to increasing of the friction force.

2 Boundary Friction of the Surfaces with Regular Microgeometry

For incomplete contact the properties of the intermediate medium in the gaps between the contacting bodies influence on the contact characteristics and the friction force. In this section the model of sliding contact is considered under the assumption that there are no adhesive stress in the gap between the surfaces, and no shear stress within the contact spots. The model is applied to analyze the boundary friction, for example, if there is a thin film of lubricant at the contacting surfaces.

The contact problem for a rigid body with regular surface geometry sliding with the constant velocity V along the x-axis on the boundary of a thin viscoelastic layer bonded to a rigid base is considered. The shape of the wavy surface is described by the periodic function (Fig. 2):

$$f(x,y) = h - \frac{h}{4}\left(\cos\left(\frac{2\pi x}{l}\right) + 1\right)\left(\cos\left(\frac{2\pi y}{l}\right) + 1\right) \qquad (h << l) \qquad (7)$$

Here h and l are the height of asperities and the distance between them, respectively.

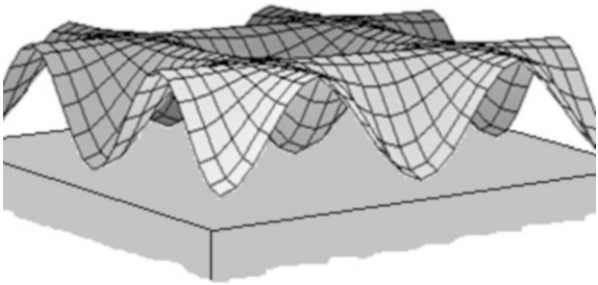

Fig. 2 Sliding contact of the indenter with periodic surface relief on the viscoelastic layer

The mechanical properties of the viscoelastic layer are described by the one-dimensional Kelvin model with spectrum of relaxation times:

$$\sigma_i + \frac{\lambda_i}{1+\alpha_i}\frac{d\sigma_i}{dt} = \frac{E_{1i}}{1+\alpha_i}\left(\varepsilon + \lambda_i \frac{d\varepsilon}{dt}\right) \qquad p = \sum_{i=1}^{n} \sigma_i \tag{8}$$

Here, p is a pressure, ϵ is a deformation, and α_i, λ_i, E_{1i} are the model parameters.

The strip method was used in [4] for solving the contact problem. The problem was reduced to the linear system of equations $\{w\} = [S]\{p\}$ to calculate the contact pressure and the deformed shape of the surface in the gaps. The matrix of coefficients $[S]$ was calculated analytically.

The contact problem was solved for various periodic functions describing the surface relief. The results were used to analyze the contact characteristics under various load/velocities conditions including the complete contact. The influence of the surface relief parameters and the sliding velocity on contact pressure distribution and on the mechanical component of friction force was studied. The results of calculations make it possible to conclude [4] that increasing of the velocity under the same loading conditions leads to asymmetry of the pressure distributions at each contact spot, and to decreasing the each contact spot area ("flowing up" effect).

The maximum contact pressure increases as the velocity increases. For high velocities the contact pressure is distributed symmetrically in respect to the axis of coordinates. The dependence of the friction force on sliding velocity has the same features as in the case of complete contact (see Fig. 1). Decreasing of the asperity height and the distance between them (values of h and l) leads to the complete contact under lower nominal pressure. The friction force increases as the asperity density increases.

3 Sliding Contact with Adhesive Interaction

In sliding contact of dry surfaces the adhesive (molecular) attraction arises in the gap between the contacting bodies. The adhesive attraction is usually modeled by the negative adhesive stress $p = -p_a(\delta)$ acting on the boundary of the interacting bodies outside the contact region, δ is the distance between the surfaces.

Maugis–Dugdale model is often used to describe the adhesive stress in which the dependence of the adhesive stress on the gap between the surfaces has a form of one-step function [5]

$$p_a(\delta) = \begin{cases} p_0, & 0 < \delta \le \delta_0 \\ 0, & \delta > \delta_0 \end{cases} \tag{9}$$

where δ_0 is the maximum value of the gap for which the adhesive attraction acts. The surface energy γ is specified by the relation:

$$\gamma = \int_0^{+\infty} p_a(\delta)\, d\delta = p_0 \delta_0 \tag{10}$$

The periodic contact problems for a sliding contact of a rigid body with wavy surface [6] and surface with two-periodic regular relief [7] over a viscoelastic layer were considered taking into account the adhesive stress (9) in the gap between the bodies. The Kelvin model (8) with one relaxation T_σ and one retardation T_ϵ times was used to describe the mechanical properties of the layer. The boundary conditions for the contact pressures and displacements are formulated with taking into account various regimes of the gap filling: saturated contact, discrete contact with saturated adhesive interaction, and discrete contact with zones of adhesive interaction and zones of free boundary.

The results indicate that due to adhesion a significant increase in the real contact area and hysteretic friction force arises, the contact saturation occurs at lower loads, and a contact between surfaces exists even for negative (tensile) loads. The results show that the transition from discrete to saturated contact in the presence of adhesion occurs at lower loads than without adhesion. Adhesion essentially increases the friction force.

Figure 3 illustrates the effect of the distance between asperities. The calculations were made for the sliding contact of the indenter with two-periodic regular waviness described by Eq. (7). The coefficient of friction $\mu = T/P$ is calculated for two values of the dimensionless distance between asperities of the wavy surface: $l/h = 3$ (curves 1 and 1′) and $l/h = 6$ (curves 2 and 2′). Results for solid lines 1 and 2 are calculated for the following parameters: $\alpha = 10$, $\kappa = 0.4$, $\lambda = 15$, where $\alpha = T_\epsilon/T_\sigma$ is the viscosity parameter, $\kappa = \frac{l^2}{2\pi^2 HVT_\epsilon}$ is the velocity parameter, $\lambda = p_0 \left(\frac{H}{E\gamma}\right)^{1/3}$ is the adhesion parameter, H is the layer thickness. Results for dashed

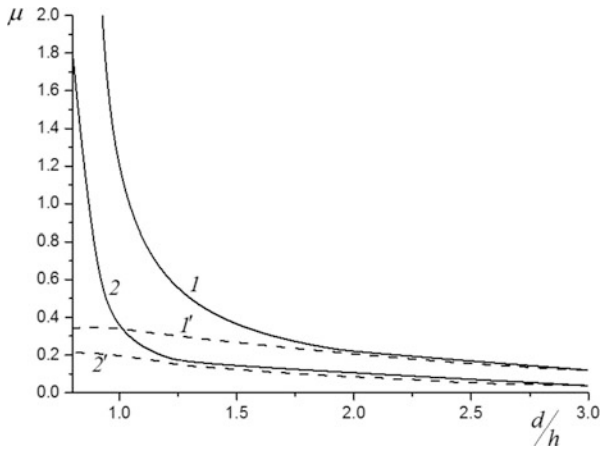

Fig. 3 Coefficient of friction vs. dimensionless normal penetration

lines $1'$ and $2'$ are calculated for the same parameters α and κ but with no adhesion taken into account ($\lambda = 0$).

The results indicate that decreasing the distance between asperities leads to increasing the coefficient of friction. Adhesive interaction between the contacting surfaces increases the friction coefficient; the effect of adhesion is especially significant for small distance between contacting bodies.

4 Conclusions

The models were developed to study the effect of surface microgeometry in sliding contact of viscoelastic bodies. The various conditions in the gap between the contacting surfaces were considered: complete contact, boundary friction, and the contact of dry surfaces with adhesive interaction.

Based on the solutions of the corresponding contact problems it was established that the dependence of the mechanical component of the friction force is non-monotonic function of velocity for any boundary conditions. The maximum value of the friction coefficient is higher for smaller distance between asperities and for bigger inclination of the asperity side. Decreasing the distance between asperities leads to smaller effect of adhesion but higher effect of hysteretic losses. The results can be used for analysis of contact characteristics and the mechanical component of friction force at various microgeometry scales.

The models developed make it possible to evaluate the influence of microgeometry parameter on contact characteristics and friction force for dry and wet surfaces, and to control of these characteristics by choosing the optimal surface relief.

Acknowledgement The research was supported by Russian Science Foundation (No. 14-29-00198).

References

1. Bowden FP, Tabor D (1964) The friction and lubrication of solids. Part 2. Clarendon, Oxford
2. Kragelsky IV, Dobychin MN, Kombalov VS (1982) Friction and wear: calculation methods. Pergamon Press, Oxford
3. Goryacheva IG, Goryachev AP (2016) Contact problems for the stamp with periodic relief sliding over a viscoelastic half-plane. Appl Math Mech 80(1):1–14
4. Sheptunov BV, Goryacheva IG, Nozdrin MA (2013) Contact problem of die regular relief motion over viscoelastic base. J Frict Wear 34:83–91
5. Maugis D (1991) Adhesion of spheres: the JKR-DMT transition using a Dugdale model. J Colloid Interface Sci 150:243–269
6. Goryacheva IG, Makhovskaya YY (2010) Modeling of friction at different scale levels. Mech Solids 45:390–398
7. Goryacheva IG, Makhovskaya YY (2015) Sliding of a wavy indenter on the surface of viscoelastic layer in the presence of adhesion. Mech Solids 4:98–111

Peculiarities of the Magnetic Behavior of Pipe Steels with Different Initial Stress–Strain States Under Elastic Deformation

E.S. Gorkunov, A.M. Povolotskaya, S.M. Zadvorkin, and Yu.V. Subachev

Abstract The effect of the value of preliminary plastic deformation viewed as an initial stress–strain state on the magnetic behavior of X70 pipe steels under elastic tension and compression is studied. Magnetic characteristics were measured both in a closed magnetic circuit and with the use of attached transducers along the direction of applied loading. The plastic deformation history affects the magnetic behavior of the material during subsequent elastic deformation, as plastic strain induces various residual stresses, and this necessitates taking into account the initial stress–strain state of products when developing magnetic techniques for the determination of their stress–strain parameters in operation.

1 Introduction

The increasing output of pipe products is accompanied by ever increasing on the strength of pipe steels, their resistance to corrosion and pipe geometry. However, such important parameter as the level of residual stresses in pipes is tested only in the stage of production, without consideration of the fact that a pipe may suffer additional uncontrollable plastic deformation during transportation to the installation site and during installation. As a result, the condition of pipes after pipeline laying may differ greatly from their condition when they leave the production plant. This may result in higher material damage rates, higher probability of emergencies, and shorter service lives of pipelines.

E.S. Gorkunov (✉) • A.M. Povolotskaya • S.M. Zadvorkin • Yu.V. Subachev
Institute of Engineering Science, RAS (Ural Branch), 34 Komsomolskaya str., 620049 Ekaterinburg, Russia
e-mail: ges@imach.uran.ru; us@imach.uran.ru; zadvorkin@imach.uran.ru; subachev@imach.uran.ru

H. Irschik et al. (eds.), *Dynamics and Control of Advanced Structures and Machines*, DOI 10.1007/978-3-319-43080-5_17

Nondestructive magnetic techniques are currently finding increasing application in diagnosing the stress–strain state of pipes. The development of such techniques was discussed in numerous studies, e.g., [1–6], but practically all of them ignore the history of the material in the form of previous plastic strain.

This paper studies the effect of previous plastic strain in the form of elastic–plastic tensile deformation of a pipe steel on the behavior of some of its magnetic characteristics under subsequent elastic uniaxial tension/compression in order to reveal the nature of the thus-induced magnetic anisotropy and to determine parameters that can be used to evaluate acting elastic strains.

2 Experimental Procedure and Material

Control-rolled pipe steel of strength class X70 (according to the API classification) was studied. Flat test specimens were cut out from a 1.420 mm pipe along the direction of rolling. The gauge length of the specimens with a cross-section of 5.95×46 mm was 120 mm. The specimens were in the as-machined condition.

In stage I, the specimens were subjected to uniaxial tension to various values of plastic strain σ, namely 0.08; 0.23; 0.49, and 1.65 %, and their magnetic characteristics were determined. The loading–relieving diagrams for each specimen are presented in Fig. 1. In stage II, the specimens plastically pre-deformed in stage I underwent elastic tension and compression, the magnetic characteristics being simultaneously measured in a closed magnetic circuit and with attached magnetic devices along the direction of applied loading.

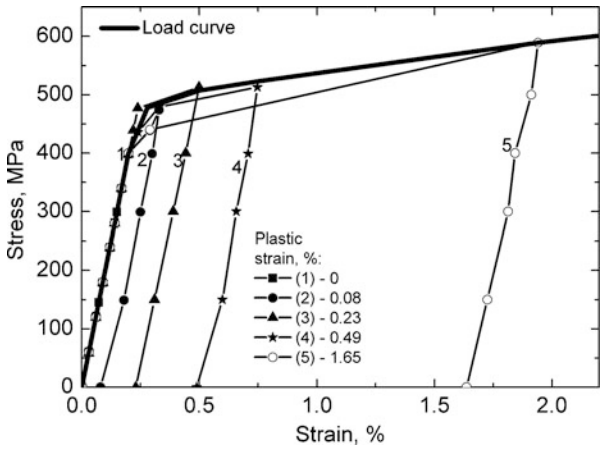

Fig. 1 Loading–relieving diagrams for the test specimens

3 Results and Discussion

Figure 2 presents magnetic characteristics as dependent on tensile stresses, which were obtained in the stage of plastic deformation to a certain level and under subsequent relief. The magnetic behavior of the specimens under tension agrees with the current ideas of the processes occurring in the magnetic structure of steels under force effects. Similar results of studying the effect of elastic–plastic tension on magnetic behavior were obtained earlier and discussed in [7, 8].

It follows from Fig. 2 that, when the specimens are unloaded after plastic strain, the magnetic characteristics change irreversibly; and the higher the value of plastic strain, the greater these irreversible changes. The higher values of the coercive force in the relieved state than those in the loaded state can be explained as follows: under relief, significant residual compressive elastic stresses arise along the direction of tension in a considerable number of grains, and prerequisites emerge for the formation of an "easy magnetization plane" magnetic texture, when it is

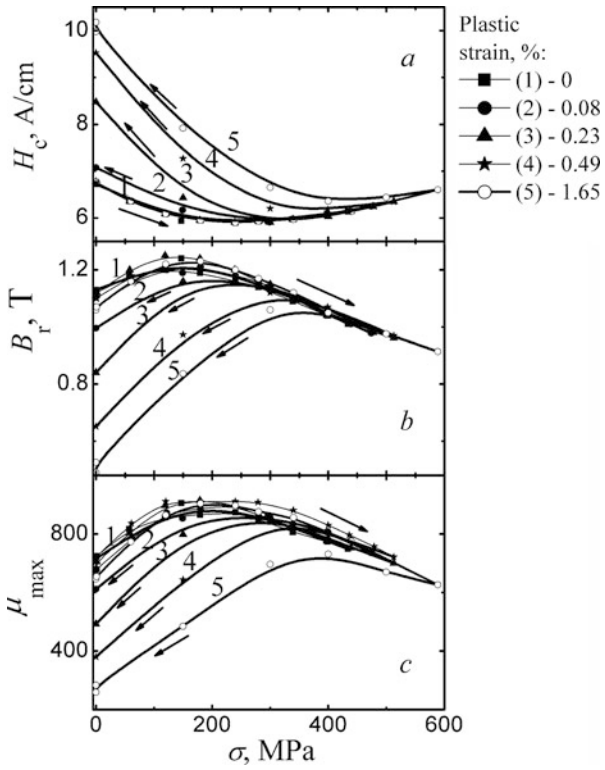

Fig. 2 Coercive force H_c (**a**), residual induction B_r (**b**), and maximum magnetic permeability μ_{max} (**c**) as dependent on tensile stresses under loading to different values of plastic strain followed by stress relieving: 0 (curve 1); 0.08 % (2); 0.23 % (3); 0.49 % (4); 1.65 % (5)

more advantageous for the spontaneous magnetization vectors to line up in the plane normal to the tension axis and hence to the magnetization and magnetization reversal fields; as a result, the magnetization reversal is hampered, and this results in the higher values of the coercive force and the lower values of $B_r(\sigma)$ and $\mu_{max}(\sigma)$. These results agree with those obtained in [6, 9], where significant difference in the coercive force values in the loaded and relieved states under plastic tension were also observed on steel specimens.

For a vivid demonstration of the effect of plastic strain on the magnetic behavior of the specimens, Fig. 3 shows the values of magnetic characteristics after stress relief, reduced to the values in the no-load state, as dependent on the value of plastic strain. There is a monotonic variation of magnetic characteristics with growing plastic strain. It follows from Fig. 3 that these parameters are the most sensitive at residual elongations ranging between 0 and about 0.5 %.

The monotonic behavior of the magnetic characteristics with growing plastic strain enables these parameters or their combination to be used to evaluate the strain state of a pipe that results from pipe manufacture, transportation, and installation and which must be considered later on, when testing the stress–strain state during operation. Note that uniaxial tension plastic strain can be evaluated by the values of the coercive force in the strain range from 0 to about 0.5 %, and it can be evaluated by the values of residual induction and maximum magnetic permeability in the entire range of plastic strain up to necking.

Figure 4 shows the magnetic characteristics of the specimens as dependent on applied stresses measured in a closed magnetic circuit under elastic tension/compression after previous plastic tension to various levels. Note that, under tension, the growth of previous plastic strain is accompanied by an increasing rate of change in the magnetic characteristics, particularly at the initial stage of tension, their behavior for the specimens with different initial uniaxial tension

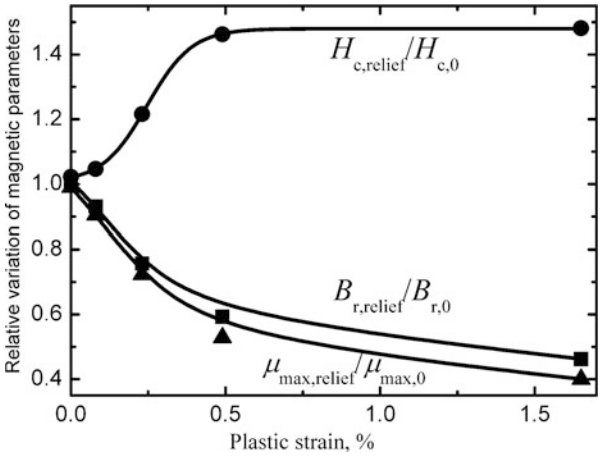

Fig. 3 Relative variation of magnetic parameters after stress relief from the value of plastic strain

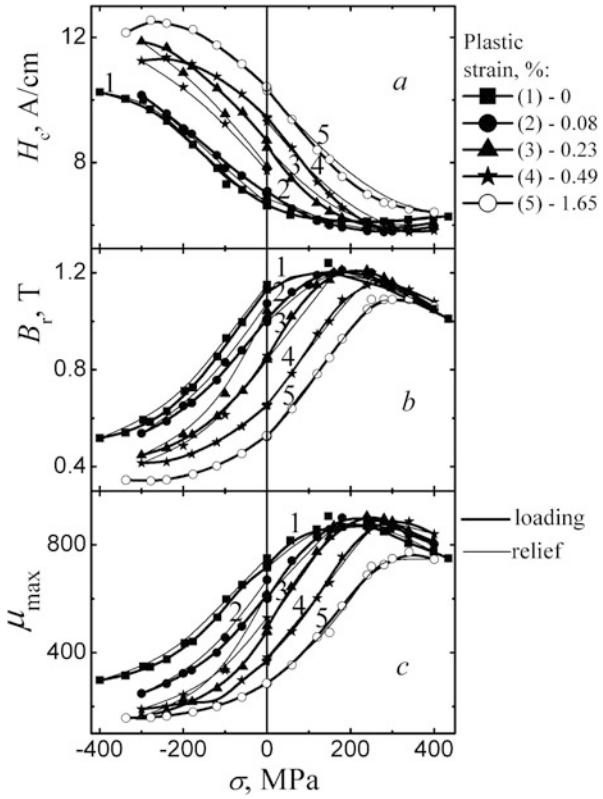

Fig. 4 Applied external stress dependences of coercive force H_c (**a**), residual induction B_r (**b**), and maximum magnetic permeability μ_{max} (**c**) measured in a closed magnetic circuit. The plastic strain values are 0 (1), 0.08 % (2), 0.23 % (3), 0.49 % (4), and 1.65 % (5)

stress-states remaining unchanged. When the tensile stress values increase, the magnetic characteristics change nonmonotonically, with extreme points. It follows from Fig. 4 that, as the values of plastic pre-strain grow, the extreme points shift to the regions of higher stresses, this being the most pronounced on the dependences $B_r(\sigma)$ and $\mu_{max}(\sigma)$. The values of stresses at which there are minimum coercive force values and, correspondingly, peaks on the dependences $B_r(\sigma)$ and $\mu_{max}(\sigma)$ are attributed to a partial compensation of a part of residual internal compressive stresses by external elastic tensile stresses at these moments [10]. When external tensile loading is applied, the absolute values of stresses decrease at sites with residual compressive stresses, whereas the stress values keep increasing at sites with residual tensile stresses. At the instant the stresses become zero in most of the volume with compressive stresses, the coercive force is minimum, since the stress gradients are minimum in this state. As the external tensile load increases, the tensile stresses grow everywhere in the material, and this is accompanied by an increase in the coercive force. It is obvious that the higher the value of plastic

pre-strain, the higher the level of residual internal compressive stresses, and hence the higher is the value of stresses at which there is a minimum of the coercive force and the wider is the range of applied elastic stresses where the magnetic behavior is monotonic.

The dependences of the magnetic characteristics that are obtained during subsequent relief (after tension) coincide with the similar dependences for loading, this being indicative of the reversibility of magnetization reversal in the elastic region both under loading and when the load is removed.

Affected by compressive stresses growing to 240 MPa, the magnetic characteristics vary monotonically. Note that the dependences $H_c(\sigma)$, $B_r(\sigma)$, and $\mu_{max}(\sigma)$ for the specimens plastically pre-strained to not more than 0.23 % are monotonic in the whole range of compressive stresses (curves 1, 2, and 3 in Fig. 4), whereas the dependences $H_c(\sigma)$, $B_r(\sigma)$, and $\mu_{max}(\sigma)$ for the specimens with high values of plastic pre-strain (curves 4 and 5 in Fig. 4) have extrema at about 240 MPa, which are uncharacteristic of elastic compressive deformation. The extrema are caused by a transition to the plastic strain region as a result of the Bauschinger effect. The extrema are caused by the destruction of the "easy magnetization plane" magnetic texture under plastic compression of the steel and easier magnetization reversal along the direction of compression. The latter cause, in its turn, disconnects the loading–relieving curves under the effect of compressive stresses, and this is observed on the dependences $H_c(\sigma)$, $B_r(\sigma)$, and $\mu_{max}(\sigma)$. Moreover, the more severe the pre-strain, the greater is the disconnection of the curves $H_c(\sigma)$, $B_r(\sigma)$, and $\mu_{max}(\sigma)$ measured during loading and relieving, or, in other words, the more pronounced are the irreversible changes in the magnetic characteristics.

In practice, it is easier to measure the magnetic parameters with the use of attached transducers, which are therefore more often used for magnetic inspection under field conditions, particularly, for testing large objects, such as large-diameter pipes. Test results obtained with the use of attached transducers are depicted in Fig. 5 showing the values of the coercive force H_{ce} and the rms values of magnetic Barkhausen noise voltage U (measured when the transduced is placed on the specimens along the direction of applied loading) as dependent on applied stresses.

It follows from a comparison between Figs. 4 and 5 that in the tension region there is a qualitative similarity between the dependences $H_c(\sigma)$ and $H_{ce}(\sigma)$ obtained, respectively, by measurements in a closed magnetic circuit and with an attached transducer. The differences in the behavior of the dependences $H_c(\sigma)$ and $H_{ce}(\sigma)$ under compressive stresses, namely the absence of the disconnection on the loading and relief curves, which is present in Fig. 4a, and the monotonic change (without extrema, as distinct from curves 4 and 5 in Fig. 5a) in the values of the coercive force with increasing compressive stresses for all the plastically pre-strained specimens are due to the fact that the results shown in Fig. 5a were obtained by attached transducers after the measurements in a closed magnetic circuit, i.e., they are the results of the second compression cycle. In this case, the stress relief after the plastic strain occurring under compression in the first measurement cycle is, according to [11], always reversible.

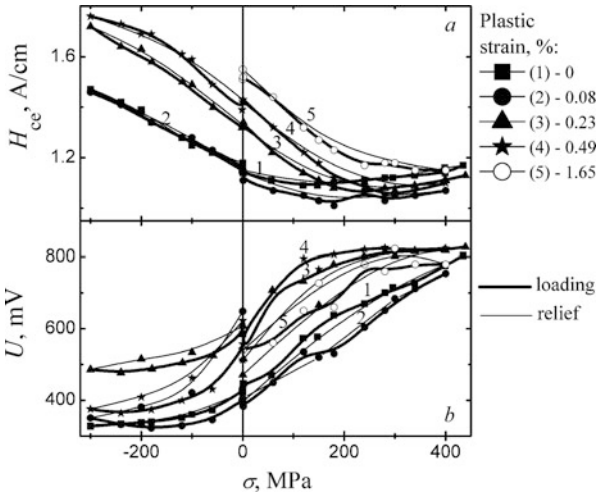

Fig. 5 Coercive force H_{ce} (**a**) and rms voltage U (**b**) measured by attached transducers as dependent on applied external stresses. The plastic strain values are 0 (1), 0.08 % (2), 0.23 % (3), 0.49 % (4), and 1.65 % (5)

It follows from Figs. 4 and 5 that, at applied elastic stresses ranging approximately between −200 and 120 MPa, the magnetic characteristics of all the specimens plastically pre-strained to different amounts vary monotonically and thus can be used to test acting elastic stresses.

4 Conclusion

A monotonic behavior of the magnetic characteristics of the steel (coercive force, residual induction, and maximum magnetic permeability) with increasing plastic strain has been revealed. This enables these parameters or their combination to be used to evaluate the strain state resulting from pipe making, transportation, and installation.

Due to residual stresses induced by plastic strain, the prehistory in the form of plastic strain affects the magnetic behavior of the material during its subsequent elastic deformation, and this necessitates considering the initial stress–strain state of a metallic structure when developing magnetic techniques to determine its stress–strain parameters in operation.

For the steel studied, the range of elastic stresses (between −200 and 120 MPa) has been determined where the magnetic characteristics measured in the longitudinal direction vary uniquely and hence are usable for evaluating acting elastic stresses.

Acknowledgements The study was partially financed by UB RAS project no. 15-10-1-22 and budget theme (state registration no. 01201354598).

References

1. Sadrtdinov RA, Geitsan VB, Surkov YuP, Rybalko VG, Novgorodov DV, Surkov AYu (2010) On the possibility of evaluating the stressed state of pipelines using a magnetic method. Russ J Nondestruct Test 46(2):84–91
2. Muzhitskii VF, Sultanov MK, Zagidulin RV, Makarov PS (2006) A multiparameter method for evaluating stressed-strained states of steel articles and pipelines. Kontr Diag 8:17–22
3. Nichipuruk AP, Stashkov AN, Kostin VN, Korkh MK (2009) Possibilities of magnetic inspection of plastic deformations preceding failures of low-carbon steels constructions. Russ J Nondestruct Test 45(9):616–622
4. Gorkunov ES, Mitropol'skaya SY, Zadvorkin SM, Shershneva LS, Tueva EA (2010) Application of magnetic methods for evaluating stresses and deformation in steels for trunk pipelines. Tyazh Mashinostr 10:2–6
5. Muzhitskii VF, Popov BE, Bezlyudko GY, Zarudnyi VV, Levin EA (1996) Magnetic monitoring of the stress-strain state and residual safe life of the steel structures of hoisting cranes. Russ J Nondestruct Test 32(2):97–102
6. Gorkunov E, Ulyanov A, Zakharov V (2014) Estimation of biaxial strains by a coercimetric method. In: CD-Proceedings of the 11th ECNDT' 2014, Prague
7. Gorkunov ES, Povoltskaya AM, Solov'ev KE, Zadvorkin SM (2010) The influence of the magnetoelastic effect on the hysteretic properties of medium-carbon steel during uniaxial loading. Russ J Nondestruct Test 46(9):638–644
8. Gorkunov ES, Subachev YuV, Povolotskaya AM, Zadvorkin SM (2013) The influence of an elastic uniaxial deformation of a medium-carbon steel on its magnetostriction in the longitudinal and transverse directions. Russ J Nondestruct Test 49(10):584–594
9. Kuleev VG, Tsar'kova TP, Nichipuruk AP, Voronin VI, Berger IF (2007) On the origin of essential differences in the coercive force, remanence, and initial permeability of ferromagnetic steels in the loaded and unloaded states upon plastic tension. Phys Met Metallogr 103(2):131–141
10. Kuleev VG, Gorkunov ES (1997) Mechanisms of the effect of internal and external stresses on the coercivity of ferromagnetic steels. Russ J Nondestruct Test 33(11):741–753
11. Bernshtein ML, Zaimovskii VA (1970) Structure and mechanical properties of metals. Metallurgiya, Moscow

Cable-Stayed Bridges: A Monitoring Challenge

L. Faravelli

Abstract The monitoring of cable-stayed bridges has a core aspect: the cables. They are a significant component of the structural skeleton and are in so large number that a one-by-one response measurement is often too ambitious. In this paper, a footbridge is studied with only 16 cables in double symmetry. Despite the evident simplification of the problem, several aspects met in the process of collecting the data are worth being reported.

1 Introduction

The overall safety of large span bridges, such as cable-stayed and suspension bridges, relies on an adequate understanding, design, and management of some crucial elements: the cables [1–3]. They are characterized by tension forces that vary in time due to the effects of both vehicle/pedestrian crossing and environmental excitations. The estimation of the time-varying cable tension forces from cable vibration measurements or special force sensors on the cables is important for the maintenance and safety assessment of cable-based bridges. Consequently, several theoretical studies were finalized in the first decade of the millennium [4–13].

Vibration-based methods for estimating cable tension forces use a relation between the natural frequency of the cable vibrations and the tension force in the cable. In particular, approximate empirical formulae can be found in the literature to calculate the tension from the measured frequency by accounting of sag extensibility and flexural rigidity.

L. Faravelli (✉)
Department of Civil Engineering and Architecture, University of Pavia, via Ferrata 3, Pavia, Italy
e-mail: lucia@dipmec.unipv.it

H. Irschik et al. (eds.), *Dynamics and Control of Advanced Structures and Machines*, DOI 10.1007/978-3-319-43080-5_18

In other words, one is supposed to collect data on the vibration of every single cable, either in real time or periodically. In the former case one relies on ambient vibration (i.e., the cables are excited by the wind action and/or traffic effects), while in the latter case one is allowed to adopt suitable impact forces.

In this paper, a simple timber pedestrian bridge is studied and a hammer is used to excite the more significant cable. The harmonic structure of the response is found, an attempt of tension reconstruction is developed and details of the cable damping properties are discussed.

2 Cable-Stayed Bridge Case Study

Figure 1 gathers the photographs of four significant cable-stayed bridges recently constructed and today in service. The one in the bottom is fully equipped to satisfy the in-service needs: to collect estimates of the tension in the stays, and to quantify the effects of their variation on the deck's modal features, paying the necessary attention to the temperature effects [14].

The study reported in this paper refers to a timber footbridge in service in Northern Italy which is characterized by eight primary stays of diameter 44 mm of length 27 m and anchored at the height of 14.63 m [15]. A couple of internal cables were instrumented by a transversal uni-axial accelerometer and a vertical uni-axial accelerometer. The operator impacts the hammer on the former cable in the transversal direction, then moves to the parallel cable, and impacts it along the vertical direction. The two, recorded signals are plotted in Fig. 2, together with the associated periodograms, as achieved by the software [16]. It is seen that the transversal acceleration peak corresponds to the fifth harmonics, while the vertical acceleration peak corresponds to the fourth harmonics. Despite the attention is often focused on the first frequency (2.18 Hz in the case under investigation), a special remark applies to the nature of the harmonics. With reference to the vertical component, Fig. 3a shows that only retaining frequency components up to 25 Hz the peak is shortly reached and its value is consistent. The other two lines (red and cyan) show the delay and the loss of intensity when the filter cut off is set at 10 and 5 Hz, respectively.

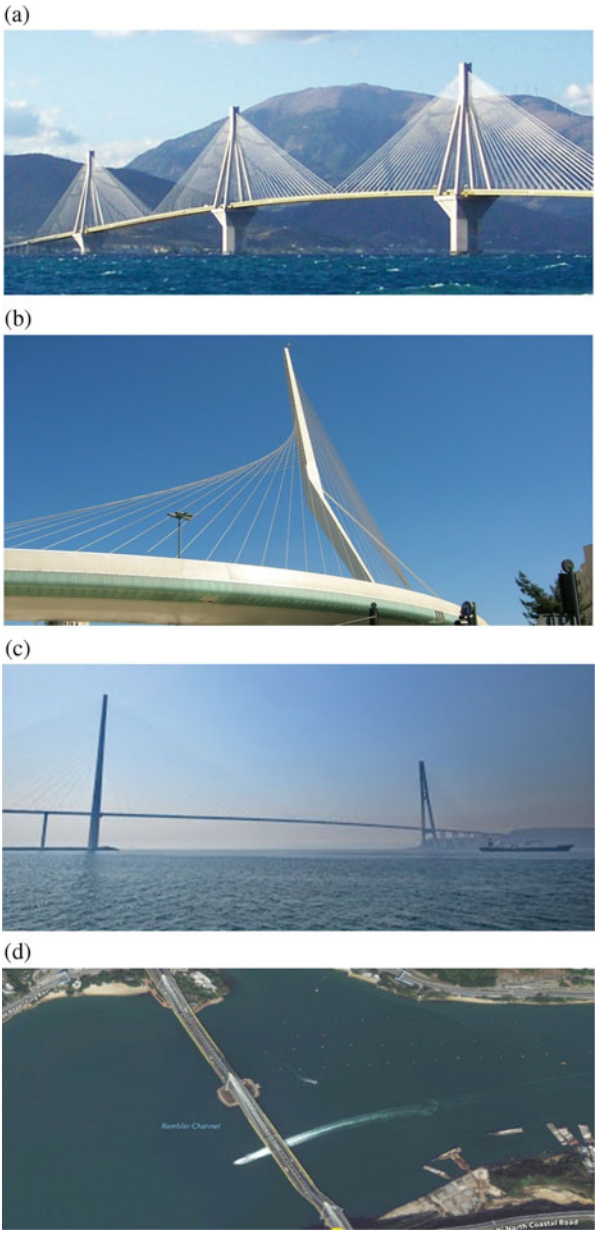

Fig. 1 Cable-stayed bridges all around the world. (**a**) Rion–Antirion bridge, Greece; (**b**) Chords bridge, Israel; (**c**) Russky bridge, Russia; (**d**) Ting Kau bridge, Hong Kong

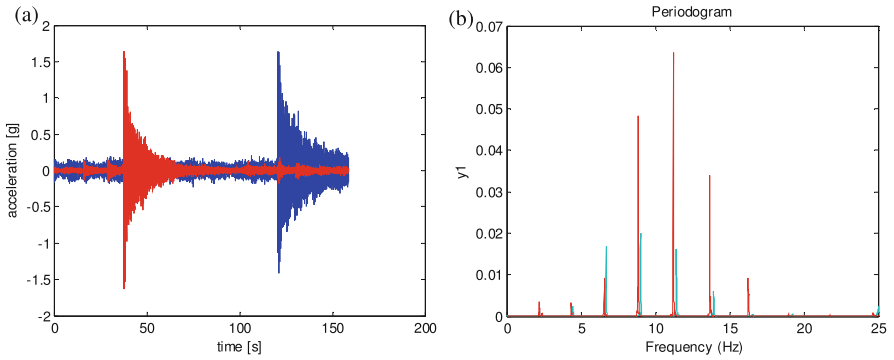

Fig. 2 (**a**) Recorded acceleration time histories: the first peak is for the horizontal transversal component, the second peak for the vertical one; (**b**) associated periodograms. The first peak is at 2.18 Hz

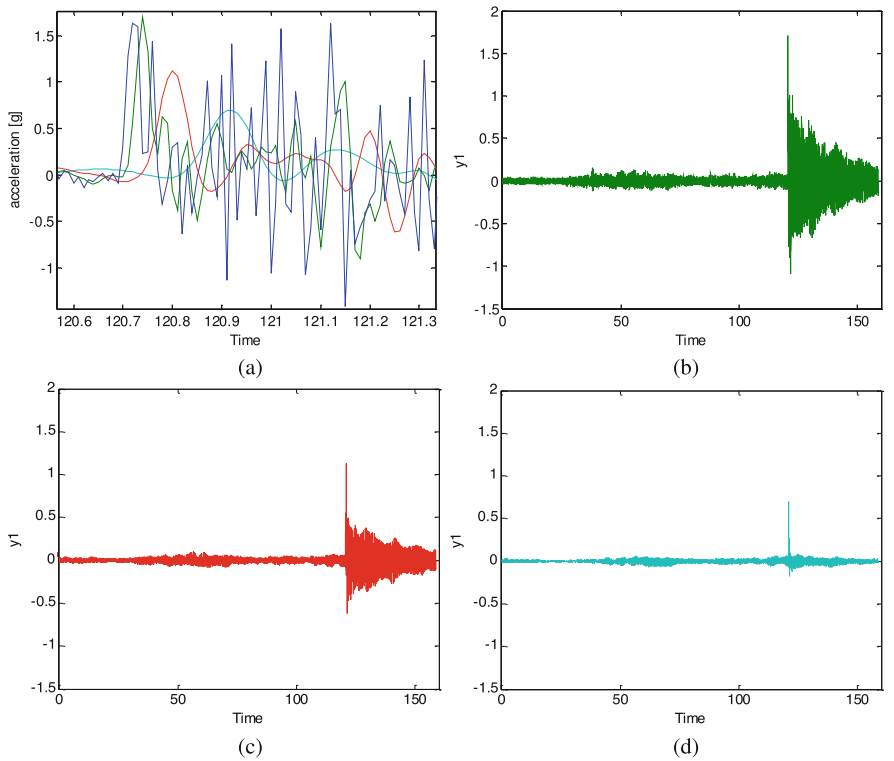

Fig. 3 (**a**) Recorded vertical acceleration time history (zoom); (**b**) the signal filtered by pass band up to 25 Hz; (**c**) the signal filtered by pass band up to 10 Hz; (**d**) the signal filtered by pass band up to 5 Hz

3 Numerical Model

As discussed in [17, 18], the main features associated with recorded signal can be reproduced by a numerical model provided a sufficient number of nodes and elements are introduced and the analyses run in large strain. In particular, for the cable under investigation, 24 elements were considered. To have the same frequency a tension of 101 [kN] had to be produced (see [15]) and this was obtained by a horizontal displacement of the top node of 1.15 cm in the negative direction. Figure 4 shows the estimates of axial force and vertical displacement in the nodes.

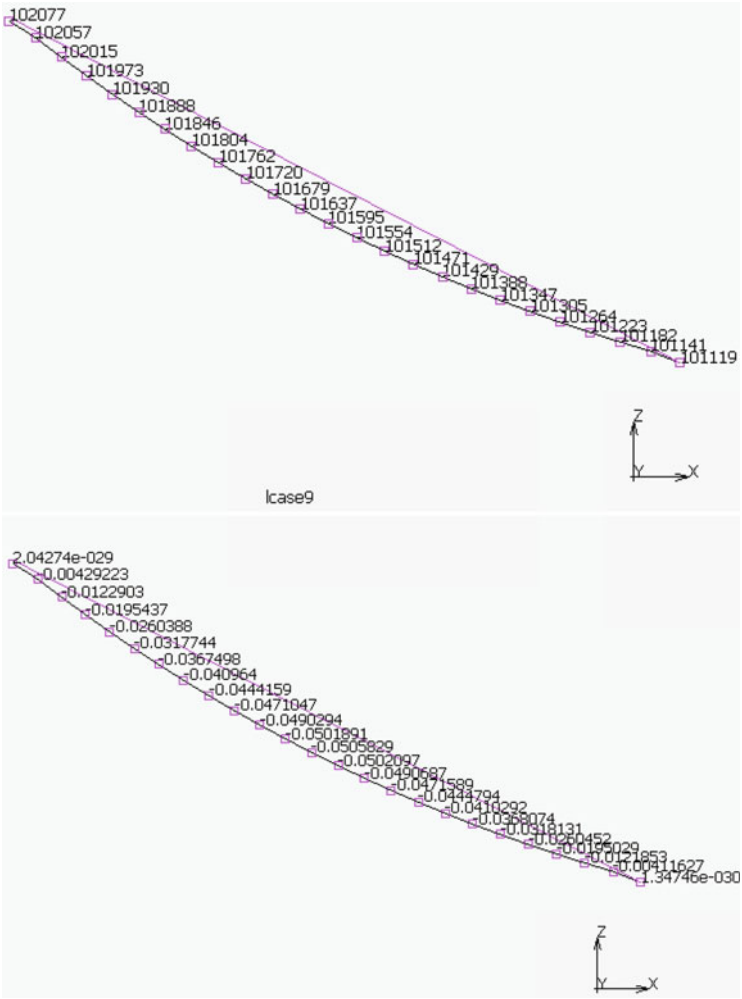

Fig. 4 Numerical estimates of the axial forces [N] along the cable (*top*) and numerical estimates of the vertical displacement [m] along the cable (*bottom*)

4 Validation of the Numerical Model

The validation/updating of the achieved numerical model includes two steps:

1. to build a suitable model for the impacting excitation, and
2. to discuss the damping properties of the system.

The only constraint within step 2 is the acceleration peak, i.e., 1.5 g. But also the peak sequence has to be taken into account. In the experiment the first peak was higher, in absolute value, than the subsequent negative one. The time history of the impacting force is a pulse of given duration.

Figure 5 compares the acceleration time histories numerically achieved for the two cases of duration 0.185 and 0.030 s, respectively. It is seen that the latter case produces an excessive second peak and this suggested to work with the first value. The associated periodogram is given in Fig. 6, where the peaks are well detected but the relative values of the peaks do not agree with that seen in Fig. 2b. As said, a comparison of the spectrum in Fig. 6 with the one in Fig. 2b shows that the two first peaks are too large. This suggests to refine the damping and, in particular, to introduce a damping matrix proportional to the mass matrix, which penalizes the low frequencies. The result is plotted in Fig. 7. A further refinement on the contribution of the stiffness matrix to the damping matrix would be required to fix the large frequency ordinates.

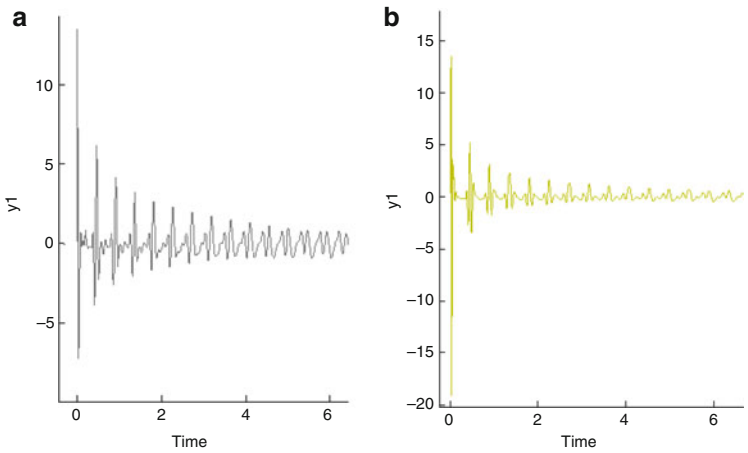

Fig. 5 Acceleration response from the numerical model under an impact excitation of duration: (**a**) 0.185 s; (**b**) 0.030 s

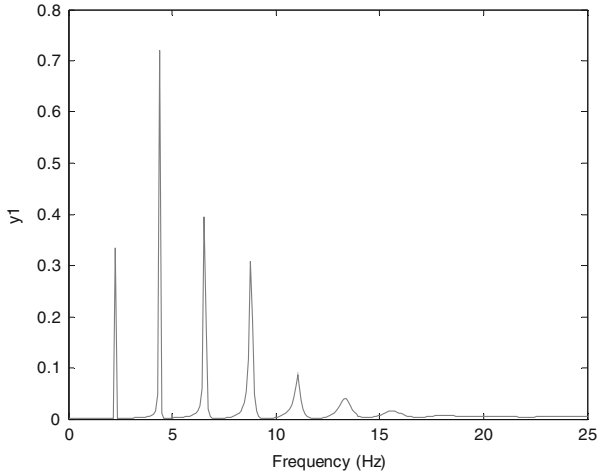

Fig. 6 Periodogram for the time history in Fig. 5a

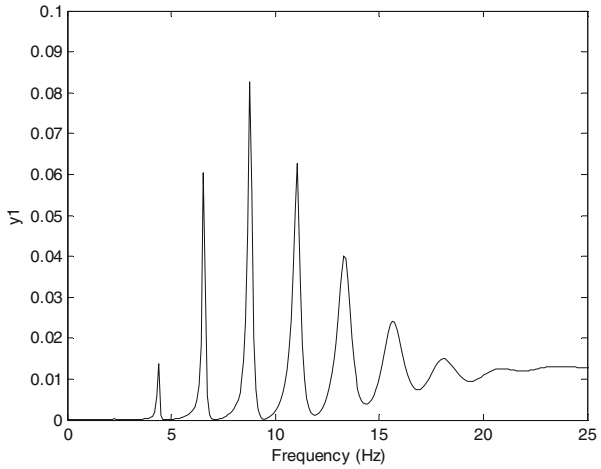

Fig. 7 Periodogram for the response time history obtained for an impact duration of 0.185 s and a damping proportional to the mass matrix (a factor 0.5 is used)

5 Conclusions

Starting from the availability of the results of an experimental campaign on a timber footbridge, attention was focused on tests carried out by exciting the cables by a hammer.

The recorded signals provided the modal features of the cable. By them, a numerical, finite element model in large strain was developed and an estimate of

the cable tension was achieved. Finally, the damping properties were outlined and the way to incorporate them in the numerical model was discussed.

Acknowledgements The authors gratefully acknowledge the financial support provided by the corresponding Athenaeum Research Grants.

References

1. Kim BH, Park T (2007) Estimation of cable tension force using the frequency-based system identification method. J Sound Vib 304:660–676
2. Casas JR (1994) A combined method for measuring cable forces: the cable-stayed Alamillo Bridge, Spain. Struct Eng Int 4(4):235–240
3. Kim BH, Shin HY (2007) A comparative study of the tension estimation methods for cable supported bridges. Int J Steel Struct 7(1):77–84
4. Ren WX, Liu HL, Chen G (2008) Determination of cable tensions based on frequency differences. Eng Comput 25(2):172–189
5. Russell JC, Lardner TJ (1998) Experimental determination of frequencies and tension for elastic cables. J Eng Mech 124(10):1067–1072
6. Humar JL (2000) Dynamics of structures. Prentice-Hall, Upper Saddle River
7. Fang Z, Wang J (2012) Practical formula for cable tension estimation by vibration method. J Bridg Eng 17:161–164
8. Sim SH, Li J, Jo H, Park JW, Cho S, Spencer BF Jr, Jung HJ (2014) A wireless smart sensor network for automated monitoring of cable tension. Smart Mater Struct 23(2):025006
9. Zui H, Shinke T, Namita YH (1996) Practical formulas for estimation of cable tension by vibration method. ASCE J Struct Eng 122(6):651–656
10. Liao W, Ni Y, Zheng G (2012) Tension force and structural parameter identification of bridge cables. Adv Struct Eng 15(6):983–996
11. Cho S, Lynch JP, Lee JJ, Yun CB (2010) Development of an automated wireless tension force estimation system for cable-stayed bridges. J Intell Mater Syst Struct 21(3):361–376
12. Li H, Zhang F, Jin Y (2014) Real-time identification of time-varying tension in stay cables by monitoring cable transversal acceleration. Struct Control Health Monit 21:1100–1111
13. Yang Y, Li S, Nagarajaiah S, Li H, Zhou P (2016) Real-time output-only identification of time-varying cable tension from accelerations via complexity pursuit. ASCE J Struct Eng 142(1):04015083
14. Ni YQ, Wang YW, Xia YX (2015) Investigation of mode identifiability of a cable-stayed bridge: comparison from ambient vibration responses and from typhoon-induced dynamic responses. Smart Struct Syst 15(2):447–468
15. Casciati S (2016) Human induced vibration vs. cable-stay footbridge deterioration. Smart Struct Syst 18(1):17–29
16. Matlab (2016) Matlab user's manual. Mathworks Inc., Lowell
17. Faravelli L, Ubertini F (2009) Nonlinear state observation for cable dynamics. J Vib Control 15(7):1049–1077
18. Bortoluzzi D, Casciati S, Elia L, Faravelli L (2015) Design of a TMD solution to mitigate wind-induced local vibrations in an existing timber footbridge. Smart Struct Syst 16(3):459–478

Dynamics and Control of Motion for Systems Containing Internal Moving Masses

F.L. Chernousko

Abstract Dynamical systems are considered that consist of a main rigid body and one or several movable internal bodies. The internal bodies interact with the main one by forces created and controlled by drives but do not interact with the environment. The motion of the internal bodies affects the main body, and it can move progressively under the influence of resistance forces produced by the environment. Different kinds of resistance forces are considered including Coulomb's friction, piecewise linear and quadratic resistance. Periodic motions of the internal bodies and the corresponding translational motion of the main body are analyzed. The average speed of the system locomotion is evaluated and optimized with respect to the system parameters and control.

1 Introduction

Consider a dynamical system that consists of main rigid body and one or several internal bodies that can move relative to the main one. The main body is placed inside the environment that exerts resistance forces upon this body, see Fig. 1. The resistance forces can be caused by the fluid outside the main body (Fig. 1a) or by the friction of the body over a rough plane (Fig. 1b). The internal bodies interact with the main one by forces created and controlled by drives but do not interact with the environment. The motion of the internal bodies affects the main one, and it can move under the influence of the outer resistance forces.

If the internal bodies perform specific periodic motions within the bounded volume inside the main body, the latter can, under certain conditions, perform a translational movement in the external environment.

This principle of locomotion can be useful for mobile robots. An advantage of these robots is that they do not need any outer propelling devices such as wheels, legs, and propellers. They can be readily made hermetic without any protruding devices. Such robots can be useful for the motion inside vulnerable and aggressive media, in narrow slots and tubes to perform various technological operations. This principle of locomotion was applied to robotic systems in [3, 8, 11, 12].

F.L. Chernousko (✉)
Institute for Problems in Mechanics, Pr. Vernadskogo 101-1, Moscow 119526, Russia
e-mail: chern@ipmnet.ru

H. Irschik et al. (eds.), *Dynamics and Control of Advanced Structures and Machines*, DOI 10.1007/978-3-319-43080-5_19

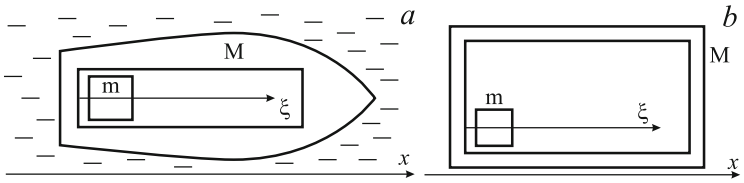

Fig. 1 Mechanical systems

The dynamics of systems controlled by the periodic motions of internal masses was first analyzed in [4, 5] for the case of Coulomb's friction force acting upon the main body. The average speed of locomotion was evaluated. Optimal parameters of the internal periodic motion were found that correspond to the maximum average locomotion speed. Experimental data confirming the obtained theoretical results are presented in [9, 10].

Other cases of resistance forces acting upon the main body were considered in [2, 6, 7]. Here, optimal parameters and optimal controls were also found. The case of two internal masses moving along horizontal and vertical directions was analyzed in [1].

In this paper, the results on dynamics and optimization for systems controlled by internal moving masses are described, summarized, and discussed.

2 Mechanical Systems

A mechanical system consists of a main body of mass M and an auxiliary internal body of mass m. The main body moves in the outer medium and is subjected to the resistance force R, see Fig. 1. The internal body can move inside the main one and does not interact with the outer medium. Denote by x and v the absolute displacement and velocity, respectively, of the main body, and by ξ, u, and w the displacement, velocity, and acceleration, respectively, of the internal body relative to the main one.

The kinematic equations have the form

$$\dot{x} = v, \quad \dot{\xi} = u, \quad \ddot{\xi} = \dot{u} = w,$$

whereas the dynamical equation can be written as follows:

$$\dot{v} = -\mu w + r(v), \tag{1}$$

where the following notation is introduced:

$$R = (M + m)r, \quad \mu = m(M + m)^{-1}.$$

Several kinds of resistance forces acting upon the main body are considered, namely the dry friction obeying Coulomb's law:

$$r(v) = -kgv \mid v \mid^{-1}, \quad \text{if} \quad v \neq 0, \quad \mid r(v) \mid \leq kg, \quad \text{if} \quad v = 0; \tag{2}$$

linear resistance:

$$r(v) = -kv; \tag{3}$$

and quadratic resistance:

$$r(v) = -kv \mid v \mid . \tag{4}$$

The coefficients k in Eqs. (2)–(4) are constant in the case of isotropic resistance. For the anisotropic resistance, these coefficients depend on direction of motion:

$$k = k_+, \quad \text{if} \quad v > 0; \quad k = k_-, \quad \text{if} \quad v < 0. \tag{5}$$

3 Internal Motions

Let the internal body move periodically with period T relative to the main body, so that for all t

$$\xi(t + T) = \xi(t). \tag{6}$$

We assume that this motion is bounded:

$$0 \leq \xi(t) \leq L. \tag{7}$$

Without loss of generality, suppose that the internal body starts its motion at the left end of the interval $[0, L]$ and reaches the right end of this interval at the instant of time θ. Then we have

$$\xi(0) = \xi(T) = 0, \quad \xi(\theta) = L, \quad u(0) = u(\theta) = 0, \quad \theta \in (0, T). \tag{8}$$

Let us consider two simple versions of possible internal motions satisfying (6)–(8).

1. The relative velocity *u(t)* is piecewise constant and has two phases (Fig. 2):

$$u(t) = u_1, \quad \text{if} \quad t \in (0, \theta); \quad u(t) = -u_2, \quad \text{if} \quad t \in (\theta, T). \tag{9}$$

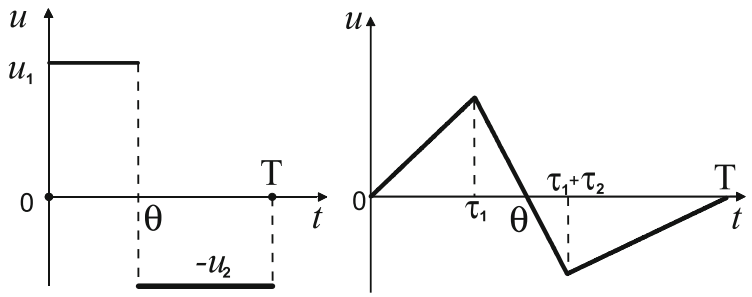

Fig. 2 Velocity control and acceleration control cases

Velocities u_i in (9) are assumed to be bounded by a given constant U:

$$0 < u_i \le U, \quad i = 1, 2. \tag{10}$$

2. The relative acceleration *w(t)* is piecewise constant and has three phases:

$$w(t) = w_1, \quad \text{if} \quad t \in (0, \tau_1), \quad w(t) = -w_2, \quad \text{if} \quad t \in (\tau_1, \tau_1 + \tau_2),$$
$$w(t) = w_3, \quad \text{if} \quad t \in (\tau_1 + \tau_2, T). \tag{11}$$

Here, τ_1 and τ_2 are positive constants, accelerations w_i are bounded by constant W:

$$0 < w_i \le W, \quad i = 1, 2, 3. \tag{12}$$

The two cases described above will be referred to as velocity and acceleration control cases, respectively. They correspond to different possibilities of actuators controlling the relative motion of the internal body. The graphs of the relative velocity for these cases are shown in Fig. 2. Note that each of these control modes has the minimal possible number of intervals of constant control compatible with the conditions imposed by (6)–(8): two intervals for the velocity control and three for the acceleration control.

The following requirements are imposed on the motion of the main body:

(a) The velocity *v(t)* is periodic with the same period T as the period of the internal motion in (6): $v(t + T) = v(t)$ for all t.
(b) For the initial velocity $v(0) = v_0$, two alternative assumptions are made: either $v_0 = 0$, or v_0 is a free parameter to be chosen.

The total displacement of the system for the period of motion Δx and its average velocity V are defined as

$$\Delta x = x(T) - x(0), \quad V = \Delta x / T. \tag{13}$$

We will determine the optimal parameters of the velocity and acceleration controls that correspond to the maximum average speed V for various resistance forces under the imposed conditions (a) and (b).

4 Linear and Quadratic Resistance

Consider first the case of the linear isotropic resistance defined by Eq. (3). By integrating both sides of Eq. (1) over period T, it can be shown easily that $\Delta x = 0$ for any periodic internal motion $\xi(t)$. Hence, in the linear isotropic medium, the main body will only oscillate about some mean position, and the progressive motion is impossible.

The optimal velocity control described by Eqs. (9) and (10) was obtained for the cases of anisotropic linear and quadratic resistance [7].

We assume that the initial velocity v_0 in condition (b) is chosen so as to maximize the average velocity V. Then the maximum average velocity for the linear anisotropic case described by (3) and (5) is given by

$$V_{\max} = \mu U^2 L^{-1}(1-e_1)(1-e_2)(1-e_1e_2)^{-1}(k_+^{-1}-k_-^{-1}), \tag{14}$$

where the following notation is used:

$$e_1 = \exp(-k_- T/2), \quad e_2 = \exp(-k_+ T/2), \quad T = 2L/U.$$

The velocity $V_{\max}$ in (14) is positive, if and only if the resistance for the forward motion is smaller than for the backward one: $k_+ < k_-$.

Similarly, the case of the quadratic anisotropic resistance defined by (4) and (5) has been considered. Contrary to the linear resistance, here the maximum average velocity is positive even in the isotropic case. We have

$$V_{\max} = -(kT)^{-1}\log(1-\mu^2 k^2 L^2) > 0, \quad T = 2L(1-\mu kL)^{-1}U^{-1}, \quad \mu kL < 1.$$

More general case of resistance forces was analyzed in [2]. For a wide class of functions $r(v)$ in Eq. (1), the optimal relative acceleration $\ddot{\xi}(t)$ subject to the bounds $|\ddot{\xi}| \leq W$ was found that provides the maximum value of Δx and V for a given T. The optimal control $\ddot{\xi}(t)$ has up to four different intervals; on two of them, the control reaches the bounds imposed; the other two intervals are singular control arcs where the velocity of the main body $v(t)$ is constant.

5 Dry Friction

Consider now an important case of the dry friction obeying Coulomb's law (2). This case under the condition that $v_0 = 0$ was analyzed in [5]; for free v_0 that can be chosen in an optimal way, it was investigated in [6]. The analysis for the anisotropic friction is rather complicated. Here, we will present some final results only for the case of isotropic friction with coefficient k.

For the velocity control defined by Eqs. (9) and (10) and for the case with $v_0 = 0$, we have

$$V_{\max} = 0.5(\mu k L g)^{1/2}, \tag{15}$$

if the maximal admissible U in (10) satisfies the inequality

$$U \geq u_0, \quad u_0 = (kLg/\mu)^{1/2}. \tag{16}$$

If inequality (16) is violated, the motion under consideration is impossible.

For the velocity control and the case where v_0 can be chosen arbitrarily, we have

$$V_{\max} = (\mu k L g)^{1/2}(2U^2 - u_0^2)(2Uu_0)^{-1}, \tag{17}$$

if the following inequality:

$$U \geq 2^{-1/2}u_0 \tag{18}$$

is satisfied. Otherwise, the motion is impossible.

Comparing inequalities (16) and (18), we see that the case with a free value of v_0 can be realized in a wider range of admissible velocities U. Under the condition $U \geq u_0$ where the both types of motion can be implemented, the motion with a free value of v_0 provides a higher average velocity $V_{\max}$ (compare (15) and (17) for $U \geq u_0$), which is quite natural.

Let us consider now the acceleration control defined by (11) under the condition $v_0 = 0$. Here, the motion is possible, if and only if the maximal possible acceleration W of the internal body in (12) satisfies the inequality

$$Y = \mu W(kg)^{-1} > 1. \tag{19}$$

Under this condition, the maximal possible velocity of the main body is given by formulas [5]:

$$\begin{aligned} V_{\max} &= (\mu k L g/2)^{1/2} F(Y), \\ F(Y) &= (Y-1)[Y(Y+1)]^{-1/2}, \quad \text{if} \quad 1 < Y \leq 2+\sqrt{5}, \\ F(Y) &= [Y(Y+1)]^{1/2}, \quad \text{if} \quad Y > 2+\sqrt{5}, \end{aligned} \tag{20}$$

where Y is defined by (19).

The analysis of optimal motions for the velocity and acceleration control cases showed that, for the velocity control, the motion of the main body consists of alternating forward and backward motions, whereas for the acceleration control, there are only forward motions and intervals of rest.

Let us compare the maximal speeds of motion (15) and (20) for $v_0 = 0$ and unbounded internal motions, i.e., for $U \to \infty$ and $W \to \infty$.

We obtain

$$V_1 = 0.5(\mu k L g)^{1/2}, \quad V_2 = 0.707(\mu k L g)^{1/2}$$

for the velocity and acceleration control cases, respectively. Thus, the maximal speeds are of the same order of magnitude, the acceleration control providing a higher speed.

If the main body contains two internal bodies moving in the horizontal and vertical directions, respectively, this can give additional possibilities to increase the average speed of locomotion. The internal body moving in the vertical direction causes the change in the normal reaction and, hence, in the friction force acting upon the main body. Optimal control of two internal bodies moving along horizontal and vertical directions within the main one was obtained in [1].

The principle of locomotion based upon the controlled displacement of internal masses was implemented in a number of experimental models. In Fig. 3, the internal motion is performed by an inverted pendulum that oscillates about the vertical equilibrium position [9]. The system called capsubot and shown in Fig. 3 contains an internal mass that is driven by an electromagnetic actuator and oscillates inside the main body [10]. The cart shown in Fig. 4 carries eccentric rotating wheels and moves along a horizontal plane. Here, the internal masses move both in the horizontal and vertical directions.

Mini-robots based on the locomotion principle described above that can move inside tubes were created in the Institute for Problems in Mechanics [8]. These vibro-robots are driven by electromagnetic actuators and move inside horizontal,

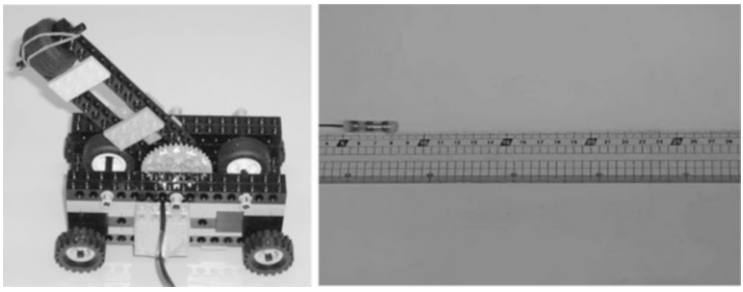

Fig. 3 Inverted pendulum and capsubot

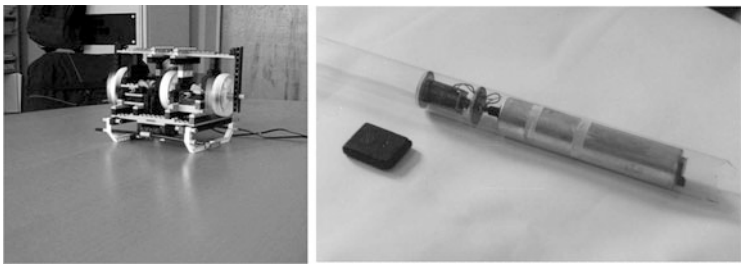

Fig. 4 Cart with rotors and vibro-robot in a tube

vertical, sloping, and curved tubes of a diameter of 4–50 mm with a speed of 0.1–0.3 m/s. They can carry various sensors and perform inspection as well as other operations (Fig. 4).

6 Conclusions

Locomotion of a rigid body controlled by internal moving masses is discussed. Certain classes of periodic motions of the internal masses are examined. The system can move inside a resistive medium; different types of resistance forces are considered. The average velocity of locomotion is evaluated. The optimal parameters of the internal motion are found that correspond to the maximum locomotion speed. Experimental models of mobile robots are described that implement the principle of locomotion analyzed in the paper.

Acknowledgements The work was supported by the Russian Foundation for Basic Research (Projects 14-01-00061 and 15-51-12381).

References

1. Bolotnik NN, Figurina TYu (2008) Optimal control of the rectilinear motion of a rigid body on a rough plane by the displacement of two internal masses. J Appl Math Mech 72(2):126–135
2. Bolotnik NN, Figurina TYu, Chernousko FL (2012) Optimal control of the rectilinear motion of a two-body system in a resistive medium. J Appl Math Mech 76(1):1–14
3. Breguet J-M, Clavel R (1998) Stick and slip actuators: design, control, performances and applications. In: Proceedings of the international symposium micromechatronics and human science (MHS). IEEE, New York, pp 89–95
4. Chernousko FL (2005) On the motion of a body containing a movable internal mass. Dokl Phys 50(11):593–597
5. Chernousko FL (2006) Analysis and optimization of the motion of a body controlled by a movable internal mass. J Appl Math Mech 70(6):915–941

6. Chernousko FL (2008) On the optimal motion of a body with an internal mass in a resistive medium. J Vib Control 14(1–2):197–208
7. Chernousko FL (2008) The optimal periodic motions of a two-mass system in a resistant medium. J Appl Math Mech 72(2):202–215
8. Gradetsky V, Solovtsov V, Kniazkov M, Rizzotto GG, Amato P (2003) Modular design of electro-magnetic mechatronic microrobots. In: Proceedings of the 6th international conference climbing and walking robots (CLAWAR), Catania, Italy, pp 651–658
9. Li H, Firuta K, Chernousko FL (2005) A pendulum-driven cart via internal force and static friction. In: Proceedings of the international conference "physics and control", St.-Petersburg, Russia, pp 15–17
10. Li H, Firuta K, Chernousko FL (2006) Motion generation of the Capsubot using internal force and static friction. In: Proceedings of the 45th IEEE conference decision and control, San Diego, CA, USA, pp 6575–6580
11. Schmoeckel F, Worn H (2001) Remotely controllable mobile microrobots acting as nano positioners and intelligent tweezers in scanning electron microscopes (SEMs). In: Proceedings of international conference on robotics and automation, vol 4, New York, pp 3903–3913
12. Vartholomeos P, Papadopoulos E (2006) Dynamics, design and simulation of a novel microrobotic platform employing vibration microactuators. Trans ASME J Dyn Syst Meas Control 128:122–133

Elaborations from the TKB Monitoring Database

S. Casciati and L. Elia

Abstract The ambient vibration is one of the viable output data-only structural dynamic testing options by winds and typhoons. This contribution aims to present the application of a reliable method such as the stochastic subspace identification implemented in a general-purpose software. One of the greatest infrastructures built in Hong Kong, i.e., the Ting Kau Bridge, is addressed as a case study. Results reveal that the proposed method detects both frequencies and mode shapes despite the reduced number of sensors adopted.

1 Introduction

One of the most active areas in the civil engineering field is certainly structural health monitoring. A large amount of system identification techniques has been developed and enhanced since the past few decades. Indeed, the main purpose is to estimate the modal parameters of a mathematical model of the structure under study. Parameters identification via dynamic measurements is a discipline originally improved in aerospace and mechanical engineering as found in literature [1–3], among the others. In the civil engineering context, the parameters to be estimated by dynamic measurements come directly from the modal nature, i.e., frequencies, damping ratios, and mode shapes [4]. Such parameters will supply a basis for the input to the finite element model, but also provide the necessary feedback for detecting and locating damage.

Structural dynamic testing is basically subdivided into three main classes: (1) forced vibration testing, (2) free vibration testing, and (3) ambient vibration testing. The output-only modal identification techniques are gathered in two groups, (1) the frequency domain methods, and (2) time domain methods [5]. In civil engineering,

S. Casciati (✉)
Department of Civil Engineering and Architecture, University of Catania, Piazza Federico di Svevia, Siracusa, Italy
e-mail: saracasciati@msn.com

L. Elia
Department of Civil Engineering and Architecture, University of Pavia, via Ferrata 3, Pavia, Italy
e-mail: lorenzo.elia@unipv.it

H. Irschik et al. (eds.), *Dynamics and Control of Advanced Structures and Machines*, DOI 10.1007/978-3-319-43080-5_20

sensors are placed at different locations to record the output. But the difficult task is to identify the input or the excitation level on a real structure under its service conditions.

The benchmark started in [6] focuses on the mechanism behind the output-only modal identification, the deficiency in modal identifiability, and the criteria to evaluate robustness of identified modes.

In this contribution, the stochastic subspace identification (SSI)-data driven method as found in the MACEC tool [7] is employed for the identification of modal parameters.

2 The Governing Relations

Hereinafter, a briefly overview of the governing relations is shown. Ambient vibration testing requires developments by modal parameter identification methods. Therefore, the choice of authors fell on the SSI method well implemented in the MACEC [7] environment working within the commercial software MATLAB [8].

Since literature is rich of contribution about this theme, the reader is referred to [9–12] among the others.

Modal analysis of a structure develops along three principal steps, namely the data collection, the system identification, and the determination of modal features, such as eigenvalues, damping ratios, eigenvectors, and so forth [13]. The above-mentioned toolbox, i.e., MACEC, is able to handle with each step in the modal analysis procedure, and it saves for the data collection.

The tool is applied for verifying the modal parameter under the first set of blind data provided by the benchmark study where the contribution is included.

3 The Ting Kau Bridge, Hong Kong

The Ting Kau Bridge (TKB) is a cable-stayed bridge situated in Hong Kong and it connects the Tsing Yi Island to the Tuen Mun Road [14]. There are four spans: the two main ones are 448 and 475 m long, while the side-spans are 127 m long. There are three slender towers (170, 198, and 158 m high, respectively) along the deck that is divided into two carriageways 18.8 m width. There are also steel girders along the edges of the deck, and each 13.5 m there are connecting crossgirders, which link the 5.2 m gap between the carriageways. Furthermore, 384 stay-cables are installed and support the deck.

More than 230 sensors were installed on the TKB, within a long-term SHM system conceived by the Hong Kong SAR Government Highways Department, as shown in Fig. 1. In this contribution, only the data collected by the accelerometers placed on the deck are considered. Indeed, in each section from A to K in Fig. 2, two accelerometers are placed on the east and west side of the deck and they measure the

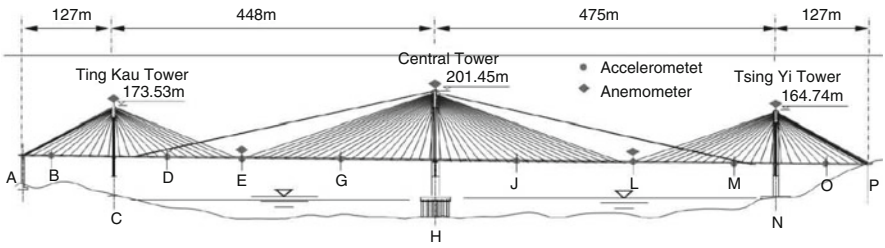

Fig. 1 Deployment of the devices installed on the bridge

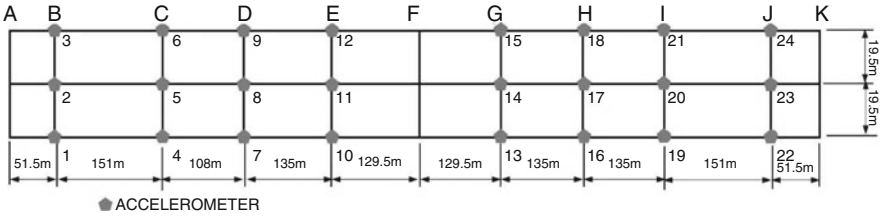

Fig. 2 Actual deployment of accelerometers at the bridge deck (sections A–K)

vertical acceleration, while another set of accelerometers is placed across the central crossgirder and measures the transverse acceleration. For sake of completeness, the sampling frequency is 25.6 Hz.

4 Collected Records and Elaborations

Different sets of data are collected and used in order to carry out the modal identification. The available field measurements consist of ten sets of monitored nodal acceleration and wind speed. In particular, one relies on six sets recorded under weak excitations and four sets under typhoon excitations, as reported in Tables 1 and 2. In addition, a further set of data without knowing the excitation condition is provided. Such set is properly called "blind dataset" [15]. Figure 3 shows the time history of the wind velocity resulting in the external force for Sample 6 in Table 1, in condition of weak wind. The mean hourly speed is equal to 4.21 m/s and the data were gathered on August 12, 1999, by a set of anemometers, which constantly record the pressure and the speed of the wind. Twenty four sensors installed at the bridge deck record the accelerations due to the external excitation (i.e., the wind or the typhoon) and Fig. 4 shows the response recorded by the first channel as stated in Fig. 2. For sake of completeness, one specifies that such sensor records the vertical

Table 1 Data samples under weak wind conditions

Sample	Time duration	Mean hourly wind speed (m/s)
Sample 1	15:00–16:00 28 Dec 1999	2.00
Sample 2	15:00–16:00 18 Feb 1999	3.40
Sample 3	15:00–16:00 01 Mar 1999	3.34
Sample 4	15:00–16:00 21 Jun 1999	3.41
Sample 5	15:00–16:00 24 Jul 1999	6.17
Sample 6	15:00–16:00 12 Dec 1999	4.2

Table 2 Data samples under typhoon conditions

Sample	Time duration	Mean hourly wind speed (m/s)
Maggie	03:00–04:00 07 Jun 1999	22.11
Sam	02:00–03:00 23 Aug 1999	15.62
York	06:00–07:00 16 Sep 1999	21.72
York	15:00–16:00 16 Sep 1999	15.91

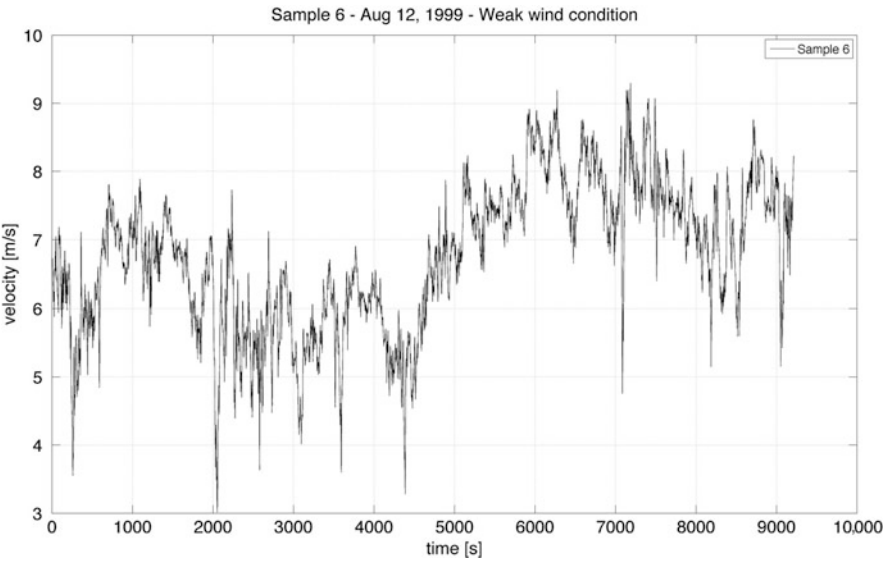

Fig. 3 Plot of the velocity for Sample 6 under weak wind conditions

acceleration. Let now consider the sample "Typhoon Maggie" (see Table 2), whose speed is 12.11 m/s and whose recording occurred on June 7, 1999. Toward the data provided, the acceleration of the first channel is shown in Fig. 5, which corresponds to the first sensor placed on the east side of the deck. According to the same procedure, the first set of blind data is considered too. In this set of data, the external condition remains unknown. One of the challenges carried out in the benchmark launched in [15] was exactly the use of these "blind" datasets for obtaining further

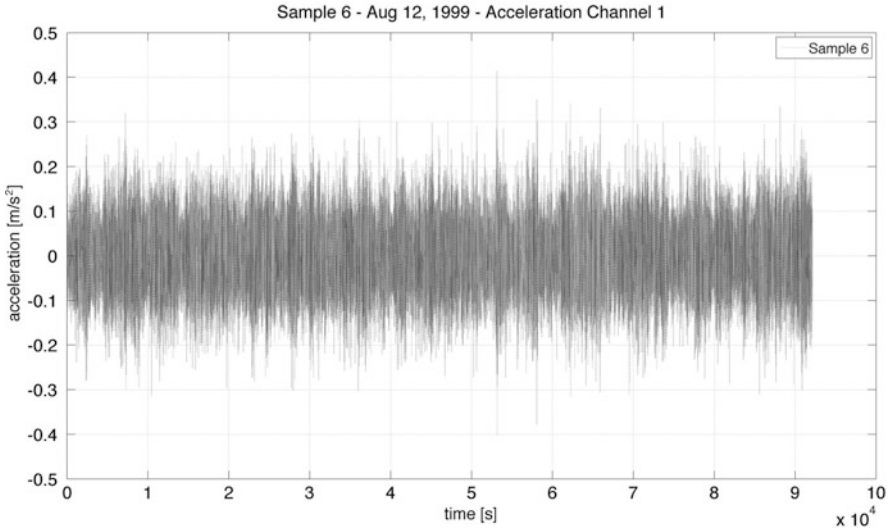

Fig. 4 Response recorded by the first channel (weak wind condition)

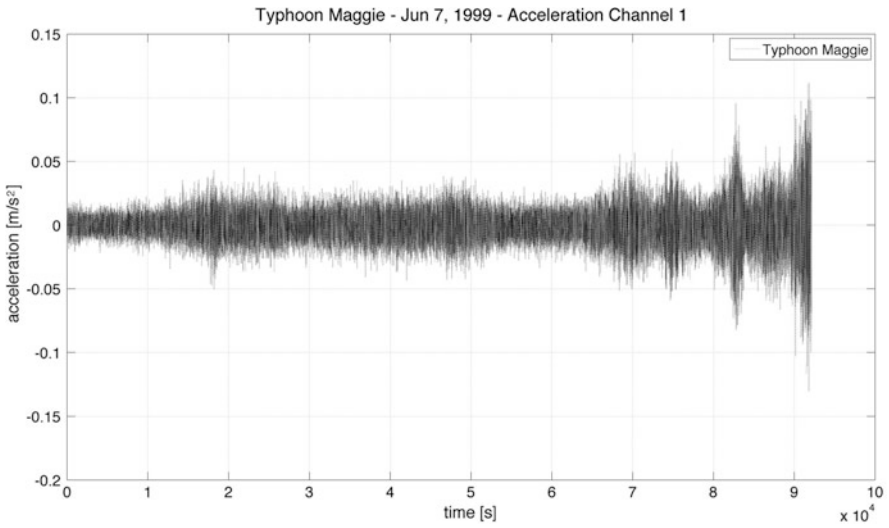

Fig. 5 Acceleration of the first channel (Typhoon Maggie sample)

modal information. Figure 6 illustrates the accelerogram corresponding to the first channel. The recorded signals are processed in the MATLAB environment for outlining the dominating frequencies.

Hereinafter, a set of figures (from Figs. 7, 8, and 9) and remarks are reported. When comparing the three periodograms, one has evidence that the record of Fig. 6, despite a little more than negligible noise, already contains a mapping of

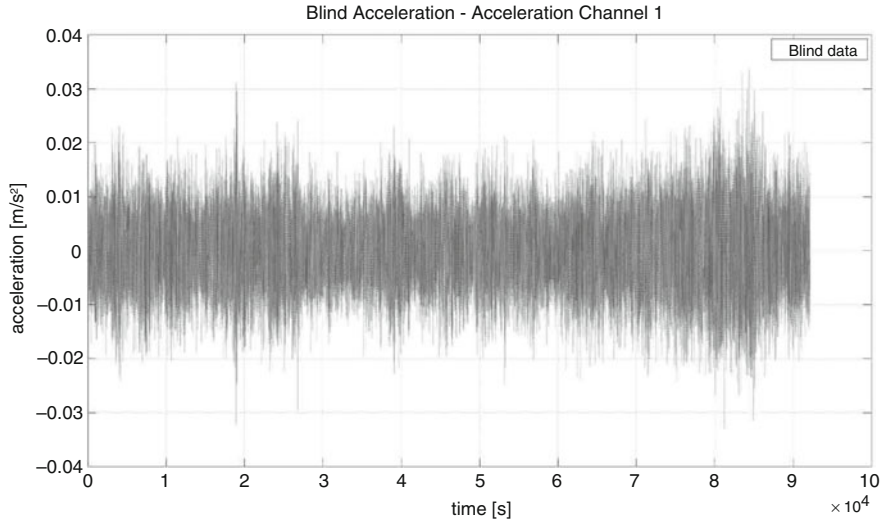

Fig. 6 Acceleration of the first channel (first sample of blind dataset)

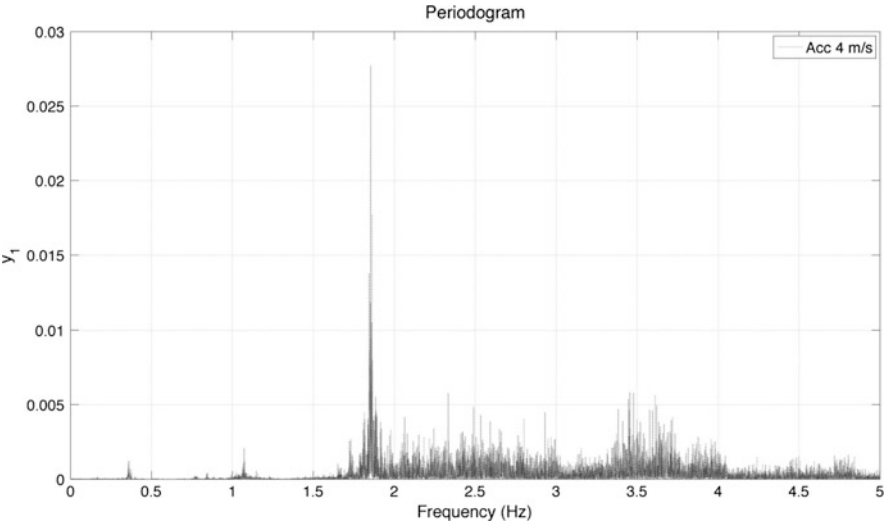

Fig. 7 Periodogram of the acceleration signal recorded at station 1 under the external excitation labelled as "Sample 6"

the frequencies involved. Then the stationary wind excitation of Fig. 4 enhances the peak near 2 Hz, with the ordinates in Fig. 7 higher than those in Fig. 8, which corresponds to the typhoon. For it, the geometric nonlinearity associated with the cable response seems to translate the values of the significant frequencies (around 1 Hz) due to the fluctuation of the tension in some cables.

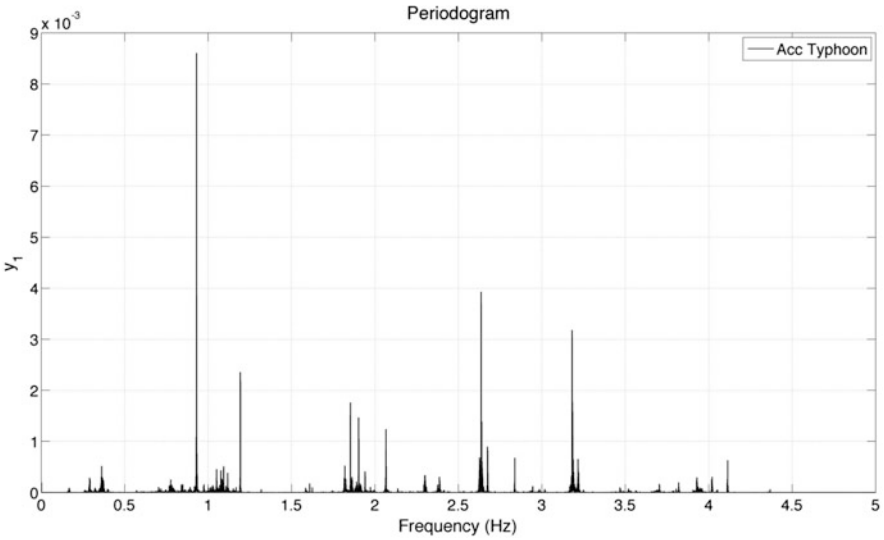

Fig. 8 Periodogram of the acceleration signal recorded at station 1 under the external excitation labelled as "Typhoon Maggie"

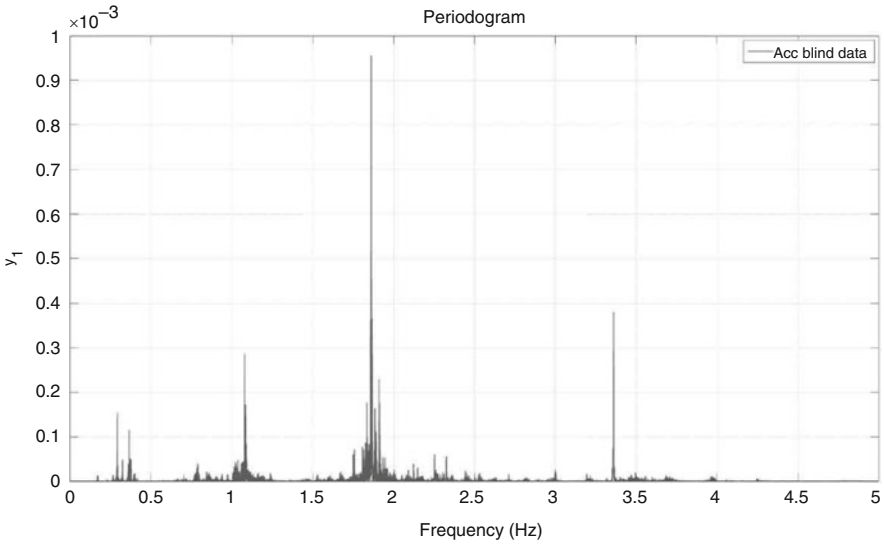

Fig. 9 Periodogram of the acceleration signal recorded at station 1 under the external excitation labelled as "Blind dataset"

5 Conclusions

This contribution exploits the availability of a significant amount of recorded data collected for the cable-stayed bridge, TKB, which is located in Hong Kong.

Despite no damage was detected along the structural system, the geometrically nonlinear response of the cables translates into different modal responses depending on the excitation intensity.

In particular, under a typhoon excitation, the periodogram peaks seem to move, as predicted by the theory, but, in order to achieve conclusions, a deeper investigation covering the whole set of accelerometers deployed along the deck would be required.

Acknowledgements The authors gratefully acknowledge the financial support provided by the corresponding Athenaeum Research Grants.

References

1. Ewins DJ (1986) Modal testing: theory and practice. Research Studies Press Ltd., Baldock
2. Ljung L (1987) System identification: theory for the user. Prentice-Hall, Englewood Cliffs
3. Juang JN (1994) Applied system identification. Prentice-Hall, Englewood Cliffs
4. Zhou G-D, Yi T-H, Zhang H, Li H-N (2015) Energy-aware wireless sensor placement in structural health monitoring using hybrid discrete firefly algorithm. Struct Control Health Monit 22(4):648–666
5. Peeters B, De Roeck G (2001) Stochastic system identification for operational modal analysis: a review. J Dyn Syst Meas Control 123(4):659–667
6. Ni YQ, Wang YW, Xia YX (2015) Investigation of mode identifiability of a cable-stayed bridge: comparison from ambient vibration responses and from typhoon-induced dynamic responses. Smart Struct Syst 15(2):447–468
7. Reynders E, De Roeck G, Schevenels M (2014) MACEC 3.3 user's manual, Department of Civil Engineering, Catholic University of Leuven, Belgium
8. Matlab (2016) Matlab user's manual. Mathworks Inc., Lowell
9. Van Overschee P, De Moor B (1996) Subspace identification for linear systems: theory, implementation and applications. Kluwer Academic, Dordrecht
10. Peeters B, De Roeck G (1999) Reference-based stochastic subspace identification for output-only modal analysis. Mech Syst Signal Process 13(6):855–878
11. Chen HP, Huang TL (2012) Updating finite element model using dynamic perturbation method and regularization algorithm. Smart Struct Syst 10(4–5):427–442
12. Reynders E, De Roeck G (2008) Reference-based combined deterministic-stochastic subspace identification for experimental and operational modal analysis. Mech Syst Signal Process 22(3):617–637
13. Casciati S, Elia L (2016) Potential of two metaheuristic optimization tools for damage localization in civil structures (submitted for publication)
14. Bergermann R, Schlaich M (1996) The Ting Kau bridge, Hong Kong. Struct Eng Int 6(3):152–154
15. Department of Civil & Environmental Engineering, The Hong Kong Polytechnic University (2015) Benchmark study on modal identifiability. http://zn903.com/benchmarkstudy/

Reduced Order Models and Localized Nonlinearity: An Approach to the Design of Meta-Structures

F. Casciati

Abstract Impact events on soil media cause vibrations that propagate all around the impact site. These vibrations can be mitigated by the construction of suitable buried barriers. A recent proposal suggests of realizing them by meta-structures characterized by a nonlinear response. Their design requires repeated analyses of the whole system made of soil and barriers. A simplification is achieved by building the reduced order model of the linear system and incorporating the nonlinear effects as suitable external actions.

1 Introduction

As often occurred in the last decades, scientific neologisms are first acquired by electronics, where the term meta-structure means a structure based upon meta-materials and meta-material denotes any material that obtains its electromagnetic properties from its structure rather than from its chemical composition. But in Wikipedia (https://en.wikipedia.org/wiki/Metamaterial#Structural) one also reads: "Structural metamaterials provide properties such as crushability and light weight. Using projection micro-stereolithography, microlattices can be created using forms much like trusses and girders". Starting from this point of view, one easily reaches a quite different concept, still named meta-structure, as adopted in [1], where the authors "propose to use an array of resonating structures (herein termed a "metastructure") buried around sensitive buildings to control the propagation of seismic waves". Thus the topic addressed by the last term in the title is clarified. Just for sake of completeness, this term is also used by modern painters (http://www.blackbookgallery.com/meta-structures) and in a socio-epistemological context [2].

The idea of buried barriers in vibration mitigation is not new and implementations are mainly associated with the traffic induced vibration [3–5]. This was synthesized by the FP7 research project RIVAS (http://www.rivas-project.eu/index.php?id=8), which recently celebrated its closure conference. But extensions to the

F. Casciati (✉)
Department of Civil Engineering and Architecture, University of Pavia, via Ferrata 3, Pavia, Italy
e-mail: fabio@dipmec.unipv.it

H. Irschik et al. (eds.), *Dynamics and Control of Advanced Structures and Machines*, DOI 10.1007/978-3-319-43080-5_21

protection from seismic [6], machine foundation [7] or blast [8] generated waves are easily found in the literature. Also the technology insight in this barrier is quite broad and spans from passive [9] to active [10] solutions.

Once the concept has been introduced, the next step is how to design such a technological solution to the problem of vibration mitigation. The numerical model has to simulate soil–structure interaction [11] and, as usual in these cases, the size of the problem is quite large. On the other side, the barriers are better designed to behave in a nonlinear way, making the problem nonlinear. Thus standard model order reduction (MOR) schemes [12] could not be adopted, since they only hold for linear problems, and much more sophisticated schemes [13, 14] for the reduction of nonlinear systems to be required.

Indeed an extension of standard MOR to include cases with localized nonlinearities was recently introduced [15], with an application to the problem of falling helicopter impact. Such a problem is approached in this paper with focus on the consequence of the nonlinearity assumed for the protection barriers.

2 MOR Governing Relations

With reference to a dynamic transient analysis problem, the governing partial differential equation system is reduced to a set of ordinary derivative differential equations by finite element discretization. Introducing the so-called state space representation, only linear derivatives of time are considered, with the number of equations being doubled. One writes

$$\dot{\boldsymbol{z}}(t) = \boldsymbol{A}\boldsymbol{z}(t) + \boldsymbol{B}\boldsymbol{u}(t), \tag{1}$$

where $\boldsymbol{z}$ is the state variable vector of size $2N$, the superimposed dot denotes time derivative, $\boldsymbol{u}$ is the vector of the external excitations, of size p, and $\boldsymbol{A}$ and $\boldsymbol{B}$ are time invariant matrices of sizes $2N$ by $2N$ and $2N$ by p, respectively. The state variables are not supposed to have any physical meaning. But they are linked to any set of observables variables $\boldsymbol{y}(t)$ (denoted as "observed variables") by a second set of equations, this time of the algebraic type

$$\boldsymbol{y}(t) = \boldsymbol{C}\boldsymbol{z}(t) + \boldsymbol{D}\boldsymbol{u}(t). \tag{2}$$

An often-met situation sees the vector $\boldsymbol{y}$ ordered to give N (relative to the base) displacements followed by N (relative) velocities, so that, if $\boldsymbol{z}$ coincides with $\boldsymbol{y}$, $\boldsymbol{C}$ becomes an identity matrix of size $2N$ and $\boldsymbol{D}$ is assumed to be 0.

Model reduction procedures are discrete versions of Ritz–Galerkin analyses: they seek solutions in the subspace generated by a transformation matrix $\boldsymbol{T}$ [12]. Among different alternative schemes one adopts here the approach that re-writes Eq. (1) in a different basis system and apply to the obtained balanced system a truncation using

Hankel singular values; the basis transformation also applies to Eq. (2) and after truncation just a bit of information is lost.

Equations (1) and (2) can be re-written adding the suffix "*R*" (for reduced) to all the quantities except the observed variables [12] when the reduced order model is pursued by balanced truncation

$$\dot{\boldsymbol{z}}_R(t) = \boldsymbol{A}_R \boldsymbol{z}_R(t) + \boldsymbol{B}_R \boldsymbol{u}(t), \tag{3}$$

$$\boldsymbol{y}(t) = \boldsymbol{C}_R \boldsymbol{z}_R(t). \tag{4}$$

The number of state variables is now n, with n significantly lower than $2N$. As discussed in [15], the whole procedure and hence the suitable value of n is significantly affected by the size and nature of the matrix $\boldsymbol{C}$ as well as by the actual acceleration considered in the problem formulation.

Assume now that the structural problem contains localized material nonlinearities. Equations (1) and (2) become

$$\dot{\boldsymbol{z}}(t) = \boldsymbol{A}\boldsymbol{z}(t) + \boldsymbol{B}\boldsymbol{u}(t) + \boldsymbol{R}\boldsymbol{q}(t), \tag{5}$$

$$\boldsymbol{y}_{\mathrm{NL}}(t) = \boldsymbol{C}_{\mathrm{NL}} \boldsymbol{z}(t), \tag{6}$$

$$\boldsymbol{q}(t) = \boldsymbol{f}(\boldsymbol{u}(t), \boldsymbol{y}_{\mathrm{NL}}(t)), \tag{7}$$

where the nonlinearities are accounted for the vector q, related to the current state and the displacements $\boldsymbol{y}_{\mathrm{NL}}$ in the nodes surrounding the nonlinearity domains. They are simply related to the state variables via the matrix $\boldsymbol{C}_{\mathrm{NL}}$.

Equations (5) and (6) are linear and hence standard MOR applies:

$$\dot{\boldsymbol{z}}_R(t) = \boldsymbol{A}_R \boldsymbol{z}_R(t) + \boldsymbol{B}_R \boldsymbol{u}(t) + \boldsymbol{R}_R \boldsymbol{q}(t), \tag{8}$$

$$\boldsymbol{y}_{\mathrm{NL}}(t) = \boldsymbol{C}_{\mathrm{NL},R} \boldsymbol{z}_R(t), \tag{9}$$

$$\boldsymbol{q}(t) = \boldsymbol{f}(\boldsymbol{u}(t), \boldsymbol{y}_{\mathrm{NL}}(t)), \tag{10}$$

3 The Helicopter Impact Exemplification

The study reported in this paper refers to a heliport, i.e., a civil infrastructure of the type shown in Fig. 1. The case study is fully described in reference [15] to which the reader is referred to. In this short note there is just room for discussing some of its features with reference to Figs. 2 and 3.

The geometry of Fig. 2 is modified by subdividing the internal large elements in two and inserting buried walls along axis y for a length twice the plate diameter (Fig. 2).

Fig. 1 Heli-surface of the hospital of Livorno in Central Italy

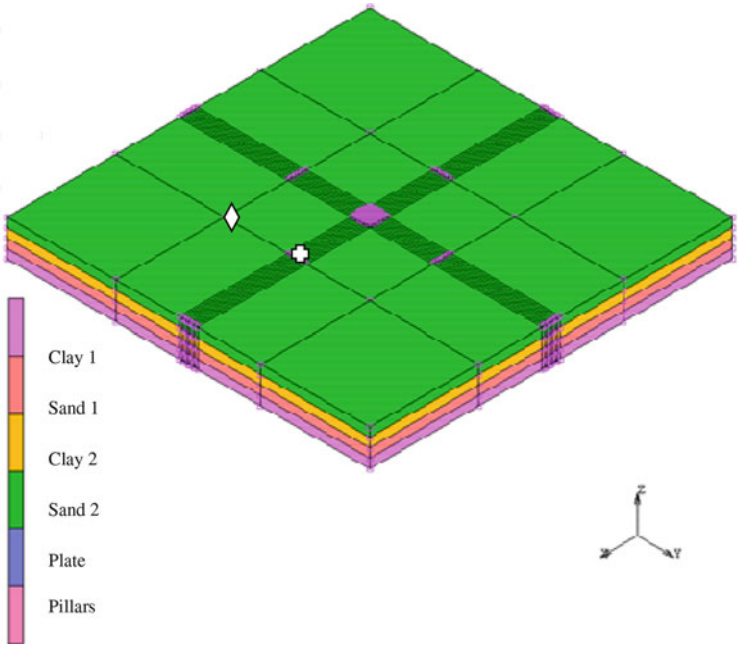

Fig. 2 Finite element discretization with focus on the materials

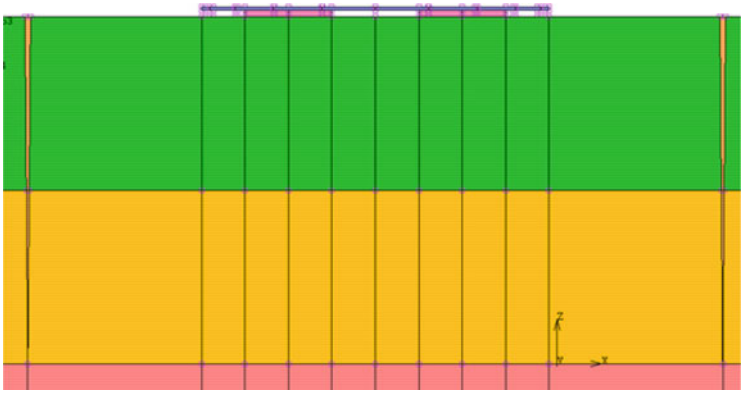

Fig. 3 Details of the plate and the buried walls

4 Some Displacement Time Histories

The positive effect of building buried walls in term of mitigation of the propagating acceleration was already discussed in [15]. In this paper, one just reports the response in terms of:

1. horizontal (along x) displacement in the point marked by a cross in Fig. 2;
2. vertical displacement in the points marked by a cross and a diamond in Fig. 2.

Figures 4, 5, and 6 compare the response computed after an impact in the centre of the plate for linear elastic walls, with the response one achieves when a nonlinear function is adopted in Eq. (10). The nonlinearity is introduced by computing the ratio ζ of the absolute value of each displacement component in every wall border node with a limit value, say 0.005 m. If the ratio is higher than 1, the corresponding column entries in k_d of the walls stiffness matrix are put equal to 20 % of their original value k. Otherwise each matrix entry k is rearranged in k_d by the relation:

$$k_d = k\,[0.8(1-\zeta) + 0.2]\,. \tag{11}$$

Of course any other equation can be incorporated in the numerical model and the structural response simulated. The response time histories were obtained on the same reduced order model developed for the linear system and, hence, the computational effort is quite reduced when compared with that required by the transient dynamic analysis of the initial full model. This reduced computational effort allows the designer to design the walls' constitutive law in the more suitable way, achieving, if convenient, the implementation of a "meta-structure" concept.

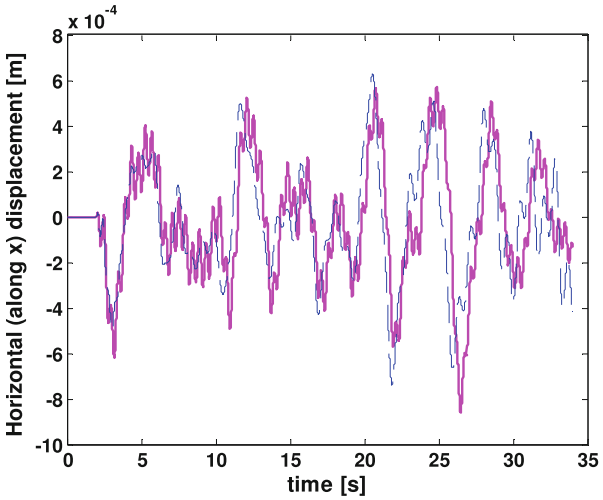

Fig. 4 Time histories of the horizontal (along x) displacement in the point marked by a *cross* in Fig. 2: linear (*dashed line*) versus nonlinear response (*solid line*)

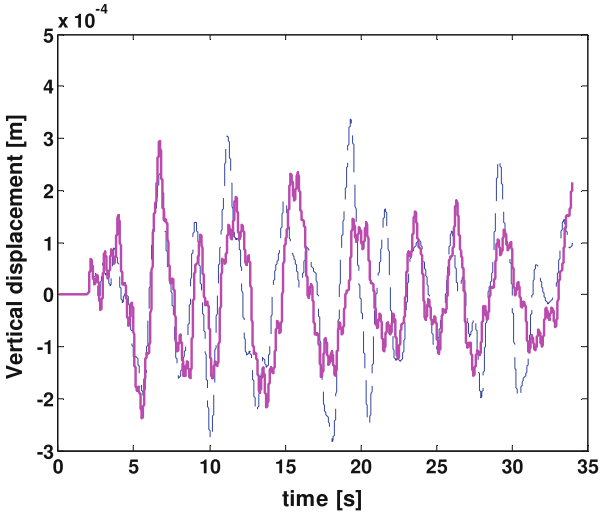

Fig. 5 Time histories of the vertical displacement in the point marked by a *cross* in Fig. 2: linear (*dashed line*) versus nonlinear response (*solid line*)

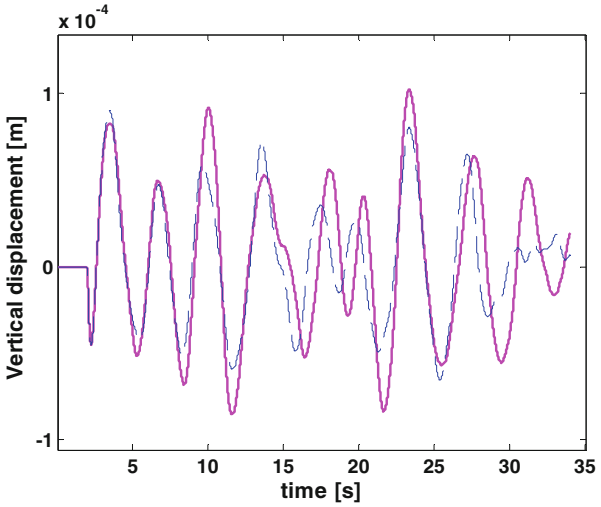

Fig. 6 Time histories of the vertical displacement in the point marked by a *diamond* in Fig. 2: linear (*dashed line*) versus nonlinear response (*solid line*)

5 Conclusions

The MOR approach, which was proposed in [15] for linear systems incorporating regions of limited extension made by nonlinear material, is applied to the study of mitigation of the vibration propagating after a helicopter land impact by buried walls.

The timely aspect of this proposal is that there is a ferment in the area of introducing walls more and more sophisticated. In particular the idea of realizing them by meta-structures seems to be particularly fascinating for future implementations.

Acknowledgements The author gratefully acknowledges the financial support provided by the Athenaeum Research Grant.

References

1. Krödel S, Thomé N, Daraio C (2015) Wide band-gap seismic metastructures. Extreme Mech Lett 4:111–117 (early view)
2. Minati G, The meta-structures project (2015). http://arxiv.org/ftp/arxiv/papers/0903/0903.0592.pdf
3. Hunaidi O (2000) Traffic vibrations in buildings, construction technology updates, no. 39, NRC-CNRC
4. Andersen L, Nielsen SRK (2005) Reduction of ground vibration by means of barriers or soil improvement along a railway track. Soil Dyn Earthq Eng 25:701–716

5. Talja A, Törnqvist J (2010) Traffic-induced building vibration – a tool for planning of land use. In: Proceedings: SB10 Espoo: sustainable community - building SMART, held in September 2010, Espoo, Finland
6. Celebi E, Fırat S, Beyhan G, Cankaya I, Vural I, Kırtel O (2009) Field experiments on wave propagation and vibration isolation by using wave barriers. Soil Dyn Earthq Eng 29:824–833
7. Alzawi A, ElNaggar MH (2011) Full scale experimental study on vibration scattering using open and in-filled (GeoFoam) wave barriers. Soil Dyn Earthq Eng 31:306–317
8. Murillo C, Thorel L, Caicedo B (2009) Ground vibration isolation with geofoam barriers: centrifuge modeling. Geotextiles Geomembr 27:423–434
9. Cacciola P, Tombari A (2015) Vibrating barrier: a novel device for the passive control of structures under ground motion. Proc R Soc A 471:20150075. http://dx.doi.org/10.1098/rspa.2015.0075
10. Wang JG, Sun W, Anand S (2009) Numerical investigation on active isolation of ground shock by soft porous layers. J Sound Vib 321:492–509
11. Casciati S, Borja RL (2004) Dynamic FE analysis of south Memnon colossus including 3D soil-foundation-structure interaction. Comput Struct 82(20–21):1719–1736
12. Casciati S, Faravelli L (2014) Quantity vs. quality in the model order reduction (MOR) of a linear system. Smart Struct Syst 13(1):99–109
13. Farhat C, Avery Ph, Chapman T, Cortial J (2014) Dimensional reduction of nonlinear finite element dynamic models with finite rotations and energy-based mesh sampling and weighting for computational efficiency. Int J Numer Methods Eng 98(9):625–662
14. Farhat C, Chapman T, Avery Ph (2015) Structure-preserving, stability, and accuracy properties of the energy-conserving sampling and weighting method for the hyper reduction of nonlinear finite element dynamic models. Int J Numer Methods Eng 102(5):1077–1110
15. Casciati F, Faravelli L (2016) Dynamic transient analysis of systems with material nonlinearity: a model order reduction approach. Smart Struct Syst 18:1–16

Contact of Flexible Elastic Belt with Two Pulleys

A.K. Belyaev, V.V. Eliseev, H. Irschik, and E.A. Oborin

Abstract The drive belt set on two pulleys is considered as a nonlinear elastic rod deforming in plane. The modern equations of the nonlinear theory of rods are used. The static frictionless contact problem for the rod is derived. The nonlinear boundary value problems for the ordinary differential equations are solved by the finite differences method and by the shooting method by means of computer mathematics. The belt shape and the stresses are determined in the nonlinear formulation which delivers the contact reaction and the contact area. The developed method allows performing calculations for any set of geometrical and stiffness parameters.

1 Introduction

The technical calculations of the belt drives are usually based on the ideas of an inextensible string and the Eulerian formula. However modelling of high loaded drives requires taking into account elastic deformations of the belt. In the previous works [5, 6, 11] the model of an extensible string is used, and the contour motion with the constant trajectory is explored. The model of a rod with (at least) bending stiffness is needed because the friction force loading does not act on the belt axis.

A number of works consider the significant effect of bending stiffness on the belt drive dynamics [2, 8, 9]. In finite-element modelling [1, 3, 10], the penalty formulations are used for obtaining the conditions in the contact area. In the works [1, 12] the concentration of reactions at the contact area boundaries is noted. However accurate solutions even for the static problem with the large deformations inherent to real drives have not been developed. For large deformation problems

A.K. Belyaev
Institute for Problems in Mechanical Engineering, Russian Academy of Sciences, Saint-Petersburg, Russia

V.V. Eliseev
Peter the Great Saint-Petersburg Polytechnic University, Saint-Petersburg, Russia

H. Irschik • E.A. Oborin (✉)
Johannes Kepler University, Linz, Austria
e-mail: evgenii.oborin@jku.at

H. Irschik et al. (eds.), *Dynamics and Control of Advanced Structures and Machines*, DOI 10.1007/978-3-319-43080-5_22

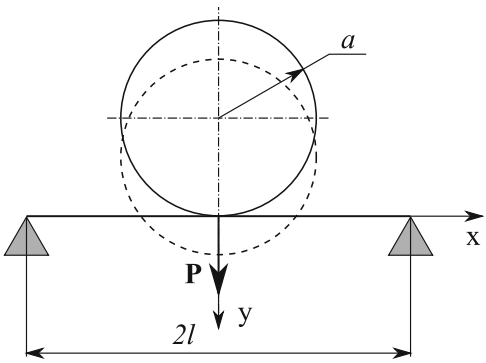

Fig. 1 Contact of straight beam and cylinder

the nonlinear theory of rods is necessary. The corresponding theory of rods [4] and computer mathematics allow us to formulate and solve difficult nonlinear problems.

The goal of this work is an application of the nonlinear elastic rod theory in the contact problem of fitting the belt as a ring to the frictionless pulleys in order to find strains and forces, reactions, and localization of reactions [7, 13]. Before starting we consider the linear model (see Fig. 1) to explain the localization of the reactions.

In this problem a stiff cylinder with the radius a is pressed against the center of a simply supported beam with the increasing force P. At first the force is concentrated at the contact point, and the deflection of the beam is $\varepsilon = Pl^3A/6$. Here the bending compliance is A, the length of the beam is $2l$. The curvature of the beam at the contact point becomes $AM = APl/2$. When it reaches the value $1/a$, i.e., $P = P^* = 2/Ala$, the contact zone expands. The displacement of the cylinder points is

$$v(x) = \varepsilon - a + \sqrt{a^2 - x^2} = \varepsilon - \frac{x^2}{2a} - \frac{x^4}{8a^3} + \cdots \tag{1}$$

Assuming the full contact (when the points of the beam lie on the cylinder), we obtain the contact pressure $p(x) = A^{-1}v^{IV}$. Since $p < 0$ the full contact is not present, and the contact area is concentrated at the ends of the interval ($x = \pm s_1$). The value s_1 is determined by matching the solutions at the different segments. The dependence $P(\varepsilon)$ becomes nonlinear. Below in Sect. 3 we will use this result to formulate the nonlinear contact problem.

2 Nonlinear Classical Theory of Rods Deforming in Plane

Elastic rods may be considered as Cosserat material lines, whose particles have the translational and rotational degrees of freedom [4]. In Fig. 2 the rod is shown in two configurations: before and after the deformation.

The rod axis is defined by the dependence of the position vector $\boldsymbol{r}(s)$ on the material coordinate. A triple of unit vectors $\boldsymbol{e}_k(s)$ is connected with every particle

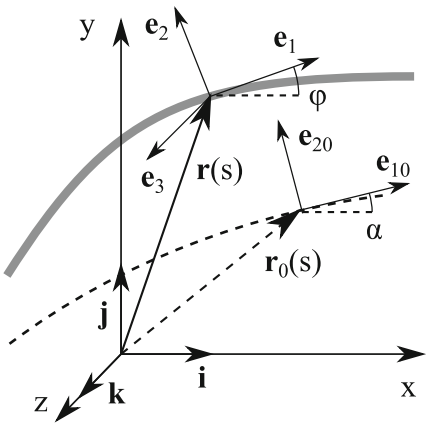

Fig. 2 Initial (*dashed line*) and deformed (*solid line*) rod configurations: position vectors, local basis, angles

to establish an angular orientation. In Fig. 2 index zero indicates the values before deformation. We restrict ourselves to the model without extension, then the variable s is the arc coordinate in both configurations.

The external loads are the force $\boldsymbol{q}$ and the moment $\boldsymbol{m}$ distributed per unit length. The internal interaction is defined by the force $\boldsymbol{Q}$ and the moment $\boldsymbol{M}$, whose signs depend on the direction of s. The full system of equations involves equations of balance of forces and moments, definitions of strains, and elasticity relations [4].

In this work we consider the plane problem of the belt fitted on two pulleys. Thus vectors $\boldsymbol{r}, \boldsymbol{Q}, \boldsymbol{e}_1, \boldsymbol{e}_2$ lie in the plane of the drawing. The unit vectors $\boldsymbol{e}_{10}, \boldsymbol{e}_{20}$ are rotated with regard to $\boldsymbol{i}$,$\boldsymbol{j}$ by an angle $\alpha(s)$ (around the z-axis). After the deformation we have $\boldsymbol{e}_1, \boldsymbol{e}_2$ and the angle $\varphi = \alpha + \theta$. In the general theory a rotation tensor $\boldsymbol{P} = \boldsymbol{e}_i \boldsymbol{e}_{i0}$ is introduced, but in the plane problem just one angle θ is sufficient. The moment vector $\boldsymbol{M} = M\boldsymbol{k}$; $\boldsymbol{k} = \boldsymbol{e}_3 = \boldsymbol{e}_{30}$ is directed along the z-axis. The vector of bending strain is $\theta'\boldsymbol{k}$, where prime indicates differentiation with respect to s.

The equations of the full system [4] are simplified:

$$\boldsymbol{Q}' = -\boldsymbol{q},\ M' = -\boldsymbol{k} \cdot \boldsymbol{r}' \times \boldsymbol{Q} = -x'Q_y + y'Q_x,\ \theta' = AM,\ \boldsymbol{r}' = \boldsymbol{P} \cdot \boldsymbol{r}_0'. \tag{2}$$

A is the bending compliance. Since $\boldsymbol{r}_0' = \boldsymbol{e}_{10}$, and thus $\boldsymbol{P} \cdot \boldsymbol{e}_{k0} = \boldsymbol{e}_k$, we can write

$$\boldsymbol{r}' = \boldsymbol{e}_1 \Rightarrow x' = \cos\varphi,\ y' = \sin\varphi. \tag{3}$$

3 Contact Problem Formulation

The scheme of the belt on two equal pulleys (with the radius a) is depicted in Fig. 3. Motivated by the above linear model (see Sect. 1), we begin the analysis under the assumption of the contact at discrete points. The half of the center distance before the deformation equals $d = R - a$ and then it is increasing by a given value ε. We aim

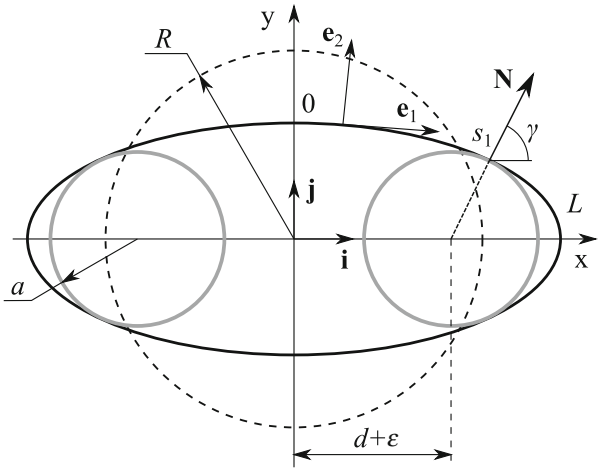

Fig. 3 Fitting of the ring on the pulleys. Here *solid circles* are the pulleys, *dashed circle* is the initial belt configuration and *solid line* is the deformed configuration

at computing the deformation and the contact forces to obtain a given kinematical loading ε. The problem has two axes of symmetry, thus the consideration of first quarter $0 < s < L = \pi R/2$ is sufficient. The load $\boldsymbol{q}$ is just the reaction force from the pulley $\boldsymbol{N}$ that is concentrated in the contact point with the unknown coordinate s_1: $\boldsymbol{q} = \boldsymbol{N}\delta(s-s_1)$ (here δ is the Dirac delta-function). Then the equations of balance of forces and moments in (2) are integrated as:

$$\begin{aligned} &\boldsymbol{Q} = -\boldsymbol{N}h\,(s-s_1) + \boldsymbol{Q}_0; \\ &M = \boldsymbol{k}\cdot[(\boldsymbol{r}-\boldsymbol{r}_1)\times\boldsymbol{N}h\,(s-s_1) - \boldsymbol{r}\times\boldsymbol{Q}_0] + M_*. \end{aligned} \tag{4}$$

Here $h(\ldots)$ is the unit step function (Heaviside), $\boldsymbol{Q}_0, M_*$ are the vector and the scalar constants of integration. In the absence of friction the contact force $\boldsymbol{N}$ is directed perpendicular to the pulley. We denote γ as the angle of the force to the x-axis: $\boldsymbol{N} = N(\boldsymbol{i}\cos\gamma + \boldsymbol{j}\sin\gamma)$. At the contact point we have $\varphi = \gamma - \pi/2$. At the ends of the interval, transverse forces equal to zero: $\boldsymbol{Q}(0) = \boldsymbol{Q}_0 = Q_0\boldsymbol{i}$, $\boldsymbol{Q}(L) = -Q_L\boldsymbol{j}$. From the equation of balance of forces for the quarter of the rod, it follows:

$$\boldsymbol{Q}|_0^L + \boldsymbol{N} = 0;\ N\cos\gamma = Q_0 \equiv P/2,\ Q_L = N\sin\gamma. \tag{5}$$

The tension Q_0 at the top point equals to the half of the force P moving the pulleys apart. The tension in the right point $Q_L = P\tan\gamma/2$. The bending moment

$$M = N\,[(x-x_1)\sin\gamma - (y-y_1)\cos\gamma]\,h\,(s-s_1) + yQ_0 + M_* \tag{6}$$

with the contact point $\boldsymbol{r}_1 = x_1\boldsymbol{i} + y_1\boldsymbol{j} = (d+\varepsilon+a\cos\gamma)\,\boldsymbol{i} + a\sin\gamma\,\boldsymbol{j}$.

We note that in the considered model without axial extension the coordinate s remains the arc coordinate also after the deformation. Thus, $\alpha = -s/R$, $\varphi = \theta - s/R$. The derived system of ordinary differential equations (ODE) can be solved partly due to the existence of the first integrals. Within both segments of the interval $(0, L)$, there is $\boldsymbol{Q} = \text{const}$, and then it follows:

$$A^{-1}\theta'' = y'Q_x - x'Q_y = Q_x \cos(s/R - \theta) - Q_y \sin(s/R - \theta).$$

Introducing the variable $\varphi(s)$ as above, we obtain the equation:

$$A^{-1}\varphi'' - Q_x \cos\varphi - Q_y \sin\varphi = 0. \tag{7}$$

It is integrated in terms of elliptic functions as in the classical problems [4]:

$$\begin{gathered} A^{-1}\varphi'^2/2 - Q_x \sin\varphi + Q_y \cos\varphi = c_1 = \text{const}; \\ \int \frac{\mathrm{d}\varphi}{\sqrt{c_1 + Q_x \sin\varphi - Q_y \cos\varphi}} = s\sqrt{2A} + c_2. \end{gathered} \tag{8}$$

However it is difficult to determine c_1, c_2 that are different at both segments.

We suggest another approach, which is more advantageous. The unknown constants of the problem are s_1, γ, Q_0, M_*. The unknown functions are $\theta(s), x(s), y(s)$. Considering the constants as functions, we equate their derivatives to zero (see, e.g., this well-known method in [9]). Adding the expressions θ', x', y', we arrive to the ODE system of seventh order. The boundary conditions are

$$\begin{gathered} s = 0\colon\ \theta = 0,\ x = 0;\ s = L\colon\ \theta = 0,\ y = 0; \\ s = s_1\colon\ \theta = \theta_1 = s_1/R + \gamma - \pi/2,\ x = x_1 = d + \varepsilon + a\cos\gamma,\ y = y_1 = a\sin\gamma. \end{gathered} \tag{9}$$

Four conditions at the ends $s = 0, L$ are not enough for the seventh order system. Conditions at the contact point should be taken into account.

The formulated problem with the condition in the internal point is not usual and is not solved in particular by the shooting method. We can transform it to the tenth order system at the interval $[0, 1]$ with the appropriated number of conditions. Instead of the coordinate s we introduce a new variable $\xi \in [0, 1]$ by setting

$$s = \begin{cases} \xi s_1, & s < s_1, \\ L - \xi(L - s_1), & s > s_1. \end{cases} \tag{10}$$

The relation between the derivatives is $\dot{(\dots)} = m(s)(\dots)'$ (the point means differentiation with respect to ξ); here $m = s_1$ at the first interval and $m = s_1 - L$ at the second one. We shall consider the solutions at these two intervals as two different unknowns.

4 The Solution Using Computer Mathematics

Constructing a column of the unknowns $Y(\xi)$ with ten elements, we have

$$Y = \left(s_1\ \gamma\ Q_0\ M_*\ \theta^{(1)}\ x^{(1)}\ y^{(1)}\ \theta^{(2)}\ x^{(2)}\ y^{(2)}\right)^T,$$

then we arrive to the following system of ODEs:

$$\dot{Y} = F(\xi, Y) = \left(0\ 0\ 0\ 0\ F_4\ F_5\ F_6\ F_7\ F_8\ F_9\right)^T,$$

$$F_4 = mAM,\ F_5 = m\cos(\theta^{(1)} - s/R), F_6 = m\sin(\theta^{(1)} - s/R). \tag{11}$$

Components F_7, F_8, F_9 differ by the expressions m, M, θ at the segments (6). We should add to the system (see the end of Sect. 3 and (11)) the boundary conditions (9). This boundary value problem (BVP) is solved by means of computer mathematics, namely by the finite difference method using Wolfram Mathematica and by the shooting method using Mathcad. The results of both methods are equal.

In the example calculation the radius of the ring is $R = 0.55$ m, the radius of the pulleys is $a = 0.15$ m, the half of center distance is $d = 0.4$ m. The Young's modulus is $E = 0.1$ GPa, and the section is a square with the side equal 0.01 m. In a series of calculations the increment ε of distance d is increased from zero to the limiting value due to the inextensibility. Figure 4 corresponds to the displacement $\varepsilon = 0.228$ m. Herewith the angle $\gamma = 0.713$, the coordinate $s_1 = 0.758$ m (with the length $L = 0.864$ m), and the force $P = 2Q_0 = 19.6$ N.

However the calculations did not reveal such pronounced gaps of the belt from the pulley as in Fig. 3. The configuration of the belt differs from the pulley circle and intersects it. We can assume full contact along with a concentrated contact reaction. Its value is $N = Q_0/\cos\gamma = 13.0$ N. The difference between Figs. 3 and 4 requires further study presented in what follows.

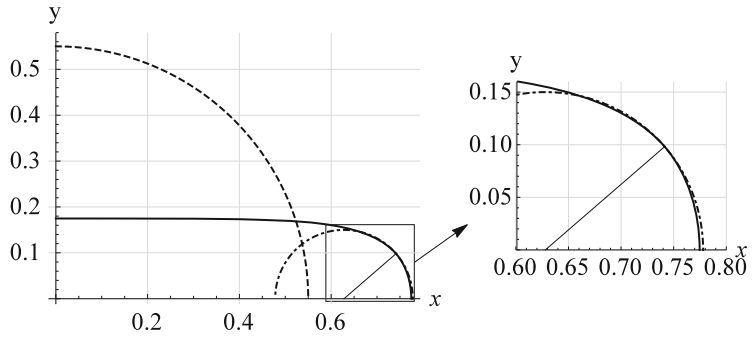

Fig. 4 Belt and pulley: overall picture and intersection. *Dashed circle* is the initial belt, *dash-dot line* is the pulley, *solid line* is the deformed belt, and *thin line* depicts the contact point

5 Version with Full Contact of Belt and Pulleys

Here we assume the full (distributed) contact of the belt on the pulley when $s > s_1$. Projecting Eq. (2) on the tangent (index 1) and the normal (index 2), we obtain

$$Q_1' + a^{-1}Q_2 + q_1 = 0,\ Q_2' - a^{-1}Q_1 + q_2 = 0 \tag{12}$$

(taking into account the equalities $\boldsymbol{e}_1' = -a^{-1}\boldsymbol{e}_2,\ \boldsymbol{e}_2' = a^{-1}\boldsymbol{e}_1$). But $q_1 = 0$, because friction is absent. Transverse force Q_2 vanishes since the moment is constant

$$\varphi = a^{-1}(L-s) - \pi/2,\ M = A^{-1}\left(R^{-1} - a^{-1}\right),\ Q_2 = -M' = 0. \tag{13}$$

Then from (12) we obtain $Q_1 = \text{const} = aq_2$, the tension and the contact pressure are constant. Adding obvious expressions x, y at the pulley circle, we obtain all the set of formulas at the contact area having the unknown pair of constants s_1, q_2.

Let us turn to the free interval $s < s_1$. Here the above shown relations are applicable: $\boldsymbol{Q} = Q_0\boldsymbol{i},\ Q_0 = P/2,\ M = yQ_0 + M_*$. The last helps us to derive the relation for M_*. At the point $s = s_1$ the moment is continuous and $y = a\sin\gamma$ with angle $\gamma \equiv (L - s_1)/a$. Using (13) we write

$$M_* = -a\sin\left(a^{-1}(L-s_1)\right)Q_0 + A^{-1}(R^{-1} - a^{-1}). \tag{14}$$

As in (10) we introduce the coordinate ξ. Thus we obtain a BVP for the ODE system of fifth order (boundary conditions are almost the same as in (9)):

$$\dot{s}_1 = 0,\ \dot{Q}_0 = 0,\ \dot{\theta} = s_1AM,\ \dot{x} = s_1\cos\left(\theta - \xi s_1/R\right),\ \dot{y} = s_1\sin\left(\theta - \xi s_1/R\right);$$
$$\xi = 0\colon\ \theta = 0,\ x = 0;\ \xi = 1\colon\ \theta = \theta_1,\ x = x_1,\ y = y_1. \tag{15}$$

Solving problem (15) by means of computer mathematics, for $\varepsilon = 0.228\,\text{m}$ we obtain $s_1 = 0.672\,\text{m}$, $Q_0 = 43.8\,\text{N}$, $\gamma = 1.28$.

Friction is absent, therefore at the point s_1 the tension is continuous: $Q_0\sin\gamma = Q_1$, so $q_2 = P\sin\gamma/2a = 280\,\text{N/m}$. But the concentrated reaction $N = P\cos\gamma/2 = 12.5\,\text{N}$ arises. This value is less than the same one for the point contact problem.

Figure 5 displays the dependence of the angle $\gamma(\varepsilon)$ and the force $P(\varepsilon)$ that moves apart the pulleys. Initially the contact is at one point: $\gamma = 0$ until the value $\varepsilon \approx 0.19\,\text{m}$. This is consistent with the linear model in Fig. 1. But the dependence of force $P(\varepsilon)$ (Fig. 5) is nonlinear right away, because here we deal with geometric nonlinearity. Quantitative differences are observable at large values of ε.

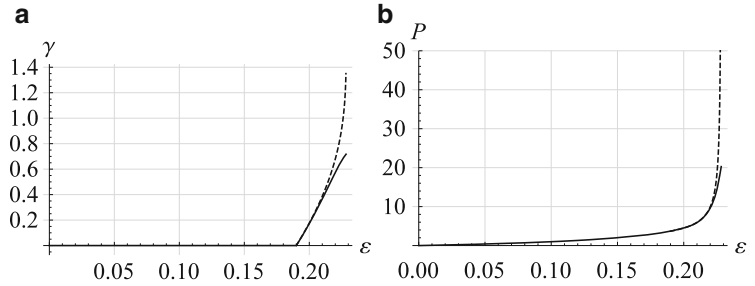

Fig. 5 Numerical results: (**a**) angle of reaction inclination; (**b**) force moving apart pulleys. Here *dashed line* depicts the full contact, and *solid line* depicts the point contact

6 Conclusion

We formulated and solved two contact problems for plane rods for modelling the process of fitting of the belt on the pulleys. Difficulties of solving the nonlinear BVP of tenth and fifth order were overcome by means of computer mathematics. We considered two formulations: the point contact and the full contact, the latter being the preferable one. The strains in both formulations nearly coincide, but the reactions of the pulleys are different. We determined the forms of belt, the stress states, the contact pressure with its localization. The developed method allows us performing multivariant calculations easily.

Acknowledgements This research is carried out in the framework of the joint project of the Russian Foundation for Basic Research (grant No. 14-51-15001) and the Austrian Science Fund (FWF, grant No. I 2093 International Project).

References

1. Čepon G, Boltežar M (2009) Dynamics of a belt-drive system using a linear complementarity problem for the belt–pulley contact description. J Sound Vib 319(3–5):1019–1035
2. Ding H, Li D-P (2014) Static and dynamic behaviors of belt-drive dynamic systems with a one-way clutch. Nonlinear Dyn 78(2):1553–1575
3. Dufva K, Kerkkänen K, Maqueda L, Shabana A (2007) Nonlinear dynamics of three-dimensional belt drives using the finite-element method. Nonlinear Dyn 48(4):449–466
4. Eliseev V (2006) Mechanics of deformable solid bodies. St.-Petersburg State Polytechnical University Publishing House, St. Petersburg
5. Eliseev V (2009) A model of elastic thread for transmissions with flexible coupling. St.-Peterbg State Polytech Univ J 84:192–195 [St. Petersburg State Polytechnical University Journal is the English title from the official cite]
6. Eliseev V, Vetyukov Y (2012) Effects of deformation in the dynamics of belt drive. Acta Mech 223(8):1657–1667
7. Galin LA (2008) Contact problems. Springer, Dordrecht

8. Hwang S-J, Perkins N (1994) High speed stability of coupled band/wheel systems: theory and experiment. J Sound Vib 169(4):459–483
9. Kong L, Parker RG (2005) Steady mechanics of belt-pulley systems. J Appl Mech 72(1):25–34
10. Sinwel A, Gerstmayr J (2010) Modelling an axially moving beam using the absolute nodal coordinate formulation. In: Proceedings of 7th international conference on engineering computational technology. Civil Comp Press, Stirlingshire, p 112
11. Vetyukov Y, Eliseev V, Krommer M (2015) Modeling the dynamics of a flexible belt drive using the equations of a deformable string with discontinuities. IFAC-PapersOnLine, 48(1):604–609
12. Wasfy TM, Leamy M (2002) Effect of bending stiffness on the dynamic and steady-state responses of belt-drives. In: ASME design engineering technical conference, pp 217–224
13. Wriggers P, Laursen TA (2006) Computational contact mechanics. Springer, Berlin

Control over Internet of Oscillations for Group of Pendulums

Mikhail S. Ananyevskiy and Alexander L. Fradkov

Abstract The problem of control for group of pendulums is considered. Control goal is the synchronization of several remote pendulums over Internet. Some theoretical approach is presented. It is based on some experiments about statistic data of delays for control over Internet. Simulation results for several pendulums are presented. Experiments "in hardware" results are also presented (hardware—pendulums, constructed with Lego Mindstorms NXT, software—cloud mechatronic laboratory, http://cmlaboratory.com).

1 Introduction

Global network gives the opportunity for global interconnection and global control of mechatronic systems. But control over network has some difficulties—the existence of non-stationary delays in digital channel. According to OSI classification (Open System Interconnection, ISO/IEC 7498-1) there are seven abstraction layers of interconnection: physical, data link, network, transport, session, presentation and application. Common models of digital channel used for research of control over network correspond to the second layer—data link, this is not good. To describe control over Internet model of network layer or transport layer should be used. Today there are no such model of delays good for theory of feedback control.

There are some papers about control of mechatronic systems over special kind of network—Internet [1–6]. In paper [7] several experiments for control of teleoperators over different types of communication channels are presented: commercial Internet, wireless LAN, and Ethernet LAN, the feedback was based on a video-signal from different applications (iChat/Skype, HaiVision, Hai1000, Hai200, etc.). The problem of stabilizing inverted pendulum over local net was studied in [8].

M.S. Ananyevskiy (✉) • A.L. Fradkov
Institute for Problems of Mechanical Engineering, Russian Academy of Sciences, V.O., Bolshoj pr., 61, St. Petersburg 199178, Russia
e-mail: msaipme@gmail.com; fradkov@mail.ru

H. Irschik et al. (eds.), *Dynamics and Control of Advanced Structures and Machines*, DOI 10.1007/978-3-319-43080-5_23

In this paper the problem of synchronization for group of pendulums on cart over Internet is investigated. Control goal is to force the in-phase synchronization. Plan of the paper is following: first the property of digital network channels is studied, then some theoretical approach is developed, after some simulation with Matlab Simulink Desktop RealTime Toolbox is presented and final the results of experiment "in-hardware" with pendulums constructed of Lego Mindstorms NXT and with software of Cloud mechatronic laboratory (http://cmlaboratory.com) are presented.

2 Digital Network Channel

Delays in network interconnection depends on: topology of network (could change in time), hardware of network (routers, switches, bridges, etc.), software of network (algorithms for network packets transmission, routing, network balance algorithms, etc.), network load (including reflected, dos, ddos, etc.), hardware and software of receiver and transmitter block (computer), receiver and transmitter block load (computer), protocol for network interconnection (tcp/ip, udp/ip, etc.) and so on.

To understand the influence of delays on control quality some statistics for several network channels was collected: for local net, for wireless LAN, for Internet between USA and Russia. Each control pulse forms a packet which is sent over net, the difference between send time and received time is the delay (of course clocks on transmitter and receiver computers should be synchronized). The results are presented in Figs. 1, 2, and 3.

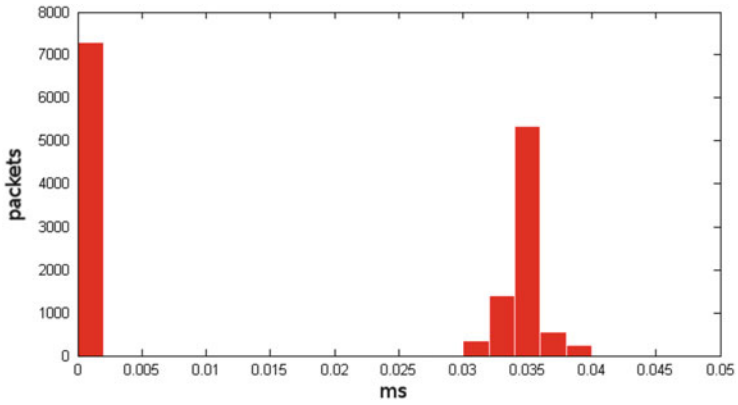

Fig. 1 Histogram of delays (local network)

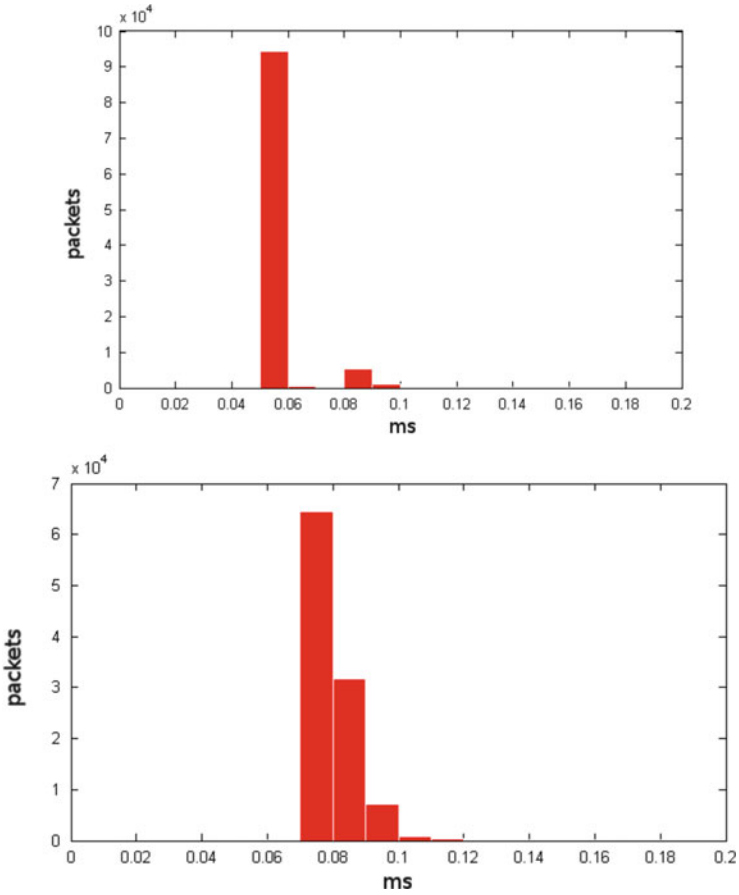

Fig. 2 Histogram of delays for wireless LAN: on *top*—free wireless LAN, on *bottom*—load wireless LAN

Distribution of delays is not normal, it is not corresponding to some standard distributions. It has large spread, localization in several intervals, and usually a little number of huge delays. For control of systems with fast oscillations (period "near" 1 s) such delays could make a problem.

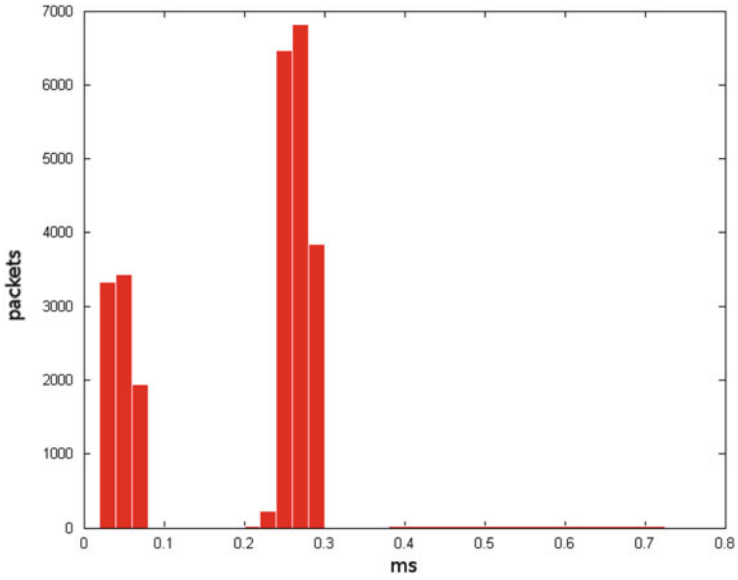

Fig. 3 Histogram of delays for Internet between USA and Russia

3 Theoretical Approach

Consider a group of remote systems "pendulum on cart" interconnected over the network digital channel. The control goal is to synchronize all pendulums.

With some idealistic assumptions (the mass of cart is greater than the mass of pendulum, system has no friction) one can write the following simplified equation:

$$ml^2\ddot{\phi}_k(t) + mgl\sin\phi_k(t) = -u_k(t)ml\cos\phi_k(t), \qquad k = 1,\ldots,K, \tag{1}$$

where m—pendulum mass (equal for all pendulums), l—pendulum length (equal for all pendulums), g—free fall acceleration, $u_k(t)$—control for kth pendulum (kth pendulum cart acceleration).

The master–slave approach is used. First pendulum is marked as "master", all other are marked as "slaves". For synchronization the star topology is used: each slave system is synchronized to master independently.

Master pendulum is excited by speed-gradient method [9]:

$$u_1(t) = -\Gamma\nabla_{u_1}\frac{d}{dt}\left(E(\phi_1(t),\dot{\phi}_1(t)) - E_*\right), \tag{2}$$

here E_*—goal value for energy, $\Gamma > 0$—parameter. After some calculations the following control algorithm for master slave system is obtained:

$$u_1(t) = -\gamma \left(E(\phi_1(t), \dot{\phi}_1(t)) - E_*\right) \cos(\phi_1(t))\dot{\phi}_1(t), \tag{3}$$

here $\gamma > 0$—parameter.

For slave system synchronization a PD-regulator is used:

$$u_k(t_{k+1}) = \alpha_k(\phi_1(t_n) - \phi_k(t_n)) + \beta_k(\dot{\phi}_1(t_n) - \dot{\phi}_k(t_n)), \qquad k = 2, \ldots, K, \tag{4}$$

where parameters α_k and β_k are obtained by modified Fridman's method.

For pendulum with mass $m = 1\,\text{kg}$ and length $l = 0.25\,\text{m}$, it was analytically proved in [10] that PD-regulator with parameters $\alpha = 17.7$, $\beta = 3.875$ synchronized slave system to master if delays are lower than 0.099 s.

4 Simulation Results

For computer simulation the Matlab Simulink Desktop RealTime Toolbox was used. Three computers were connected over local network. First computer simulated the master pendulum system, second—the slave pendulum system, and third—the regulator. Pendulum parameters were mass $m = 1\,\text{kg}$, length $l = 0.25\,\text{m}$, simulation time was 20 s, regulator parameters were: $\alpha = 17.7$, $\beta = 3.875$. Protocol for network interconnection was UDP/IP. Sample time for UDP receiver was 0.01 s, so delays were greater than 0.01 s. In Fig. 4 results of simulation are presented. Pendulums were synchronized.

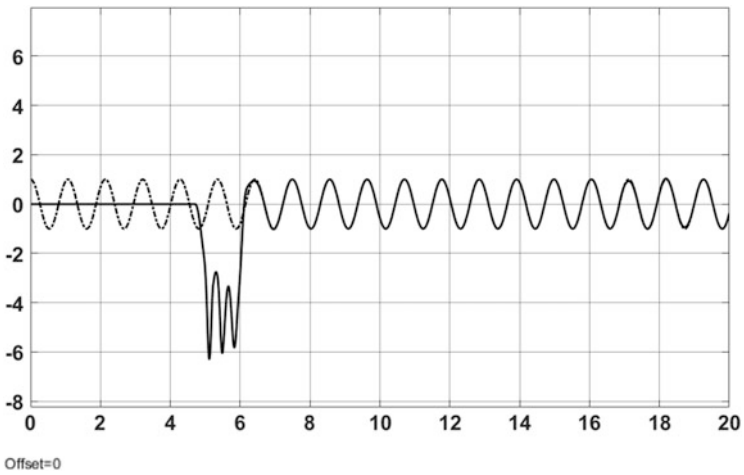

Fig. 4 Computer simulation for master–slave synchronization of two pendulums over the local network. *Dot line*—master system, *solid line*—slave system

5 Experiments Results

For experiment "in-hardware" two similar pendulums on cart were constructed with Lego Mindstorms NXT (see Fig. 5). Actuator is cart motor, sensor is pendulum angular. This is very non-ideal system, the differences between these (similar) pendulums are demonstrated by free oscillations in Fig. 6. Histogram of delays is presented in Fig. 8. Plot of angular dynamics for pendulums is in Fig. 7. Data from angular sensor was received quite rarely one or two times per period (hardware limitation). Therefore the plot demonstrates that synchronization sometimes achieved (Fig. 8).

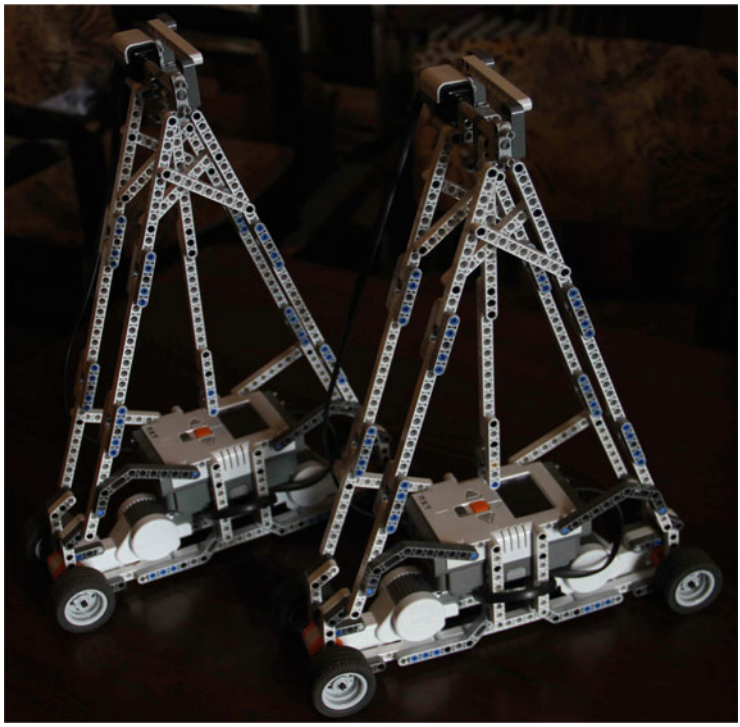

Fig. 5 Two similar pendulums on cart constructed with Lego Mindstorms NXT

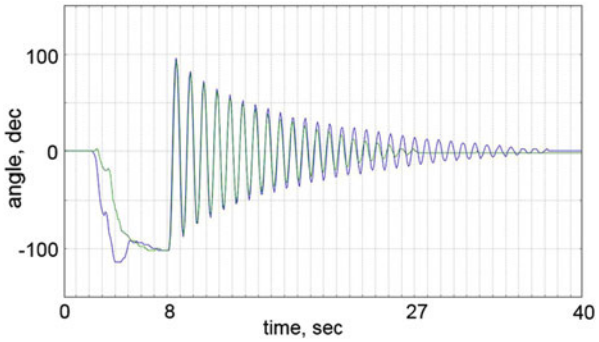

Fig. 6 Free oscillations of pendulums. Both pendulums were moved to horizontal position (angular = $\frac{\pi}{2}$) and were dropped: periods are equal, but friction is quite different

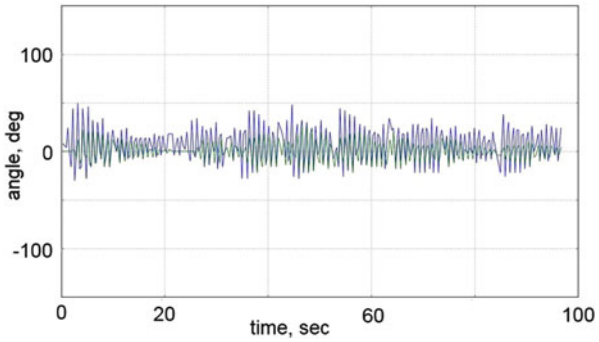

Fig. 7 Synchronization of pendulums

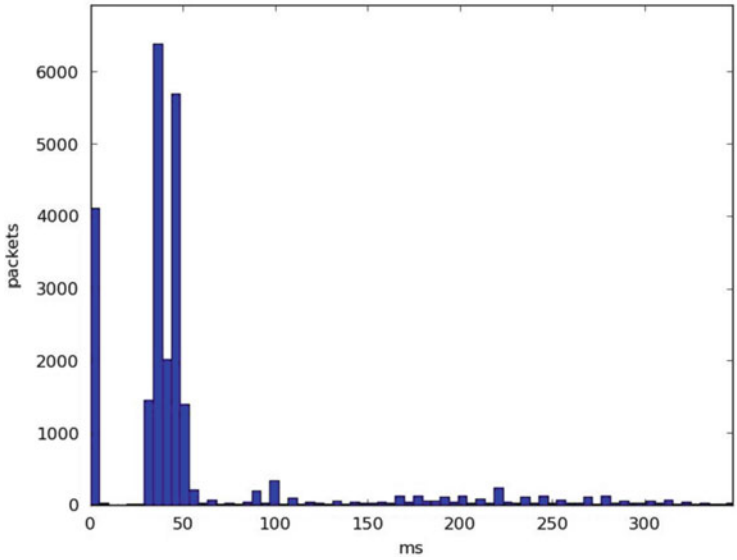

Fig. 8 Histogram of delays for control over network

6 Conclusions

The problem of control of synchronization over network for group of pendulums on cart was studied. Some statistics about delays for control over several types of network were collected. Master–slave approach for group synchronization was considered. Master pendulum was excited by speed-gradient method, each slave pendulum was synchronized to master by a PD-regulator. Simulations results demonstrated synchronization. Experiment "in-hardware" also demonstrated some synchronization (not clearly and sometimes synchronization broke).

Acknowledgements The work was partially supported by the grant of RFBR 14-08-01015 and the grant of SPbSU 6.38.230.2015. The results of Sect. 4 were obtained in IPME RAS and supported solely by Russian Scientific Foundation (grant 14-29-00142).

References

1. Andrievsky B, Andrievsky A (2012) State estimation of non-autonomous Lurie systems over the limited-band communication channel with time delay and uniform quantization. Cybern Phys 1(4):228–236
2. Andrievsky B (2013) Information transmission based on adaptive synchronization of chaotic Lorenz systems over the digital communication channel. Cybern Phys 2(1):10–14

3. Andreu D, Fraisse P (2003) Internet enhanced teleoperation: Toward a remote supervised delay regulator. In: IEEE international conference on industrial technology, Maribor, Slovenia, December 10–12
4. Book WJ, Lane H, Love LJ et al. (1996) A novel teleoperated longreach manipulator testbed and its remote capabilities via the internet. In: IEEE international conference on robotics and automation (ICRA), Minneapolis, MN, April 22–28, pp 1036–1041
5. Debus T, Stoll J, Howe RD, Dupont P (2000) Cooperative human and machine perception in teleoperated assembly. In: Experimental robotics VII. The fifth international symposium, Honolulu, HI, December 10–13
6. Fradkov AL, Andrievsky B, Ananyevskiy M (2014) State estimation and synchronization of pendula systems over digital communication channels Eur Phys J Spec Top 223(4):773–793
7. Lum MJH, Rosen J, King H et al (2009) Teleoperation in surgical robotics - network latency effects on surgical performance. In: 31st annual international conference of the IEEE EM Minneapolis, Minnesota, USA, September 2–6
8. Natale OR, Sename O, Canudas-de-Wit C (2004) Inverted pendulum stabilization through the ethernet network, performance analysis. In: Proceedings of the American control conference (ACC'04), Boston, MA, June 30–July 2
9. Fradkov AL, Miroshnik IV, Nikiforov VO (1999) Nonlinear and adaptive control of complex systems. Kluwer, Dordrecht
10. Ananyevskiy MS, Seifullaev RE, Nikitin DA, Fradkov AL (2014) Synchronization of nonlinear systems over intranet: cart-pendulum case study. In: 2014 IEEE international conference on control applications (CCA) part of 2014 IEEE multi-conference on systems and control, October 8–10, Antibes, France

Effect of the Load Modelling Strategy on the Dynamic Response Prediction of Bridges Subjected to High-Speed Trains

Christoph Adam and Patrick Salcher

Abstract The paper evaluates the effect of various modelling strategies for the bridge–train interaction system on the prediction of the dynamic bridge response. Trains crossing the bridge with constant high-speed are described either by a series of moving single forces representing their static axle loads or by a planar mass-spring-damper multi-body system. The outcomes of the latter model serve as reference solution because vehicle–bridge interaction (VBI) is explicitly considered. In an application problem the vertical bridge peak response is derived based on models of different degree of sophistication. From the outcomes it can be concluded that the impact of high-speed trains on a bridge by means of single forces (representing the static train axle loads) provides accurate results if bridge damping is increased and additional dynamic distributed mass is added to the bridge to account indirectly for VBI effects.

1 Introduction

The assessment of the serviceability and load-bearing capacity of railway bridges is usually based on the outcomes of static structural analysis amplified by a dynamic amplification factor. The demands of bridges along railway lines for high-speed trains are, however, higher than for bridges crossed by trains with moderate speeds, because they may be excited to a state of resonance during the train passage, amplifying dynamically deformations and stresses. Resonance occurs if the frequency (or its multiple) of the repetitive arrival of the train wheels corresponds to a natural frequency of the bridge structure. Sway forces of the train vehicles originating from track irregularities and wheel hunting moments may also induce resonance. Consequently, dynamic structural analysis is required to predict the response realistically. Since train and bridge represents a complex interacting system, its local and global dynamic behaviour can only be captured by a sophisticated structural model. With increasing model complexity, however,

C. Adam (✉) • P. Salcher
Unit of Applied Mechanics, University of Innsbruck, Innsbruck, Austria
e-mail: christoph.adam@uibk.ac.at

H. Irschik et al. (eds.), *Dynamics and Control of Advanced Structures and Machines*, DOI 10.1007/978-3-319-43080-5_24

computations in the design process of structures become inaccessible for many engineers in practice. Furthermore, the most sophisticated structural model may be computationally too expensive for certain investigations, where also a lesser level of detail would be appropriate. Simplified approaches of analysis reduce the modelling effort, and they require less parameters, which are usually readily available. These models can be built by engineers with less specialized experience, and response predictions are available within a narrow time frame since the computational cost is much lower compared to numerical analysis based on a complex model.

In the comprehensive text book of [12] various modelling strategies are described, discretizing the bridge by means of simple beam models or detailed two- and three-dimensional finite element models, which comprise structure, rails, sleepers, and ballast. The more complex models even may capture rail irregularities. The passing train may be modelled by moving single forces representing the static axle loads of the train, or more realistically, by a complex mass-spring-damper (MSD) multi-body system. While in the first approach interaction between the subsystems bridge and train cannot be explicitly considered, in the second approach coupling between the subsystems (and, thus, interaction) is achieved through different assumptions discussed in the literature, see, e.g., [9]. Liu et al. [5] have evaluated both approaches comparing the outcomes based on the single force model and discrete MSD systems of various levels of detail. The authors of these and many other studies come to the common conclusion that the modelling strategy and the underlying simplifications affect the accuracy of the response prediction of bridge and/or train. However, as outlined in [5], it has still not been completely revealed under which condition a simple moving single force model predicts sufficiently accurate the bridge response or a more complex dynamic interaction model should be utilized.

The present paper aims at contributing to the discussion how certain degrees of simplifications of the train model affect the prediction of the dynamic bridge response. Some of the results discussed here have been presented at the Vienna Congress on Recent Advances in Earthquake Engineering and Structural Dynamics, see [10]. For further details it is referred to [9].

2 Assessment of Various Load Modelling Strategies

Based on the following example problem the effect of load model simplifications and vehicle–bridge interaction (VBI) on the dynamic bridge response prediction is investigated. The considered bridge is a simply supported beam-like steel structure carrying a single rail-track. For the purpose of this study the bridge is modelled as *Euler–Bernoulli* beam with span $L = 22.0\,\text{m}$, bending stiffness $EI = 3.94 \times 10^{10}\,\text{Nm}^2$, and mass per unit length $\rho A = 9660\,\text{kg/m}$ (i.e. the total mass of this structure ρAL is 212.520 kg), see Fig. 1a. The fundamental natural frequency f_g of this beam is 6.55 Hz. For steel bridges, [3] proposes a modal damping coefficient of $\zeta = 0.5\,\%$. According to this standard for bridges with span L less than 30 m

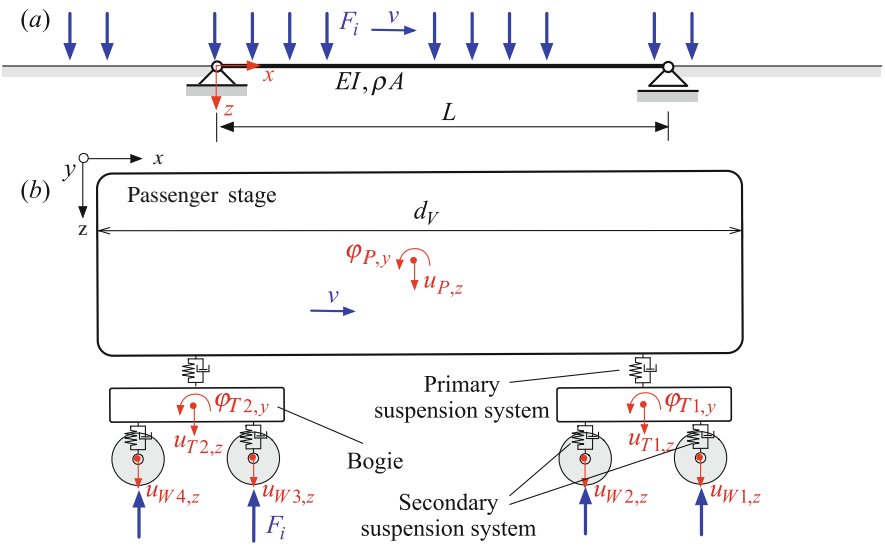

Fig. 1 (**a**) Beam representation of a simply supported bridge travelled by single forces representing the crossing train. (**b**) Planar mass-spring-damper model of one car of the *Railjet* train

modal damping can be increased to consider the response reduction effect of VBI. For the considered bridge ζ can be increased by $\Delta\zeta = 0.17\,\%$ [3]. It is assumed that crossing of a *Railjet* train [7] consisting of a power car and seven identical passenger cars excites the bridge to vibrations. For this study the five subsequently defined modelling approaches of this train–bridge interacting system are evaluated comparing the dynamic response predictions derived by these models.

1. Mass-spring-damper model. The two-dimensional ten-degrees-of-freedom (10 DOF) MSD system per car of the Railjet train depicted in Fig. 1b, composed of rigid bodies connected through springs and dashpot dampers, is utilized. Coupling of the bridge (Fig. 1a) and train (Fig. 1b) subsystem is achieved through the so-called *corresponding assumption*. For details of this model see [9]. Mass, mass moments of inertia, and damping parameters of the model components are listed in [6, 9]. Because in this approach VBI is directly considered, to the *Euler–Bernoulli* beam the modal damping coefficients for steel bridges, $\zeta = 0.5\,\%$, are assigned.
2. Single force model: SF. Each single force represents the corresponding static axle loads of the *Railjet* train, as shown in Fig. 1b. Magnitudes of the single forces and load spacing are provided in [7]. To the *Euler–Bernoulli* beam the modal damping coefficients for steel bridges, $\zeta = 0.5\,\%$, according to [3] are assigned.
3. Single force model: SF+$\Delta\zeta$. Modal bridge damping coefficients ζ are *increased* by $\Delta\zeta = 0.17\,\%$ according to [3] to account for VBI effects.

4. Single force model: SF+$\Delta\zeta$+$\Delta\rho A$. Increased bridge damping $\zeta + \Delta\zeta$. The *total train mass* is uniformly *smeared*, $\Delta\rho A = 2684$ kg/m, and added to the distributed mass ρA of the beam bridge model to account for the coupled train mass as proposed in [7].
5. Single force model: SF+$\Delta\zeta$+$\Delta\rho A_W$. Increased bridge damping $\Delta\zeta$. The *mass* of all *wheel axles* of the train is uniformly *smeared*, $\Delta\rho A_W = 317$ kg/m, and added to the distributed mass ρA of the beam bridge model.

The numerical analysis of the beam deflection and beam acceleration is based on a modal expansion of the *Euler–Bernoulli* beam considering the first five modes. For the single force model the details of the procedure of analysis are found, for instance, in [1]. The substructure approach used here to account for full train–bridge interaction based on the planar MSD train model is described in [11].

In Fig. 2 for these five model representations the peak acceleration max $|\ddot{w}|$ and the dynamic deflection amplification factor S_w of the bridge are plotted against the train speed v in the range from 10 to 85 m/s. Herein, S_w is the dynamic peak deflection of the beam (at any location along the span) related to corresponding static deflection. The black lines correspond to the responses based on the MSD

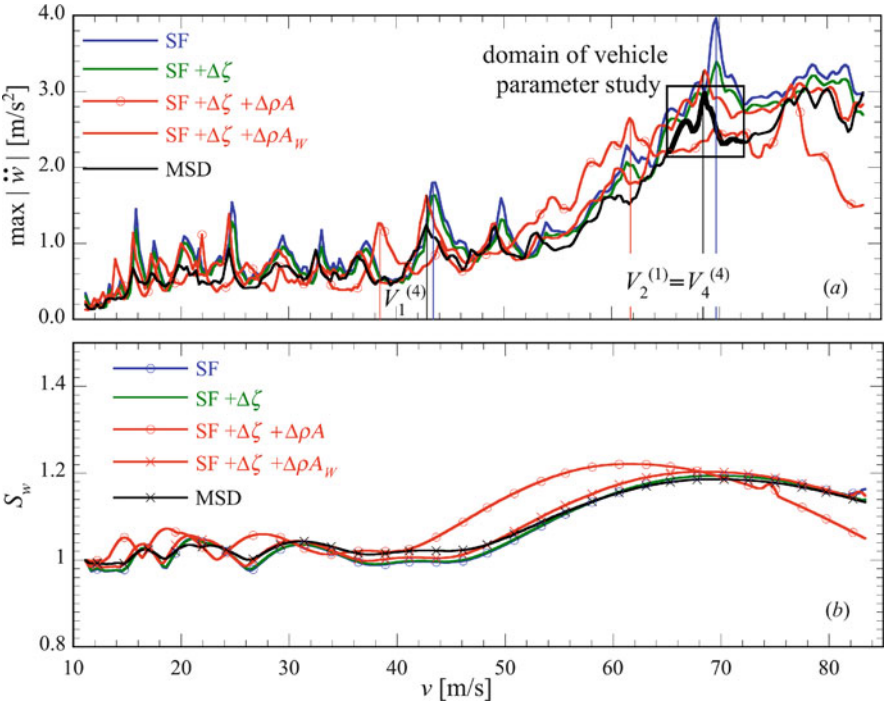

Fig. 2 Dynamic peak bridge response prediction based on different modelling as function of the train speed v. (**a**) Peak acceleration (modified from [10]). (**b**) Dynamic deflection amplification factor

train interaction model, which serves as reference solutions, because it assumingly delivers the most realistic outcomes. The results based on the plain single force load model (SF) are shown in blue. The grey lines refer to the response predictions of the beam with increased damping subjected to the single force model (SF+$\Delta\zeta$). The red lines represent the peak response of the bridge model with increased damping and added smeared train mass (SF+$\Delta\zeta$+$\Delta\rho A$) and added wheel axle mass ($\Delta\zeta$+$\Delta\rho A_W$), respectively, loaded by the single force load model. The peak acceleration response shown in Fig. 2a by the black line shows that compared to the MSD model the SF model overestimates the peak acceleration in the almost entire speed range, and thus, confirms that it leads to quite conservative response prediction. At critical speeds, i.e., speeds where the bridge is excited to a state of resonance, and thus, the response exhibits a local maximum, this overestimation can exceed 100 % compared to the MSD reference solution, in particular at lower speeds. This is not only a result of neglecting the response reduction effect of VBI but can also led back to the shift of the resonance domains to higher speeds. Exemplarily, in Table 1 for the different models the predictions of the two resonance speeds $V_1^{(4)}$ and $V_2^{(1)} = V_4^{(4)}$ are specified, which are also shown in Fig. 2a by vertical lines. Note that the definition of the critical speeds $V_i^{(j)}$ can be found, for instance, in [12]. Inspection of the results reveals that models SF and SF+$\Delta\zeta$, where only the bridge mass is taken into account and the train mass is completely disregarded, overestimate the critical speed $V_1^{(4)}$ by 1.4 % and $V_2^{(1)} = V_4^{(4)}$ by 1.5 % compared to the MSD interaction model. This may become critical if the analysis based on such a simplified modelling approach predicts a critical response peak beyond the considered speed range, although it is in reality within the operational speed limits. If bridge damping is increased according to [3] to account for VBI effects, the peak accelerations are closer to the results of the MSD train interaction model, but they are in general still conservative. Adding the mean smeared train mass to the bridge mass (model SF+$\Delta\zeta$+$\Delta\rho A$) leads to a considerably different peak acceleration predictions in the entire speed range compared to the MSD reference solution. According to Table 1 this modelling approach underestimates the critical speeds by more than 10 %. As a consequence, also the corresponding peak accelerations are in general too small. The difference to the more accurate MSD model response prediction cannot be accepted, and thus, this modelling approach should be applied for short bridges with great care only [7].

Table 1 Resonance speeds based on different train load representations

	Resonance speed $V_1^{(4)}$		Resonance speed $V_2^{(1)}$	
Load model	$V_1^{(4)}$ (m/s)	Difference (%)	$V_2^{(1)}$ (m/s)	Difference (%)
MSD (reference)	42.8	–	68.7	–
SF	43.4	+1.4	69.7	+1.5
SF+$\Delta\zeta$	43.4	+1.4	69.7	+1.5
SF+$\Delta\zeta$+$\Delta\rho A$	38.4	−10.3	61.7	−10.2
SF+$\Delta\zeta$+$\Delta\rho A_W$	42.8	0.0	68.7	0.0

Furthermore, adding the total train mass (which is more than 25 % of the beam mass) to the beam mass reduces the fundamental frequency $f_g^{(\Delta\rho A)}$ to 5.80 Hz, compared to $f_g = 6.55$ Hz of the beam bridge. On the other hand, if only the wheel axle mass is distributed uniformly along the bridge with increased damping (model $\Delta\zeta{+}\Delta\rho A_W$), resonance speeds and peak accelerations are close to the reference solution of the MSD model, compare with Table 1 and Fig. 2a. The fundamental frequency $f_g^{(\Delta\rho A_W)}$ of this model is 6.45 Hz, which is about 1.5 % less than the corresponding outcome of the beam bridge. In contrast to the peak acceleration, the dynamic deflection amplification factor S_w depicted in Fig. 2b is smoother with respect to speed v, indicating that higher modes contribute only minor to the bridge peak deflection. It is also observed that all models except the smeared train mass model SF+$\Delta\zeta$+$\Delta\rho A$ deliver a similar prediction of the peak deflection, and the differences are not significant. Model SF+$\Delta\zeta$+$\Delta\rho A$ is not appropriate because the resonance speeds are considerably underestimated, as discussed before.

3 Parameter Variation in Mass-Spring-Damper Vehicle Model

Assuming that the MSD vehicle model results in the most accurate response prediction, the previous example shows the importance of considering VBI, in particular when predicting the acceleration response. Adding the distributed train mass to the bridge mass overestimates the effect of the train mass on the bridge, because common high-speed trains are in general designed to provide a high passenger riding comfort. A high passenger riding comfort is achieved if the passenger stage of the train cars is dynamically decoupled from the track (and bridge). Consequently, in real trains the natural frequencies of the passenger stage are well separated from the bogies and the bridge. As discussed in [5], the equivalent single-degree-of-freedom (SDOF) models shown in Fig. 3 can be used to estimate the fundamental natural frequencies of car components. The SDOF systems modelling vertical vibrations of the bogie, z_2, (Fig. 3a) and of the passenger stage (car body), z_3, (Fig. 3b) exhibit the

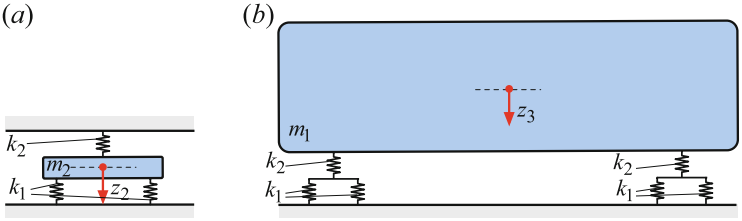

Fig. 3 Simple SDOF systems used to estimate the natural frequency of bogie and passenger stage. (**a**) Bogie frequency model. (**b**) Passenger stage frequency model

Table 2 Comparison of vehicle model parameters and bogie and passenger stage frequencies of selected European high-speed trains

Parameter	Unit	*Railjet* [6, 7]	*ETR500Y* [2]	*Thalys* [4]	*Eurostar* [4]	*ICE-2* [2]
m_1	kg	51,000	34,231	40,900	37,300	30,000
m_2	kg	2300	2760	4200	5000	2500
k_1	10^3N/m	320.0	180.5	2450.0	910.0	1800.0
k_2	10^3N/m	1600.0	808.7	2090.0	2200.0	720.0
f_{body}	Hz	0.54	0.49	1.38	1.01	1.16
f_{bogie}	Hz	6.23	4.06	6.32	5.19	5.73

following natural frequencies [5]:

$$f_{\text{bogie}} = \frac{1}{2\pi}\sqrt{\frac{2k_1 + k_2}{m_2}}, \quad f_{\text{body}} = \frac{1}{2\pi}\sqrt{\frac{2}{\left(\frac{1}{k_2} + \frac{1}{2k_1}\right) m_1}} \tag{1}$$

where m_1 denotes the bogie mass and m_2 the mass of the passenger stage. The linear spring stiffness coefficients k_1 and k_2 model the stiffness of the primary and secondary suspension system, compare with Table 2. In Table 2 estimates for the bogie and car body frequencies evaluated according to Eq. (1) are listed for five different European high-speed trains. Primary and secondary suspension stiffness, and bogie and passenger stage mass of these trains have been extracted from studies specified in Table 2. It is readily observed that for all trains the car body frequency f_{body} is below the lowest estimates of the frequency for high-speed railway bridges according to [3]. In all cases f_{body} is well separated from the bogie frequency f_{bogie}. For the example bridge problem discussed before, the bogie frequency of the *Railjet* train is less than the bridge fundamental frequency. Thus, only the wheels, which are in permanent contact with the bridge as defined in the corresponding assumption for bridge–MSD interaction, contribute to the dynamic active mass of the bridge model. Consequently, modelling approach SF+$\Delta\zeta$+$\Delta\rho A_W$ yields the most accurate response prediction of all non-interacting single force models. However, it should be noted that for other train–bridge systems this simplified approach of adding the wheel mass may be insufficient.

An MSD vehicle model requires many more parameters than a single force train representation, which are, however, not always readily available for each operating train or they may be inaccurate. Furthermore, depending on the train type these parameters such as mass, mass moments of inertia, spring and dashpot coefficients of the various vehicle parts vary in a large range, as indicated by Liu et al. [5] and Kouroussis et al. [4], see also Table 2. These parameters have a large impact on the *vehicle* response. Parametric studies such as [5] have shown that under certain circumstances also the *bridge* response might be sensitive to variations of parameters such as stiffness, damping, and mass of the train model.

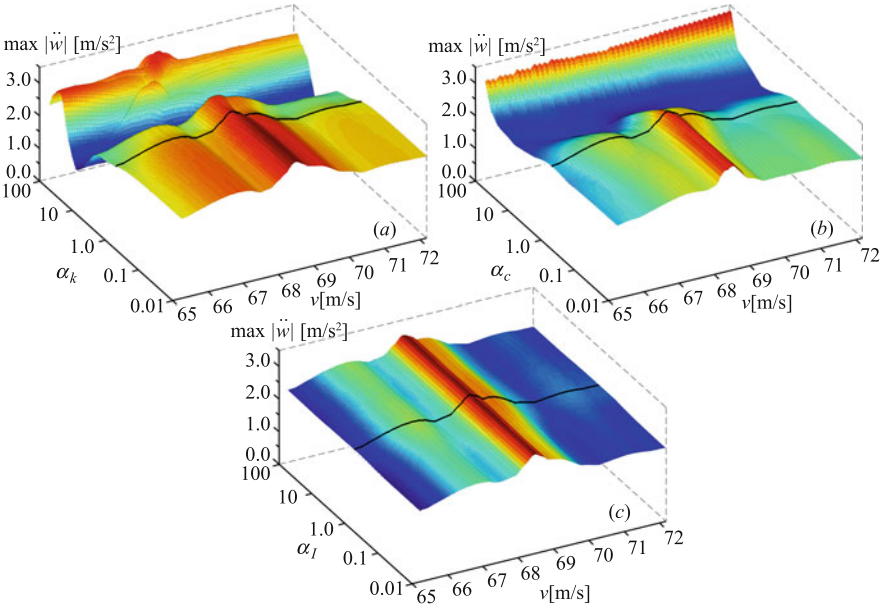

Fig. 4 Influence of (**a**) vehicle stiffness, (**b**) vehicle damping, and (**c**) vehicle mass moments of inertia on the acceleration response. The *black line* corresponds to the reference response with $\alpha_k = \alpha_c = \alpha_I = 1.0$. Modified from [10]

Subsequently, based on the planar MSD vehicle modelling approach the sensitivity of the response of the considered example bridge to vehicle parameter variation is analysed, inspecting its effect on the maximum acceleration around the resonance peak at $V_2^{(1)}$ in the speed range $v = 65.0$–72.0 m/s. In Fig. 2a the considered response domain is framed. In a first study the stiffness coefficients of all springs are varied simultaneously, multiplying each of these coefficients by the non-dimensional stiffness variation factor α_k ranging from 0.01 to 100. In two additional studies the effect of damping and mass moments of inertia variation is assessed separately, utilizing the damping and mass moment of inertia variation coefficients α_c and α_I.

In Fig. 4 the peak acceleration is plotted against the corresponding variation factor α_k, α_c, α_I, respectively, in the considered range of the train speed. Black lines represent the reference solution for $\alpha_k = \alpha_c = \alpha_I = 1.0$, also shown in Fig. 2a. The impact of spring stiffness variation is visualized in Fig. 4a. In the parameter range of α_k between 0.01 and 5 the peak response is almost constant with respect to α_k. In this range the vehicle components above the axles are basically decoupled from the bridge, and only the wheel and axle masses interact with the structure. Thus, the single force model where the wheel axle mass is added to the beam mass delivers the previously discussed accurate response approximation. A major influence on the response is observed when increasing the stiffness by a factor of

$\alpha_k = 10$. In this parameter domain the peak acceleration exhibits a minimum due to a strong interaction of train and bridge. A further increase of stiffness decreases the interaction, and hence, the peak response grows again. A similar effect on the bridge response, however, less pronounced, is observed when varying the initial damping parameter $\alpha_c = 1$, see Fig. 4b. Here, for parameters beyond the global minimum, i.e., $\alpha_c > 10$, very large damping is imposed to the structure, and thus, no local resonance peak can be observed. A variation of the mass moments of inertia of this vehicle model, as depicted in Fig. 4c, has only a minor impact on the peak acceleration response of this example bridge. This result confirms that considering the pitching effect of the vehicle is not of particular importance for an accurate bridge response prediction, and more simple interaction models can also be used, such as proposed in [5, 8].

4 Summary and Concluding Remarks

From the outcomes of this study it can be concluded that models describing the impact of high-speed trains on a bridge by means of single forces (representing the static train axle loads) are very capable of providing accurate results, in particular, if bridge damping is increased and additional dynamic distributed mass is added to the bridge to account indirectly for VBI effects. It has been shown that for the discussed application problem the added mass should correspond to the wheel axle mass instead of the total train mass. Single force models are versatile because different train types can be considered without changing the modelling strategy. In contrast, deriving a more sophisticated MSD vehicle model, whose parameters are often unknown, makes this train modelling approach cumbersome for applications in engineering practice, in particular, because different types of trains must be considered. For conventional, regular, and articulated trains different MSD vehicle models are needed, and for each train the suspension system may be different with respect to component parameters, geometry, and composition. A main advantage of MSD train models is that train–bridge interaction is explicitly taken into account, and thus, rail irregularities can be captured. Furthermore, simultaneously the vehicle response is provided.

References

1. Adam C, Salcher P (2013) Dynamic effect of high-speed trains on simple bridge structures. Struct Eng Mech 51:581–599
2. Doménech A, Museros P, Martínez-Rodrigo MD (2014) Influence of the vehicle model on the prediction of the maximum bending response of simply-supported bridges under high-speed railway traffic. Eng Struct 72(C):123–139
3. Eurocode 1 (2003) Eurocode 1: EN 1991–2: actions on structures

4. Kouroussis G, Conti C, Verlinden O (2012) A comparison of environmental vibratory effects of railway rolling stock using a compound multibody-finite element model. In: Pombo J (ed) Proceedings of the first international conference on railway technology: research, development and maintenance (railways 2012), Las Palmas de Gran Canaria, Spain, 18–20 April 2012, paper no. 124, 19 pp
5. Liu K, De Roeck G, Lombaert G (2009) The effect of dynamic train–bridge interaction on the bridge response during a train passage. J Sound Vib 325(1–2):240–251
6. Mähr TC (2008) Theoretische und experimentelle Untersuchungen zum dynamischen Verhalten von Eisenbahnbrücken mit Schotteroberbau unter Verkehrslast (in German). Doctoral thesis, TU Vienna
7. ÖBB Infrastruktur (2011) ÖBB Infrastruktur: Richtlinie für die dynamische Berechnung von Eisenbahnbrücken (in German)
8. Rigueiro C, Rebelo C, da Silva LS (2010) Influence of ballast models in the dynamic response of railway viaducts. J Sound Vib 329(15):3030–3040
9. Salcher P (2015) Reliability assessment of railway bridges designed for high-speed traffic: modelling strategies and stochastic simulation. Doctoral thesis, University of Innsbruck
10. Salcher P, Adam C (2013) Modelling strategies for bridges subjected to high-speed trains. In: Adam C, Heuer R, Lenhardt W, Schranz C (eds) Proceedings of the Vienna Congress on Recent Advances in Earthquake Engineering and Structural Dynamics (VEESD 2013), Vienna, Austria, 28–30 August 2013, paper no. 94, 10 pp
11. Salcher P, Adam C (2015) Modeling of dynamic train-bridge interaction in high-speed railways. Acta Mech 226(8):2473–2495
12. Yang YB, Yau JD, Wu YS (2004) Vehicle-bridge interaction dynamics. With applications to high-speed railways. World Scientific Publishing Company Incorporated, Singapore

Mechanical Properties of Epoxy Resins Filled with Nano-Silica Particles

Tadaharu Adachi, Markus Karamoy Umboh, Tadamasa Nemoto, Masahiro Higuchi, and Zoltan Major

Abstract In this research, the mechanical properties of epoxy composite filled with nano-silica particles with different crosslinking densities were experimentally studied to clarify the interaction effects between nano-particles and the network structure in matrix resins. The composite materials were prepared by adding 240-nm silica particles to the bisphenol A diglycidyl ether with a volume fraction of 0.2. The bending elastic moduli of the composites were dependent on only the volume fraction of the particles regardless of the particle size and network structures. Filling the nano-silica particles was clarified to improve the bending strength and fracture toughness of the composites with a fine network structure. However the particles acted as defects, reducing the mechanical properties of composites with rough network structures.

T. Adachi (✉)
Department of Mechanical Engineering, Toyohashi University of Technology, 1-1 Hibarigaoka, Tempaku, Toyohashi 441-8580, Japan
e-mail: adachi@me.tut.ac.jp

M.K. Umboh
Department of Mechanical Engineering, Sam Ratulangi University, Jl. Kampus Universitas Sam Ratulangi Bahu, Manado 95115, North Sulawesi, Indonesia
e-mail: markus_umboh@yahoo.com

T. Nemoto
Department of Applied Chemistry, Kobe City College of Technology, 8-3 Gakuenhigashi-cho, Nishi-ku, Kobe 651-2194, Japan
e-mail: nemoto@kobe-kosen.ac.jp

M. Higuchi
School of Mechanical Engineering, Kanazawa University, Kakuma-machi, Kanazawa, Ishikawa 920-1192, Japan
e-mail: higuchi-m@se.kanazawa-u.ac.jp

Z. Major
Institute of Polymer Product Engineering, Johannes Kepler University, Al-tenbergerstrasse 69, 4040 Linz, Austria
e-mail: Zoltan.Major@jku.at

H. Irschik et al. (eds.), *Dynamics and Control of Advanced Structures and Machines*, DOI 10.1007/978-3-319-43080-5_25

1 Introduction

Epoxy composites filled with silica particles are widely applied to various engineering fields, especially the packaging material of electrical devices, etc., because of excellent mechanical, insulation properties, etc. Generally composite is believed to be reinforced by filling particles, fibers, etc., to improve properties. By decreasing the size of the filling particles, namely nanocomposites, properties are expected to be improved more.

The mechanical properties of nanocomposites have been investigated in several previous studies. Particularly the effects of the particle size and volume fraction of the particles on the properties were considered to clarify the mechanism of property improvement. The mechanical properties of composites strongly depend on the network structure and shape of the silica particles, as found by Yamamoto et al. [1], Moloney et al. [2–4], and Adachi et al. [5–7], on the size, shape, and specific surface of the silica particles, as clarified by Nakamura et al. [8–10], and also on distributions of particle size obtained by Preghenella et al. [11], Kitey et al. [12], Butcher et al. [13], and Kwon et al. [14, 15]. In almost all papers, filling with smaller particles was found to be effective to improve mechanical properties. Not only the size of the particles but also the internal structure in the matrix resin, namely the interaction between the particles and the internal structure in the matrix resin should be investigated to improve the mechanical properties of the composites. To consider the interaction effect on the mechanical properties of epoxy composites filled with nano-silica particles, we utilized non-stoichiometric curing of the epoxy matrix resins to vary not the size of the silica particles but the network structure of the matrix epoxy resins. The concept of the non-stoichiometric curing is illustrated schematically in Fig. 1 to consider the interaction. Because the curing is conducted under the stoichiometric condition, the network structure in the epoxy matrix resin is fine. The network structure after non-stoichiometric curing is rough in comparison with the structure after the stoichiometric curing. Therefore, the interaction between the particles and the internal structure can be studied by manufacturing epoxy composites with different network structures. By using this concept, we have reported and discussed the dynamic compression behavior [16], elastic modulus, strength [17], and fracture toughness [18] of the epoxy composites with different network structure in the matrix resins. This paper summarized these results.

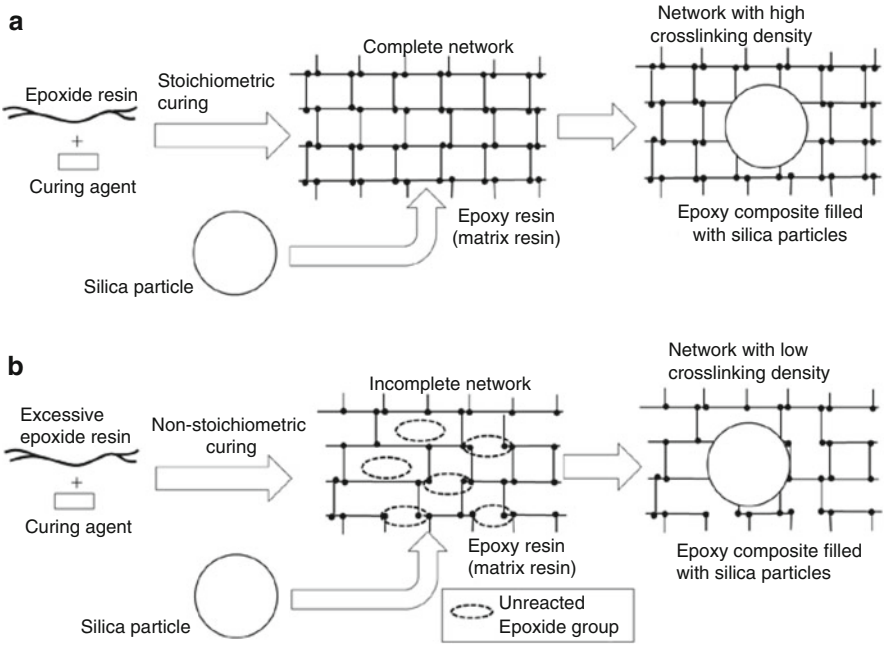

Fig. 1 Schematic internal structure in epoxy filled with nano-silica particles. (**a**) Stoichiometric curing. (**b**) Non-stoichiometric curing

2 Materials

The specimen materials were epoxy resin filled with spherical silica particles. The epoxy resin was cured after mixing bisphenol A diglycidyl ether (DGEBA) (Asahi Kasei E-Materials, AER 2603) with methyl tetrahydrophthalic anhydride (New Japan Chemical, Rikacid MH-700) as the curing agent, 2,4,6-tris (dimethyl aminomethyl) phenol (Mitsubishi Chemical, jER BMI12) as the accelerator, and the particles. The equivalent weight of the DGEBA was 188 g/equivalent, and the acid anhydride equivalent weight of the curing agent was 162 g/equivalent. The weight ratio of the resin, the agent, and the accelerator was 100:86:0.5 according to stoichiometry.

The filler was silica particles with a median diameter of 240 nm (Tatsumori, SO-C1). The surfaces of the particles were not chemically coated to avoid agglomeration of the particles in the matrix during mixture before curing. The volume fraction of the silica particles was constantly 0.2 for every composite.

The mixture ratio of the DGEBA to the curing agent was varied to manufacture the composites and neat epoxy resins with different crosslinking densities. The mixture ratio of the epoxy resin to the curing agent was defined as the epoxy-equivalent-weight ratio (EEWR) expressed by the DGEBA weight over the stoichiometric DGEBA weight in the mixture. The EEWRs were prepared in a range

Table 1 Specimen materials

Material	Epoxy resin (weight ratio)				Volume fraction of particles
	DGEBA	Current agent	Accelerator	EEWR	
Composite	100	86	0.5	1.0	0.2
	160	86	0.5	1.6	0.2
	200	86	0.5	2.0	0.2
	240	86	0.5	2.4	0.2
	280	86	0.5	2.8	0.2
	320	86	0.5	3.2	0.2
Neat epoxy	100	86	0.5	1.0	0.2
	160	86	0.5	1.6	0.2
	200	86	0.5	2.0	0.2
	240	86	0.5	2.4	0.2
	280	86	0.5	2.8	0.2
	320	86	0.5	3.0	0.2

EEWR epoxy-equivalent-weight ratio
EEWR=1.0: stoichiometric curing. EEWR≠1.0: non-stoichiometric curing

from 1.0 to 3.2, and the accelerator was kept constant at 0.5, as listed in Table 1. The composite and neat epoxy resin with the EEWR=1.0 had complete network structures, and the ones with the EEWR>1.0 had incomplete, namely rough network structures. The composites and neat epoxy resins with the EEWRs>3.2 were not produced because the materials were too weak to measure viscoelastic properties. The composites and neat epoxy resins with EEWRs<1.0 because unreacted curing agents could be transferred from the cured resins.

The silica particles were blended with the epoxy resin containing the curing agent and accelerator until all particles dispersed without agglomeration. The mixture was cured in an aluminum mold coated with a teflon sheet after degassing. The curing process was two steps of pre-curing, where the mixture was kept at 373 K for 2 h to gel the matrix resin, and post-curing, which greatly affected the crosslinking reaction of the resin. The post-curing was performed at 403 K for 15 h.

The thermo-viscoelastic properties of the composites and neat epoxy resins were measured with a dynamic viscoelastometer (UBM, Rheogel-E4000) using a non-resonance tensile mode with a frequency of 10 Hz. The measurements were conducted at 1 K intervals ranging from 223 to 493 K to characterize glass transition temperatures and crosslinking densities. The glass transition temperatures, T_g, were determined at peaks of the maximum $\tan\delta$ of their loss moduli. The crosslinking density, n, of the matrix resins was calculated from the dynamic storage moduli, E', in a rubbery state: $T_g + 30$ to $T_g + 50$ K of the neat epoxy resins according to [19, 20],

$$E' = 3nRT, \tag{1}$$

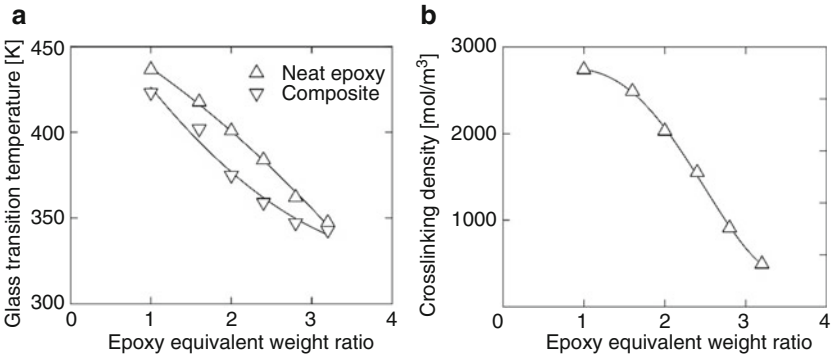

Fig. 2 Characterizations of specimen materials. (**a**) Glass transition temperature. (**b**) Crosslinking density of epoxy matrix resin

where R and T are the gas constant ($= 8.3145\,\mathrm{J/(mol\,K)}$) and the absolute temperature.

The characterized results are shown in Fig. 2. The glass transition temperature decreased as the EEWR increased, namely far from stoichiometric curing. The glass transition temperature of the composites was lower than the one of the neat epoxy resins regardless of the EEWR because of the interaction between the nano-particles and the network structure in the matrix resins. The composites with the epoxy matrix resins having different network structures could be prepared because the crosslinking density of the matrix resin was found to decrease as the EEWR increased.

3 Experimental Procedure

Three-point bending tests were conducted at room temperature in accordance with ASTM standard D790-07 to measure the bending elastic moduli and the bending strengths. The specimens were 100 mm long, 15 mm wide, and 5 mm thick. The span length between the supports was 60 mm. The constant deflection rate was 50 μm/s at the loading point by using a universal materials testing machine (Shimad-zu, AGS-J). Because every measured load-deflection curve was approximately linear until breaking, the bending elastic modulus, E_B, and bending strength, σ_B, of each specimen were determined using the following equations:

$$E_B = \frac{L^3 m}{4WB^3}\,,\ \sigma_B = \frac{3P_{\max}L}{2WB^2}, \tag{2}$$

where m, P_{max}, W, B, and L are the slope of the initial linear portion of the load-deflection curve, maximum load, width, thickness, and span length of the specimens, respectively.

Single-edge-notched bending tests were carried out at room temperature to measure the mode I fracture toughness according to ASTM standard D5045-99. The specimens were 100 mm long, 20 mm high, and 5 mm wide. The length of pre-crack at the middle point of the specimen and span length between the supports were 10 and 60 mm, respectively. The constant deflection rate at the loading point was 50 μm/s by using the universal materials testing machine. Because every measured load-deflection curve was linear until fracture, the linear fracture mechanics could be applied to evaluate the fracture toughness of each material. Namely, the critical stress intensity factor, K_{IC}, could be calculated as fracture toughness by using the following equation:

$$K_{IC} = \frac{3}{2}\frac{P_{max}L\sqrt{a}}{WB^{3/2}}\left[\frac{1.99-\alpha\,(1-\alpha)\left\{2.15-3.93\left(\alpha+2.7\alpha^2\right)\right\}}{(1+2\alpha)\,(1-\alpha)^{3/2}}\right],\ \alpha=\frac{a}{W}, \tag{3}$$

where P_{max}, B, L, W, and a correspond to the maximum load, width, span length, height, and pre-crack length of the specimens.

4 Results

Figure 3 shows the mechanical properties of the neat epoxy resins and composites. In this figure, the triangles and inverted triangles are the averages of the composites and the neat epoxy resins calculated from more than five experimental results. The error bars indicate the standard deviations of the experiment data, and the solid lines in Fig. 3b, c shows the fitting curves.

The bending elastic moduli of both materials were compared in Fig. 3a. The moduli increased in the neat epoxy resins slightly as the crosslinking densities of the resins decreased. The measured moduli of the composites were in agreement with the solid line in this figure evaluated using the mixture law of Lewis and Nielsen [21] with the measured results of the neat epoxy resins. Because the law was calculated only with the volume fraction of the particle and the elastic moduli of the particle and the matrix, the elastic moduli of the epoxy composites was found to be independent of the network structure in the matrix resins.

Figure 3b shows the bending strengths of both materials. The strength of the composites with high crosslinking densities above approximate 2000 mol/m^3 was a little larger than that of the neat epoxy resin with the same crosslinking density. In contrast, the strengths of the composites with the crosslinking density below 2000 mol/m^3 were much smaller.

Figure 3c shows the fracture toughness of each material. Similar to the results of the strength, the fracture toughness of the composites with high crosslinking

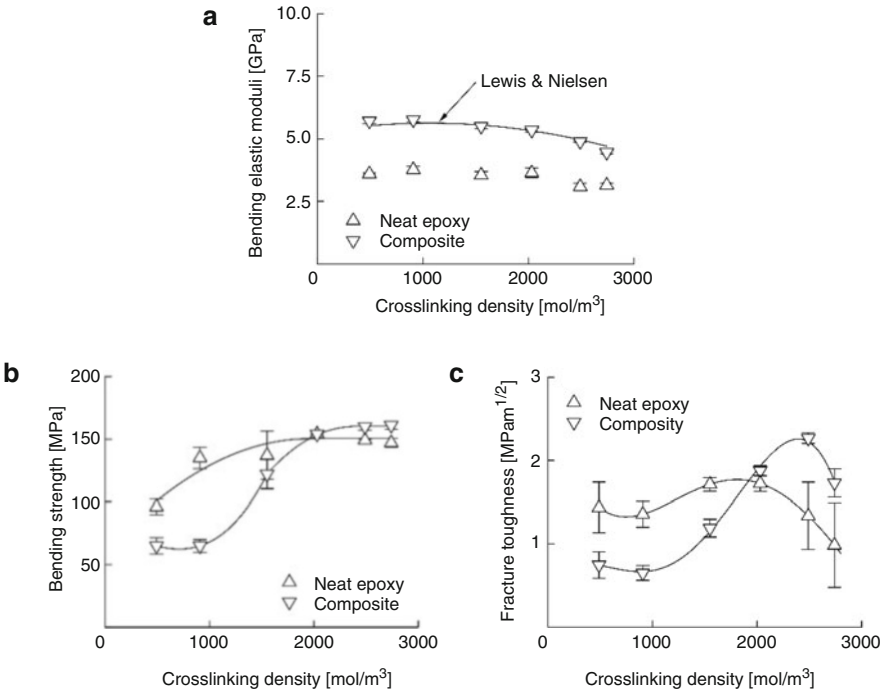

Fig. 3 Mechanical properties. (**a**) Bending elastic modulus. (**b**) Bending strength. (**c**) Fracture toughness

density above approximate 2000 mol/m^3 was much larger than that of the neat epoxy resins with the same crosslinking densities, In contrast, the fracture toughness of the composites with the crosslinking density below 2000 mol/m^3 decreased rapidly.

The results of the bending strength and fracture toughness mean that the matrix resin was not always reinforced by the particles and that the particles in the matrix resin with low crosslinking density acted as defects in these properties.

5 Discussion

The properties were normalized using the following parameter to clarify the reinforcement effect of filling the particles on the mechanical properties:

$$f_{\mathrm{Nor}} = \frac{f_{\mathrm{Comp}} - f_{\mathrm{Epoxy}}}{f_{\mathrm{Epoxy}}}, \tag{4}$$

where f is the mechanical properties of the bending elastic modulus, bending strength, and fracture toughness. Its subscripts of Nor, Comp, and Epoxy denote

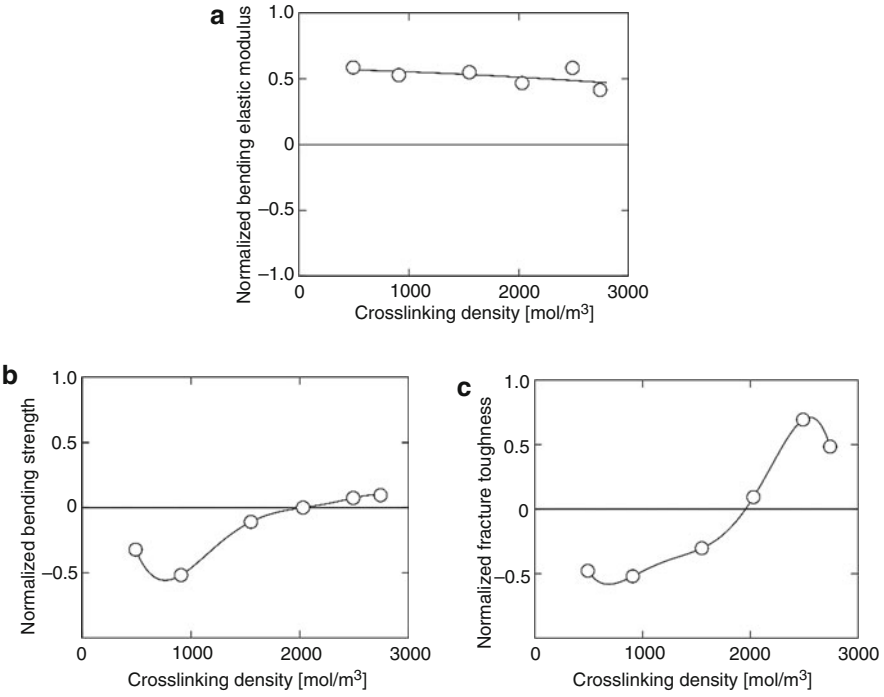

Fig. 4 Normalized mechanical properties. (**a**) Bending elastic modulus. (**b**) Bending strength. (**c**) Fracture toughness

the normalized mechanical property and the properties of the composites and neat epoxy resins, respectively. The positive f_{Nor} means that filling the particles reinforced the epoxy matrix.

The normalized mechanical properties are shown in Fig. 4. The normalized elastic modulus in Fig. 4a was roughly constant regardless of the crosslinking density of the matrix resin. The normalized bending strength was positive above the crosslinking density of 2000 mol/m^3. Below the crosslinking density of 2000 mol/m^3, which is the composites with rough network structures in the matrix resins, the particles were found clearly to be defects, reducing the bending strength and fracture toughness. We found that the particles reinforced the resins with crosslinking densities higher than 2000 mol/m^3 to improve the strength and fracture toughness of the composites.

The crosslinking density where the normalized fracture toughness was zero was the same as the one where the normalized bending strength was zero. This result suggests that the interaction between the particles and the network structure in the matrix resin affected the fracture toughness and also the strength, although the fracture toughness was more sensitive to the interaction.

6 Conclusion

The mechanical properties of epoxy composites filled with nano-silica particles with different crosslinking densities were experimentally studied to clarify the interactive effects between nano-particles and the network structure in matrix resins. The epoxy composite materials filled with the silica particles of 240 nm in diameter were prepared by curing non-stoichiometrically to change the crosslinking densities of the matrix resins. The bending elastic moduli of the composites were found to be dependent on only the volume fraction of the particles regardless of the particle size and network structures. The nano-silica particles were clarified to improve the bending strength and the fracture toughness of the composites with the fine network structure above a crosslinking density of 2000 mol/m^3, although the particles acted as defects, reducing the mechanical properties of the composites with rough network structures below 2000 mol/m^3. The interaction between the nano-particles and the network structure in the matrix resin improved the fracture toughness rather than the bending strength. Therefore, the particles size or the network structure in the matrix resin must be optimized to improve the mechanical properties of the composites taking into account the interaction.

Acknowledgements This work was supported by the Japan Society for the Promotion of Science (JSPS), KAKENHI, Grant Number 25420013.

References

1. Yamamoto I, Higashihara T, Kobayashi T (2003) Effect of silica-particle characteristics on impact/usual fatigue properties and evaluation of mechanical characteristics of silica-particle epoxy resins. Int JSME J 46:145–153
2. Moloney AC, Kausch HH, Stieger HR (1983) The fracture of particulate-filled epoxide resins. J Mater Sci 19:208–216
3. Moloney AC, Kausch HH, Kaiser T, Beer HR (1987) Review determining the strength and toughness of particulate filled epoxide resins. J Mater Sci 22:381–393
4. Moloney AC, Cantwell WJ, Kausch HH (1987) Parameters determining the strength and toughness of particulate-filled epoxy resins. Polym Compos 8:314–323
5. Adachi T, Araki W, Nakahara T, Yamaji A, Gamou M (2002) Fracture toughness of silica particulate-filled epoxy. J Appl Polym Sci 86:2261–2265
6. Adachi T, Osaki M, Araki W, Kwon SC (2008) Fracture toughness of nano- and micro-spherical silica-particle-filled epoxy composites. Acta Mater 56:2101–2109
7. Adachi T, Higuchi M, Araki W (2010) Mixture law including particle-size effect on fracture toughness of nano- and micro-spherical particle-filled composites. Acta Mech 214:61–69
8. Nakamura Y, Yamaguchi M, Kitayama A, Okubo M, Matsumoto T (1991) Effect of particle size on fracture toughness of epoxy resin filled with angular-shaped silica. Polym 32:2221–2229
9. Nakamura Y, Yamaguchi M, Okubo M, Matsumoto T (1991) Effect of particle size on impact properties of epoxy resin filled with angular shaped silica particles. Polym 32:2976–2979

10. Nakamura Y, Yamaguchi M, Okubo M, Matsumoto T (1992) Effects of particle size on mechanical and impact properties of epoxy resin filled with spherical silica. J Appl Polym Sci 45:1281–1289
11. Preghenella M, Pegoretti A, Migliaresi C (2006) Atomic force acoustic microscopy analysis of epoxy-silica nanocomposites. Polym Test 25:443–451
12. Kitey R, Tippur HV (2005) Dynamic crack growth in particulate bimaterials having discrete and diffuse interfaces: Role of microstructure. Eng Fract Mech 72:2721–2743
13. Butcher RJ, Rousseau CE, Tippur HV (1998) A functionally graded particulate composite: preparation, measurements and failure analysis. Acta Mater 47:259–268
14. Kwon SC, Adachi T, Araki W, Yamaji A (2005) Effect of particle size on fracture toughness of spherical-silica particle filled epoxy composites. Key Eng Mater 207–300:207–212
15. Kwon SC, Adachi T, Araki W, Yamaji A (2006) Thermo-viscoelastic properties of silica particulate reinforced epoxy composites: considered in terms of particle packing model. Acta Mater 54:3369–3374
16. Adachi T, Oishi K, Higuchi M, Umboh MK, Major Z (2013) Non-stoichiometric curing effect on dynamic mechanical properties of bisphenol A-type epoxy resins. J Jpn Soc Exp Mech 13:s148–s153
17. Umboh MK, Adachi T, Oishi K, Higuchi M, Major Z (2013) Mechanical properties of nano-silica particulate-reinforced epoxy composites considered in terms of crosslinking effect in matrix resins. J Mater Sci 48:5148–5156
18. Umboh MK, Adachi T, Nemoto T, Higuchi M, Major Z (2014) Non-stoichiometric curing effect on fracture toughness of nanosilica particulate-reinforced epoxy composites. J Mater Sci 49:7454–7461
19. Bignotti F, Pandini S, Baldi F, De Santis R (2011) Effect of the resin/hardener ratio on curing, structure and glass transition temperature of nanofilled epoxies. Polym Compos 32:1034–1048
20. Ward IM (1990) Mechanical properties of solid polymers, 2nd edn. Wiley, New York
21. Nielsen LE, Landel RF (1994) Mechanical properties of polymers and composites, 2nd edn. Marcel Deckker, New York